THE UNIVERSITY OF
SYDNEY

The Galactic ecosystem:

Outflow and infall in the halo of the Milky Way

Vanessa A. Moss

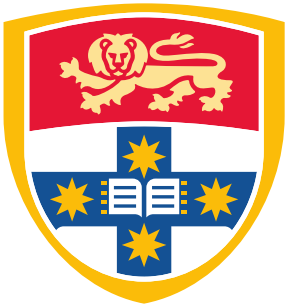

A thesis submitted in fulfilment of
the requirements for the degree of
Doctor of Philosophy
Faculty of Science
University of Sydney

June, 2015

Abstract

The evolution, dynamics and eventual fate of galaxies is largely determined by access to and distribution of their primary fuel: atomic neutral hydrogen. Neutral hydrogen is not only pervasive in the disk of galaxies such as the Milky Way, but can also be found in the hot halo surrounding galaxies. The signatures of hydrogen detected in galactic haloes are caused by three key processes: outflow, due to energetic events associated with the galactic disk; infall, due to interactions with other nearby galaxies or the intergalactic medium; and circulation within the galactic ecosystem.

In this thesis, a nearby Galactic supershell GSH 006−15+7 is studied, in order to understand how supershells are able to circulate cold gas between the disk and halo. By analysing HI self-absorption in the shell wall, the spin temperature of the gas is constrained to be cold and dense. Based on the morphology of the supershell and its estimated distance, GSH 006−15+7 has a likely origin in the Sagittarius OB 1 association of young stars. There is also evidence that the shell is transitioning into a chimney structure based on fragmentation at high Galactic latitudes, with an associated ionised hydrogen feature indicating a potential position of break-out into the Milky Way halo. This result is supported by findings in optical emission lines of high energy activity.

Anomalous velocity gas deviates from that expected of Galactic rotation, and as such pinpoints hydrogen that is part of the cycle of outflow, infall and circulation. The Galactic All Sky Survey (GASS) of southern-sky neutral hydrogen is used to catalogue anomalous velocity gas in the halo of the Milky Way. Both classical high-velocity clouds and anomalous velocity clouds are included in the catalogue. With their lower velocities, anomalous velocity clouds are intrinsically closer to Galactic rotation and hence can be expected to probe the bridge between the Galactic disk and the halo. The GASS catalogue features unprecedented combination of high sensitivity with high angular and spectral resolution in the southern sky, and will be useful for studies of anomalous velocity gas on various scales. Several GASS clouds are followed up, some of known origin, at high angular resolution with the Australia Telescope Compact Array in order to determine the relative influences of origin and environment in clouds showing evidence of interaction.

By combining the population of GASS high-velocity clouds with a very sensitive survey of neutral hydrogen in the halo, a Milky Way halo hidden from typical surveys of neutral hydrogen due to sensitivity limits is revealed, where the brightest neutral hydrogen merges with a diffuse prevalent medium that is likely to contribute just as much gas content as the bright high-velocity clouds. These results are consistent with findings in other wavelengths indicating the presence of more hydrogen in the halo than detected in the high-velocity cloud population. If the detected diffuse gas follows predicted supernova-driven models of cooling, then these two populations of neutral hydrogen combined can potentially account for the entire Galactic star formation rate.

Overall, the studies in this thesis have revealed an active and dynamic Galaxy that maintains strong connections between its disk and the surrounding halo environment, in which neutral hydrogen remains a pivotal and powerful key to unlocking its evolutionary past and star-forming future.

Acknowledgements

It's hard to remember how the late-2010 version of myself began this PhD journey, and even harder to remember the numerous people who contributed in both large and small ways throughout the last few years. This list of acknowledgements is an attempt to do so, and I hope I've managed to cover everyone.

Firstly, thank you very much to my supervisors. Thank you Naomi, for teaching me so much about the study of the Galaxy, for structuring my PhD cleverly so that the first six months would help a previously continuum-observer learn about this mysterious third dimension called 'velocity', and for helping me transition from a confused, bewildered first-year PhD into a more confident, analytical researcher. Thank you Tara for keeping me aware of the big picture, for your advice throughout my PhD, and for helping me keep the balance between methodology and science. Thank you both for giving me the freedom to be independent throughout my PhD, and for being there to guide me when I got stuck.

A huge thanks to Anne Green, who was the reason and inspiration behind my decision at the start of university to continue on to Physics Honours, and who has always been a source of wisdom and guidance in all my time at USyd. Thank you to my mentor Andrew Walsh, who has been an indispensable pillar of advice, feedback, friendship and fun throughout my PhD on things both work-related and not. To Kevin Mahony, who convinced me back in high school that physics wasn't all about wedges and pulleys and made the subject both fun and understandable. To everyone who supervised me as an undergraduate in student research projects, giving me an idea of what research would be like at higher levels. To Joe Khachan, our chats have been a highlight throughout my time at uni. To the amazing and inspiring Josh Peek, who has been an awesome part of my HI world from the start – Galaxy represent! Thank you to Shari, who has been there to offer advice and for chats about anything and everything from the beginning.

To the students of the 2010 ATNF synthesis school and co-discoverers of the ATCA geocache: Anita, Jay, Graeme, Justin, Stephan, Johannes, Kitty, Glen – you guys made the very start of my PhD awesome, and made the ASA meetings a reunion of happy fun times. To the fellow members of Running Away From Ponies: Chris, Anita, Graeme and Glen – keep running! To my friends in other physics places and tearoom buddies: Andrew, Brett, Daniel, Joel, Sam, Dave, Silvy, Phil, Maki, Matt, Hannah, Michael, Tom, Madusha - you guys rock like an Onix. To my IT pals who inspire me to be a better coder: Tim, Dom, Smerity, Ben. To Ansart先生, 平井さん and Montgomeryさん, who have always been so keen to hear about my physics adventures. To Jessie, who I haven't seen as frequently as I would like during my PhD – can't wait to go cruising with you! Thank you to Niels Bohr who was the first example for a younger me that scientists were not just distant stereotypical figures (Bohr bietet mehr!), and to Anna Oldsen who offered valuable advice on choosing future studies at a critical time.

Thank you to the University of Sydney having me for ten years (and counting!). During my candidature I received the financial support of an Australian Postgraduate Award. Thanks to Eve, Sang, Alexis, and the administrative team for their assistance over the years with both admin and teaching. Thanks to the many USyd academics, postdocs and PhD students who have aided me in various quests over the years – I don't want to try and name you all because I'll forget someone, but you are awesome! Special thanks to my coffee buddy and fellow SNR-hunter Sarah Reeves, and to my co-conspirators in the back corner (Pat Noble, Chris Betters, John Ching, Yitping Kok). Thank you to Bryan Gaensler and the Extreme research group for the weekly fun and for giving me a research group to call home these past few years, I've learnt so much from all of you.

Thank you to CSIRO Astronomy and Space Science for having me in their co-supervision program and for providing support, funding and resources over the course of my PhD and during thesis time. Thanks especially Julie Tesoriero and Vicki Drazenovic who have helped me out with various admin things over my time as a CASS student, and to Simon Johnston, Baerbel Koribalski and George Hobbs during my time in the student program. To the awesome folks at the Australia Telescope Compact Array in Narrabri, who made observing and being duty astronomer some of the highlights of my PhD. Thanks to Robin Wark for always being the fountain of knowledge about everything ATCA both work-related and fun-related. Thanks to Jamie Stevens for always being able to answer any question I could possibly have about data and ATCA. Thanks to Marg for making my stays go smoothly and for always being so cheerful and friendly. Thank you to Nathan Pope, who has saved me from network problems innumerable times! Thanks to other CSIRO people that have offered advice during my time there: Phil Edwards, Tasso Tzioumis, Jo Dawson, Aidan Hotan, Alex Hill, Lisa Harvey-Smith, Max Voronkov, Matt Whiting, Malte Marquarding, Peter Kamphuis, Robert Braun, Russell Jurek and James Allison. Thanks also to the fantastic astronomers at AAO, who are way too many to count!

Thank you to all the staff and guides at Sydney Observatory, you guys are the coolest and I have so much enjoyed giving tours on astronomy alongside you. Thank you particularly to Toner Stevenson and Geoff Wyatt for humouring and encouraging my random inventions for tours, and to Mo for making every shift enjoyable and for keeping me caffeinated (I'll pay back that tab some day). And thank you to everyone who came on tours with me, for helping me to better develop my abilities to speak in front of people, for all the great questions, and for being my captive audience for 1.5 hours. Thank you to everyone involved with .Astronomy and who attended .Astronomy 5, you guys blew my mind with your awesomeness and introduced me to a whole other side of astronomy.

To the Cougars/Doh'nuts, some of who I've played basketball with for 13 years now - you guys kept me sane and prevented the PhD from turning me into a complete doughnut. More recently, to the Lemmings, who filled my Sunday evenings with fun before Monday struck again. To Aurelia, Razgris, Duvan and DM, for providing a fun distraction from my imminent thesis completion. Thanks to the animals in my life, for keeping my life interesting and encouraging me to go outdoors sometimes: Harry, Tesla, Tiger, the snails (at one point), and the baby snails (at another). I miss your ridiculous unending happiness, Tiger. Thank you to 1D, which oddly turned out to be the music of choice during the final throes of thesis. Thank you to AXL, who helped me traverse Sydney – you'll make it to the Moon yet.

Thank you to the extremely awesome people who helped to proof-read my thesis and various sections of it, including my collaborators (Naomi McClure-Griffiths, Tara Murphy, Alex Hill, Greg Madsen, Jo Dawson, D.J. Pisano, Alyson Ford, and Jay Lockman), Geoff Sims (CONFUSE EMISSION!), Mum and Glen Rees. Thank you also to my awesomely excellent and thorough thesis reviewers for their comments: Tobias Westmeier, Snezana Stanimirovic and Mary Putman. Thank you Elaine Sadler for patiently understanding as I slowly plodded through thesis comments, super excited to be a part of #teamflash!

Thank you, finally, to my parents and my brother Rayner: thanks for always being there and for all your help over the years, I couldn't have got here without you. Sorry you didn't get to see the end of thesis times, Dad - we miss you. Thanks also to my extended Sydney family: Aunty Liz, Uncle Hii and other brother Matt. Thanks to my second family in the UK: Tally, Pete, Craig, Becky, Margaret, Martin, can't wait to see you when I'm thesis-free! And lastly, thank you to Glen, who has seen me through my whole thesis and been there for me throughout, you're the best.

Statement of originality

This thesis describes work carried out in the Sydney Institute for Astronomy at the University of Sydney and at CSIRO Astronomy and Space Science between 2010 and 2014. Except where otherwise acknowledged, the work presented in this thesis is my own. Throughout I have chosen to adopt the first person plural to reflect the collaborative nature of research. The following summarises the contributions of others to chapters other than the introduction and conclusion, which were constructed and written by myself only.

Chapter 2
Acknowledgements are reproduced as they appeared in the original paper:
We are grateful for the use of 21 cm continuum data from the HIPASS survey (Calabretta et al., 2011, in preparation) for the HISA background calculation. This research has made use of the SIMBAD *database, the* VIZIER *catalogue access tool and* ALADIN*, operated at CDS Strasbourg France and the* WEBDA *tool, operated at the Institute for Astronomy of the University of Vienna. WHAM and SHASSA are each supported by the US National Science Foundation. Smooth remote operations of WHAM are made possible by L. M. Haffner, K. A. Barger, and K. P. Jaehnig at the University of Wisconsin-Madison and the excellent staff at the Cerro Tololo Interamerican Observatory, particularly O. Saa. We also would like to thank J.R. Dawson, T. Murphy, F.J. Lockman, K.J. Brooks, J.E.G. Peek, J.A. Green, S.L. Breen, J.M. Rathborne, T. Robishaw, S.A. Farrell, M.L.P. Gunawardhana and G.A. Rees for helpful discussions during this research.*

Chapter 3
The Wisconsion H-Alpha Mapper data (pointed observations of Hα, Hβ, [S II], [N II], [O III] and He I) was observed by Alex Hill. The Hα, [S II], [O III] and He I data was reduced by Alex Hill, and the Hβ and [N II] data was reduced by Joanne Barnes. The January 2013 observations of the Cuttlefish with the Australia Telescope Compact Array were taken by Eromanga Adermann and reduced by me in February 2014. The March 2014 observations of the Cuttlefish with the Australia Telescope Compact Array were both observed and reduced by me, and combined with the January 2013 data.

Chapter 4
Acknowledgements are reproduced as they appeared in the original paper:
We would like to acknowledge our anonymous referee for their constructive suggestions, A.J. Green and A.J. Walsh for useful discussions during the development of this paper, R. Jurek for assistance with the application of his blind matched filtering detection algorithm and C.R. Purcell for help with the manuscript format. This research made use of APLpy, an open-source plotting package for Python hosted at http://aplpy.github.com.

Chapter 5
Archival data from Australia Telescope Compact Array projects C1139 (PI: Bruens), C1470 (PI: Ford) and C1747 (PI: McClure-Griffiths) was included in the analysis. The data for C1139 and C1470 was downloaded from the Australia Telescope Online Archive and reduced by me. The data for C1747 was obtained from Naomi McClure-Griffiths in reduced form. Alex Hill observed the last three hours for C2849 on the 22nd June 2013. All other observational data was both observed and reduced by me.

Chapter 6

The Parkes Radio Telescope is part of the Australia Telescope National Facility which is funded by the Commonwealth of Australia for operation as a National Facility managed by CSIRO. The Robert C. Byrd Green Bank Telescope is operated by the National Radio Astronomy Observatory, which is a facility of the US National Science Foundation operated under cooperative agreement by Associated Universities, Inc. VM is grateful for support from both the University of Sydney and CSIRO Astronomy and Space Science which facilitated this work. This research made use of APLpy, an open-source plotting package for Python hosted at http://aplpy.github.com, and the MIRIAD software package developed by the ATNF. Figure 6.1 was produced using VizSpec, developed by VM. We would also like to thank J.R. Dawson, A.S. Hill, S.L. Breen and G.A. Rees for helpful discussions and feedback during this research.

Vanessa A. Moss
Sydney, Australia
June 2015

/

Contents

[†]This chapter is published in a peer-reviewed journal.

Chapter

1 THE ROLE OF NEUTRAL HYDROGEN IN GALACTIC ECOSYSTEMS

Overview

This chapter summarises the influence of neutral hydrogen on the evolution of galaxies, focusing on the Milky Way. Emphasised here particularly are developments in astronomy related to the main themes of this thesis: the neutral hydrogen spectral line, supershells, anomalous velocity gas, high-velocity clouds and the structure of the Galactic halo.

1.1 A history of neutral hydrogen in the Milky Way

The history of neutral hydrogen (denoted as HI) in astronomy and its detection is tied closely to the early development of radio astronomy. The first radio signals from space were detected serendipitously by Karl Jansky in 1932 during his work with Bell Labs (Jansky, 1932, 1933a,b), and were described as interference that was correlated with the sidereal day and corresponding movement of the sky. Five years later, Grote Reber built a parabolic dish in his backyard specifically to trace these celestial radio signals, and produced the first maps of the radio sky (for early results, see Reber, 1940, 1944). While the discovery and detection of 'cosmic static' was initially challenging to the established field of astrophysics (which was dominated by optical astronomy at the time), these early discoveries soon began a boom in radio astronomy (Pawsey & Hill, 1961) that continues to the current day.

In the early 1940s, Jan Oort realised the potential importance of radio astronomy, particularly if it could lead to the detection of atomic and molecular radio lines. He communicated this to Henrik van de Hulst who, in 1944, predicted the detection of the neutral hydrogen atomic line at a frequency of 1420.4058 MHz. This low-energy emission, produced by the low probability spin-flip transition of the hydrogen atom (2.9×10^{-15} s^{-1}), would be easily detectable celestially due to the immense quantity of hydrogen in the universe. The first detection of the atomic HI line followed in 1951, at almost the same time in the US, Australia and Europe (Ewen & Purcell, 1951; Muller & Oort, 1951; Pawsey, 1951; Christiansen & Hindman, 1952), leading to the first models of Galactic structure based on observations of the HI spectral line (Hulst, Muller & Oort, 1954; van Woerden, Rougoor & Oort, 1957).

A decade later, Muller, Oort & Raimond (1963) reported the discovery of *hydrogène neutre dans la couronne galactique* (neutral hydrogen in the Galactic corona), describing neutral hydrogen that had been detected in the halo of the Milky Way at high velocity relative to the Sun. This was the first reported discovery of what has since become known as anomalous velocity gas (including high-velocity gas, intermediate-velocity gas and low-velocity gas, all of which are measured with respect to the Galaxy). Oort (1966) published a detailed analysis of possible interpretations of the high-velocity gas, which had by then become referred to as high-velocity clouds (HVCs). In it, he described potential Galactic and extragalactic origins for HVCs, and in the years since this noteworthy paper, each of Oort's proposed hypotheses for HVC origins has been observationally confirmed to some degree.

Heiles (1976) published the discovery of expanding neutral hydrogen structures, using the Weaver & Williams (1973) survey. These holes in the Galaxy, dubbed 'shells' and 'supershells', were consistent with the theoretical picture of an interstellar medium driven by the turbulent activity of supernova explosions as constructed by Cox & Smith (1974) and expanded by McKee & Ostriker (1977). The first catalogues of supershells were subsequently compiled (Heiles, 1979; Hu, 1981; Heiles, 1984), although the southern hemisphere was for the most part neglected due to the lack of large-scale sensitive HI surveys at the time. Later, less coherent structures in the disk known as 'chimneys' were argued to be the later stage of evolution for supershells (Low & McCray, 1988; Dove, Shull & Ferrara, 2000), forming after the supershell has blown out and fragmented at large heights above the disk and allowing for the transport of metals to the halo. There are currently many examples of supershells and of chimneys in the Milky Way, but no clear examples of supershells undergoing the pivotal transition into a chimney, during which they are expected to release cold gas into the halo as a critical part of the theorised galactic fountain cycle.

The study of HVCs similarly progressed during that time, although remaining focused mostly on studies of individual clouds or complexes (Smith, 1963; Hulsbosch & Raimond, 1966; Mathewson et al., 1966; Kuilenburg, 1972; Giovanelli, Verschuur & Cram, 1973a). This culminated in the first complete northern sky survey of HVCs (Hulsbosch & Wakker, 1988), and the resulting catalogue (Wakker, 1991; Wakker & van Woerden, 1991) which organised groups of clouds apparently spatially and spectrally associated into 'complexes'. Progress in surveys of the southern sky HVCs came later, with the first complete survey released by Putman et al. (2002). There were two key limitations of this survey: firstly, the HI Parkes All Sky Survey (HIPASS) data were not very sensitive to structures on scales larger than 7°, and secondly, the velocity resolution at ~15 km s^{-1} (smoothed to 26 km s^{-1} for the HVC source-finding) was coarse compared to the resolution needed to spectrally resolve Milky Way gas and HVCs, which is understandable given that HIPASS was primarily an extragalactic survey of neutral hydrogen.

Along with the study of halo sub-structure in the form of HVCs came investigations into the global properties of the Galactic halo. The initial findings that the halo was dominated by neutral hydrogen at negative velocities with respect to the Local Standard of Rest (LSR) were biased by the lack of complete, sensitive southern sky surveys, which revealed the opposite trend; this was later revealed to be an artifact of the LSR frame of reference around the Galactic anticentre (Wakker, 1991). The all-sky HVC catalogue of Wakker & van Woerden (1991) was widely regarded as one of the most complete surveys of the Galactic halo, and it was suggested that future searches for high-velocity gas would be complete for column densities $N_{HI} > 2 \times 10^{18}$ cm^{-2}. While a large fraction of HI in the southern sky could be attributed to the interacting Magellanic system, most of it remained of unknown origin. The discovery of high-velocity absorption in the halo

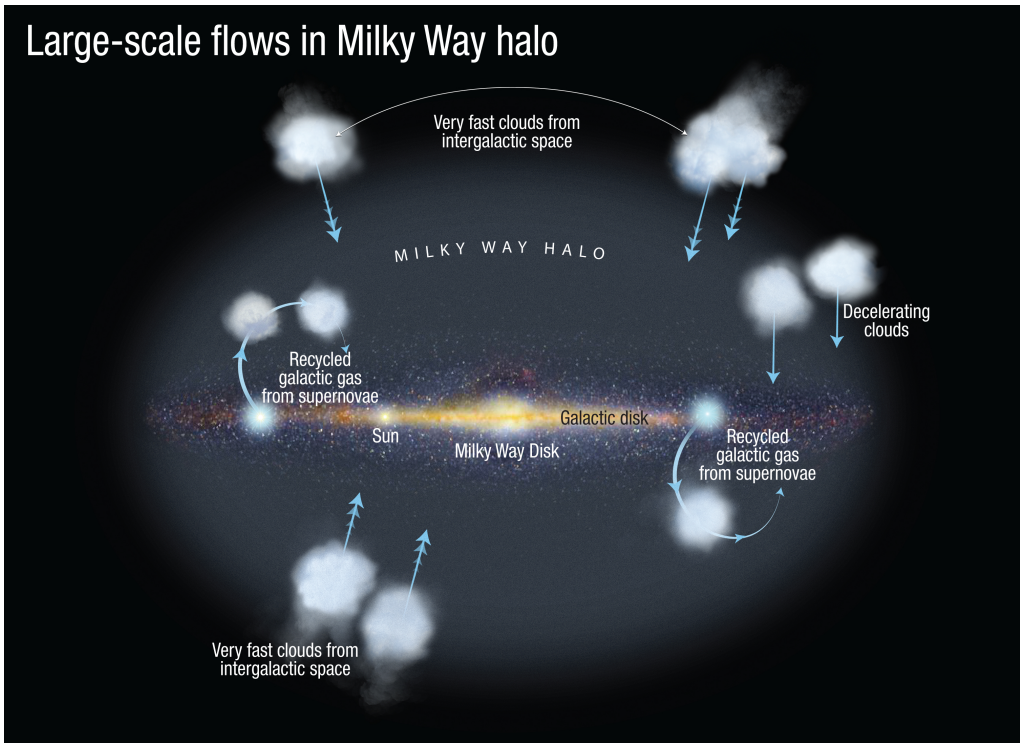

Figure 1.1: Artist's impression of the Milky Way, highlighting the two key forces dominating the Galactic ecosystem: outflow powered by energetic supernovae in the disk and infall via accreting extragalactic gas. Illustration credit: NASA, ESA, and A. Feild (STScI). Science Credit: NASA, ESA, and N. Lehner and C. Howk (University of Notre Dame).

via ultraviolet (UV) surveys towards extragalactic sources (Savage et al., 1993; Bowen & Blades, 1993) revealed even lower column densities, due to the higher sensitivity of absorption-line surveys compared with emission-line surveys. Although these UV absorption surveys targeted only a few sightlines, their high sensitivity to low column-density gas began to suggest that the Milky Way was surrounded by very faint, diffuse gas that could not be detected by the less sensitive searches in HI (Bekhti et al., 2009; Lehner & Howk, 2011), and that this gas may contain significant mass due to its apparent ubiquity in the halo. Of particular importance in the context of UV absorption surveys was that they indicated significant amounts of ionisation in the envelopes surrounding HVCs (Shull & Slavin, 1994; Shull et al., 2009). This was in alignment with the prediction of Spitzer (1956) of a hot, ionised Galactic corona that would allow for cloud confinement. While hot gas of 10–20% metallicity can eventually cool on Gyr timescales (Collins, Shull & Giroux, 2007), and thus potentially produce a mass infall rate of ~1 $M_\odot$ yr^{-1} based on the Si III HVCs detected in UV absorption (Shull et al., 2009), the current state of low column-density neutral gas and how it relates to the bright HVCs below the sensitivity limits of most HI surveys remains unknown.

A key question underlying and connecting the study of supershells, the study of HVCs, and the study of the halo is the question of galactic evolution: how do galaxies obtain new gas for continued star formation? This process of forming new stars (and the ability to do so based on available gas reservoirs) decides the ultimate fate of a galaxy, and takes place within the balance between outflow and infall in an individual galactic ecosystem as represented in Figure 1.1. In the case of the Milky Way, determining the process by which

new stars are able to form is of particular importance as the estimated star formation rate of the Galaxy of ~1–3 $M_\odot$ yr^{-1} (Robitaille & Whitney, 2010) has long been at odds with various estimated rates of accretion of new gas to form these stars, which are often orders of magnitude lower (Putman, Peek & Joung, 2012). Recent studies have suggested that the galactic fountain cycle is key to the accretion of gas onto the disk from the halo, as this process allows mixing of cold gas with warm halo gas potentially leading to net accretion that agrees with the predicted star formation rate (Fraternali et al., 2013a).

This thesis aims to investigate these critical aspects of the Galactic ecosystem via the key themes of supershells, anomalous velocity gas and large-scale halo structure, in order to contribute new insight into the complex processes that influence disk-halo interaction in galaxies such as the Milky Way.

1.2 Supershells: giant holes in galaxies

Large and often expanding structures seen in neutral hydrogen in both the Milky Way and in other galaxies, known as supershells, are typically formed as the net result of several supernovae within a relatively small vicinity of each other, with the energetic expansion driving the neutral hydrogen outwards. Young supershells can be more circular and reminiscent of supernova remnants, while older supershells quickly lose symmetry due to both the different locations of supernovae influencing their expansion and to their interactions with the surrounding interstellar medium. Their evolutionary state can thus be traced through any evidence (or lack) of expansion, dividing the supershell population into either expanding or stationary shells. The oldest supershells generally maintain very little coherent structure, and are re-classified as chimneys once they are observed to have undergone blow-out into the Galactic halo. In the fountain model of the Galactic ecosystem, supershells are believed to play a critical role in the cycling of gas from the disk to the halo.

There have been various catalogues of supershells in the Milky Way, with the path first paved by the work of Heiles (1979) using the survey of Weaver & Williams (1973). The three key catalogues following this initial survey were that of Hu (1981), Heiles (1984) and McClure-Griffiths et al. (2002). The Heiles and Hu catalogues covered only the northern hemisphere, reaching as far south as declination of $\delta = -30°$, while the McClure-Griffiths et al. (2002) catalogue covered the southern hemisphere but only between Galactic longitudes of $b \leq 10°$ due to the survey limitations of the Southern Galactic Plane Survey (McClure-Griffiths et al., 2005). We highlight these four catalogues in Figure 1.2, particularly to emphasise the incompleteness of catalogued supershells in the southern hemisphere.

Recent attempts to produce more complete catalogues using automated search algorithms include that of Ehlerová & Palouš (2005) and Suad et al. (2014), both of which found several hundred supershell candidates compared with the 172 shells in total identified by the four previous catalogues. These newer surveys have highlighted the need to clearly define the properties of a supershell because of the strong danger of falsely identifying shells in automated searches. It is critical to ensure consistency in the case of comparison between different catalogues, as well as better trace the fine line between supershells and HI shells related to singular supernova remnants. An example of this can be seen in the recent study of four shells by Park et al. (2013), specifically targeting HI shells associated with expanding supernova remnants. When dealing with comparison between the various surveys, it becomes particularly important to note exactly how a supershell is defined in each case and what method was used to identify shells, given the strong impact of these selection effects on the resulting shell population.

The Magellanic Clouds, being the nearest neighbouring galaxies to the Milky Way, have provided a unique opportunity to investigate supershells/superbubbles and their structure on galaxy-scales, at high angular resolution and at different wavelengths (Kim et al., 1999; Hatzidimitriou et al., 2005; Sankrit & Dixon, 2007; Fujii et al., 2014). In other galaxies such as these, supershell identification may seem to be more straightforward due to the advantage of seeing the entire picture, particularly in the case of face-on galaxies. However, again it becomes critical to carefully consider what defines a supershell, particularly in order to differentiate between actual holes and gaps between spiral arms, and between supernova remnants and supershells. Dawson et al. (2013) explicitly dealt with this problem, first differentiating between supershells (radii < 180 pc) and their larger counterparts 'supergiant shells' (radii > 180 pc), which are expected to have a more significant and influential effect on the interstellar medium of a galaxy and then needing to implement ways of reliably tracing the edges of shells in the context of their merging with the local background. Conversely, the study of Blair & Long (1997) identified cavities in NGC 300 on the scale of a few hundred parsecs or less, categorising these cavities as supernova remnants rather than supershells on kiloparsec scales.

Earlier studies varied in their focus: Brinks & Bajaja (1986) catalogued 141 holes in M31 ranging from 100 to 1000 pc across, Deul & den Hartog (1990) catalogued 37 holes in M33 ranging from 40 pc to 1 kpc, and Kamphuis, Sancisi & van der Hulst (1991) studied an extreme supershell with a size of 1.5 kpc expanding and interacting with the HI layer of M101. More recent investigations into supershells in other galaxies have included: the study of Boomsma et al. (2008a), which concluded that stellar feedback was likely the dominant process behind the 121 holes detected in NGC 6946; the study of Warren et al. (2011), which found that multiple generations of star formation were needed to explain the structures observed in various dwarf galaxies; and the study of Bagetakos et al. (2011), which surveyed large-scale structure in several nearby galaxies to catalogue over 1000 holes between 100 pc and 2 kpc in size. There is clearly a blurry line in the definition of a supershell that remains somewhat subjective, particularly as the stars that formed the shells are generally long gone and no longer detectable.

1.3 Anomalous velocity gas in the halo of the Milky Way

An interstellar cloud is a region of neutral, ionised or molecular gas that is denser than the surrounding interstellar medium, and hence can be considered as an isolated structure. If these clouds have velocities that are anomalous compared with the rotation of the Galactic disk, they are then classified based on the magnitude of their velocities. The earliest classification related cloud velocities to the LSR reference frame, which is measured with reference to the solar neighbourhood in the Galactic disk: high-velocity clouds (HVCs) consisted of clouds with velocities greater than ~100 km s^{-1}, clouds with velocities in the range 40–100 km s^{-1} were considered to be intermediate-velocity clouds (IVCs), and low-velocity clouds (LVCs) were any clouds with velocities less than 40 km s^{-1} but still 'forbidden' by a chosen model of Galactic rotation (Kuntz & Danly, 1996). Contrary to HVCs, LVCs and IVCs are considered to be almost entirely related to Galactic phenomena.

It is important to note here that the velocity ranges are not strictly defined, especially given that models of Galactic rotation are generally only accurate to ~10 km s^{-1} at best. Further, as described within this thesis, modern practice considers cloud velocities relative to either the velocity by which they deviate from an assumed model of Galactic rotation (deviation velocity) or their velocities relative to the Galactic Standard of Rest frame (GSR).

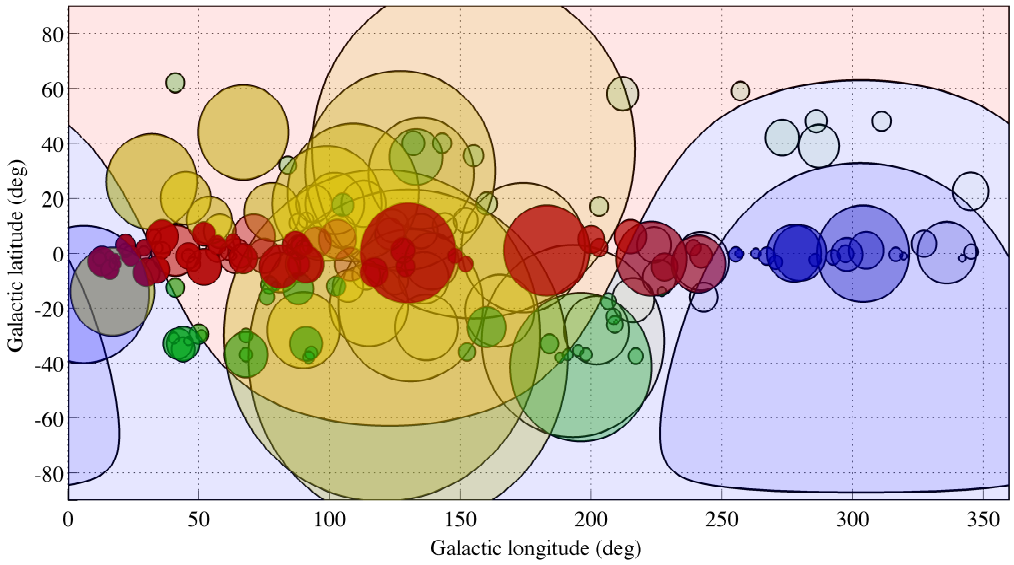

Figure 1.2: The distribution of known Galactic supershells in Galactic coordinates. Shown are the supershells catalogued by Heiles (1979) in red, Hu (1981) in green, Heiles (1984) in yellow and McClure-Griffiths et al. (2002) in blue, with the size of circles indicating the size of the shell. The northern hemisphere is highlighted in red, while the southern hemisphere is highlighted in blue. Of these four separate catalogues of supershells, only that of McClure-Griffiths et al. (2002) covers the southern hemisphere, while each of the others surveys only as far south as declination $\delta = -30°$. The survey of McClure-Griffiths et al. (2002) represents the most comprehensive search for supershells in the southern hemisphere, but even this search was limited to the Galactic latitudes of $|b| \leq 10°$ of the extended Southern Galactic Plane Survey. As such, the imprint of the southern hemisphere is clearly evident in the known supershell distribution, indicating that there are still a considerable number of supershell structures to be identified.

The Oort interpretations

Oort (1966) published one of the first reviews of HVC studies, summarising six potential hypotheses for the origins of anomalous velocity gas (particularly high-velocity gas) in the halo of the Milky Way. Since that time, studies have found evidence for origins in many of these early predictions, with continued debate about which origin is likely dominant. Because of the foresight of the paper as well as the continuing relevance of each possible HVC origin listed by Oort, the Oort interpretations are used as the basis for this section to draw connections between past and present interpretation of anomalous velocity gas. Below, each Oort prediction is summarised with examples of where it has been either confirmed or ruled out.

a) Parts of nearby supernova shells

This hypothesis was largely dismissed by Oort on account of the observed distribution of HVCs across the sky and their velocities, which in turn would imply an improbably high number of nearby young supernova remnants in a very small spatial vicinity (i.e. three supernovae within 20 pc having all gone off in the last 10^5 years). He further dismissed runaway halo stars exploding at different distances due to the incongruities in energy and mass requirements to explain the distribution of HVCs on the sky, concluding that unless

they were extremely nearby (which was already very improbable), the majority of the HVC population could not be explained by supernova remnant material.

There has been no change since Oort's conclusion that the majority of HVCs cannot be explained as parts of supernova shells. The Heiles (1984) catalogue of supershells contains clouds at velocities approaching that of the lowest velocity HVCs, but not high enough to be representative of the HVC population. There has also been evidence found of IVCs which are most likely due to supernovae nearby, such as the IVC studied by Higgs, Kerton & Knee (2001), and it is currently thought that the majority of IVCs can be explained in the context of supernovae and their effects on galaxies (de Gouveia Dal Pino et al., 2009). Strong evidence for the connection between star formation/supernovae in the disk and neutral hydrogen clouds in the halo was provided in the work of Ford et al. (2008); Ford, Lockman & McClure-Griffiths (2010), with three times as many halo clouds found where the Milky Way's bar merges with a major spiral arm compared with a minor spiral arm.

There has been suggestion that some HVCs can form at high latitude due to triggered star formation in the walls of expanding supershells (Ivezic & Christodoulou, 1997). Contrary to this, there are also cases where structures that look like supershells and supernova remnants appear to have been caused by the impacts of HVCs in the disk of a galaxy, either the Milky Way (McClure-Griffiths et al., 2008) or in other galaxies (Rand & Stone, 1996), although the majority of Galactic supershells are related to star formation rather than HVC infall (Ehlerova & Palous, 1996). In general, the consensus regarding HVC origin currently rules against supernova shells as a primary source, in agreement with Oort's original conclusions, but supernovae likely play a key role in the generation of IVCs and LVCs.

b) Condensations formed in a gaseous corona of high temperature

Oort identified this potential interpretation of HVC origin by referring to the work of Field & Saslaw (1965) and Dieter (1964), who suggested that cool clouds could potentially condense in a corona of high temperature. Oort dismissed this interpretation, based on what he cited as an unreasonably high coronal density needed to keep clouds in equilibrium rather than evaporating. He further pointed out that even if the coronal density were as high as 0.01 cm^{-3} or more, that the observed velocities of clouds could not be explained as they would have been strongly affected and reduced by coronal friction. Since then, the idea of condensation within the halo has become more prominent and more widely accepted as a potential explanation for the HVC population. Although there is strong agreement between models of condensed gas in hot halos and the observed non-Magellanic population of HVCs (Peek, Putman & Sommer-Larsen, 2008), the estimated resulting accretion rate of ~0.2 $M_\odot$ yr^{-1} is too low to match the Milky Way's star-formation rate.

Recent simulations by Joung, Bryan & Putman (2012) investigated the conditions under which cool clouds are able to condense from a hot halo medium, based on variations in density, initial height, cloud size and metallicity. They found that the ability to condense depended on whether the cloud is able to cool faster than it is accelerated to the speed of sound. If the cooling time of a cloud takes longer than this acceleration, the cloud would be disrupted by instabilities before being able to condense. Further, linear perturbations were unable to form cold clouds in their simulation, suggesting that perturbations of larger amplitude would be needed to facilitate condensation (such as filamentary flows, satellite debris, galactic fountain clouds or non-luminous dark matter halos). These conclusions indicate that the condensation scenario is not necessarily preclusive of other Oort interpretations, such as d), e) and f.i), and may in fact be a critical part of the overall process of accretion.

c) Ejected from the galactic nucleus

The centre of the Milky Way is an active place due largely to the resident supermassive black hole, and hence it is not unreasonable to predict that some high-velocity neutral hydrogen could be ejected into the halo as part of the energetic processes taking place in the Galactic centre. Oort had issues with this interpretation on the basis of both the spatial and velocity distributions of clouds: HVCs are found all over the sky in a distribution that does not seem related to the Galactic centre, and their velocities are difficult to explain due to the amount of negative velocity gas found in the anti-centre hemisphere. Overall, Oort dismissed this interpretation as not being able to explain the majority of the HVC population.

The conclusion on this interpretation has not changed since 1966, and is still believed to be unable to account for most HVCs. However, infrared detections of thermal X-rays indicating a large-scale Galactic wind (Bland-Hawthorn & Cohen, 2003) combined with the discovery of the 50° Fermi bubbles in gamma rays at the centre of the Milky Way (Su, Slatyer & Finkbeiner, 2010) have provided strong evidence that the Milky Way has undergone extremely energetic activity in its centre. Although the physical origin of the bubbles remains unknown (Yang, Ruszkowski & Zweibel, 2014), it is likely that these signatures are the remnants of either nuclear star-formation (Crocker & Aharonian, 2011; Crocker et al., 2011) or past activity of the Milky Way's active galactic nucleus (Cheng et al., 2011). Recent work by McClure-Griffiths et al. (2013) has traced compact HVCs towards the Galactic centre that have likely been entrained as part of this outflow, although just 86 clouds were discovered up to heights of ~700 pc. While there is clearly some contribution to halo gas due to Galactic centre activity, it remains unlikely that a significant proportion of HVCs can be explained in this way.

d) Ejected as cool clouds from the disk

This theory proposes that the majority of HVCs are formed due to events in the disk (either energetic/explosive or gradual) and hence expelled into the halo. Given the energies required to produce both the height of the HVCs above the Galactic plane and their velocities, there are some connections of this interpretation with Oort interpretation a). Even in 1966, Oort noted that hypotheses d) and e) appeared to be the most likely as origins for anomalous velocity gas. Oort suggested that in either case, the majority of gas would be of Galactic origin due to its velocity; non-decelerated intergalactic gas would be expected to have much higher velocities than observed, and in the case of deceleration would sweep up Galactic interstellar mass. Interestingly, he noted that under certain assumptions an estimated 1 to 2 $\times$ 10^6 solar masses of hydrogen could be swept up from the disk although he was most concerned about this figure in the context of replenishing the corona with new gas. He also pointed out that, based on predictions of one massive Type II supernova every 500 years, an estimated 4 $\times$ 10^6 solar masses could be transported to the halo in this way. This would result in gas coming down in regions of less activity, manifested as high-velocity clouds of gas as observed, in alternating periods of influx and expulsion.

The concept of cyclical periods of infall and outflow of gas is now commonly referred to as the Galactic fountain cycle, the terminology popularised by Shapiro & Field (1976), and remains one of the most popular candidates for HVC origin. The Galactic fountain, or the combined efforts of several stars going supernova in a small region or association, is certainly responsible for the majority of the low-velocity cloud population, although there will be some contamination by HVCs that have been decelerated (Stanimirović et al., 2006), as well as by projection-affected HVCs that are travelling perpendicular to the

line of sight as described in Peek et al. (2009). Simulations of a multi-phase interstellar medium driven by supernovae reproduce the predicted 'breathing' in phases of outflow and infall (Hill et al., 2012), and this model remains competitive in being able to explain a significant fraction of the Milky Way halo gas. Alternative less-energetic events have also been considered in providing an origin for some of these clouds, such as photolevitation of clouds due to radiation pressure on dust grains (Franco et al., 1991).

However, metallicity is widely known to be a key separator between gas of Galactic versus extragalactic origin, as intergalactic gas accreted from outside the Milky Way would be expected to have considerably lower than solar metallicity. Studies of the metallacities of anomalous velocity clouds in the Milky Way have revealed a general difference in metallicity between HVCs and IVCs (Wakker, 2001). Many IVCs have been found to have metallicities close to solar, while typical HVCs have metallicities about 0.1 solar. These findings lend weight to the theory that most HVCs are external material and most IVCs have an origin in the Galactic disk.

The study of the halo of NGC 891 (Bregman et al., 2013) revealed a galaxy that appears to be mostly dominated by outflow via a galactic fountain, while in the Milky Way's case there have been studies revealing low metallicity in some HVC complexes (Wakker, 2004), near-Magellanic metallicity in the Magellanic stream (Fox et al., 2013) and near-solar metallicity in other HVC complexes (van Woerden & Wakker, 2004). Not surprisingly, the relative influence of infall versus outflow thus appears to vary depending on the physical properties of the host galaxy and its surrounding environment. Currently, this interpretation remains plausible for explaining a large portion of halo gas, particularly at lower velocities closer to that of Galactic rotation.

e) Due to intergalactic gas accreted by the Galactic System

Oort considered this interpretation to be one of the most likely explanations, along with d), and in fact visualised a galaxy in which the two processes were linked together, with the coronal gas of intergalactic origin swept around by the same influx and expulsion processes described above. He raised two key questions regarding this origin for HVCs: 1) how the swept-up hydrogen due to incoming clouds can remain neutral, and 2) whether the densities required to achieve this are feasible. Although limited by incomplete data, he noted that both the necessary amount of cooling and high-enough density seemed reasonable and within margins of error. He also concluded from the observed distribution of clouds that there were at least two or three different 'streams' in the halo, which would be suggestive of either three different extragalactic systems that the Milky Way is interacting with or inhomogeneously distributed primordial gas.

Accretion of intergalactic gas has long remained a key player in potentially explaining the origin of the HVC population. However, although the accretion of intergalactic gas has been widely acknowledged in this way, explaining the exact process of this accretion has remained the subject of debate. Kereš et al. (2005) proposed that accretion of gas into the Milky Way system could occur in one of two ways: hot-mode (largely spherical) or cold-mode (along CDM filaments), and the question of which dominates in a given galaxy (and how this then connects to an observed neutral hydrogen cloud population) remains an active subject of research. There is currently much evidence in favour of extragalactic origin dominating the HVC population, particularly given the extreme velocities of the clouds and the inferred height above the disk for clouds with known distances (Peek et al., 2007), the dominance of the Magellanic system on the halo at positive LSR velocities, the low metallicities associated with various clouds and complexes (van Woerden & Wakker, 2004), and the large amount of dwarf galaxy accretion necessary to sustain Galactic star-

formation over large periods of time (Putman, Grcevich & Peek, 2008). However, it is still unclear how these clouds can be accreted onto the Milky Way, regardless of their origin.

Recent progress has been made in the work of Marinacci et al. (2010), Marasco, Marinacci & Fraternali (2013); Marasco, Fraternali & Binney (2013) and Fraternali et al. (2013b), with a new focus on the influence of the Galactic fountain cycle on the mixing of coronal gas with disk gas. Their model results suggest that the motion of fountain clouds through the halo medium creates a turbulent wake within which coronal material is efficiently mixed with high metallicity gas, triggering cooling in the coronal gas and leading to the eventual accretion of new cold material for star formation. This model of mixing in the Galactic halo is a strong contender in explaining both the origin of HVCs and the Galactic star formation rate, and is in agreement with cosmological simulations showing that hot-mode accretion, rather than cold flows, should dominate accretion processes of Milky-Way type galaxies at redshifts less than 1 (Kereš et al., 2009). The recent work of Fox et al. (2014), based on UV absorption studies of Magellanic gas, suggests that the Magellanic system alone may be able to provide inflow of 3.7-6.7 $M_\odot$ yr^{-1} if it survives its passage to the Galactic disk, an important result that may provide answers to the existing observed gap between the accretion of gas and the measured star-formation rate.

f.i) Small satellites of the Galactic System

Oort's original interpretations grouped satellites of the Milky Way and independent galaxies of the Local Group in the same category, but due to their significantly different properties and the impact on interpretation as related to HVCs, I have separated them here. Small satellites of the Galactic system refers primarily to dwarf galaxies, of which the Magellanic Clouds can be considered a subset. Both satellites and independent galaxies as an interpretation for HVCs were ruled out by Oort on the grounds of the degree of association seen between HVCs on orders of 30°, which would be impossible to achieve at large distance from the Milky Way. Additionally, the detection of interstellar absorption lines indicated distances of less than 1 kpc for some clouds.

The lack of stars detected in HVCs combined with their large angular size continues to rule out this origin for the large majority of the population. Recent work has shown that there is no stellar content in a sample of HVCs down to extremely low brightness levels (Willman et al., 2002), despite other similarity to dwarf spheroidal galaxies in the halo. However, the Magellanic clouds and overall system are obviously a key example of this process in action, and contribute a large proportion of high-velocity gas to the halo in the region surrounding them. In this context, Oort interpretation e) and f.i) are related, as both primordial gas and gas stripped from dwarf galaxies can be classed as intergalactic gas accreted by the Milky Way. As research into HVC origin currently stands, intergalactic gas accreted from both the intergalactic medium and from galaxy interactions appears to be the dominant mechanism by which the Milky Way acquires new gas. How it is accreted and which source plays a bigger role still remains undetermined.

f.ii) Independent galaxies in the "local group"

As in f.i), Oort dismissed independent galaxies in the Local Group based on both angular scale and local interstellar absorption. There have been studies since of HVCs that may be members of the Local Group (Blitz et al., 1999; Braun & Burton, 1999), although these studies typically focus on the most compact HVCs and cannot explain the properties of the entire HVC population. In addition, the lack of HVC analogues in other groups of galaxies (Pisano et al., 2004) suggests that the majority of HVCs are located at distances less than 160 kpc, making models suggesting Local Group distances unlikely. That is not

to say that a small fraction of the total HVC population may in fact be related to the Local Group, however it is clear now that this does not provide an explanation for the majority of HVCs.

Plöckinger & Hensler (2012) dismissed any Galactic origin for HVCs, including the fountain cycle, and instead focused on either relics of cosmological structure formation or remnants of galaxy collisions (tidal disruption or dwarf galaxies), pointing out that the key separator between the two potential origins would be the relative dominance of dark matter. Their models, when compared with observations of the HVC population, indicate that the majority of HVCs are not dark-matter dominated and as such do not have a cosmological origin. They concluded that the proximity of HVCs to their host galaxy further suggest an origin in stripped-off gas from galaxy interactions, in accordance with Oort interpretation f.i), or condensations from the diffuse intergalactic medium, as in Oort interpretation b). In the end, it seems unlikely that there is one single valid origin for HVCs but instead several, and the total accretion rate onto the Milky Way may be the result of the combination of different origins influencing each other, such as extragalactic gas interacting with the Galactic fountain cycle as suggested by Marinacci et al. (2010).

1.4 The multi-wavelength halo of the Milky Way

Over time, multi-wavelength diagnostics have been developed to discern the overall structure of the halo, including HVCs, with varied success. These diagnostics have been employed primarily in the quest to determine the dominant origin of the high-velocity gas in the halo and to measure the physical properties of clouds. Below some of the diagnostics that have been developed and their implications are described, as well as their limitations.

Radio

Radio observations have played a central role in the study of the halo and of HVCs from as early as the discovery of the celestial HI line, given that many HVCs are only detectable physically and practically in HI, particularly on large scales. The majority of HVCs were discovered and catalogued based on HI observations (Wakker & van Woerden, 1991; Putman et al., 2002), with their hydrogen content being key in their potential role as accreting gas for new star-formation. HI has also been the main line through which HVCs and extra-planar gas around other galaxies have been detected (Tenorio-Tagle & Bodenheimer, 1988; Westmeier, Braun & Thilker, 2005; Westmeier et al., 2007; Sancisi et al., 2008; Kamphuis et al., 2011). Of particular interest in radio has been the discovery, detection and study of head-tail HVCs (Meyerdierks, 1991; Brüns et al., 2000; Bekhti et al., 2006; Putman, Saul & Mets, 2011), which are examples of cometary-like HVCs undergoing interactions with their environment. These head-tail HVCs have the potential to reveal the properties of HVCs (such as direction of travel, dark matter content, origin, magnetic field influence) as well as their surrounding medium, and can provide new insight into disk-halo interaction on both small and large scales. Their core-envelope structure has been studied in the context of shedding light on the multi-phase medium in HVCs, their existence in a hot halo and the conditions necessary to produce these properties, where the difference in line-width may be due to turbulence, internal temperature structure within the clouds or some combination of both factors (Wolfire et al., 1995; Sternberg, McKee & Wolfire, 2002).

In relation to the confinement of HVCs and how they survive in a hot halo environment, magnetic fields have been considered both theoretically (Jones, Ryu & Tregillis, 1996;

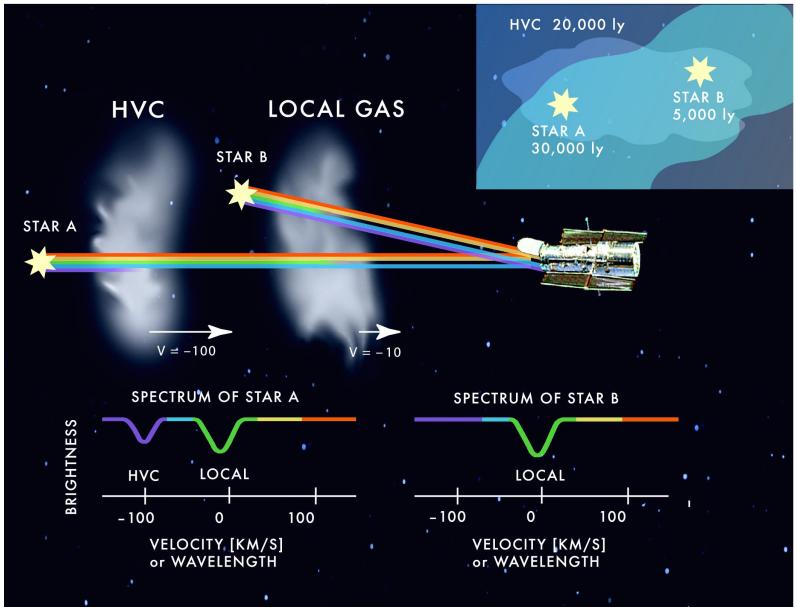

Figure 1.3: Visualisation of optical absorption towards background stars, demonstrating how this method can determine the distance to a HVC based on absorption within the stellar spectrum at the same velocity as the HVC. Image credit: Ingrid Kallick, accessed from http://www.astro.wisc.edu/~flack/.

Konz, Brüns & Birk, 2002; Kwak, Shelton & Raley, 2009) and observationally through the detection of enhanced rotation measure at 1.4 GHz in the vicinity of HVCs (McClure-Griffiths et al., 2010; Hill et al., 2013) using the catalogue of Taylor, Stil & Sunstrum (2009). Searches for molecular gas in HVCs have been mostly unsuccessful prior to the ability to perform UV measurements, and to date there have been no detections of CO in any HVC (Wakker et al., 1997; Dessauges-Zavadsky, Combes & Pfenniger, 2007), a tentative detection in HCO+ (Combes & Charmandaris, 2000) and some successes in detecting the presence of molecular hydrogen in various clouds (Richter et al., 1999; Gringel et al., 2000; Sembach et al., 2001; Richter et al., 2001a; Wakker, 2006). Using the HCO+ line as a diagnostic in radio may prove useful in future in lieu of CO, however the physical conditions of the cloud (particularly the metallicity) will continue to play a strong role in determining the possibility of detection.

Optical

After radio, optical diagnostics have played the largest role in determining the properties of gas in the halo and its potential origin. With the exception of recently-detected young stars associated with the Leading Arm of the Magellanic system (Casetti-Dinescu et al., 2014), various searches have found little evidence of stars or star-formation going on within the HVCs themselves both in our Galaxy and near others (Simon & Blitz, 2002; Davies et al., 2002; Willman et al., 2002; Hopp, Schulte-Ladbeck & Kerp, 2003; Siegel et al., 2005; Wolfe et al., 2013a). The presence of Hα emission in many HVCs, suggesting a high ionising flux incompatible with that of the intergalactic medium, has been used to argue for HVCs being local rather than associated with the Local Group (Tufte et al., 2002; Putman et al., 2003), as well as to determine the physical relation between the ionised and neutral hydrogen in Complex L (Haffner, 2005). This is supported by results from observations of HVCs around other galaxies such as M31 and M83 (Thilker et al., 2004;

Westmeier, Brüns & Kerp, 2008; Miller, Bregman & Wakker, 2009), which found evidence of HVCs exclusively in close proximity to the host galaxies rather than scattered in the space between.

Optical absorption lines have provided the best estimate of HVC metallicity and have been an important distinguisher of cloud origin. Complex M has been a commonly-studied HVC complex due to the high levels of ionisation found in absorption at its velocity at an extremely nearby distance of less than 4.4 kpc as well as associated X-ray emission, indicating that it is best interpreted as condensed Galactic fountain gas returned to the disk (Danly, Albert & Kuntz, 1993; Herbstmeier et al., 1995; Yao, Shull & Danforth, 2011). Similarly, Complex C has been found to have high ionisation, a low metallicity of 0.15 solar and a distance less than 11 kpc (Richter et al., 2001b; Tripp et al., 2003; Fox et al., 2004; Wakker et al., 2007; Collins, Shull & Giroux, 2007), suggesting that this HVC complex represents an infall of primordial intergalactic gas that has mixed with some higher metallicity disk gas.

As well as determining metallicity, optical absorption towards background stars can be used to set an upper limit distance to HVCs based on any detected absorption in the star's spectrum as shown in Figure 1.3. Although the method often results in a non-detection and hence a lower limit on the distance to an HVC (Boer et al., 1994; Wakker et al., 1996), there have been some important upper limits to distance set this way (de Boer & Savage, 1983; Danly, Albert & Kuntz, 1993; Wakker, 2001; Smoker, Fox & Keenan, 2011). More recently, larger scale surveys have greatly increased the detection rate and enabled statistically significant samples to be obtained, with results suggesting that the halo contains large amounts of ionised gas that is likely to play a key role in the continued accretion of the Milky Way (Lehner & Howk, 2011). These results also showed evidence for HVC sky coverage of ~60%, which is considerably more than the 20–30% indicated by HI surveys (Lehner et al., 2012). This intriguing result indicates that there is a great deal of the high-velocity sky not detected in HI because it is dominated by ionised gas at lower column densities, which is supported by a drop-off in neutral gas fraction below column densities of $N_{HI} < 10^{18}$ cm^{-2}.

Infrared

Infrared emission has primarily been used to search for dust content in HVCs, under the assumption that hydrogen clouds of Galactic origin should have a considerably higher dust content than that of extragalactic origin. Searches had been mostly unsuccessful leading up to the mid-2000s (Wakker & Boulanger, 1986), suggesting either an absence of dust (as would be expected in HVCs of extragalactic origin) or a depleted level of dust compared with the disk. The updated processing of the Infrared Astronomical Satellite (IRAS) in the form of IRIS (Miville-Deschênes & Lagache, 2005) combined with extremely sensitive Spitzer Space Telescope observations led to a tentative detection of association between dust and a HVC on the edge of Complex C (Miville-Deschênes et al., 2005), although this led to a further non-detection of CO in the same cloud (Dessauges-Zavadsky, Combes & Pfenniger, 2007). There have since been similar studies seeking dust in HVCs with minimal success (Collaboration et al., 2011; Williams et al., 2012), suggesting that most HVCs do not contain any significant amount of dust.

The absence of dust in LVCs was also used to identify HVCs travelling perpendicular to the line-of-sight at projection-affected velocities (Peek et al., 2009), with this study highlighting the need to be extremely careful in determining dust association with HVCs due to the large angular size of most HVCs and the effect of chance coincidence between HI and infrared. The Bot et al. (2009) study of high-latitude 'cirrus' in the Galactic

halo found significant variation from field to field rather than a 1:1 correlation between HI and infrared emission, which most likely was due to the combined effects of multiple components in the field causing confusion. A similar study using Planck data examined 14 different latitude regions on the sky for their LVC, IVC and HVC content, and compared this with dust emissivity, finding high degrees of correlation for LVCs and IVCs but very little for HVCs (Collaboration et al., 2011). The detection or absence of dust will continue to play an important role in determining HVC origin, although the ability to rule out chance coincidences using a method similar to that developed by Peek et al. (2009) remains crucial.

X-rays

Searches for X-rays in HVCs have been a relatively recent development, based on the discovery of interacting HVCs (particularly those with head-tail structure) and the associated ram-pressure stripping expected to go along with these interactions. The first detections of X-rays associated with HVCs were found in Complex C (Hirth, Mebold & Mueller, 1985) and Complex M (Herbstmeier et al., 1995), suggesting that X-rays indicated HVC interaction with the ambient medium independent of origin, as Complex C is believed to be extragalactic while Complex M is thought to be Galactic. This led to a larger scale search for X-rays by Kerp et al. (1999), with detections towards Complex C, D and GCN that indicated potential association. They noted the challenge of this method, however, given that there is other gas along the line of sight that may also contribute to the detected X-ray excess and could in fact be responsible for it rather than the HVCs.

Simulations of X-rays in HVCs have found that shock-heating is the most consistent with observations rather than mixing, provided the HVCs have enough initial speed to shock-heat the ambient gas in front of them (Shelton, Kwak & Henley, 2012). Of future interest, given the many large-scale surveys of head-tail HVCs, is the potential of stacking the heads of HVCs in soft X-rays to search for the average faint signatures of shock-heating in a large sample of interacting clouds. X-rays have also been used to determine the structure of the overall halo (Nicastro et al., 2005; Gupta et al., 2012), finding that the warm-hot phase of the Milky Way seen in X-rays indicates the existence of a large ionised reservoir and can potentially account for the baryons missing from our Galaxy.

1.5 Thesis outline

This thesis deals primarily with the concept of the galactic ecosystem: the cycle of neutral hydrogen within the Milky Way and other galaxies that is driven by the processes of outflow and infall. I focus specifically on outflow in the form of supershells, and in the structure of the Galactic halo as mapped by the HVC population. My work revolves around the new insight into the Milky Way obtained using the Galactic All Sky Survey (GASS) as visualised in Figure 1.4, with its high sensitivity, angular resolution and, most importantly, spectral resolution making it one of the best maps of the southern sky in neutral hydrogen to date. Below, I give a brief summary of each chapter.

Chapter 1 has introduced the field of study, giving context based on the literature to the concept of a galactic ecosystem and how infall and outflow can be traced in the halo of a galaxy.

Chapter 2 reproduces my published paper on GSH 006−15+7, a large supershell structure identified in the GASS data. This paper is a case study of what is one of the nearest supershells to the Sun at an estimated distance of 1.5±0.5 kpc. GSH 006−15+7 is a particularly unique example of a supershell for three reasons. Firstly, it features a transi-

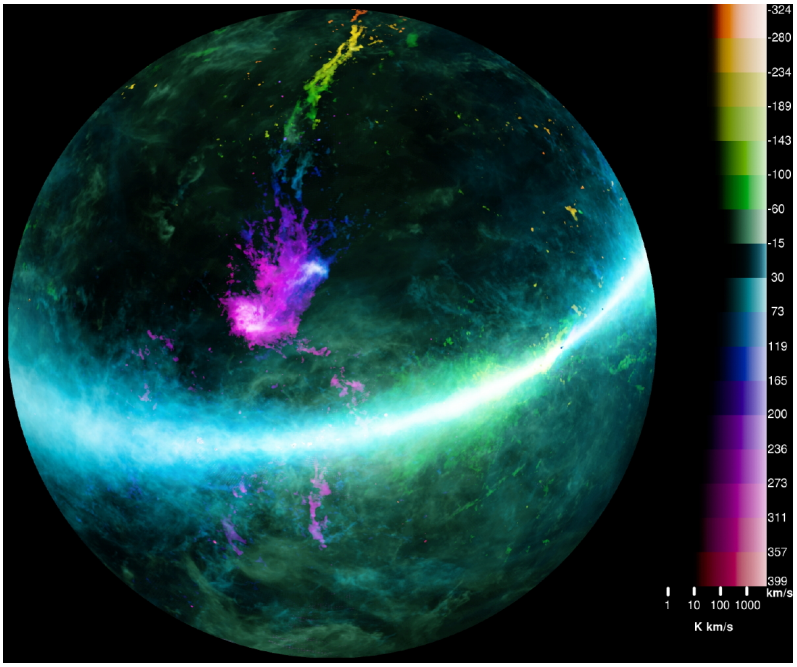

Figure 1.4: Visualisation of the Galactic All Sky Survey as an integrated intensity map colour-coded based on v_{LSR} velocity. Gas at different velocities is highlighted based on the colourbar on the right, with the most positive velocities at ~400 km s^{-1} shown in purple and the most negative velocities at ~ −400 km s^{-1} shown in red. The majority of Galactic neutral hydrogen appears at velocities close to 0 km s^{-1}, with the Magellanic system standing out prominently at velocities over the whole range. Credit: S. Janowiecki.

tion from HI emission to HI self-absorption along the shell walls as the brightness of the Galactic background increases near the plane of the Milky Way. Secondly, its coherent morphology identifies a clear region where the originating source stars would be expected to be located. Finally, a high-latitude Hα feature was identified near the edge of the shell furthest away from the Galactic plane, where the supershell would be potentially starting to fragment during the process of blow-out.

Chapter 3 summarises the preliminary follow-up work so far into characterising this aforementioned Hα feature, dubbed the Cuttlefish for its morphology and for brevity. Of particular focus are the pointed WHAM observations that were obtained at the position of the peak in the Hα emission, in the optical emission lines of Hα, Hβ, [S II], [N II], [O III] and He I. Also included is high-resolution HI data that was obtained with the Australia Telescope Compact Array, to resolve the neutral hydrogen at an angular resolution more comparable to that of the Hα continuum. Of particular interest is the fact that every single WHAM line observed was detected, including a very strong detection of [O III] which suggests a hard spectrum with significant energy input.

Chapter 4 reproduces my published paper on the Galactic All Sky Survey (GASS) catalogue of high-velocity clouds (HVCs) and anomalous velocity clouds (AVCs). The clouds that form the catalogue were identified using flood-fill source-finding, which enabled the cataloguing of connected structures as well as more isolated blob-like structures. The velocity criterion of the catalogued clouds includes all clouds down to a minimum deviation velocity of 30 km s^{-1} from Galactic rotation. The GASS catalogue of HVCs is the most up-to-date large-scale southern survey of high-velocity neutral hydrogen in the Milky Way

halo at relatively high angular resolution, and is able to fully resolve the physical spectra of HVCs due to its velocity resolution of 1 km s^{-1}. The chapter focuses on the construction of the catalogue itself, the large-scale properties of the HVC and AVC population, and comparison with other similar surveys of HVCs to check consistency.

Chapter 5 presents the first results of follow-up on clouds identified using the GASS catalogue of HVCs. This follow-up used the Australia Telescope Compact Array to map ten clouds showing evidence of interaction with their surrounding medium at high angular resolution, from different regions in the Galactic halo: the Magellanic Leading Arm, Complex L and Galactic Centre Negative. These observations were combined with previous observations of other clouds in the Leading Arm as well as halo clouds associated with a star-forming region in the Galactic disk to form a total sample of 15 clouds. With this population, featuring mostly clouds of known origin, the question was asked: does the origin or the environment dominate the physical properties of interacting clouds in the halo of the Milky Way? Using only the high-resolution HI, various methods were used to determine whether there are significant differences in the physical signatures of Galactic versus extragalactic clouds.

Chapter 6 focuses on the large-scale structure of the Galactic halo as revealed by the combination of bright dense clouds in the GASS catalogue of HVCs with faint diffuse gas detected in a random sightline survey of the halo completed with the 140-ft Green Bank radio telescope. These two different surveys for high-velocity gas target neutral hydrogen of considerably different properties, suggesting a multi-phase halo dominated by both bright dense clumps in the forms of HVCs and a pervasive ambient gas of low brightness. These results are consistent with findings in other wavelengths suggesting the presence of more neutral hydrogen in the halo than typically detected by surveys of HVCs, and have important implications for the overall structure of neutral hydrogen in the Galactic halo and the effects this may have on the expected star formation rate.

I summarise the main conclusions and findings of each chapter in Chapter 7, highlighting avenues for future work and development in the field in the context of the key aspects of disk-halo interaction in the Galactic ecosystem as identified at the beginning of this chapter.

Chapter

2

GSH 006−15+7†

Overview

This chapter first appeared in Monthly Notices of the Royal Astronomical Society: *GSH 006−15+7: A local Galactic supershell featuring transition from HI emission to absorption* (Moss et al., 2012).

†This chapter is published in a peer-reviewed journal.

2.1 Introduction

The pervasiveness of neutral hydrogen (HI) in the universe has ensured its centrality in both Galactic and extragalactic studies, from star-forming regions to supernovae to disk-halo interaction. Large shell-like structures detected in HI, known as supershells (Heiles, 1976), are an important driving force in the Galactic ecosystem, circulating material within the disk, evacuating dense regions and encouraging new star formation (Cox & Smith, 1974; McKee & Ostriker, 1977; Bruhweiler et al., 1980; McCray & Kafatos, 1987; Weisz et al., 2009). It is theorised that supershells also provide a pivotal link between the disk of a galaxy and the material in its halo (Dove, Shull & Ferrara, 2000), indicating that there should be shared properties between halo clouds that are Galactic in origin and supershells on the verge of blowing out of the Galactic disk (Lockman, 2002; Ford et al., 2008).

Supershells are believed to be formed through the combined effects of multiple supernovae exploding in a region on the order of parsecs to hundreds of parsecs in size, often around an OB association (Heiles, 1979). It is not clear whether this combined effort occurs during one generation of high-mass stars or whether it is the outcome of many generations of stars within a region (Oey et al., 2005), but the resulting supershell of expanding neutral hydrogen undoubtedly requires significant energy input, from 10^{52} to as much as 10^{54} erg, in order to become a physical structure hundreds of parsecs in size. The lifetime of a typical supershell is of the order of 10^7 years (Tenorio-Tagle & Bodenheimer, 1988), meaning that these structures significantly outlast their parent supernova remnants ($\sim 10^5$ years, Guseinov & Yusifov, 1985) and can trace past star formation (Weisz et al., 2009; Anathpindika, 2011; Cannon et al., 2011) as well as induce new star formation (Ortega et al., 2009). It is generally difficult to identify the stars which formed an old supershell, given that most of the high-mass stars will have been extinguished as supernovae in the

process of forming the shell (McCray & Kafatos, 1987). If a potential powering source is identified, it is possible to assess whether the formation of the vacuous cavity can be accounted for by its winds and/or supernovae (Brown, Hartmann & Burton, 1995; Shull, 1995; McClure-Griffiths et al., 2001; Smith, 2006); in most cases, however, it is impossible to find a source region in an old shell ($t > 5$ Myr).

We report on the discovery of a Galactic supershell, GSH 006−15+7, an object which exhibits a coherent structure over an angular size of ~ 25°. In Section 2.2, we describe its observed and derived properties in the context and theory of known Galactic supershells and investigate multi-wavelength data in order to characterise GSH 006−15+7. In Section 2.3, we use the unusual property of transition from HI emission to self-absorption visible in the walls of the shell to derive spin-temperature, kinetic temperature and optical depth, which allows us to better estimate the mass of the shell. Finally, in Section 2.4, we look for potential powering sources that could account for the energy required to form the shell. This supershell presents an interesting case study as one of the nearest large supershells. It highlights the potential dangers of assuming negligible optical depth when estimating mass from column density as well as being a possible example of a supershell in the transition stage between expansion and blowout. Based on the candidate powering sources, we also find evidence in favour of an origin for the supershell in the Sagittarius spiral arm.

2.2 GSH 006−15+7: Morphology and physical properties

GSH 006−15+7 was discovered within the Galactic All-Sky Survey (GASS) data set, a recent southern-sky HI line data survey (McClure-Griffiths et al., 2009; Kalberla et al., 2010). GASS covers the entire sky with declination $\delta \leq 1°$ at an angular resolution of ~16 arcmin, a velocity resolution of ~1 km s^{-1} over the velocity range $-400 \leq v \leq 500$ km s^{-1} and with an RMS brightness temperature of ~55 mK. The data set was produced using the 21 cm multibeam receiver on the Parkes 64 m radio telescope.

General morphology

The shell is named GSH 006−15+7 after its central longitude (~6°), central latitude (~−15°) and systemic velocity[1] ($v_{LSR} \sim 7$ km s^{-1}). GSH 006−15+7 is an example of a well-defined supershell of large angular size, comparable to those described in previous surveys for Galactic supershells (Heiles, 1979; Hu, 1981; Heiles, 1984; McClure-Griffiths et al., 2002). It extends over longitudes of $l = [356, 16]°$ and latitudes of $b = [-28, 2]°$, and is evident over the velocity range $v_{LSR} \sim 5$–11 km s^{-1}. Fig. 2.1 shows the shell in the velocity slice corresponding to its assumed systemic velocity[2], $v_{LSR} \sim 7$ km s^{-1}, while Fig. 2.2 shows its morphology over the multiple velocity slices in which it is apparent. We expect that there is emission due to the shell at velocities below 5 km s^{-1} which cannot be discerned due to the confusion of local emission. Table 2.1 provides a summary of all observed and derived properties.

The shell is teardrop-shaped with its apex crossing through the Galactic plane and extends to a latitude of −25°. This teardrop morphology suggests an origin in the Galactic plane, with material elongated in the latitude direction. GSH 006−15+7 is an asymmetric structure as there is no convincing evidence of an upper-latitude counterpart with respect to the Galactic plane. The region the shell occupies is confused due to its low velocity,

[1] All velocities are quoted with respect to the Local Standard of Rest (LSR).

[2] We note that the systemic velocity here is taken to be the apparent central velocity of the shell, which also corresponds to the point of maximum absorption in its spectral profile (Section 2.3).

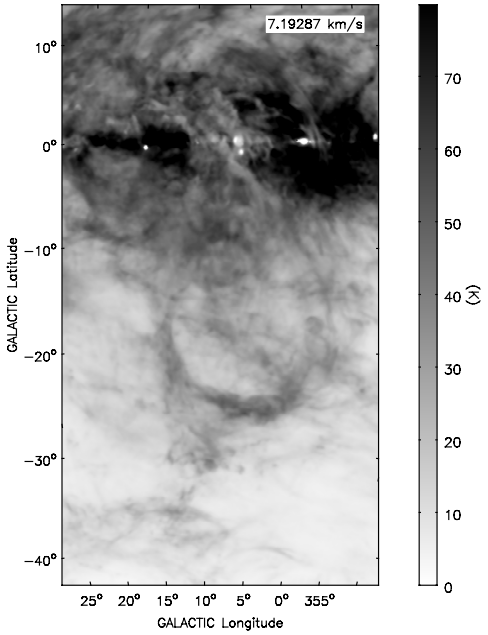

Figure 2.1: HI image of GSH 006−15+7 at the systemic velocity of 7 km s^{-1}. The brightness ranges from 10−80 K on a linear scale. This velocity slice has a width of ∼1 km s^{-1}.

resulting in considerable overlap with local emission, but the shell remains quite well-defined over a large angular size. We examine the structure of the shell at high latitude for evidence of fragmentation and breakout (Section 2.2), and find an apparent break in the shell wall at $l \sim 10°, b \sim -25°$, particularly at the lowest velocities (see Fig. 2.3). There is also a transition from HI emission to absorption on the upper right wall of the shell towards the Galactic plane over $b = [-7.0, -3.0]°$, typically indicative of dense cool gas (Section 2.3).

Distance and size

The small velocity v_{LSR} of the shell and its longitude close to the Galactic centre make kinematic distance estimates uncertain as rotation curves here are poorly defined with significant velocity crowding. To deal with this uncertainty, we first calculate the kinematic distances and then constrain the results based on knowledge of supershell origins and dynamics. We use a standard Galactic rotation curve (Fich, Blitz & Stark, 1989) to estimate the distance to the shell based on the systemic velocity of ∼7 km s^{-1}, namely

$$\frac{\omega}{\omega_0} = 1.00746\left(\frac{R_0}{R}\right) - 0.017112, \tag{2.1}$$

where ω is angular velocity, ω_0 is the angular velocity of the Sun, R_0 is the Sun's distance from the Galactic centre and R is Galactocentric distance, using $R_0 = 8.3$ kpc and $\Theta_0 = 246$ km s^{-1} in agreement with the most recent literature (Ghez et al., 2008; Gillessen et al., 2009; Bovy, Hogg & Rix, 2009). For an input longitude, latitude and velocity of $l = 6°$, $b = -15°$, $v = 7$ km s^{-1} (the central coordinates of the shell and its systemic velocity), the resulting distance is $d \sim 2.0$ kpc for the near distance, and $d \sim 15.5$ kpc for the far distance. We do not further consider the far distance estimates due to the large angular size of the shell and corresponding physical size at such a distance. Due

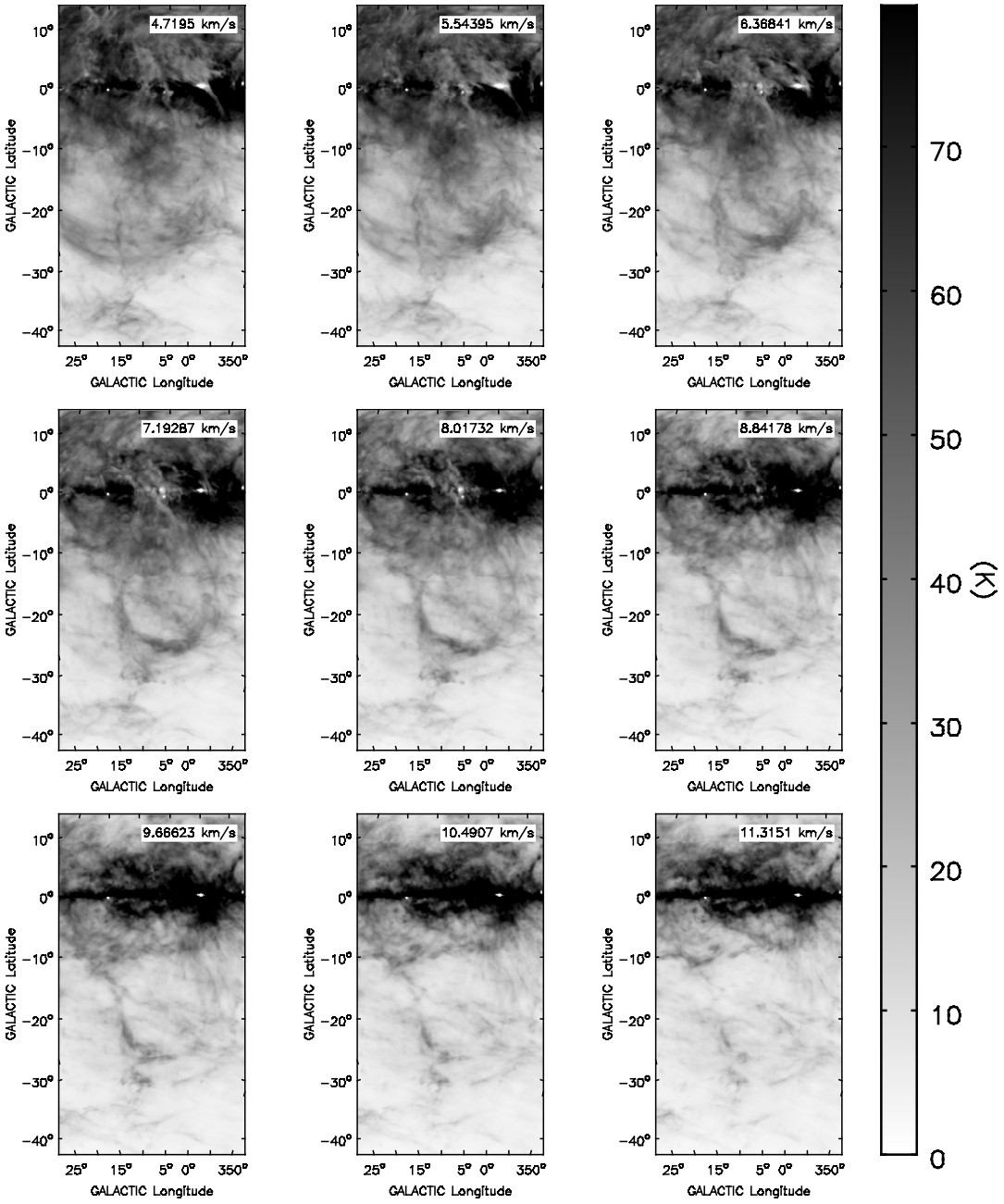

Figure 2.2: HI velocity slices of GSH 006−15+7, over the velocity range 5–11 km s^{-1} in steps of ∼1 km s^{-1}. The brightness ranges from 10−80 K on a linear scale. Due to overlapping local emission at lower velocities, we see the structure of the shell most clearly at higher velocity although it is fainter.

Table 2.1: Basic parameters for GSH 006−15+7.

Parameter	Value
Centre l	6.0°
Centre b	−15.0°
Central v_{LSR}	+7 km s^{-1}
Distance	1.5±0.5 kpc
Dimensions (angular)	30°× 20°
Dimensions (physical)	790 × 520 pc
v_{exp}	~8 km s^{-1}
E_e	~10^{52} erg
Mass	3±2 × 10^6 $M_\odot$
Age	15±5 Myr

to the large angular scale of GSH 006−15+7, we concentrate on longitude $l = [7, 10]°$ and latitude $b = [-2, 1]°$. This is the region where we might expect to find a powering source based on shell morphology, and results in a near distance range of $d = [1.2, 1.6]$ kpc. Rotation curve distance estimates generally provide a distance that can be off by as much as 2–3 kpc due to peculiar motions and local irregularities, an effect which is amplified particularly at low velocities (Gómez, 2006; Baba et al., 2009). If we consider the velocity gradient for the position of the shell over the velocity range [1, 10] km s^{-1}, this gradient equates to 0.3 kpc (km s^{-1})$^{-1}$, which indicates the magnitude of the error on the distance calculation. We hence use circumstantial factors to better constrain the distance to GSH 006−15+7.

Looking towards the Galactic centre at longitudes between [0, 10]° on the near side of the Milky Way, we expect to cross the Sagittarius arm (1–2 kpc away), the Scutum-Centaurus arm (~ 3 kpc away), the Norma arm (> 4 kpc away) and the near 3 kpc arm (> 5 kpc away), where distances are estimated based on the best knowledge of Milky Way spiral structure using available data (Churchwell et al., 2009). We note that there is a significant amount of star formation associated with a distance between 1.2 and 1.8 kpc, in the Sagittarius arm (Steiman-Cameron, Wolfire & Hollenbach, 2010), which agrees well with the kinematic distance of the shell. At a further distance of 3 kpc, if GSH 006−15+7 were located on the Scutum-Centaurus arm, we calculate the dimensions of the shell as ~1600 × 1000 pc. This would place the shell in the highest dimensions of known shells, especially for an object observed as a spatially coherent structure without clear signs of blowout. Based on this we believe that the shell is located near the Sagittarius arm and assign it a distance of 1.5±0.5 kpc, with the errors reflecting the range of our kinematic distances.

At an adopted distance of 1.5 kpc, the shell's angular dimensions of 30°× 20° (latitude extent × longitude extent) translate into physical dimensions of 790 × 520 pc. Based on these dimensions we can obtain a characteristic radius, $R_{sh} = \sqrt{R_{maj} \times R_{min}}$ ~ 300±100 pc. We adopt this characteristic radius in order to estimate the properties of the supershell and to compare it with the known supershell population. A characteristic radius of ~300 pc places the supershell in the largest 40 per cent of supershells, where the median shell radius is ~210 pc (Heiles, 1979; McClure-Griffiths et al., 2002). However, this sample is biased towards small nearby shells due to the difficulty in resolving small shells at any significant distance. If we instead take both distance and radius into account by dividing the shell

radius R_{sh} by the shell distance d_{sh},

$$\delta = \frac{R_{sh}}{d_{sh}} \tag{2.2}$$

where R_{sh} and d_{sh} are in parsecs, we see that the median $\delta \sim 0.05$ and that GSH 006−15+7 lies within the top 3 per cent of supershells with $\delta = 0.2$, indicating that it is one of the nearest physically large supershells discovered so far. This is notable as the majority of other physically large supershells are quite distant in comparison with GSH 006−15+7, most likely due to the difficulty in identifying objects of large angular size. If the shell does extend nearly 800 pc off the Galactic plane as calculated, then we expect that it is almost reaching the expected scale height of Galactic HI (Dickey & Lockman, 1990).

Mass, energy and age

To estimate the mass of the shell, we first approximate its shape as a cone situated on top of a sphere. Summing the flux over only those velocity slices in which the shell is visible, we produce a zeroth-moment map from which to extract measures of column density (assuming small optical depth), calculated as

$$N_{HI} = 1.823 \times 10^{18} \int_{v_0}^{v_1} T_B \; dv, \tag{2.3}$$

where N_{HI} is the neutral atomic hydrogen column density in cm^{-2}, v_0–v_1 represents its spectral extent in km s^{-1} and T_B is the observed brightness temperature in K. The mean column density was found by averaging the column density measured at different points along the wall of the shell. Assuming an axisymmetric wall width of the shell, we then use the background-corrected column density of the shell. The background was approximated by sampling the column density away from the shell at several points and averaging to find the mean background, avoiding other regions of emission. This gives a mean corrected zeroth-moment of ∼117 K km s^{-1} with a standard deviation of ∼15 K km s^{-1}. We convert the measured size of the cone and sphere from degrees to parsecs assuming a distance of 1.5 kpc and derive a mean column density of $N_{HI} \sim 2 \times 10^{20}$ cm^{-2}.

Once accounting for the presence of helium (a factor of 1.4), our estimate for the mass of the shell comes to $M \sim 10^6$ M$_\odot$ with a number density of ∼1.3 atoms cm^{-3} in the shell and an ambient density of ∼0.7 atoms cm^{-3} over the entire volume. Although there is foreground material present, using correlation between HI and infrared data shows that the effect of this material on our mass estimate is negligible. We note that our estimate here, typically used to estimate column densities of supershells, is affected by the necessary assumption that the gas is optically thin, and we correct for this assumption in Section 2.3.

We derive an initial estimate of the total energy of the supershell by calculating the kinetic energy associated with its mass and velocity. We assume the mass to be as estimated (∼10^6 M$_\odot$). Based on the large physical size of the shell and lack of a clear expansion signature in our data, we assume a late-evolution expansion velocity of 8 km s^{-1}, which is generally assigned when shells are in their final phase of expansion and the expansion velocity is comparable to random gas motions (Heiles, 1979). This gives $E_K = 0.5 M v_{exp}^2 \sim 6 \times 10^{50}$ erg. If we assume that E_K represents 20 per cent of the total energy input due to efficiency of energy transfer (McCray & Kafatos, 1987; Dawson et al., 2008), then we would expect the total input energy to be ∼3×10^{51} erg, which is likely to be an underestimate of the total shell energy based on other supershells of comparable size. We can also obtain a theoretical estimate of the expansion energy required to form the shell as described analytically (Weaver et al., 1977; McCray & Kafatos, 1987), such that

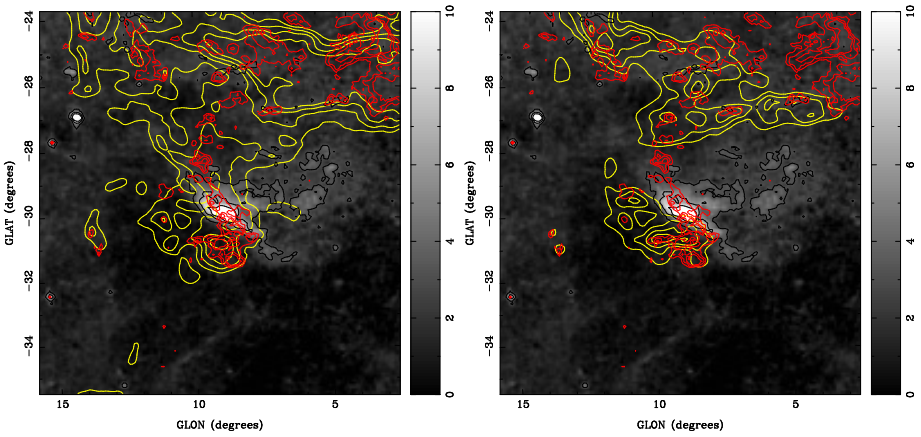

Figure 2.3: Map of Hα emission (greyscale) near GSH 006−15+7 (Finkbeiner, 2003). In all images, the contours show HI emission (yellow, at 25, 30, 35 K) at ~7 km s^{-1} (left) and ~10 km s^{-1} (right), 100 μm dust (red, at 8, 9, 11 MJy/Sr) and Hα emission (black, at 3, 6, 9 R). At 7 km s^{-1}, we see strong HI/IR correlation.

$$R = 97 \text{ pc}(N_* / n_0)^{1/5} t_7^{3/5} \tag{2.4}$$

and

$$v_{exp} = 5.7 \text{ km s}^{-1}(N_* / n_0)^{1/5} t_7^{-2/5} \tag{2.5}$$

where R is the radius in parsecs, N_* is the number of stars with M > 7 M$_\odot$ (including both stars that have gone or will go supernova), n_0 is the ambient density in cm^{-3}, and t_7 is the age in units of 10^7 years. To incorporate the level of certainty to which we can specify n_0 and R, we consider the range n_0 = [0.5, 1.0] cm^{-3} (to account for uncertainties consistent with the ambient density predicted above) and R = [200, 400] pc (to account for the asymmetry of the shell). By solving Equations 2.4 and 2.5 simultaneously, we find that t_7 = [15, 30] Myr and N_* = [6, 47]. This corresponds to an input energy of [1, 10] × 10^{52} erg, assuming that each star contributes 10^{51} erg from stellar winds and 10^{51} erg from its subsequent supernova. Overall these energy estimates suggest a formation energy of the order of 10^{52} erg, which is most likely the degree of accuracy to which we can predict the formation energy without further data or modelling.

For comparison to the overall distribution of supershell energy as performed above for radius (Heiles, 1979; McClure-Griffiths et al., 2002), we find a median known supershell energy of ~9 × 10^{51} erg which places GSH 006−15+7 very close to the average formation energy of known supershells, in rough agreement with the percentile of the characteristic radius. Estimating the age of a shell is very difficult in the absence of a current powering source, and so the age represented by t_7 is highly uncertain. We can however assume an upper age limit of around 20 Myr, after which the combination of ambient pressure at large scale height, galactic shear and gravitational deceleration likely destroys most coherent structure in a supershell and leads to breakout (Tenorio-Tagle & Bodenheimer, 1988; Mashchenko, Thilker & Braun, 1999).

Multi-wavelength properties

We investigated available multi-wavelength data to determine if other emission processes are evident. Previously detected emission in supershells include Hα, soft X-rays, polarised radio continuum and 100 μm emission (Heiles, Haffner & Reynolds, 1999; West et al., 2007;

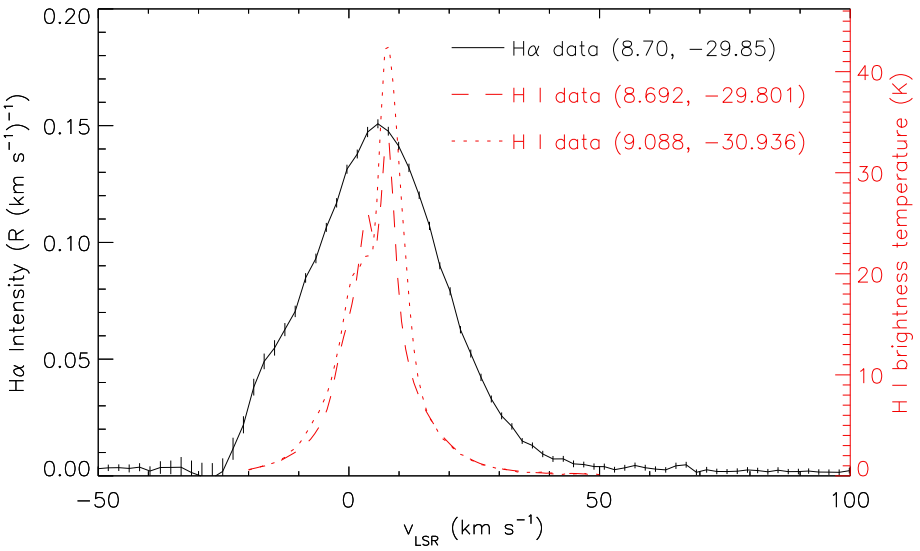

Figure 2.4: Hα spectrum obtained with WHAM. This is an on−off spectrum, as described in the text. An HI spectrum from an average of the GASS beams falling within the WHAM beam is shown with the dashed red line; an average of HI spectra from GASS beams falling within a beam the size of the WHAM beam but centred in a nearby knot of bright HI is shown with the dotted red line. The geocoronal Hα line is incompletely subtracted near $v_{LSR} = -20$ km s^{-1}.

McClure-Griffiths et al., 2001). We find no convincing evidence of soft X-rays (Snowden et al., 1995) (due to confusion) or 1420 MHz polarised emission (Testori, Reich & Reich, 2008) associated with the shell. We also looked at the Hα data from the Southern H-Alpha Sky Survey Atlas (SHASSA; Gaustad et al., 2001) Hα imaging survey compiled by Finkbeiner (2003). Based on extinction (Schlegel, Finkbeiner & Davis, 1998) and optical depth estimates (Madsen & Reynolds, 2005) in this region of the Galaxy, we can place an upper limit on the intensity of any possible Hα emission by noting that we see no emission within the main shell structure ($b \sim -20°$) or along the shell walls ($b \sim -25°$) at limits of [1.2±0.5, 2.0±0.5] R[3] respectively, which, given estimated optical depths of $\tau = [0.23, 0.46]$ at 656.26 nm, corresponds to maximum surface brightnesses of [1.5±0.6, 3.1±0.8] R.

At higher latitudes where the shell may be fragmenting, we note an evident Hα structure in the SHASSA data at $l \sim 8°$, $b \sim -30°$ with an angular extent of ∼2° and a peak brightness of ∼15 R. This structure is on the interior of the fragmentary HI emission seen at high latitudes (described in Section 2.2). We find that the HI at lower velocities correlates well with IRIS 100 μm emission (Miville-Deschênes & Lagache, 2005). Fig. 2.3 shows the emission in HI, Hα and 100 μm at different velocities, showing correlation between the shell and the Hα feature. To verify that the morphological association of the Hα and HI corresponds to physical association, we obtained an Hα spectrum with the Wisconsin H-Alpha Mapper (WHAM; Haffner et al., 2003, 2010) towards the region of the cloud with the brightest Hα emission in the SHASSA data, $(l, b) = (8.70, -29.85)$. The data were obtained from Cerro Tololo Interamerican Observatory on the 16th November 2011. WHAM integrates all emission within its 1°-diameter beam. We also obtained an off-source Hα spectrum centred at (7.03, −33.92). We fit a single Gaussian modelling

[3]One Rayleigh (R) = $10^6/4\pi$ photons s^{-1} cm^{-2} sr^{-1}.

the geocoronal Hα line to both the on- and off-source spectra and then subtracted the geocorona-subtracted off spectrum from the geocorona-subtracted on spectrum to remove the faint, mostly-unidentified atmospheric lines that dominate the baseline at the surface brightness sensitivity of WHAM (Hausen et al., 2002). We also used the geocoronal line to calibrate the velocity scale to an accuracy of less than 0.5 km s^{-1} (Haffner et al., 2003). The resulting spectrum consists of entirely astronomical emission and is shown in Fig. 2.4. The emission is well-fit by a single Gaussian component with a mean LSR velocity of 6.7 km s^{-1}, a full width at half-maximum of 27 km s^{-1}, and an intensity of 5 R. Although the relatively large width of the Hα line precludes definitive separation from local gas, the single-component Gaussian profile and the good agreement of the velocity centroid of the Hα emission with the HI data support the association between the Hα and the HI-emitting gas which is suggested by the morphology from the SHASSA image.

While Hα is observed in nearly all directions at high latitude (Haffner et al., 2003), multiple emission mechanisms are likely responsible in different directions. Hα well off the Galactic disk is thought to be emitted either by gas which is photoionised in situ by ionising photons from OB stars in the disk which have escaped the plane (Reynolds, 1990; Haffner et al., 2009; Wood et al., 2010) or to be Hα emission from closer to the plane which has been scattered off high-latitude dust clouds (Witt et al., 2010; Seon et al., 2011). Hα can also be emitted by shock-ionised gas or by gas photoionised by a harder (soft X-ray) radiation field such as might be produced by million-degree gas in the interior of the supershell. With future observations of the [O III] λ5007 and [S II] λ6716 emission lines in combination with photoionisation modelling (Wood & Mathis, 2004; Madsen, Reynolds & Haffner, 2006), we may be able to discriminate between emission mechanisms in this Hα feature and determine how the Hα relates to the supershell.

2.3 HI self-absorption in GSH 006−15+7

A unique feature of GSH 006−15+7 is that we clearly see the upper right shell wall transition from HI emission to absorption at $b \gtrsim -6.5°$, with the deepest absorption occurring at the systemic velocity of $v \sim 7$ km s^{-1}. Fig. 2.5 shows the transitioning wall at this systemic velocity, traced with a line. The region where we might expect to find the transition point is marked with a cross, showing a shift from emission to absorption. This phenomenon is known as HI self-absorption, or HISA (Heeschen, 1955; Gibson et al., 2000). An absorption profile (such as the example spectrum shown in Fig. 2.6) can indicate the presence of cool atomic gas. We expect to see HI absorption against a diffuse background T_{bg} that has a higher brightness temperature than the spin temperature T_s of the foreground gas. However, the detection of absorption is not generally enough to constrain the spin (or excitation) temperature of the gas and so it is usually assumed, constrained based on the presence of other molecules or estimated via line width fitting (Gibson et al., 2000). In special cases, a transition from HI emission to absorption allows T_s to be measured directly at the transition point (Kerton, 2005).

We apply HISA diagnostics to this feature below in order to estimate spin temperature T_s, optical depth τ and column density N_{HI} in the shell. We note that there is some spatial proximity of GSH 006−15+7 to the local self-absorbing Riegel-Crutcher cloud at a distance of ~100 pc towards the Galactic centre (McClure-Griffiths et al., 2006a), with their angular separation varying from a few to about 15 degrees. Taking the point of maximum absorption to represent the systemic velocity of the Riegel-Crutcher cloud gives a peak absorption velocity of ~5.8 km s^{-1}, compared to the peak absorption velocity of GSH 006−15+7 at ~7.2 km s^{-1}. The two objects also show differing absorption profiles and

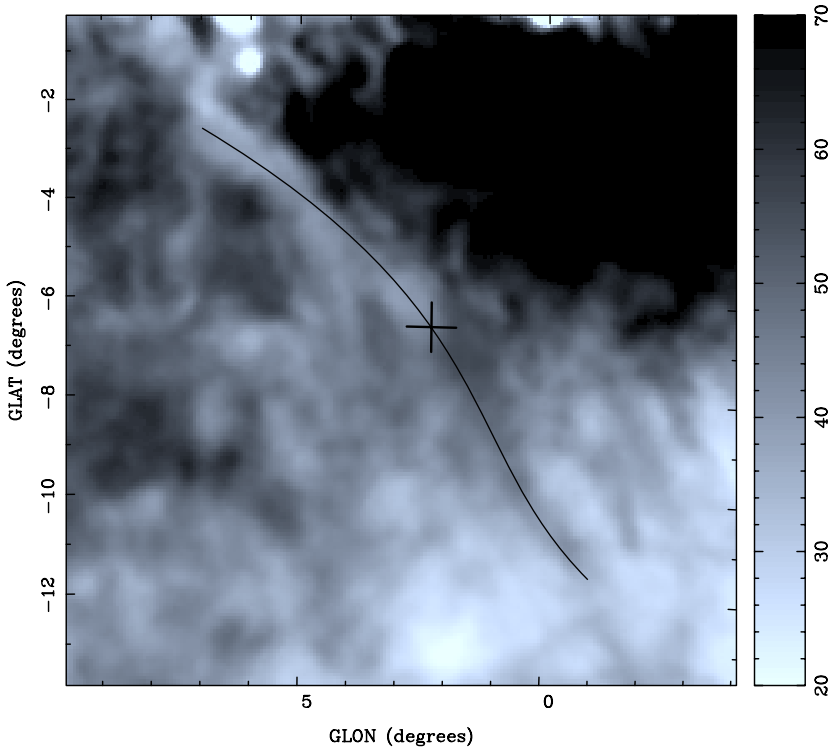

Figure 2.5: Image of the region of the shell used for HISA analysis, at the systemic velocity of ~7 km s^{-1}. We scale the data linearly from 20 K to 70 K. The line traces the position of the shell wall and the cross marks the region where GSH 006−15+7 transitions from absorption to emission.

are morphologically distinct, but with some evident overlapping absorption at latitudes > 0°. In our HISA analysis, we use only latitudes < 0° in order to avoid any confusion.

In a simplified case of absorption in the context of radiative transfer, we can define an 'on-source' brightness temperature (T_B) where we observe the absorption through the absorbing cloud (also known as the observed temperature, which in this case is the continuum-subtracted HI brightness temperature), and an 'off-source' brightness temperature (T_{bg}) where we estimate the background without the absorption present. Under the limiting, but reasonable, assumptions that any background or foreground gas has negligible optical depth (Gibson et al., 2000), the difference between the on and off is

$$T_B - T_{bg} = (T_s - T_c - pT_{bg})(1 - e^{-\tau}) \tag{2.6}$$

where T_s is spin temperature of the absorbing cloud, p is the fraction of HI emission originating behind the HISA cloud (as opposed to in front of the cloud), and T_c is the mean continuum background (Feldt, 1993). A value of $p = 1$ assumes that all HI emission originates from behind an object seen in absorption. Although we know that there is some foreground material towards GSH 006−15+7, setting $p = 1$ is a reasonable assumption given the relatively small path length to the shell. In the case of a transition from emission to absorption, the transition point marks the place where the background T_{bg} and the source T_B are equal in magnitude; in this case Equation 2.6 simplifies to

$$T_s = pT_{bg} + T_c. \tag{2.7}$$

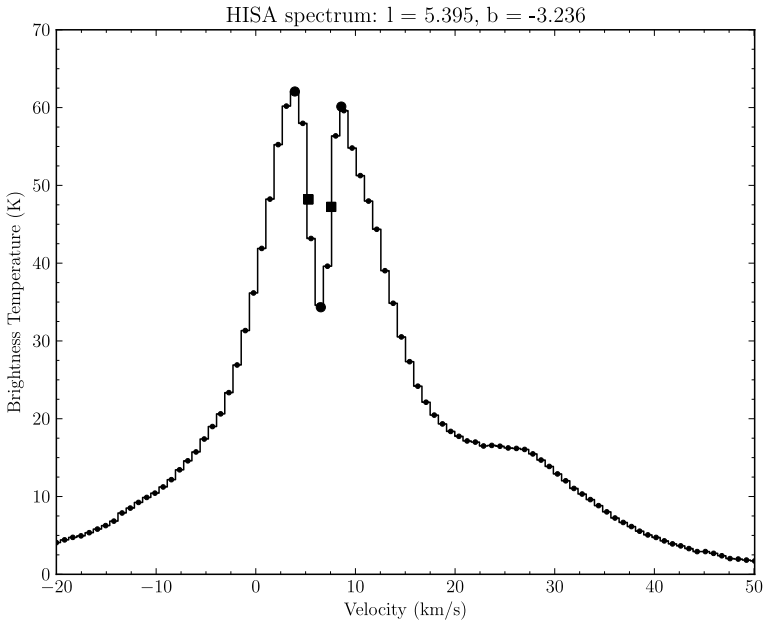

Figure 2.6: Example spectrum at a single position ($l = 5.395$, $b = -3.236$) showing the absorption due to GSH 006−15+7. The maximum absorption is predominantly seen at the systemic velocity of 7 km s^{-1} along the wall of the shell. The maxima/minima (circles) and estimated FWHM (squares) are shown overplotted on the spectrum and are used in Section 2.3 to estimate a line-width of ∼2 km s^{-1} corresponding to a spin temperature of ∼40 K.

Equation 2.7 thus allows direct calculation of the spin temperature under certain circumstances at the transition point in GSH 006−15+7, giving insight into the local properties of the HI gas. Once we estimate the spin temperature T_s, it is possible to substitute the values for T_B, T_{bg}, T_s and T_c to solve for optical depth, using

$$\tau = -\ln\left(1 - \frac{T_B - T_{bg}}{T_s - pT_{bg} - T_c}\right). \tag{2.8}$$

Using Equation 2.8 along the wall of GSH 006−15+7 under the assumption of constant T_s, we can calculate τ and use this to estimate the corresponding column density, using

$$N_{HI} = 1.823 \times 10^{18} T_s \int \tau \, d\upsilon \tag{2.9}$$

which, assuming a Gaussian form for the integral of $\tau(\upsilon)$, simplifies to

$$N_{HI} = \frac{\tau_0 T_s \Delta\upsilon}{C}, \tag{2.10}$$

where N_{HI} is the column density in cm^{-2}, τ_0 is the line centre opacity, T_s is the spin temperature in K, $\Delta\upsilon$ is the line profile width in km s^{-1} and C is a standard correction term (Gibson et al., 2000) [5.2×10^{-19} cm^2 K km s^{-1}] (Dickey & Lockman, 1990). From here, we can redo our previous mass calculation under the assumption that this newly estimated column density better represents the true value as the unlikely assumption of small optical depth is no longer made.

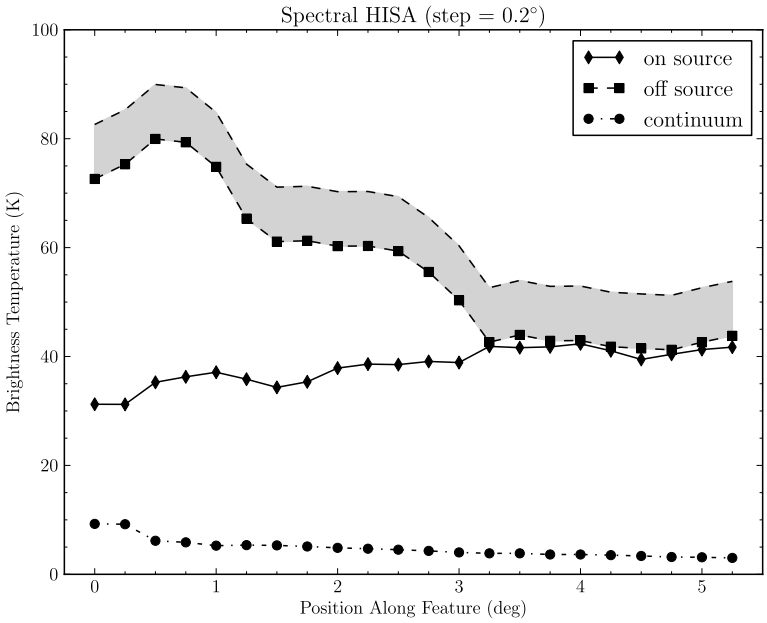

Figure 2.7: Spectrally-derived variation in brightness temperature on/off the shell arm. This plots the maximum absorption at each latitude (diamonds) versus the background temperature (squares) and the continuum background (circles, Calabretta, Staveley-Smith & Barnes (2014)), with the amount of absorption maximised along the wall of the shell. The horizontal axis is zeroed at $b = -2°$. The grey-shaded region represents the extent to which we believe the background is uncertain (~10 K), which is incorporated into the calculations. The transition point occurs where the curves meet, but the consequent emission of the shell is not clear due to the difficulty of spectrally separating emission due to GSH 006−15+7 and other emission.

HISA results for GSH 006−15+7

We examine the absorption to emission transition in velocity-longitude space along the wall of the shell at 0.2° increments over the range $b = [-7.0, -2.0]°$, obtaining the spectrum at the position of maximum absorption for each latitude point. We resample each spectrum in order to ease the location of minima and maxima along the curve, taking into account the velocity resolution of ~1 km s^{-1} in estimating the velocity width of each profile. By obtaining the minimum and maximum points that define the absorption, we adopt these as our on-source (T_B) and off-source (T_{bg}) values. We determine the continuum background (T_c) from HI Parkes All Sky Survey (HIPASS) continuum data at 1.4 GHz corrected for extended emission (Calabretta, Staveley-Smith & Barnes, 2014). The results are plotted in Fig. 2.7, showing the on-source T_B, the averaged off-source T_{bg} and the background continuum T_c.

We assume the simplest case for the background by taking the average of each pair of maxima to represent the amount to which the emission is absorbed. To investigate the error on our assumed background, we examined longitude profiles at 7 km s^{-1} at the latitude of each point used in our analysis and find the peak brightness temperature on the right side of the spatially-apparent absorption (outside the shell wall). This allows us to check how well the background derived from the velocity spectra agrees with a spatially-

determined background temperature. We find a positive trend indicating that the spectral profile does underestimate the background, with a peak deviation of ~10 K and a mean deviation of ~4 K. We thus assume that our background estimate could be underestimated by as much as ~10 K and factor this into our predictions below.

The spectral method we have used, although reliable, does not easily allow visualisation of the emission of GSH 006−15+7 beyond the transition point because it is difficult to separate the shell emission from background emission without stable background spectral profiles that can be subtracted. Due to this, we cannot use Equation 2.7 to tightly constrain the spin temperature at the transition point, but we can set an upper limit to the spin temperature by considering the combined T_B and T_c values along the wall,

$$T_{s,max} = T_B + T_c, \tag{2.11}$$

as in our simple radiative transfer this will always be an overestimate as there are likely to be sources contributing to the emission along the line of sight that are not taken into account. We thus calculate $T_{s,max}$ systematically along the shell wall and then average the results to give a mean maximum spin temperature of $\overline{T_{s,max}} \sim 40$ K. Any fluctuations in spin temperature due to the local properties of the gas in the shell wall are likely to be moderated by using the mean value. To check the value of T_s, we estimate the width of the absorption profile in Fig. 2.6 and find the FWHM ~ 2 km s^{-1}. In this case, the resulting thermal velocity dispersion σ_v is FWHM/2.36 ~ 0.8 km s^{-1} with a kinetic temperature of

$$T_k = \frac{m_H \sigma_v^2}{k}, \tag{2.12}$$

where m_H is the mass of hydrogen and k is Boltzmann's constant. This yields $T_k \sim 90$ K. For temperatures $T_k < 1000$ K in the cold neutral medium (CNM), T_k is essentially equal to T_s (Liszt, 2001; Roy, Chengalur & Srianand, 2006). However, spectral modelling of HI absorption and emission profiles demonstrates that significant line broadening relative to the spin temperature at peak opacity τ_{max} is generally seen (Heiles & Troland, 2003) and can indicate either or both of significant internal temperature structure in the gas and a turbulent contribution to the line-width measurement. Our spin temperature estimate of 40 K implies excess line-broadening of $\sigma_v \sim 0.6$ km s^{-1}, which is fully consistent with values typically found in the ISM.

Using Equation 2.8 along the absorbing wall of GSH 006−15+7 and a spin temperature of 40 K gives values of τ in the range [1.8, 5.0] with a mean of $\tau \sim 3.1$. The potential underestimation of the background of up to ~10 K is used to calculate the upper limit in the given ranges. We use the optical depths to estimate the corresponding column density, which ranges over [2.7, 7.7] $\times 10^{20}$ cm^{-2} with a mean value of $N_{HI} \sim 4.7 \times 10^{20}$ cm^{-2}. We compare this to the value estimated from the zeroth-moment map in Section 2.2 of $N_{HI} \sim 2 \times 10^{20}$ cm^{-2}, and note that the mean column density is more than double the previous estimate, which is to be expected due to eliminating the assumption of negligible optical depth.

If we assume that our new estimate better reflects the true column density and substitute this into the calculation for mass, we find that M ranges over [1.8, 5.1] $\times 10^6$ M$_\odot$ with a corresponding number density of [1.7, 4.8] atoms cm^{-3}. This is in comparison to our previously determined estimate of ~10^6 M$_\odot$ and ~1.3 atom cm^{-3}, where the assumption of zero optical depth leads to a significant underestimation of the shell mass. We note that the application of a single opacity correction factor to the entire supershell may be erroneous as it would be plausible to have systematically lower densities and opacities at larger off-plane distances, while the opacity measurement is done closer to the plane where

these would be maximised. To counter the effect of this, we use the range of resultant masses from using optically thin versus HISA as a representation of the error on the mass such that $M = 3\pm2 \times 10^6$ M$_\odot$.

2.4 Evolution of GSH 006−15+7

To investigate further the nature of the shell, we have searched for potential stellar powering sources and applied simple modelling in order to constrain the origin of GSH 006−15+7. This involves estimating the amount of energy deposited by candidate sources through stellar winds and supernovae in order to assess whether these regions could form GSH 006−15+7 based on the energy predictions we made in Section 2.2, where we found $N_* \sim 26$ and $E \sim 10^{52}$ erg.

Energy estimation and supernovae

We use multi-wavelength data and published databases to investigate the region of the Galactic plane where the walls of GSH 006−15+7 meet to search for powering sources. Of the nearby OB associations (Humphreys, 1978), Sagittarius (Sgr) OB 1 is a likely candidate based on coordinates as well as its reported distance of 1.58 kpc. The 13 high-mass stars of Sgr OB 1 are spread over 10° of longitude, which makes it difficult to assess their true association. At the reported distance of ~1.6 kpc, the mean longitudinal drift of each star from the centre of the Sgr OB 1 association corresponds to roughly 40 pc, in agreement with an average stellar drift velocity of ~5 km s^{-1} (McCray & Kafatos, 1987) and an age of around 10−20 Myr for GSH 006−15+7. We show their distribution in Fig. 2.8, as well as the distribution of the nearby and possibly associated open clusters NGC 6514, NGC 6530, and NGC 6531 (with which some of the stars of Sgr OB 1 are associated). The general area has also been referred to as Sagittarius I (Stalbovsky & Shevchenko, 1981), incorporating a number of clusters and nebulae. Overall, the entire region shows evidence of high star formation activity, and so we base our initial energy calculations on the stellar winds of the known high-mass stars.

We calculate stellar wind estimates using Sgr OB 1, of which stellar types are well known (Mason et al., 1998; Maíz-Apellániz et al., 2004) and can be used to determine effective temperature, luminosity, mass, maximum age, mass loss rate, wind terminal velocity and wind luminosity. We estimate the stellar wind mechanical luminosity as $L_{SW} = \frac{1}{2}\dot{M}V_\infty^2$, based on the observed spectral type which allows derivation of mass loss rate $\dot{M}$ and wind terminal velocity V_∞. We match the stellar types earlier than B0 to those for the Carina Nebula (Smith, 2006) and account for luminosity classes II and IV (which are generally not included in models) by raising them to the next highest class (i.e. I and III), which provides an overestimate for their energy contribution. We have also assumed that the age of each star is the lifetime of a star with its estimated mass, which gives us an upper limit. Given the resulting wind luminosity, it is then possible to estimate total energy input from these stars due to their stellar winds.

It is expected in studies of large old shells that many of their forming high-mass stars will have exploded as supernovae (SNe), as their lifetimes are on the order of a few to several million years (Chiosi, Bertelli & Bressan, 1992). As such the energy calculated from stellar winds alone of any powering region is likely to underestimate its true energy contribution, and so we assess the contribution of stars that have already gone supernova[4]. We can estimate the number of supernovae based on the initial mass function (IMF), a

[4]We refer to these stars as exploded stars.

measure of mass distribution. This can be readily done in the case of stellar clusters with a known IMF, as opposed to OB associations whose stars can be scattered across large regions of space and possibly even associated with different stellar clusters (as in the case of Sgr OB 1). We perform a cursory IMF calculation for Sgr OB 1 but emphasise that there are strong assumptions impacting this estimate. For this reason, we focus the IMF calculation on the open clusters NGC 6514, NGC 6530 and NGC 6531 due to their proximity to GSH 006−15+7, distance close to 1.5 kpc and stellar content, noting that several of the stars of Sgr OB 1 are associated with these clusters. We do not include the other positionally nearby clusters NGC 6546 (due to its large estimated age exceeding the shell's age) or Bochum 14 (due to its lack of high-mass stars and poorly known stellar composition).

For the clusters, we use UBV photometry and stellar classification of members to calculate effective temperature (log T_{eff}), bolometric correction (BC) and V-band extinction (A_V) of each star (Massey et al., 1995), using these values to then calculate the absolute magnitude (M_V), bolometric magnitude (M_{bol}) and hence luminosity (log $L/L_\odot$) (Crowther, 2004). Masses are estimated using this resulting luminosity via the mass-luminosity relationship (Eddington, 1924), with awareness that this relation is generally valid only for main sequence stars. We make the assumption that the photometry is complete from the minimum high-mass star calculated (M_{min}) to the maximum high-mass star calculated (M_{max}), with any stars higher than this mass already gone supernova. We adopt a minimum possible stellar mass of 0.5 $M_\odot$ (Kroupa, 2001) and a maximum possible stellar mass of 150 $M_\odot$ (Figer, 2005), and integrate over the range assumed complete

$$F_N(M_{min} < M < M_{max}) = \frac{\int_{M_{min}}^{M_{max}} M^\alpha dM}{\int_{0.5}^{150} M^\alpha dM}, \tag{2.13}$$

where F_N is the number fraction of stars in the given range with respect to the total and α is the slope of the initial mass function. We can therefore estimate the total number of cluster stars by dividing the number of stars N in this range by F_N. Then, we estimate the number fraction of exploded stars in the cluster,

$$F_N(M > M_{max}) = \frac{\int_{M_{max}}^{150} M^\alpha dM}{\int_{0.5}^{150} M^\alpha dM}, \tag{2.14}$$

and multiply by the total number of stars to obtain an estimate of the total number of exploded stars which we attribute to supernovae (Bruhweiler et al., 1980; Heiles, 1987). We assume that each exploded star has contributed 10^{51} erg of energy through stellar winds over its lifetime and 10^{51} erg via its supernova, giving an energy contribution of 2×10^{51} erg per exploded star.

Cluster parameters

We obtain UBV photometry and stellar types for each cluster from the online WEBDA (Web Open Cluster Database (Mermilliod & Paunzen, 2003). As we are necessarily assuming that these clusters contributed to the formation of GSH 006−15+7, we adopt a distance of 1.5 kpc to all clusters. We take the age estimates from the catalogue of Dias et al. (2002), and obtain values of mean reddening from the literature. We obtain values for the IMF slope (α) of each cluster where available, otherwise we adopt the traditional Salpeter value of $\alpha = -2.35$ (Salpeter, 1955). We use in our calculations a total of 60 stars from the three clusters described below.

Cluster [1]	$M > 8$ M$_\odot$ [2]	M$_{min}$ (M$_\odot$) [3]	M$_{max}$ (M$_\odot$) [4]	α [5]	Cluster stars [6]	# SNe [7]	Energy [8]
NGC 6514	[4, 11]	[5, 7]	[23, 65]	−2.35	[360, 520]	[2, 1]	[4.0, 2.0] $\times 10^{51}$ erg
NGC 6530	[20, 30]	[5, 8]	[28, 83]	−2.22	[590, 970]	[4, 1]	[8.0, 2.0] $\times 10^{51}$ erg
NGC 6531	[5, 9]	[4, 6]	[17, 42]	−2.29	[260, 400]	[3, 2]	[6.0, 4.0] $\times 10^{51}$ erg
Total	...	...	...	...	...	[9, 4]	[1.8, 0.8] $\times 10^{52}$ erg
Sgr OB 1	[13, 13]	[17, 19]	[43, 56]	−2.35	[2100, 2300]	[4, 3]	[1.0, 0.6] $\times 10^{52}$ erg

Table 2.2: Parameters of each cluster used to model IMF and resulting values. The columns are: (1) cluster name, (2) number of stars greater than 8 solar masses, (3) minimum mass used, (4) maximum mass used, (5) initial mass function slope, (6) extrapolated number of cluster stars based on IMF predicted number fraction, (7) number of supernovae estimated based on the mass distribution and (8) corresponding energy of these stars, assuming 10^{51} erg from stellar winds and 10^{51} erg from the supernova. In all cases for the clusters, the first number represents a mass power of 4, and the second number represents a mass power of 3. In the case of Sgr OB 1, the numbers represent masses from different sources (Martins, Schaerer & Hillier, 2005; Weidner & Vink, 2010).

NGC 6514

This object is also known as the Trifid Nebula or M20, housing an open cluster of around 360 known stars as well as various types of nebulae and dense regions of dust. The distances reported for this object are quite varied, from 0.8 kpc to over 2 kpc, however we adopt a distance of 1.5 kpc, the Dias catalogue age of 23.3 Myr and a mean reddening of $E(B-V)$ = 0.23 (Ogura & Ishida, 1975). We use an IMF slope of $\alpha = -2.35$ for this cluster.

NGC 6530

NGC 6530 is a well-studied young, active star-forming cluster associated with the Lagoon Nebula, described as the core cluster of the Sgr OB 1 association (Chen, de Grijs & Zhao, 2007) and housing roughly 350 known stars. Of the three clusters, it is the most active and also houses the highest number of O stars. Based on the literature, we adopt a mean reddening of $E(B-V) = 0.35$ (Sung, Chun & Bessell, 2000) for this cluster, the Dias catalogue age of 7.4 Myr and an IMF slope of $\alpha = -2.22$ (Prisinzano et al., 2005).

NGC 6531

This cluster is not particularly well studied due to its small number of detected stars (around 100), lack of numerous high-mass stars, nebulae or bright star forming regions. It has reported distance moduli of 11.35 (Mermilliod & Maeder, 1986), 10.70 (Forbes, 1996), 10.5 (Park, Sung & Kang, 2001) and most recently 10.47 (McSwain & Gies, 2005), giving a distance range of 1.2 to 1.9 kpc with a mean of 1.4 kpc. Its age has been estimated with a reported range of 8−11 Myr. We adopt the Dias catalogue age of 11.7 Myr, a mean reddening of $E(B-V) = 0.28$ for this object and an IMF slope of $\alpha = -2.29$ (Forbes, 1996).

Modelling the energy of the shell: stellar winds

In the case of Sgr OB 1, we estimate ~3 × 10^{51} erg of stellar wind energy, too low to account solely for the formation of GSH 006−15+7. Similarly we obtain a total cluster stellar wind energy of ~1 × 10^{51} erg, which we expect because the clusters have fewer high-mass stars overall. As only 20 per cent of these winds would have contributed to the expansion of the shell and our energy prediction was 10^{52} erg, we conclude that the stellar winds of Sgr OB 1 or the clusters could not be the sole powering source of GSH 006−15+7,

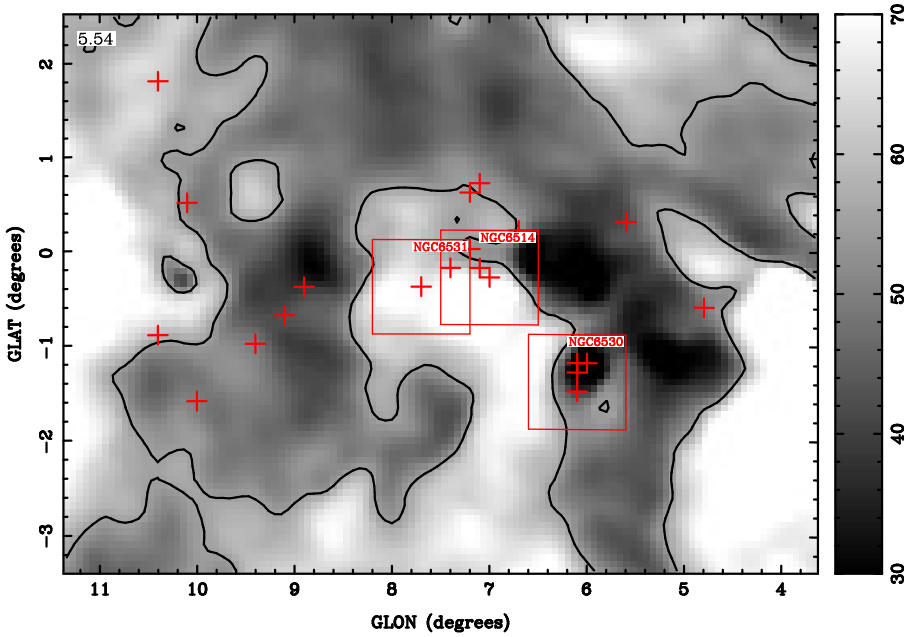

Figure 2.8: The assumed source region of GSH 006−15+7, showing the stars of Sagittarius OB 1 (red crosses) and the open clusters (red boxes) used for stellar wind estimates and for estimating the energy contribution of supernovae overlaid on a HI velocity slice at ~5 km s^{-1} (where the cavity these objects occupy is most clearly visible). The black contour is at 55 K to show the outline of the shell and the scale is linear from 30 K to 70 K.

which is not necessarily surprising given the size and age of the shell. We therefore assume that the majority of the expansion energy must have come from supernovae that are now invisible.

Modelling the energy of the shell: supernovae

We now estimate the amount of energy we could derive based on exploded stars from the clusters we have examined. As before we adopt a distance of 1.5 kpc, values of reddening from the literature and the Dias et al. (2002) catalogue cluster age estimate. The results are summarised in Table 2.2. We obtain a maximum energy input from supernovae and stellar winds (from exploded stars) of around ~2 × 10^{52} erg total. But using the same conversion efficiency of supernova energy used in Section 2.2 of 20 per cent gives us only E_{SNe} ~ 5 × 10^{51} erg.

For comparison, we perform the same calculation for the stars of Sgr OB 1 (for which we have more reliable masses) but emphasise that this approach implicitly assumes that the association's stars formed from the same mass distribution. This is likely to be an over-simplification. We adopt mass estimates from two sources (Martins, Schaerer & Hillier, 2005; Weidner & Vink, 2010) and use this to give a likely energy range. We use the standard Salpeter value of $\alpha = -2.35$ for the IMF slope and assume that the association's stars are complete from the minimum detected mass (17 $M_\odot$/19 $M_\odot$) to the maximum detected mass (43 $M_\odot$/56 $M_\odot$), where the two numbers represent mass estimates from different sources (Martins, Schaerer & Hillier, 2005; Weidner & Vink, 2010). This results in a total energy range of 0.6−1.0 × 10^{52} erg total, which is essentially in agreement with the cluster estimate as suggesting a maximum converted energy of ~2 × 10^{51} erg.

We find here that the formation of GSH 006−15+7 cannot be accounted for solely by

the supernovae and stellar winds of exploded stars from either the clusters or Sgr OB 1. The combination of stellar wind energy found in Section 2.4 ($E_{wind} \sim 5 \times 10^{50}$ erg) with that of the exploded stars ($E_{SNe} \sim 5 \times 10^{51}$ erg) is close to 10^{52} erg (with the dominant contribution being from exploded stars). We also expect that our rough assumption of 2×10^{51} erg per exploded star may in fact be an underestimate of the true energy contribution of the very high-mass stars, since the winds are likely to exceed the supernova energy for high-mass stars earlier than O6 (Abbott, 1982). It therefore seems reasonable to assume that the shell was formed by the stars in and or around the Sgr OB 1 association.

2.5 Conclusion

We have reported on the discovery, properties and analysis of a new Milky Way supershell GSH 006−15+7. This object spans longitudes of l = [356, 16]° and latitudes of b = [−28, 2]°, which translates into physical dimensions of (790±260) × (520±175) pc at an estimated distance of 1.5±0.5 kpc. The shell is elongated in the latitude direction, which is possibly due to a density gradient away from the Galactic plane. We estimate the dynamical age to be between 7–15 Myr, with the coherent structure of the shell suggesting an age less than 20 Myr based on known supershells in the Galaxy. Energy estimates suggest a formation energy of most likely ~ 10^{52} erg, with a mass estimate, corrected for optical depth, of $3\pm2 \times 10^6$ $M_\odot$.

We have found no convincing evidence of an upper shell counterpart. In the case of an absent upper shell complementing GSH 006−15+7, we can interpret this as the result of an asymmetric outflow, due possibly to inhomogeneous gas surrounding the source or a source region slightly below the Galactic plane which preferentially outflows in the direction of the lowest density. An offset of even 100 pc from the Galactic plane, depending on the vertical density distribution, is known to have a significant effect on the direction of outflow and shape of the resulting supershell (Chevalier & Gardner, 1974).

We have investigated a self-absorbing feature along the shell wall in order to place a more realistic constraint on our estimates of shell mass as well as giving an indication of gas temperature. We have found that the gas in the supershell is comparatively cool with a spin temperature of ~40 K as well as being quite optically thick (and hence dense) with $\tau \sim 3$ which is supportive of recent studies showing correlation between supershells and molecular gas formation, which requires dense cool gas (Dawson et al., 2008; Fukui & Kawamura, 2010; Dawson et al., 2011).

We see strong evidence of past star formation in the region where we would expect to find a powering source based on the morphology and physical properties of the supershell. We also find some evidence in favour of a powering source for GSH 006−15+7 via the OB association Sgr OB 1 and the nearby open clusters NGC 6514, 6530 and 6531. In analysing the energy contribution from stellar winds from existing stars and the winds/supernovae of exploded stars from Sgr OB 1 and the clusters, the estimated combined energy of ~5 × 10^{51} erg is close to the estimated requirement of ~10^{52} erg of formation energy, and is within the errors in our analysis. The absence of presently observable high-mass stars contributing significant stellar winds suggests an expansion partially, if not mostly, driven by the winds and supernovae of exploded stars, which likely originated as part of the same region occupied by Sgr OB 1 and the clusters.

Based on our analysis, we suggest that GSH 006−15+7 is in the transition stage between supershell and chimney. The filamentary structures we see in the morphology of the shell at high latitudes, evident in HI and IR with possible associated Hα emission, may be an indication that fragmentation and blowout is already beginning to take place.

Chapter

3 THE CUTTLEFISH: A HIGH-LATITUDE Hα FEATURE

Overview

This chapter represents the current preliminary progress in follow-up on the Cuttlefish, a region near the top of GSH 006−15+7 that is potentially associated with the fragmentation and transition into a chimney of the supershell, to be supplemented by future work modelling the ionisation mechanism responsible for the Cuttlefish.

3.1 Introduction

The interface between the disk and the halo of the Milky Way galaxy is a vital transition region for both infall entering the Galaxy and outflow from the disk as part of the Galactic ecosystem. Material moving up from the stellar disk through supershell blowout and star formation in a Galactic fountain model must survive the passage from low temperatures and high pressures to a hot 10^6 K halo, if it is to fall back down to the disk and be useful as star forming gas. Any material falling in through the halo must survive the temperature and pressure gradients in the opposite direction, avoiding being evaporated and ripped apart via ram-pressure interaction if it is to become fuel for continued evolution of the Milky Way. Understanding the emission we see at the disk-halo interface and what this tells us about the survival of gas passing through it is thus critical for improving our understanding of the evolution and fate of all galaxies with observable infall or outflow processes.

Here we present the investigation of this Hα feature located at a Galactic latitude of $b \sim -30°$. We hence refer to this region of emission as the Cuttlefish throughout the paper based on its morphology (as shown in Figure 3.1) and for brevity. The discovery of the Cuttlefish was published in a paper describing a nearby Galactic supershell, GSH 006−15+7 (Moss et al., 2012). This supershell is likely located in the Sagittarius arm of the Milky Way, at a distance of 1.5±0.5 kpc, and is thought to be old (10–20 Myr) given its lack of expansion velocity and dimensions of ∼800 × 500 pc at a distance of 1.5 kpc. Given the age of the supershell, we expect that it would be approaching the blowout stage whereby it would lose the currently apparent coherent shell structure and evolve into something like the chimney structures seen in other regions of the Galaxy (Normandeau, Taylor & Dewdney, 1996; McClure-Griffiths et al., 2000, 2006b; Dawson et al., 2008).

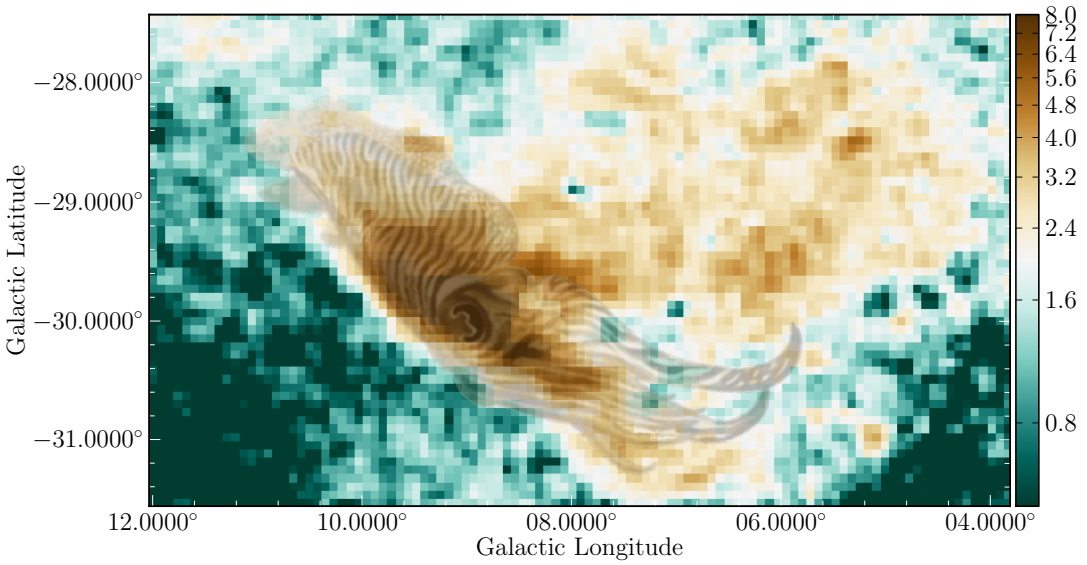

Figure 3.1: An image comparing the morphological structure of a cuttlefish (overlaid transparently) with the spatial structure in Hα from the SHASSA data (Finkbeiner, 2003) of the evident Hα feature. We see that there is some measure of resemblance of the Hα feature to a cuttlefish, hence giving context to the name of this feature.

Moss et al. (2012) proposed that the Cuttlefish Hα feature might be associated with a break out in the supershell, and could indicate that the supershell is beginning to fragment at high latitudes. This suggestion was made on the basis of velocity agreement between the HI and the Hα (at ~6 km s^{-1}) as well as morphological correlation. Based on the new data we have since collected on the region, we consider again the likely origins for the feature in Section 3.4. While it is likely that the neutral hydrogen seen at v_{LSR} ~ 7 km s^{-1} is correlated with the Hα of the Cuttlefish, the exact nature of the Hα feature and the question of association with GSH 006−15+7 depends on physical explanation of the different emission lines we see within the Cuttlefish. We emphasise that we are primarily interested in the potential association between the Cuttlefish and GSH 006−15+7 in the context of supershell break-out and disk-halo interaction, however the high-energy signatures detected in the Cuttlefish present an interesting case study of the interstellar medium independent of origin. If the Cuttlefish is indeed related to fragmentation associated with the transition of GSH 006−15+7 from a supershell into a chimney, then this has the potential to trace the physical processes that drive supershell evolution, giving insight into how supershells fragment and the multi-wavelength properties of the resulting clouds that are ejected into the halo.

We have used neutral hydrogen spectral line data from the Galactic All Sky Survey (GASS, McClure-Griffiths et al., 2009; Kalberla et al., 2010). GASS covers the entire southern sky south of declination 1° and features ~57 mK sensitivity, 16′ angular resolution and 1 km s^{-1} velocity resolution. We also obtained high-resolution follow-up interferometric data from the Australia Telescope Compact Array, in order to better define the morphological signatures of the HI gas. In this analysis, we have combined our HI data with optical spectral line data from the Wisconsin Hα Mapper (WHAM, Haffner et al., 2003) in the lines of Hα, Hβ, [S II], [N II], [O III] and He I. WHAM has an angular resolution of 1° and a velocity resolution of 15 km s^{-1}, with the sensitivity varying depending on the duration of the observations but generally on the order of 0.001 R (km s^{-1})$^{-1}$. The

emission lines we have detected (particularly those with high ionisation energy requirements) and their corresponding intensities put constraints on the ionising spectrum of the Cuttlefish. We specifically focus on the results of pointed observations here, and defer detailed imaging, analysis and modelling of potential ionising sources to future work.

In Sections 3.2 and 3.3, we show the data from GASS and WHAM that we have used to investigate the Cuttlefish. In Section 3.4, we analyse this data with a particular focus on the new insights into the physical processes producing the Cuttlefish based on the WHAM emission lines, their velocities and their relative intensities.

3.2 Radio observations

The Galactic All Sky Survey is a survey of southern-sky neutral hydrogen carried out with the Parkes 64-m radio telescope at high spectral resolution (McClure-Griffiths et al., 2009). A detailed description of the GASS data and survey techniques is given in Chapter 4. The Cuttlefish Hα feature, and its potential association with the nearby supershell GSH 006−15+7, was first discovered in multi-wavelength analysis of the GASS HI data compared with the high-resolution Hα map from the Southern H-Alpha Sky Survey Atlas (SHASSA; Gaustad et al., 2001) Hα imaging survey compiled by Finkbeiner (2003). Based on the velocity agreement between the GASS HI and WHAM Hα spectrum obtained during the investigation, physical association between the neutral and ionised hydrogen was suggested.

We obtained high-resolution follow-up data of the HI in the region surrounding the Cuttlefish with the Australia Telescope Compact Array in the EW352 configuration. These observations were carried out on 14th January 2013 using the Compact Array Broadband Backend (CABB) (Wilson et al., 2011) operating in spectral-zoom mode with six concatenated zoom bands to ensure accurate continuum subtraction, with each band contributing 211 km s^{-1} individually and combining to a total range of 738.8 km s^{-1} at a spectral resolution of 0.1 km s^{-1}. The time available for the observations was during that assigned for ATNF vacation student projects, when the Sun was located within several degrees of the Cuttlefish region, and as such the data were affected by solar interference. The majority of the solar interference was mitigated by performing calibrations using only the long baselines to CA06, as the Sun was primarily visible on the shortest baselines, and by subtracting a model of the Sun during continuum-subtraction in MIRIAD's *uvlin* task (Sault, Teuben & Wright, 1995). It was particularly important with these data to flag HI emission present in the spectrum of the primary calibrator, 1934−638, due to the supershell emission occurring at low velocities near 0 km s^{-1}.

We obtained an additional 3.5 hours of ATCA green time in order to fill in the *uv* coverage at the point where the supershell was near zenith, during which the drive time between each of the 136 mosaic pointings became significant and decreased the sensitivity of the initial data. These observations were carried out on 9th March 2014 while the ATCA was in the EW367 array configuration, and so also contributed supplementary *uv* coverage to fill in gaps in the EW352 configuration. The observations were carried out with the same specifications as the previous year's observations, except with regards to the Sun which is not located near the Cuttlefish in March. Then the data from each set of observations was combined at the *invert* stage. The overall theoretical sensitivity of the combined data is 70 mJy per beam, although we find a measured RMS of ~80 mJy per beam. The combination of EW352 and EW367 gives the data sensitivity to angular scales from 23′ down to 2′ (excluding the longest baselines to CA06).

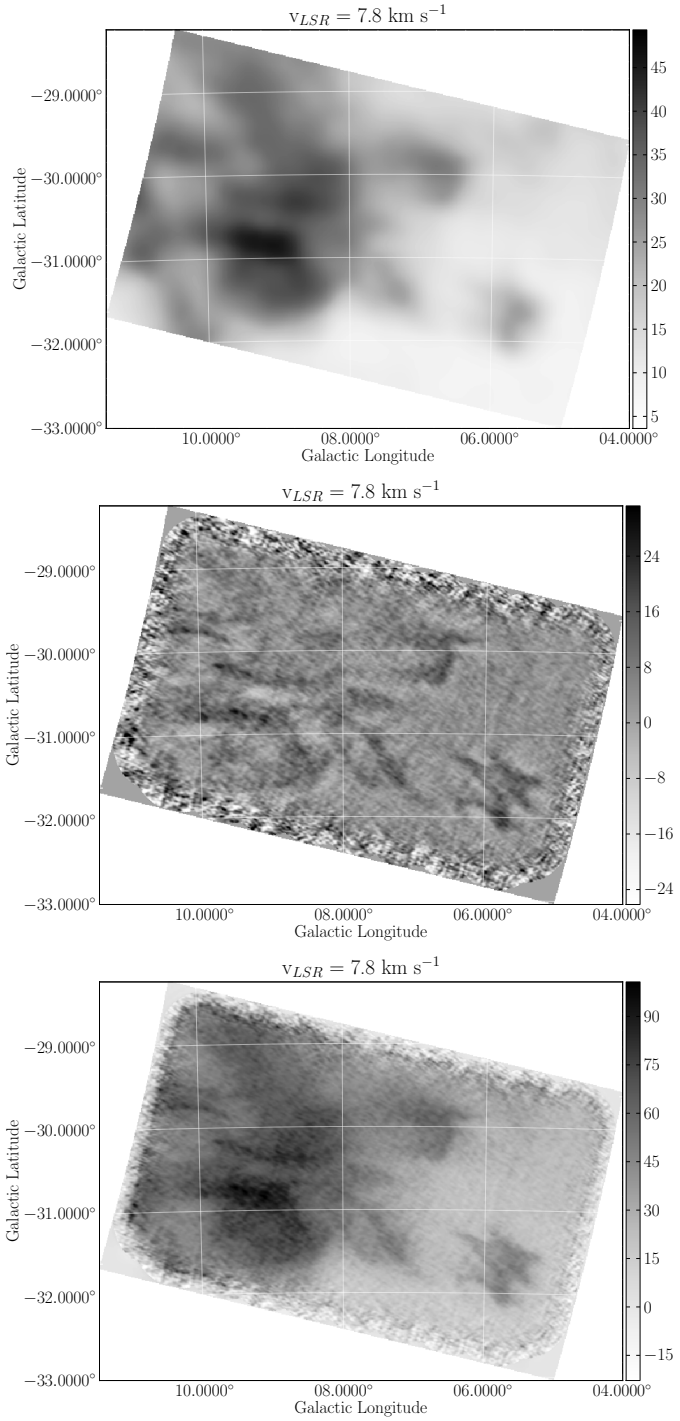

Figure 3.2: HI observations of the Cuttlefish region, in a single velocity slice at $v_{LSR} = 7.8$ km s^{-1}, in Galactic coordinates. Shown is the GASS single-dish data (top), our follow-up high resolution ATCA data (middle), and the combination of single-dish and interferometric data to recover short spacings (bottom). We see that the interferometric data resolves the GASS morphology into the expected clumpy structure at higher resolution, showing the edges of the HI defined clearly compared to the single-dish data alone.

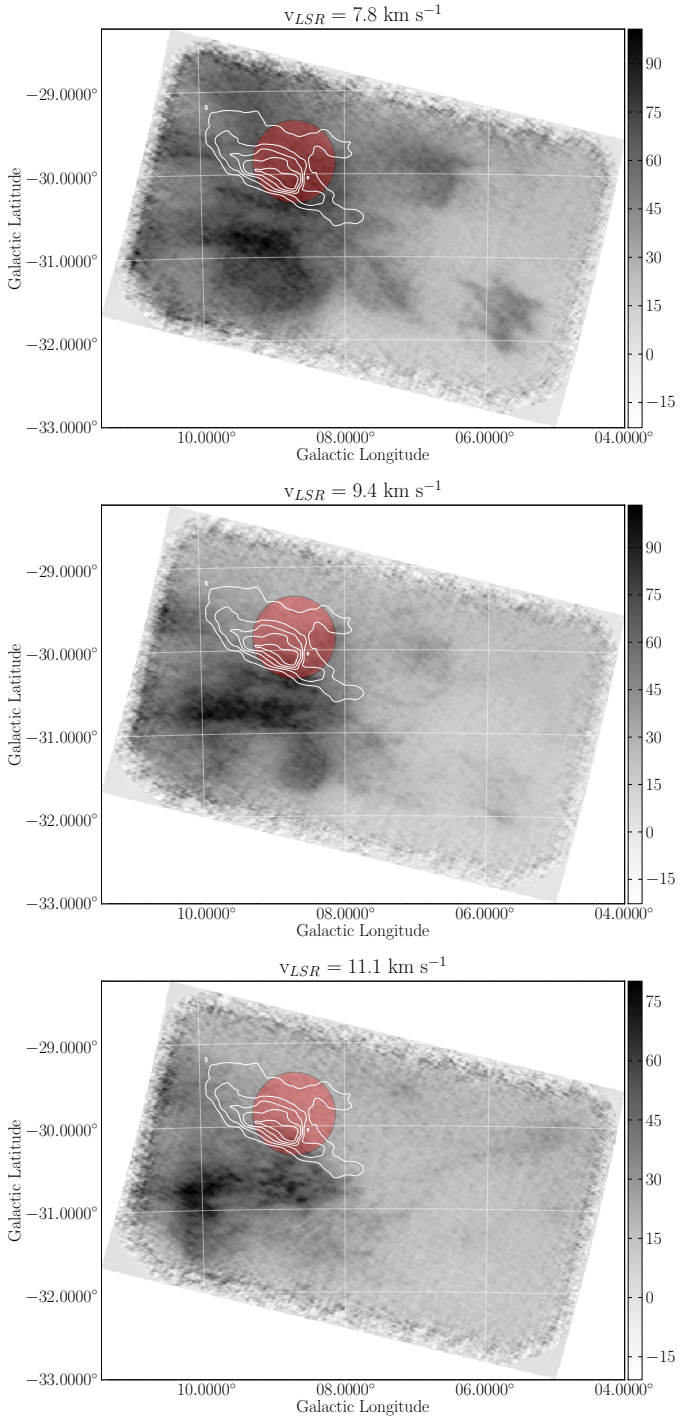

Figure 3.3: Combined HI single-dish and interferometric data overlaid with SHASSA Hα contours (white), to compare morphology between neutral and ionised hydrogen at velocities v_{LSR} = [7.8, 9.4, 11.1] km s^{-1}. At velocities of ~10 km s^{-1}, the ionised hydrogen is anti-correlated with neutral hydrogen and appears to be trailing behind the HI relative to the direction of the supershell, which is in the direction of increasing latitude. The WHAM beam is overlaid as a red circle at the position of the WHAM pointed-line observations (l = 8.7°, b = −29.85°).

Table 3.1: Optical emission lines in the Cuttlefish and their properties.

Line	Energy (eV)	I (R / km s^{-1})[a]	v_{LSR} (km s^{-1})[b]	FWHM (km s^{-1})[b]	$\sum$I (R)	$\sum$I/Hα
[S II] λ6716	10.4	0.10	3.6 ± 0.7	18.0 ± 0.3	2.0	0.44
Hα λ6563	13.6	0.14	7.6 ± 0.8	29.7 ± 0.4	4.6	1.00
Hβ λ4861	13.6	0.03	13.2 ± 4.7	35.3 ± 2.3	1.1	0.25
[N II] λ6584	14.5	0.11	7.3 ± 0.8	21.3 ± 0.4	2.6	0.56
He I λ5876	24.6	0.005	7.3 ± 9.8	12.2 ± 4.9	0.1	0.03
[O III] λ5007	35.1	0.12	7.3 ± 0.6	17.1 ± 0.3	2.2	0.48

[a] An uncertainty of 0.002 R / km s^{-1} on intensity applies to all spectra.

[b] These uncertainties do not incorporate those introduced by the 12 km s^{-1} WHAM spectral resolution.

The final interferometric dataset was regridded to a velocity resolution of $\Delta v \sim 0.8$ km s^{-1} in order for the interferometric data to be merged with the single-dish data from GASS to recover the low spatial frequencies and hence large-scale emission. The combination of Parkes single-dish with ATCA interferometric data was carried out using the MIRIAD *immerge* task with a flux combination factor of 1.1. A comparison of a single slice of our HI data is shown in Figure 3.2, at a velocity $v_{LSR} = 7.8$ km s^{-1}. We show the GASS single-dish data and ATCA interferometric data separately next to the merged image which recovers the diffuse emission missing in the high-resolution image. The combined image gives us a significantly greater insight into the morphology of the HI at velocities associated with the supershell and Cuttlefish region, and enables more reliable comparison with the high-resolution structure evident in ionised hydrogen from the SHASSA data.

We show three slices of the combined data in Figure 3.3, centred on the velocity at which there is the strongest morphological agreement between the HI and the Hα. At velocities of ~10 km s^{-1}, the ionised hydrogen is anti-correlated with neutral hydrogen and appears in the gap between the HI and the supershell wall. This morphological relationship was identified using the GASS data in Moss et al. (2012, reproduced as Chapter 2) although the edge dividing the HI and Hα was far less defined than it is using the high-resolution HI data. The combination of morphological and spectral information suggests that the HI and Hα are physically co-located and part of the same interaction process.

3.3 Optical observations

The Wisconsin H-Alpha Mapper (WHAM) is an extremely sensitive optical Fabry-Perot spectrometer, operating in the wavelength range of 4800 to 7200 Å, which has recently enabled studies of faint diffuse gas in the Milky Way associated with the warm ionised medium (Reynolds et al., 1998; Tufte, Reynolds & Haffner, 1998; Haffner et al., 2003). It has an angular resolution of 1°, a spectral resolution of 12 km s^{-1} and a 200 km s^{-1} bandwidth near the Hα line. It is primarily used in spectral mode, where each point within the 1° beam is equally sampled.

We focus here on the first results from our optical follow-up of the Cuttlefish with WHAM, specifically pointed observations in multiple emission lines at the position of the Hα peak in the SHASSA data, $l = 8.7°$, $b = -29.85°$. These observations so far have involved using WHAM in spectral mode. We have obtained pointed observations in the following lines: Hα λ6563, Hβ λ4861, [S II] λ6716, [N II] λ6584, [O III] λ5007 and He I λ5876. Each line has a prominent detection, with a notably strong detection of [O III] and a weak detection of He I. We plot each WHAM spectrum in Figure 3.4, with each line coloured based on the ionisation potential associated with the emission. Also plotted is the

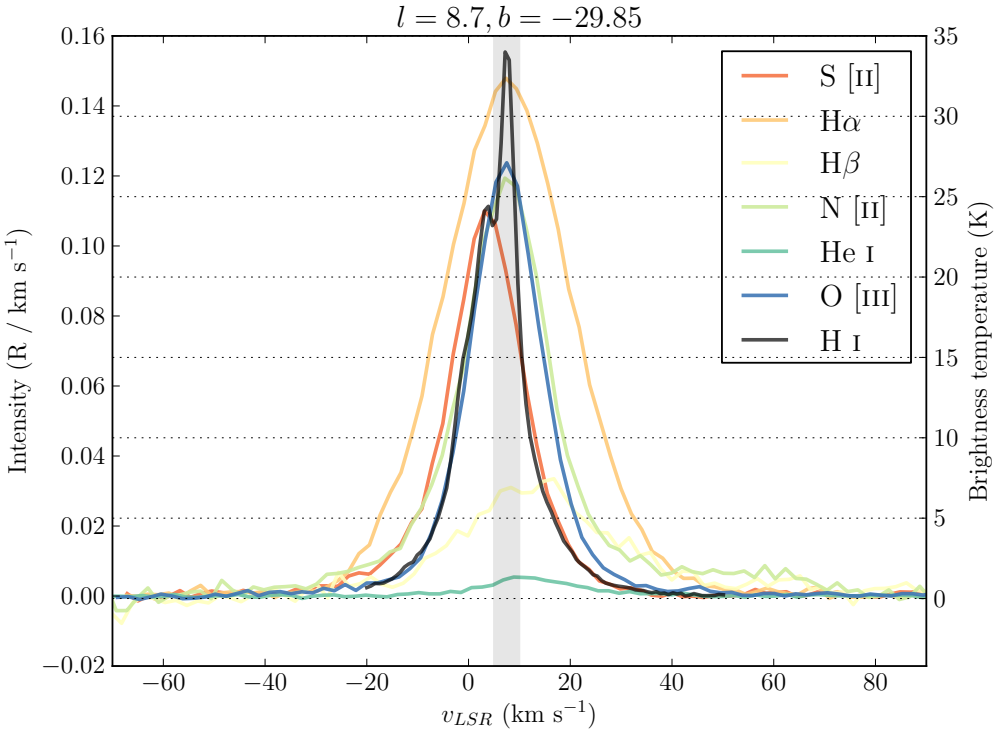

Figure 3.4: Pointed spectra from WHAM at the position of the Hα peak in emission of the Cuttlefish feature ($l = 8.7°$, $b = -29.85°$). The colour of each optical line is ranked by its respective ionisation potential using a spectral colour map, with red being the lowest energy transition and blue being the highest energy transition. The optical lines shown in order of ionisation potential are [S II] (10.4 eV, red), Hα (13.6 eV, orange), Hβ (13.6 eV, yellow), [N II] (14.5 eV, light green), He I (24.6 eV, green) and [O III] (35.1 eV, blue). The HI spectrum at the same position is shown in black, with the central velocities associated with the supershell emission (5–10 km s^{-1}) shown as a shaded grey box. The extended emission at higher velocities evident in the [N II] line is an artifact of the data reduction process. The position that these spectra were observed at is shown as a red circle in Figure 3.3.

HI spectrum at the same position in black, with a grey shaded box indicating the range of velocities mainly associated with the supershell's emission. The extended emission in [N II] is an artifact of the data reduction process. Some lines required slight manual adjustment to correct their offset from zero (due to calibration errors), with the biggest adjustment being −0.008 R for [S II]. All adjustments were significantly within the errors on fitted properties.

For each optical line, we used least-squares fitting to fit a single component Gaussian in order to extract the main physical properties of the line. We derived the integrated intensity as the integral over the Gaussian function:

$$\int I(v)\ \mathrm{d}v = \sqrt{\frac{\pi}{4\ln 2}} I_0 \sigma, \tag{3.1}$$

where I is the intensity, v is the velocity in km s^{-1}, I_0 is the peak intensity of the Gaussian fit and σ is the FWHM of the line. We show the lines and their properties in Table 3.1, as well as the relative integrated intensity fraction compared with the Hα. The high fraction of [O III] is a particularly important and interesting result due to the ionisation energies required to produce this emission, implying that there is a significantly energetic physical

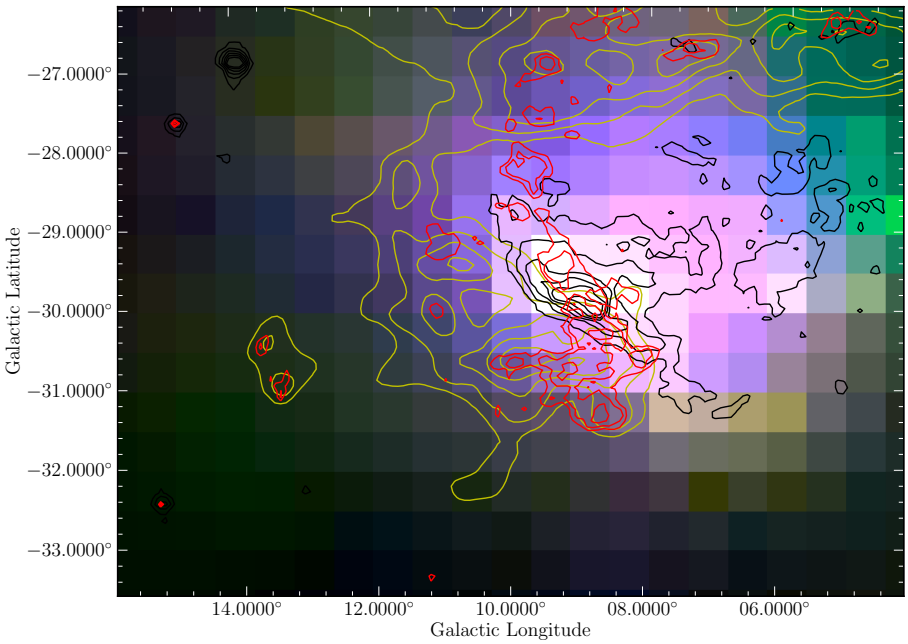

Figure 3.5: Three-colour image of the Cuttlefish feature in preliminary WHAM imaging. The emission shown is: Hα in red $\{v_{LSR} = 8.4$ km s^{-1}, range=[17.6, 65.0] mR (km s^{-1})$^{-1}\}$, [O III] in blue $\{v_{LSR} = 9.1$ km s^{-1}, range=[1.3, 16.8] mR (km s^{-1})$^{-1}\}$ and [S II] in green $\{v_{LSR} = 8.0$ km s^{-1}, range=[8.0, 49.1] mR (km s^{-1})$^{-1}\}$. Overlaid are GASS HI contours in yellow ($v_{LSR} = 9.7$ km s^{-1}, levels=[20, 25, 30, 35, 40] K), SHASSA Hα contours in black (levels=[3, 5, 7, 9, 11, 13] R) and IRIS 100 μm contours in red (levels=[8, 9, 11] MJy sr^{-1}). Based on the spatial WHAM data available so far, the correlation between the HI and the Cuttlefish Hα feature is further consolidated. Future work will focus on determining whether the Cuttlefish can be explained in a model of supershell fragmentation. The velocities of each emission map shown here are slightly different due to variation in the gridding process.

process occurring. We consider the implications of these relative intensities with respect to potential origins for the Cuttlefish feature in Section 3.4.

We show a preliminary WHAM three-colour image of the Cuttlefish in Figure 3.5. The emission maps shown in the image are Hα (red), [S II] (green) and [O III] (blue), overlaid with contours in HI (yellow), SHASSA Hα (black) and IRIS 100 μm (red). Each spectral-line image represents a velocity slice at a single v_{LSR}, in the range of $v_{LSR} = 8{-}10$ km s^{-1} due to differences in velocity gridding. The main shell wall is visible in the top of the image, with the optical emission filling the gap between the supershell wall and the higher-latitude HI. Spatially and spectrally we can further confirm physical co-location of the optical emission lines and the neutral hydrogen, with apparent proximity to the wall of GSH 006−15+7. Future work will see the complete reduction of WHAM imaging in Hα, Hβ, [S II], [N II], He I and [O III] in order to better reveal the morphological structure of the Cuttlefish region, along with spectral analysis across the region to detect changes in line properties. The results of this analysis will help to better constrain the physical properties of the Cuttlefish, in order to conclusively determine the origin of the emission and whether the supershell is definitively associated with the Cuttlefish.

3.4 Possible origins for the Hα feature

Nearby OB stars

The high line ratios of the various WHAM optical emission lines combined with an extremely strong detection of O [III] imply a hard spectrum producing the Cuttlefish, and necessitates a search for sources capable of significant ionisation. A common source of ionisation in the interstellar medium is found in high-mass OB stars, which are capable of producing high-energy optical emission via photoionisation with their harder spectra compared with other classes of stars.

Searching within 10° of the peak in Hα reveals two runaway B stars in close proximity, HD 190306 (~1° separation) and HD 189103 (~3° separation). These are a B4III C star of 5 $M_\odot$ and a B2.5IV C star of 6.6 $M_\odot$ respectively (Tetzlaff, Neuhäuser & Hohle, 2011). There are no nearby O stars in the same vicinity. HD 190306 is located at a heliocentric distance of 287 pc (Perryman et al., 1997). This corresponds to a separation of ~10 pc between the star and the Cuttlefish, if the Cuttlefish is located at the same distance as the star. HD 189103 is a spectroscopic binary located 189 pc from the Sun (Perryman et al., 1997), which would correspond to a separation of ~16 pc between the star and the peak in Hα.

In both cases, the separation on the order of 10 pc between the candidate B stars and the Hα makes association unlikely considering the typical areas of influence of B stars, and further the ionising spectrum is not hard enough to justify the production of [O III] (Abbott, 1982). The lack of OB stars nearby combined with the high [S II] and [N II] relative to Hα (Madsen, Reynolds & Haffner, 2006) also rules out an HII region origin for the Cuttlefish.

The Galactic Centre

The Cuttlefish, at a position of $l \sim 9°$, $b \sim -30°$, is located in some proximity to the centre of the Milky Way. At a distance to the Galactic centre of 8.3 kpc (Ghez et al., 2008; Gillessen et al., 2009) this feature would be ~8 kpc from the Galactic disk and be ~1.4 kpc in size, which makes association with the Galactic centre doubtful. However, the existence of the giant gamma-ray bubbles reaching ~50° from the Galactic Centre seen by the Fermi instrument (Dobler et al., 2010; Su, Slatyer & Finkbeiner, 2010) as well as recent studies of HI clouds near the Galactic centre (McClure-Griffiths et al., 2013) suggest that it is not impossible for the Hα feature to be associated, although it is unlikely given the morphological and spectral coincidence with more local neutral hydrogen gas.

Loop I and other low-velocity HI emission

Loop I, visible as a large radio feature in the southern sky, is thought to be a nearby supernova remnant at a distance of ~100 pc interacting with the Local Bubble (Berkhuijsen, 1971; Berkhuijsen, Haslam & Salter, 1971; Egger & Aschenbach, 1995). Part of this supernova remnant coincides spatially with the region of the Hα feature. In order to address possible association with neutral hydrogen at other velocities (such as that of Loop I), we examined the morphology of the HI at velocities corresponding to the approximate width of the Hα line (i.e. over the v_{LSR} range of $[-10, 25]$ km s^{-1}).

We see no evidence for the Hα being associated with emission due to Loop I at ~4 km s^{-1}. At $v_{LSR} \sim -5$ km s^{-1}, we see some evidence for spatially coincident HI, but this is inconsistent with the systemic velocity of the Hα at 7 km s^{-1} and the neu-

tral hydrogen at ~10 km s^{-1} is morphologically more convincing. At velocities of v_{LSR} > 15 km s^{-1} we see no spatially coincident HI near the Hα. We conclude that the Hα is most likely associated with the neutral hydrogen at a similar systemic velocity of ~10 km s^{-1}.

Planetary nebulae and supernova remnants

Planetary nebulae (PNe) are key producers of [O III] emission in the Milky Way, and the suspiciously high [O III] present in the Cuttlefish makes a PN origin worthy of consideration.

There are no Galactic PNe catalogued in the nearby vicinity. At such high latitudes away from the Galactic plane of $b \sim -30°$, it is entirely possible that a PN like the Cuttlefish could be uncatalogued especially given its large angular size. If the Cuttlefish were in fact a PN of an upper limit size of ~3.5 pc based on the current sample of PNe (Tweedy, Martos & Noriega-Crespo, 1995; Hewett et al., 2003), it would be at a maximum distance of 80 pc which is significantly closer to the Sun than the current closest PN known, Sh 2−216, at 120 pc (Pier et al., 1993). The Cuttlefish's large diameter of ~5° would also make it the biggest planetary nebula on the sky, bigger than the 2° diameter of the current largest planetary nebula associated with the white dwarf PG 1034+001 (Werner, Dreizler & Wolff, 1995; Hewett et al., 2003). Both of these results would place the Cuttlefish at the extreme end of PNe, as the closest, physically largest and angularly largest PN known. Statistically this makes an identification as a PN seem unlikely, although it is possible that this type of PN would have been selected against in previous surveys searching for compact Galactic PNe in the disk.

Considering the WHAM emission lines and their relative intensities, we find some incongruities with a PN origin for the Cuttlefish. Although the [O III] is very bright, it is still less than half the intensity of the Hα which would be unusual for a PN (Frew & Parker, 2010). There is no evidence for expansion in any of the lines, as would be indicated by a double-peaked spectral structure of widths upwards of 20 km s^{-1}. This could be explained if the Cuttlefish was very old and no longer expanding, and given its angular size may well be the case if it is a PN. The [S II]/Hα ratio of 0.43 found in the Cuttlefish suggests that it is more evolved than a typical PN, where ratios close to 0.5 are only seen in very evolved PNe and in shocks associated with supernova remnants (Fesen, Blair & Kirshner, 1985; Frew & Parker, 2010). Although the structure of an old PN would be dominated by its interaction with the interstellar medium, the concentration of the majority of Hα emission in a single limb as shown in the SHASSA image is unlike the majority of known PNe and resembles more of a shock front than the layers of an old PN, which lends weight to a supernova-driven origin.

Supernova remnants produce strong detectable multi-wavelength emission for thousands of years after the initial supernova across the electromagnetic spectrum. The presence of emission requiring large energies to ionise such as [O III] and He I thus suggests a potential origin for the Cuttlefish as a supernova. There are currently less than 300 confirmed supernova remnants (SNRs) in the Milky Way, and all of these are found within latitudes of $|b| < 10°$ (Green, 2009). This alone does not preclude the identification of the Cuttlefish as an SNR, as it may have been overlooked due to its high latitude and large angular size in a similar way to nearby PNe. The high energy involved in a supernova, and consequent initial expansion of gas at ~10^4 km s^{-1}, produces extreme shock signatures in the remnant's optical emission line spectrum, resulting in very high levels of ionisation in the surrounding gas. An old supernova remnant can resemble a planetary nebula, though PNe are found to be richer in nitrogen due to CNO processing by the progenitor star

Table 3.2: Comparison of Cuttlefish line intensity ratios with the Cygnus loop.

Ratio	High-ionisation filament	Low-ionisation filament	Cuttlefish
[N II] λ6584/Hα λ6563	1.04	0.99	0.57
[S II] λ6716/Hα λ6563	0.42	0.38	0.43
[O III] λ5007/Hα λ6563	4.60	1.13	0.48
He I λ5876/Hα λ6563	0.00	0.02	0.02

(Frew & Parker, 2010).

We find that $\log_{10}(\mathrm{H}\alpha/[\mathrm{S\ II}]) = 0.37$ and $\log_{10}(\mathrm{H}\alpha/[\mathrm{N\ II}]) = 0.24$, although these are lower limits as we currently only have data for [S II] λ6716 and [N II] λ6584, but not [S II] λ6731 or [N II] λ6548 as is technically required for F[S II] and F[N II] respectively. Using the updated SMB diagnostic diagram in Frew & Parker (2010) of $\log_{10}(\mathrm{H}\alpha/[\mathrm{N\ II}])$ versus $\log_{10}(\mathrm{H}\alpha/[\mathrm{S\ II}])$, we find that the Cuttlefish falls in an overlap region between supernova remnants, planetary nebulae and H II regions, although significantly away from the majority of the PNe distribution and outside of the realm of Type I PNe (Kingsburgh & Barlow, 1994). Similarly for the BPT diagnostic (Kewley et al., 2001), which helps to separate star-forming regions from AGN, we find that $\log_{10}([\mathrm{O\ III}]/\mathrm{H}\beta) = 0.28$, $\log_{10}([\mathrm{S\ II}]/\mathrm{H}\alpha) = -0.36$ and $\log_{10}([\mathrm{N\ II}]/\mathrm{H}\alpha) = -0.25$. These values place the Cuttlefish near the boundary separating HII regions from AGN, away from the bulk of both HII regions and PNe but in the vicinity of supernova remnants, WR shells and LBV nebulae (Frew & Parker, 2010).

Using the SMB or BPT diagnostic, it is not clear whether an origin as a supernova remnant or planetary nebula is more likely, but the lack of O stars nearby effectively rules out an origin as an H II region. We also compare the line intensities we observe in the Cuttlefish to those found in a detailed study of high-ionisation and low-ionisation filaments associated with a nearby supernova remnant, the Cygnus loop (Raymond et al., 1988). We summarise the ratio comparison in Table 3.2. While the [S II] and He I ratios are roughly in agreement, the [N II] and [O III] emission is considerably too low.

We will use follow-up targeted observations of [S II] λ6731 and [N II] λ6548 to determine the true position of the Cuttlefish on the SMB diagnostic diagram, which will help rule out certain interpretations of the emission origin. Future work using WHAM optical emission imaging across the Cuttlefish region will allow us to investigate any significant changes in line-ratios across the sources, and modelling of the region using photoionisation/shock models of SNRs and PNe will also facilitate the ruling out of particular origins.

GSH 006−15+7

In the case of supershell association, a few scenarios can be considered as emission mechanisms for the Cuttlefish. Supershells, as swept-up masses of interstellar medium, are expected to have very low-density interiors which would enable ionising photons from OB stars in the disk to escape to high latitudes. However, the presence of such bright localised optical emission in the form of the Cuttlefish region appears incongruent with a photoionisation scenario, as we would expect to see similar signatures along the interior of the shell wall and a more diffuse ionisation structure.

Another potential explanation for the Cuttlefish, based on its morphology, is shock ionisation or collisional ionisation. While GSH 006−15+7 is no longer in an rapidly expanding phase of evolution, an abrupt change in density at high Galactic latitudes or a particularly violent eruption of gas in the disk could prompt the sudden acceleration of gas

near the top of the supershell, causing the 'cap' to break apart in a similar way to that seen in the further-evolved Ophiuchus superbubble (Pidopryhora, Lockman & Shields, 2007).

In a similar way to the photoionisation scenario, we might expect signatures of ionisation in Hα or X-rays within the supershell. There is ongoing work investigating the potential of association between X-rays, CO and GSH 006−15+7 (Jo, Min & Seon, 2014), although confusion with X-ray shadowing due to the nearby supernova remnant Loop I would need to be convincingly ruled out in order to confirm the association of X-rays. Given the predicted age of the supershell as between 10-20 Myr, it is possible that a violent eruption could have taken place in the shell wall itself via triggered star formation leading to a SN (which seems unlikely given the low density in the shell wall) or through the SNe swept-up OB stars as part of the supershell expansion.

A final scenario involves fragmentation of the supershell wall. The low density interiors of supershells are predicted to contain hot gas from past generations of supernovae. If a coherent supershell (as GSH 006−15+7 appears to be) begins to fragment, then this hot gas will be able to escape the shell interior into the surrounding ISM. This gas, as it cools, could produce the lower energy signatures of optical emission compared with X-rays expected within the hotter shell interior. A key difficulty with modelling this scenario via radiative transfer is that it does not necessarily have to take place under equilibrium conditions, and in fact is unlikely to do so. Variations in density, temperature and elemental abundances near the Cuttlefish have also not been well-constrained at this point. That said, the wealth of optical diagnostics provided by the pointed WHAM spectral-line observations and future WHAM imaging in the same lines of the Cuttlefish region will give us strong constraints for testing theoretical models and varying parameters for the origin of the Cuttlefish. Close comparison to theoretical predictions on similar spatial scales in future, using simulations of the interstellar medium such as in (Hill et al., 2012), may also be informative as to the likely attribution of the Cuttlefish to a supernova-driven medium.

3.5 Conclusion

We have reported on the follow-up of the Cuttlefish feature, first identified in Hα in Moss et al. (2012). We have used high-resolution radio observations of neutral hydrogen with the Australia Telescope Compact Array to confirm morphological agreement between the HI and Hα in the Cuttlefish region at velocities $v_{LSR} \sim 10$ km s^{-1}, supported by velocity agreement between the HI emission and Hα emission. We have obtained pointed observations of Hα, Hβ, [S II], [N II], [O III] and He I with the Wisconsion H-Alpha Mapper (WHAM) at the position of the peak in Hα intensity, $l = 8.7°$, $b = -29.85°$. All lines were strongly detected, which was unexpected given the high ionisation potential required to ionise He I and [O III].

We have considered various origins for the Cuttlefish feature in the context of measured line properties and their relative intensities. We have been able to rule out an origin as emission associated with OB stars (and surrounding H II regions), the Galactic Centre, Loop I and HI at other velocities. It continues to appear possible to explain the Cuttlefish as part of the fragmentation of the old Galactic supershell GSH 006−15+7, although an origin as an extremely nearby supernova remnant or planetary nebula within ~ 100 pc must be considered in future work.

We have focused here on information gained from pointed line observations with WHAM. Future work will involve processing the preliminary imaging of the whole region of the Cuttlefish with WHAM (shown in Figure 3.5) in the same spectral lines to obtain spatial information on the variation in line intensity across the source. Modelling of

these results with varying density, elemental abundance, temperature and ionising source will enable us to conclusively determine the true origin of the Cuttlefish. While the presence of such bright [O III] makes an interpretation as a SNR or a PN seem plausible, the morphological relationship we have found between the HI and Hα combined with the agreement in velocity for all WHAM emission lines with the velocity of the supershell suggests that there is much more to the Cuttlefish than we have uncovered so far.

Chapter

4 HIGH-VELOCITY CLOUDS IN THE GALACTIC ALL SKY SURVEY†

Overview

This chapter first appeared in The Astrophysical Journal Supplement: *High velocity clouds in the Galactic All Sky Survey I. Catalog* (Moss et al., 2013).

†This chapter is published in a peer-reviewed journal.

4.1 Introduction

Fifty years after the discovery of high-velocity neutral hydrogen (HI) in the halo surrounding the Milky Way (Muller, Oort & Raimond, 1963), current research still seeks to understand the nature, origins and interactions of this anomalous gas which does not follow normal Galactic rotation. It is well-known that the densest forms of high-velocity HI occur as clouds organised into associations and complexes (Wakker & van Woerden, 1991). It is clear that their physical origins can be diverse, with evidence for complexes both extragalactic (Wakker, Oosterloo & Putman, 2002; Sembach et al., 2002; Lehner, Staveley-Smith & Howk, 2009; Tripp & Song, 2012) and Galactic (Lehner & Howk, 2010; Smoker, Fox & Keenan, 2011) in origin. These studies trace origins for extragalactic clouds based on their low metallicities, lack of molecular gas or association with the Magellanic system, and origins for Galactic clouds based on their higher ionisation fraction and low upper distance limits from stellar absorption lines. In northern and southern sky surveys of high-velocity clouds (HVCs) the Magellanic system (consisting of the Magellanic Clouds, the Magellanic Stream, the Magellanic Bridge and the Leading Arm) contributes a large fraction of clouds, forming a prime example of the interaction between the Milky Way and extragalactic gas. But it is also clear that a considerable amount of anomalous-velocity gas appears to be associated with interactions between the disk and the halo of the Milky Way and may in fact be of Galactic origin. high-velocity gas has been discovered in other nearby galaxies and their satellites such as M101, M31, M33, M83 and NGC 205 (Tenorio-Tagle & Bodenheimer, 1988; Westmeier, Braun & Thilker, 2005; Westmeier et al., 2007; Miller, Bregman & Wakker, 2009; Wolfe et al., 2013b) and may be related to extraplanar gas observed in more distant galaxies (Sancisi et al., 2008; Kamphuis et al., 2011), with the origins of the gas indeterminate in many cases but most likely a combination of galac-

tic activity and accretion of infalling gas to varying proportions depending on the galaxy (Boomsma et al., 2008b; Heald et al., 2011).

The first surveys of Galactic HVCs focused on the northern hemisphere, with clouds identified to be inhomogeneous and hence grouped in complexes on the basis of their spatial and spectral proximity to other clouds (Wannier, Wrixon & Wilson, 1972; Giovanelli, Verschuur & Cram, 1973b; Hulsbosch, 1978; Wakker & van Woerden, 1991). Since then, many new surveys of HI with increasing sensitivity and resolution have been released in both northern and southern hemispheres, including the Leiden-Dwingeloo survey (Hartmann & Burton, 1997), the Leiden/Argentine/Bonn (LAB) survey (Kalberla et al., 2005) and the GALFA-HI survey (Peek et al., 2012). Each new study of anomalous-velocity gas at higher angular resolution or higher spectral resolution reveals different aspects of the nature of this gas, resulting in new classes of anomalous-velocity clouds (AVCs) such as compact HVCs (Braun & Burton, 1999), ultra-compact HVCs (Brüns & Westmeier, 2004; Giovanelli et al., 2010), projection-affected low-velocity halo clouds (Peek et al., 2009) and cold/warm low-velocity clouds (Saul et al., 2012).

The high spectral resolution of new HI surveys allows us to examine the velocity structure of HVCs, which probes their physical conditions and interactions with their surroundings. Based on northern hemisphere surveys it has been found that the cloud linewidths of HVCs have a median full-width at half-maximum (FWHM) of ~20–30 km s^{-1} (Cram & Giovanelli, 1976; de Heij, Braun & Burton, 2002; Kalberla & Haud, 2006), corresponding to an upper-limit kinetic temperature of $\sim 10^4$ K. The nature of these clouds of HI as relatively cold concentrations of gas means that their existence in a hot $\sim 10^6$ K halo results in clear evidence of interaction. The form of the pressure and density gradients as a function of scale height position in the Milky Way is also thought to play a key role in the confinement and lifetime of these clouds. Based on the influences of temperature and pressure, the complex spatial and spectral structure of HVCs can provide clues about the physical properties and role of their surrounding environment in their evolution and dynamics.

We use data from the southern Galactic All Sky Survey (GASS) in HI, obtained using the Parkes 64-m radio telescope (McClure-Griffiths et al., 2009). GASS has excellent image fidelity due to its frequency-switching observing mode, and as such recovers emission on all angular scales. The second release of GASS (GASS II) features improved sensitivity and stray-radiation correction (Kalberla et al., 2010), on which we performed automated source-finding to identify HVCs. The catalogue most closely related to ours is the HIPASS HVC catalogue (Putman et al., 2002), which shares similar angular resolution and sky coverage but differs in spectral resolution and sensitivity. HIPASS was originally intended as an extragalactic survey, and as such the data used for constructing the HIPASS HVC catalogue had a low velocity resolution of 26.4 km s^{-1} (after initial smoothing) which provides a useful comparison to the GASS data with its spectral resolution of ~1 km s^{-1}. HIPASS also differs from GASS in its better sensitivity of 8 mK compared with the ~40 mK RMS sensitivity of GASS II. Taking into account both the effects of spectral resolution and sensitivity means that the two surveys are comparable to each other, though each is sensitive to different characteristics of the HVC population. HIPASS was also taken in a different observing mode, and as such even with the MINMED5 data reduction technique had limited sensitivity to emission on scales > 7°.

This paper presents a catalogue of HVCs and AVCs (anomalous-velocity clouds which do not meet the traditional velocity criteria of high-velocity gas but deviate significantly from Galactic rotation) compiled from the GASS II data. In Section 4.2, we give details of the data and source-finding procedure. Section 4.3 presents our catalogue of GASS

HVCs as well as the overall population characteristics. We consider the completeness and reliability of our catalogue in Section 4.4, in the context of comparison with the nearest similar catalogue of HIPASS HVCs. We conclude by summarising our catalogue and giving an indication of our directions for future work using the GASS HVC catalogue.

4.2 The Galactic All-Sky Survey II: data and methodology

Our catalogue is derived from the second release of GASS, which surveyed southern-sky HI (McClure-Griffiths et al., 2009; Kalberla et al., 2010), covering declinations south of $\delta = 1°$. We have used all GASS data south of 0° in the construction of our survey in order to avoid regions of increased noise near the limits of the survey and to limit our catalogue to a southern-sky survey. GASS was undertaken with the Parkes 64-m radio telescope using the 21 cm multibeam receiver and consisted of two sets of scans, one in right ascension and one in declination. The effective angular resolution of GASS is ~16′ with a spectral resolution of 1 km s^{-1} and ~57 mK RMS noise. As GASS focuses specifically on the HI content of the Milky Way, the survey velocity range is complete from −468 km s^{-1} to +468 km s^{-1}. GASS used in-band frequency-switching to assist bandpass correction while maximising the observing efficiency and maintaining sensitivity to large-scale structure. This involved recording spectra at two spectrally-close frequencies, which allows removal of continuum and time-varying system gains, as well as maximising on-source time by combining the frequency-switched pairs to create continuous bandwidth. Frequency switching in this way means that a negative copy of a spectral line will be reproduced at ±660 km s^{-1}, which is important for consideration of artifacts. The second release differs from the first with the further reduction of artifacts and RFI, as well as correction of stray radiation artifacts (arising from leakage through the sidelobes of a radio telescope due to an imperfect beam) using the Leiden/Argentine/Bonn (LAB) survey (Kalberla et al., 2005). The RMS noise of GASS II exhibits dependence on Galactic latitude, ranging from 20 mK to 60 mK depending on proximity to bright emission (Kalberla et al., 2010). In creating the GASS catalogue of HVCs, it was important to have a global sensitivity across the southern sky (particularly to be consistent with the RMS noise near the Galactic plane for source-finding), and so we adopted the originally published noise of 57 mK to guarantee reliable detections throughout the data.

Source finding methodology

To identify HVCs, we use an automated source-finding routine which adopts the flood fill algorithm. The flood fill algorithm searches for emission connected from a peak down to a user-specified threshold, and identifies this as an object or a source. We specifically adopt the algorithm developed and used by Murphy et al. (2007), but extended to a three-dimensional cube. The flood fill algorithm works in the following way:

1. Identify all peaks > the threshold peak level (T_{pk}).
2. Extend from the peak in each dimension (in our case: α, δ, v), amalgamating pixels into one source until the cutoff level (T_{min}) is reached.
3. Record this as a candidate source.

We give examples of the kinds of clouds identified by our source finder in Figure 4.1. In order to reduce the impact of noise and artifacts, we searched on cubes binned by averaging 5 channels in the spectral axis (see Section 4.2 for more details about binning). We set

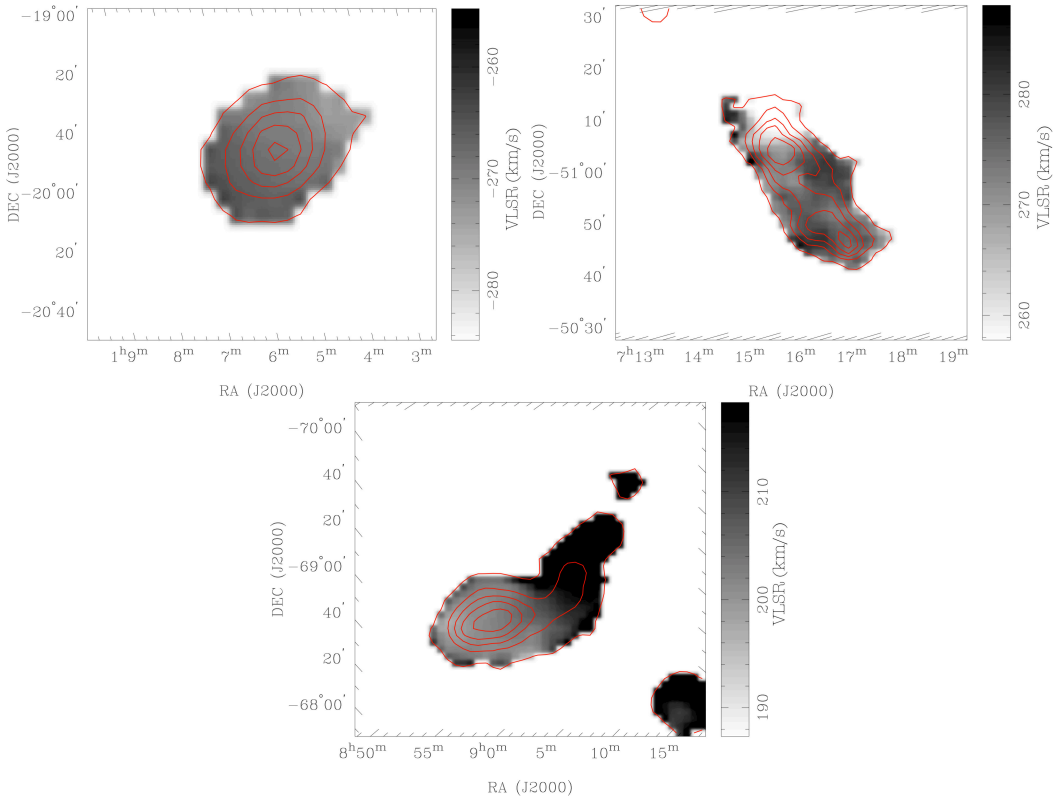

Figure 4.1: Examples of the different types of clouds evident in the GASS data. Each cloud is an example of an isolated (top left), spatial multiple-component (top right) or head-tail (bottom) cloud. The background image is the 1st-moment map showing the velocity structure of the source, with 0th-moment contours showing intensity structure in red ranging from σ to 90% of the integrated intensity peak (corresponding to 28.2, 10.7 and 58.2 K km s^{-1}) in 5 equal steps, where σ is the GASS noise of 57 mK multiplied by 2 × the spectral FWHM of each source.

a minimum source width of 3 pixels in both spatial directions, which is close to the size of the GASS beam in the spatial axes, and to 3 binned spectral channels (minimum total width of ~12 km s^{-1}). For our flood fill parameters, we choose a peak of $T_{pk} \geq 4\sigma$ and $T_{min} = 2\sigma$, extrapolating from the GASS noise of 57 mK to the binned cubes. As stated above, we adopted the RMS noise of the first release of GASS to guarantee a consistent catalogue sensitivity across the sky and near the Galactic plane, although the noise of GASS II is lower at higher Galactic latitudes. The nominal column density limit for a single channel at this noise of 57 mK is ~8.5 × 10^{16} cm^{-2}.

We examined the effect of binning by using three cubes that contain predominantly noise, calculating the change in RMS with increasing number of bins. The results are shown in Figure 4.2. We find that the GASS noise closely follows the theoretically expected trend with increasing bin number (based on Poisson statistics), although it is slightly higher than the theoretical noise. The difference across these three samples of noise peaks at a value of at most 3 mK in the case of binning by 3 bins and occurs at ~2.6 mK for the case of 5 bins. This is a very small difference overall and simply results in probing further into the noise by assuming the theoretical limit. We thus assume the N-binned RMS, σ_N, to be $\sim\sigma N^{-1/2}$, and calculate $\sigma_5 \sim 25$ mK, which gives $2\sigma_5 \sim 50$ mK and $4\sigma_5 \sim 100$ mK. We use these values as our T_{min} and T_{pk} respectively. For comparison to the data in our noise cubes, we found a 4σ 5-binned RMS of 101, 102 and 106 mK in each which is very close to the theoretical 100 mK value. Although a T_{pk} of 4σ is lower than most automated

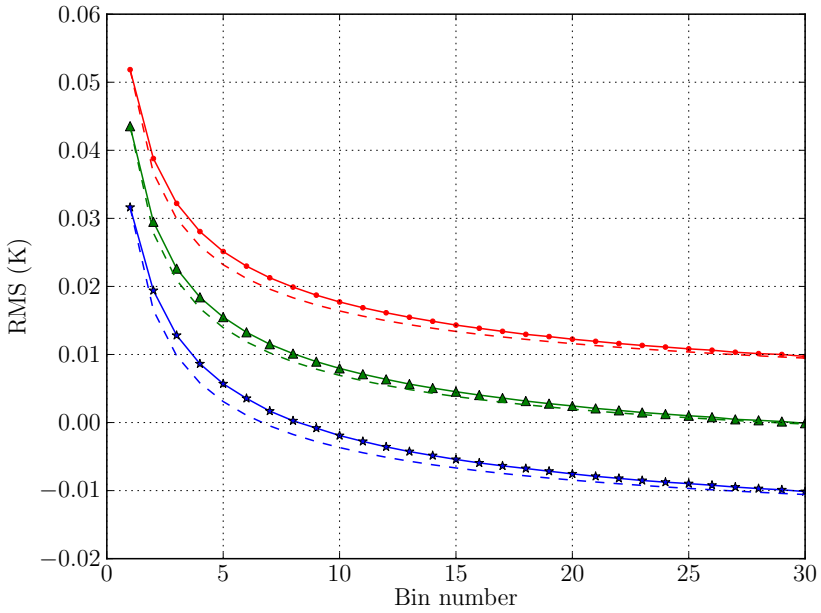

Figure 4.2: The results of spectrally binning three independent 'noise' cubes up to 30 channels are shown. Each colour represents the outcome from a different cube, offset in the top figure by 0.00 K (red, circles), -0.01 K (green, triangles) and -0.02 K (blue, stars) in order to make the behaviour of the individual lines clear. The dashed line in each case represents the expected theoretical trend following Poisson statistics. The data closely follow the theoretical noise. The difference between the RMS in the data and the theoretical RMS peaks at 3 bins for all three noise cubes, with a maximum difference of 3 mK.

source-finding, the combination of this with the 3 channel minimum in each axis increases the significance of the detections.

Data processing

One of the challenges of identifying HVCs close to Galactic velocities is distinguishing them from emission that is due solely to Galactic rotation near the centre of the Milky Way. We use the parameter of deviation velocity, which indicates how much the object's velocity deviates from a simple model of Galactic rotation where $v_{dev} = v_{LSR} - v_{model}$. As HVCs can be considered to require a deviation velocity v_{dev} of at least 50 km s^{-1} (Wakker, 1991; Wakker & van Woerden, 1997), we use this definition to help separate HVCs from Milky Way gas. To determine v_{dev}, we construct a model of the Galactic HI distribution. We have chosen to use the model of de Heij et al. (2002) to facilitate comparison with past studies of HVCs and intermediate-velocity clouds (IVCs). This model is composed of a thin disk with a constant central density in HI, $n_0 = 0.35$ cm^{-3}, and kinetic temperature, $T_K = 100$ K, within Galactocentric radius $R = 11.5$ kpc. Beyond 11.5 kpc, the midplane density in HI is

$$n = n_0 \exp\left(-\frac{R - 11.5\ \mathrm{kpc}}{3\ \mathrm{kpc}}\right). \tag{4.1}$$

In the vertical direction, the HI density follows a Gaussian distribution with

$$n = n_0 \exp\left(-\frac{(z - z_0)^2}{2\sigma_z^2}\right), \tag{4.2}$$

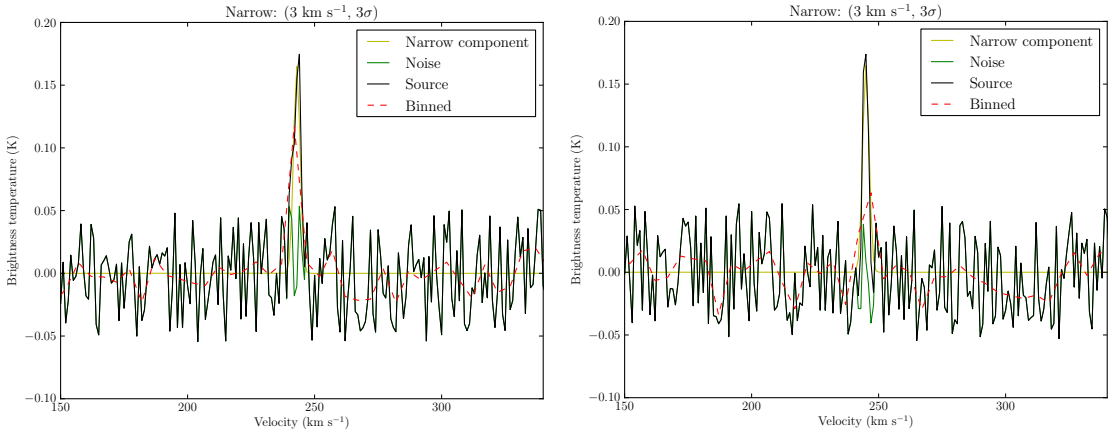

Figure 4.3: Model narrow-line clouds of peak brightness 3σ and FWHM of 3 km s^{-1}, falling within a spectral bin (left) or on a spectral bin edge (right) during the binning process. The red dashed line shows the resultant spectrum after binning each cloud by 5 channels. These plots show the potentially detrimental effects of binning on low-brightness, low-width clouds. For such a narrow and low signal-to-noise cloud, the effect of its position in the spectrum during binning is notable and significantly reduces its detectability if the cloud falls on the edge of a bin. The numbers in brackets show the FWHM and brightness of the simulated cloud.

where z is the scale height of the Milky Way in pc. For R < 11.5 kpc, $\sigma_z = 180$ pc, and $z_0 = 0$ pc. For $R > 11.5$ kpc, $\sigma_z = 180 + 80\ (R - 11.5\ \text{kpc})$ pc, and $z_0 = (R - 11.5)/6 \sin\phi + [(R - 11.5)/6]^2(1 - 2\cos\phi)$ pc. ϕ is the cylindrical Galactic azimuth (increasing in the direction of Galactic rotation) centred on the Galactic centre where $\phi = 180°$ is the direction toward the Sun. The variation of z_0 and σ_z beyond $R = 11.5$ kpc provides for the warp and flare of the Galactic disk. The Milky Way is assumed to have a flat rotation curve with $R_0 = 8.5$ kpc, $v_{rot} = 220$ km s^{-1}, and $\sigma_v = 20$ km s^{-1}.

We constructed a model using a 50 pc grid out to a Galactocentric radius of 50 kpc where

$$T_B(v) = T_K(1 - e^{-\tau_v}), \tag{4.3}$$

and where

$$\tau_v = \frac{33.52 n_0}{T_K \sigma_v} \exp\left(-\frac{v - v_r}{2\sigma_v^2}\right), \tag{4.4}$$

with all temperatures in K, velocities in km s^{-1} and densities in cm^{-3}.

Using this model, we identify the most positive and negative v_{LSR} for HI in the model with $T_B \geq 0.5$ K at every position in the sky; these velocities are the basis for calculating v_{dev}. The collective anomalous-velocity gas deviating from Galactic rotation in the Milky Way is typically categorised as low-velocity gas, intermediate-velocity gas or high-velocity gas depending on v_{LSR}, v_{dev} or a combination of the two. This had led to the existence and studies of such objects as low-velocity clouds (LVCs) and intermediate-velocity clouds (IVCs) as well as HVCs, which makes the physical distinction between each class of anomalous-velocity cloud more important as there is a significant degree of overlap between the three groups of anomalous-velocity gas. In order to guarantee detection of cloud emission peaking at deviation velocities of 50 km s^{-1} in accordance with the deviation velocity cutoff proposed by Wakker (1991) and in this context of anomalous-velocity clouds, we mask out all emission in our data that has a deviation velocity of < 30 km s^{-1}. We refer to any GASS clouds which do not meet the HVC velocity criteria (see Section 4.3)

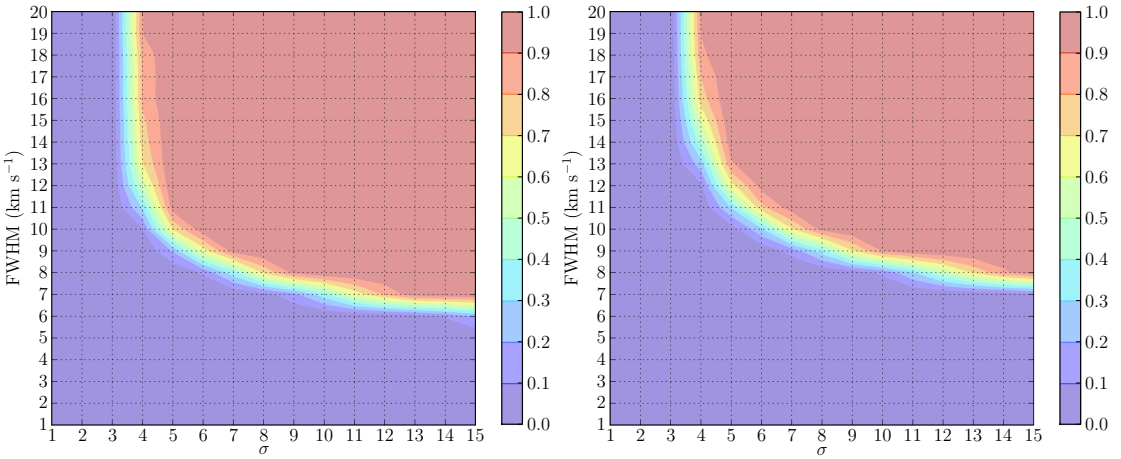

Figure 4.4: Detectability plots for model narrow-line clouds binned by 5 channels falling bin within a spectral (left) and on the edge of a spectral bin (right). The red regions represent a detectability of 90% or greater and can be used as a completeness threshold for these clouds. We see that even for narrow-line clouds of 15σ brightness, we expect to be limited to detecting clouds of greater than 7 or 8 km s^{-1} FWHM (depending on whether they fall within a spectral bin or on the edge of a spectral bin). Conversely, at the largest FWHM of 20 km s^{-1}, we are likely to be complete down to ~4σ regardless of what the peak intensity of the cloud is.

as anomalous-velocity clouds (AVCs) because they exist on the blurry boundary between IVC and HVC, and as such we refrain from classifying them in the absence of further investigation into their physical properties.

Due to the masking process, as well as the effects of frequency-switching, we found it necessary to manually remove any sources which appeared to either be poorly masked Galactic emission, artifacts near regions of 'ghosting' where some of the frequency-shifted emission is incompletely subtracted or regions of generally higher noise. The initial source-finding routine resulted in ~6000 candidate sources, which were then inspected to ensure the reliability of the final catalogue. This inspection reduced the total number of clouds to ~2000. The decision on each source was made in the context of all information available, including measured properties, spectra, moment maps and proximity to artifact regions.

Effect of binning

To investigate the effect of the spectral binning on our ability to find narrow spectral line (narrow-line) clouds, we simulated the binning process on narrow-line clouds of varying signal-to-noise ratio. We did this by generating model clouds of varying FWHM and varying peak brightness temperature embedded in Gaussian noise of 57 mK. We then performed binning on the spectrum of each cloud and measured the resulting properties of the binned spectrum. We considered both the best case scenario (a narrow cloud peaks within the edges of a spectral bin) and the worst case scenario (a narrow cloud peaks on the edge of a spectral bin) in order to understand at what level we are sensitive to narrow-line clouds when binning the data by 5 channels. The effect of a cloud's position within a spectral bin or on a bin edge is only really apparent for low brightness, very narrow clouds. This is shown in Figure 4.3 for a 3σ cloud with a FWHM of 3 km s^{-1}, where the red dashed line represents the binned spectrum. The detrimental effect on peak flux of falling on the edge of a bin is very clear for this type of cloud.

We generated model clouds over the peak brightness temperature range of [1, 15] σ

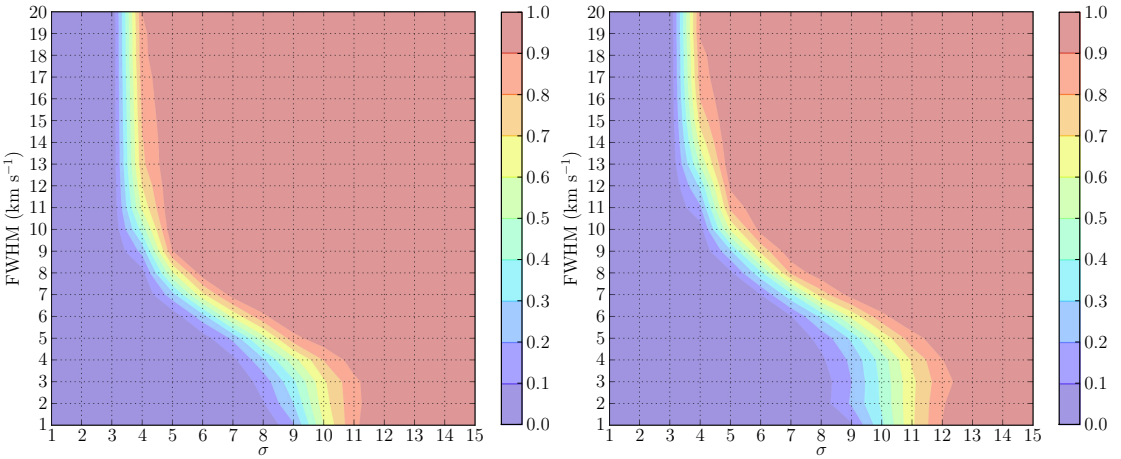

Figure 4.5: Detectability plots for model narrow-line clouds embedded within a broad component of FWHM 20 km s^{-1} binned by 5 channels falling within a spectral bin (left) and on the edge of a spectral bin (right). The red regions represent a detectability of 90% or greater and can be used as a completeness threshold for these clouds. In this case, we see that we expect to be complete even down to a FWHM of 1 km s^{-1} for clouds brighter than ~12σ. The brightness temperature σ here refers to the combined brightness of both the narrow and the broad component.

in steps of 1σ and over the FWHM range of [1, 20] km s^{-1} in steps of 1 km s^{-1} both within a spectral bin and on a bin edge. We define a cloud as detectable if, in the binned spectrum, the peak is greater than our required source-finding peak (100 mK) and if the positions on either side of the peak are greater than our required source-finding threshold (50 mK). We simulated each cloud at each FWHM and σ 1000 times to average out the effect of statistical noise, and kept track of how many clouds in each case are 'detected'. From this we generated a detectability map for clouds. This is shown in Figure 4.4. We see that we are likely to miss clouds of width less than ~8 km s^{-1} even at the maximum simulated brightness temperature of 15σ in our binned search.

We compared this result to two-component clouds, where narrow-line components are embedded within a broad component of FWHM comparable to that of the median HVC population (~20 km s^{-1}) (Bekhti et al., 2006; Kalberla & Haud, 2006). We performed the same simulations as before, except this time we added a broad component at the same position as the narrow-line component with one-third of its intensity such that the total brightness is at the simulated σ level. The detectability plots are shown in Figure 4.5. We see that the embedding of a narrow-line component within a broad component, even if it is faint, makes a considerable difference to the detectability of the source in total. We are likely to be complete down to the narrowest FWHM simulated for all clouds with a total peak brightness temperature greater than ~12σ, and complete at the same FWHM limit as without a broad component (~8 km s^{-1}) for clouds greater than 8σ.

The completeness is much higher in this case than in the isolated narrow cloud case due to the contribution of flux from the broad component during the binning process ensuring that the narrow cloud was not lost among the noise. In the GASS catalogue of HVCs, we have identified two-component clouds (either featuring a narrow-line component within a broad component or co-located components) with a **T** in the flag column (Section 4.3).

To find any isolated narrow clouds (those without a co-located broad component), we performed a targeted search for narrow clouds on the unbinned GASS II data, with a peak cutoff of 6σ (0.33 K) and a threshold of 2σ (0.11 K). This resulted in almost 3500 candidate clouds. We crossmatched these sources with those found by our main source-

finding method in order to remove any that are already accounted for and removed any with spectral extents greater than 15 channels (the minimum width after binning), which reduced the total number to 532 candidate narrow clouds. The distribution of all of these revealed a high concentration of artifacts at both positive and negative velocities near the southern Galactic pole and along the Galactic plane, as well as some associated with small regions of incompletely flagged RFI. We removed these sources from the candidate list, leaving 54 candidates to be investigated.

Almost all of these candidates appear at low deviation velocity, with many showing an artificial narrowness due to their proximity to the masked data. Only 14 candidates were kept, which were those showing a well-defined maximum in their spectrum indicating that most of the source is seen. Of the rest, 31 were removed due to their spectra being cut off by the deviation velocity mask and 9 were removed as noise. We added the 14 sources to our final catalogue, with a flag of **N** identifying them as separately found narrow-line sources. While this procedure was necessary to ensure our main source-finding had not missed a significant population of narrow-line clouds due to the effect of binning the data, we conclude that there were very few narrow clouds missed.

4.3 The GASS HVC catalogue

Our final HVC catalogue contains a total of 1693 HVCs, including 1111 positive velocity HVCs and 582 negative velocity HVCs. We also include in a separate table a catalogue of all anomalous-velocity clouds (AVCs) that do not meet the standard HVC criteria (peak deviation velocity > 50 km s^{-1} (Wakker & van Woerden, 1991) and LSR velocity > 90 km s^{-1}). A cloud only needs to fail one of these velocity criteria to be classed as an AVC. There are a total of 295 AVCs, including 197 positive velocity clouds and 98 negative velocity clouds. We note that these AVCs are likely comprised predominantly of intermediate-velocity clouds (IVCs), but as many of these clouds skirt the tenuous boundary between IVC and HVC, we designate them as AVC pending further investigation. The distribution of all positive and negative velocity clouds overlaid on their respective intensity-weighted mean LSR velocity maps is given in Figure 4.6.

Although the majority of clouds were identified using the binned data, all measurements of observable and derived physical properties were performed on the unbinned but deviation-velocity masked data. Clouds located close to the deviation-velocity cutoff were included only if their spectrum showed a well-defined maximum (indicating the peak of the source), hence distinguishing at least part of their emission from Galactic rotation. This affects 231 clouds, or ~12% of the total population.

An excerpt from the GASS HVC catalogue is given in Table 4.1 and an excerpt from the GASS AVC catalogue is given in Table 4.2, with the complete tables available for download as supplementary material in the online-only version of this paper. Below, we give detail on the derivation of each column of Tables 4.1 and 4.2.

Column 1

The full identifying name of each cloud is given in Column (1). Each cloud is given the identifier GHVC (GASS high-velocity Cloud) or GAVC (GASS anomalous-velocity Cloud) followed by its truncated Galactic coordinates (based on the position and fitted LSR (Local Standard of Rest) velocity of the best-fit spectrum, see descriptor for Column 2-3).

Column 2–3

The position of the peak in equatorial coordinates is given in Column (2) and Column

Table 4.1: Excerpt from the GASS HVC catalogue.

(1) Name (l & b & v_{LSR}) (deg & deg & km s^{-1})	(2) α (J2000) ($h:m:s$)	(3) δ (J2000) ($d:m:s$)	(4) $v_{LSR} \pm \Delta$ (km s^{-1})	(5) v_{GSR} (km s^{-1})	(6) v_{dev} (km s^{-1})	(7) FWHM$\pm\Delta$ (km s^{-1})	(8) $\log_{10} N_H \pm \Delta$ (cm^{-2})	(9) $T_{B,fit}$ (K)	(10) Area (deg^2)	(11) Δx (deg)	(12) Δy (deg)	(13) Flags	(14) HIPASS ID	(15) WW91 ID
GHVC G000.1−07.3+278	18:15:37.92	-32:26:30	278.9±3.4	279.4	226.4	13.4±6.7	18.56±18.12	0.25	0.2	0.7	0.5	-	-	-
GHVC G000.2−11.4−239	18:33:34.96	-34:06:55	-239.8±4.8	-238.7	-192.3	20.4±9.6	18.62±18.31	0.20	0.1	0.3	0.8	H_1	HVC 000.2-11.5-233	GCN_GCN
GHVC G000.6−54.7−091	22:12:32.87	-40:17:59	-91.5±1.8	-90.1	-54.0	13.6±3.5	18.72±18.13	0.26	0.3	0.9	0.9	H_2	HVC 000.9-54.8-094	$\overline{\text{N}}$
GHVC G000.5−75.7+169	23:53:10.86	-34:00:55	169.2±4.4	169.8	136.7	27.6±8.7	19.08±18.44	0.24	0.6	1.0	1.0	H_2	HVC 000.5-75.8+173	-
GHVC G000.6+21.2−103	16:31:51.30	-16:06:53	-103.3±2.7	-101.0	-60.8	25.0±5.4	19.08±18.39	0.32	0.5	0.5	2.2	H_1	CHVC 000.6+21.3-104	N
GHVC G000.9+06.0−258	17:25:04.98	-24:52:34	-258.2±4.1	-254.5	-205.7	19.8±8.2	18.79±18.29	0.32	0.4	0.3	1.5	H_1	HVC 001.1+06.1-264	GCN_GCN
GHVC G001.0−66.4−094	23:10:14.19	-37:17:08	-94.7±4.9	-93.0	-62.2	20.8±9.8	18.59±18.31	0.21	0.2	1.0	0.8	H_1	:HVC 001.1-66.4-093	$\overline{\text{N}}$
GHVC G001.2−15.4−185	18:53:02.47	-34:53:10	-185.8±1.0	-181.2	-138.3	21.4±2.0	19.75±18.33	1.39	1.1	1.0	1.3	H_1	CHVC 001.2-15.5-186	GCN_GCN,N
GHVC G001.2−67.2+122	23:14:11.89	-36:56:46	122.5±2.0	124.4	90.0	16.1±4.0	18.79±18.20	0.31	0.4	1.4	1.2	H_2	:HVC 001.5-67.3+122	-
GHVC G001.4+43.0−160	15:25:51.75	-01:37:18	-160.0±3.7	-155.8	-122.5	16.9±7.5	18.61±18.22	0.22	0.3	0.7	1.0	H_2	HVC 001.6+43.1-161	N

Table 4.2: Excerpt from the GASS AVC catalogue.

(1) Name (l & b & v_{LSR}) (deg & deg & km s^{-1})	(2) α (J2000) ($h:m:s$)	(3) δ (J2000) ($d:m:s$)	(4) $v_{LSR} \pm \Delta$ (km s^{-1})	(5) v_{GSR} (km s^{-1})	(6) v_{dev} (km s^{-1})	(7) FWHM$\pm\Delta$ (km s^{-1})	(8) $\log_{10} N_H \pm \Delta$ (cm^{-2})	(9) $T_{B,fit}$ (K)	(10) Area (deg^2)	(11) Δx (deg)	(12) Δy (deg)	(13) Flags	(14) HIPASS ID	(15) WW91 ID
GAVC G000.2−00.4−109	17:48:01.89	-28:54:26	-109.4±1.0	-108.3	-41.9	35.3±2.0	21.15±18.54	16.97	145.9	59.9	72.0	C,A,H_{113}	Complex L	N
GAVC G000.4−38.5−080	20:46:51.33	-41:09:57	-80.0±3.7	-78.7	-42.5	19.8±7.3	18.65±18.29	0.22	0.9	2.0	2.1	T,C,A	-	N
GAVC G000.9−07.0−102	18:16:05.12	-31:36:28	-102.1±5.6	-98.6	-49.6	19.3±11.2	18.58±18.28	0.22	0.2	0.5	0.6	C,A	-	N
GAVC G001.3−16.6−084	18:58:45.70	-35:15:34	-84.3±2.3	-79.4	-36.8	13.4±4.6	18.53±18.12	0.23	0.5	1.3	1.4	C,A	-	N
GAVC G001.4−13.7−093	18:46:02.57	-34:05:13	-93.1±4.3	-87.8	-45.6	15.5±8.7	18.41±18.19	0.16	0.3	1.0	0.8	C,A	-	N
GAVC G001.4−81.5+081	00:17:38.69	-31:17:59	81.3±6.3	82.1	48.8	27.2±12.6	18.76±18.43	0.21	0.2	1.4	0.7	C,A	-	-
GAVC G001.5−21.1+075	19:20:03.25	-36:40:12	75.3±1.0	80.8	32.8	6.3±2.0	18.93±17.79	0.56	1.7	2.1	2.1	T,C,A	-	-
GAVC G001.6+32.8−073	15:57:21.50	-08:02:41	-73.7±1.0	-68.2	-36.2	11.0±2.0	19.11±18.04	0.67	17.2	9.0	14.2	C,A	-	N
GAVC G001.8−04.1+108	18:06:20.81	-29:26:15	108.0±4.6	115.0	45.5	15.9±9.2	18.40±18.20	0.26	0.2	0.5	0.7	C,A	-	-
GAVC G002.1−82.5+084	00:21:42.91	-30:44:22	84.3±4.6	85.4	51.8	22.3±9.2	18.75±18.34	0.22	0.3	1.0	0.9	H_1,A	HVC 000.4-82.5+109	-

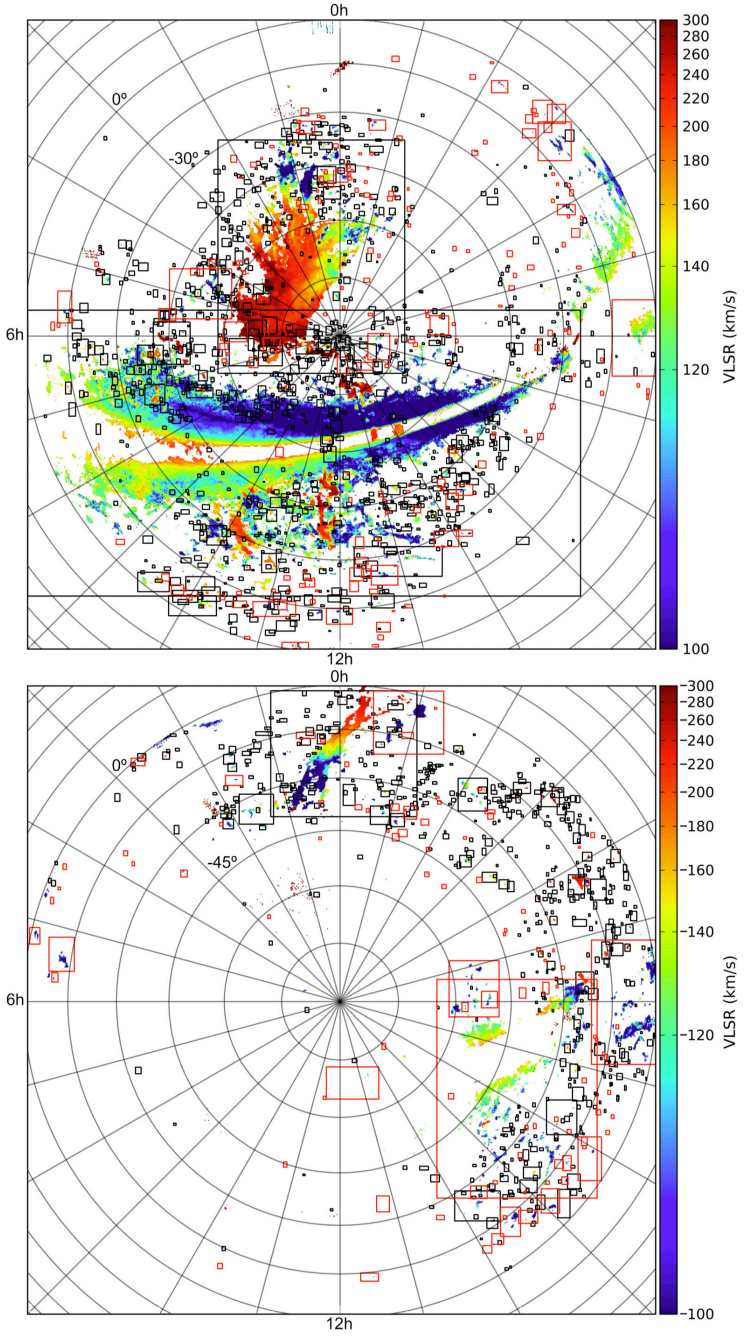

Figure 4.6: The distribution of GASS HVCs and AVCs on the sky, shown overlaid on positive and negative intensity-weighted mean LSR velocity (1st moment) maps (scaled with an arcsinh function). The projection shown is a zenith-equal-area (ZEA) projection with the south celestial pole at the centre, and each concentric ring moving outwards from the pole represents an increase of 15° in declination. An RA of 0 hours occurs at the 12 o'clock position on the diagram, increasing by 1 hour with each line anticlockwise. We see a strong concentration of clouds near the Magellanic stream, and at latitudes close to the Galactic plane. All emission with $|v_{dev}| < 30$ km s^{-1}, declination $> 0°$, $|v_{LSR}| < 50$ km s^{-1} or $|v_{LSR}| > 468$ km s^{-1} is masked out. The colourbar is set to the range 100–300 km s^{-1} in order to show velocity structure. The two large positive-velocity sources which appear to be unmasked Galactic plane emission contain clouds which deviate from Galactic rotation, and hence were included in our catalogue. HVCs are shown as black boxes, and AVCs are shown as red boxes.

Property	Mean_{HVCs}	Mean_{AVCs}	Median_{HVCs}	Median_{AVCs}	σ_{HVCs}	σ_{AVCs}
$\lvert v_{LSR}\rvert$ (km s^{-1})	182	83	167	82	71	13
$\lvert v_{dev}\rvert$ (km s^{-1})	139	42	123	41	70	6
$\lvert v_{GSR}\rvert$ (km s^{-1})	98	90	78	78	86	61
FWHM (km s^{-1})	19	16	19	16	6	6
$T_{B,fit}$ (K)	0.37	0.46	0.15	0.19	3.5	1.4
N_H (cm^{-2})	2×10^{19}	2×10^{19}	5×10^{18}	5×10^{18}	3×10^{20}	2×10^{20}
Area (deg^2)	2.5	4.2	0.3	0.7	57	20

Table 4.3: Statistical properties of the GASS HVC catalogue. The mean, median and standard deviation (σ) are shown for both the HVC and AVC populations.

(3). The peak position is determined by comparing the least-squares fitted Gaussian through the location of the peak brightness temperature across the source with the least-squares fitted Gaussian of the peak column density. These peaks are not necessarily the same position as the peak brightness temperature can be skewed positively by the presence of noise, and the peak column density is integrated over the width of the source and so may ignore a true peak that occurs at a position of narrower spectral width. The highest fitted peak is chosen to represent the true peak of the source, to account for any bias due to the influence of noise. Figure 4.7 demonstrates our means of selecting the best-fit spectrum, which is done based on which fitted peak has a greater height as well as requiring a realistic FWHM. We do not use the column density peak as default in order to avoid biasing against brighter but narrow spectra (which give a lower column density than a broader component). The error in these positions is taken to be the positional accuracy of the GASS data, which is equivalent to the beam of GASS (16′). In all cases, the area of the cloud is significantly larger than any error in the position of the peak. The increase in positional error with respect to the signal-to-noise ratio should be noted for all sources with fitted peaks < 0.2 K.

Column 4

The same best-fit peak spectrum is used to determine the peak LSR velocity, which is given in Column (4). The uncertainty in the peak velocity is the theoretical estimate of Taylor, Carilli & Perley (1999), which is given by

$$\frac{\sigma\text{FWHM}}{2T_{pk}}. \tag{4.5}$$

Column 5–6

The uncertainty in LSR velocity also applies to the error in the velocity in GSR (Galactic Standard of Rest) coordinates given in Column (5) and to the deviation velocity given in Column (6). The GSR velocity is calculated using the standard $v_{GSR} = 220 \cos b \sin l + v_{LSR}$. We estimate the deviation velocity based on the same model of Galactic rotation used to mask low deviation velocities in Section 4.2.

Column 7

The FWHM is measured using a least-squares Gaussian fitting routine, and is given in Column (7). As this was performed using a single-component fit for all sources to ensure consistency, the fitted FWHM should be treated with caution for all sources flagged in Column (11) as having two or more spectral components. The theoretical

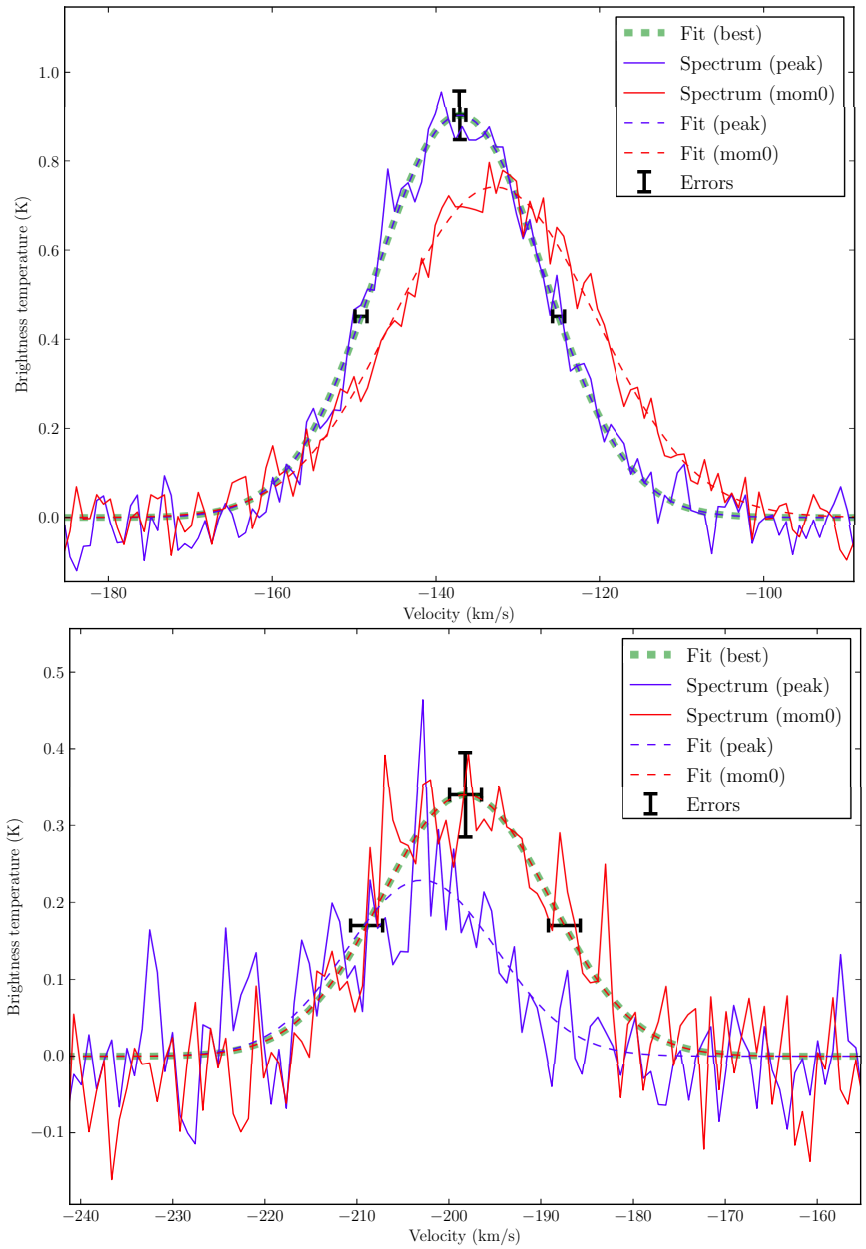

Figure 4.7: Examples of the theoretical errors applied to two separate sources. The top figure shows a high signal-to-noise source, while the bottom figure shows a fairly low signal-to-noise source. The blue curve shows the spectrum obtained at the position of the peak brightness temperature value of the source, while the red curve shows the spectrum at the position of the 0th moment peak (integrated peak). The blue and red dashed lines show the Gaussian fit to the peak and 0th moment spectra respectively. In the top figure, the peak spectrum is selected as the best-fit (based on the lower signal in the 0th moment spectrum), while the 0th moment spectrum is selected as the best-fit in the bottom figure due to the higher fitted peak (which averages out the effect of noise on top of each spectrum). The error bars in both cases represent the theoretical errors on the peak value, the peak position and the FWHM of the source. We see in each case that the theoretical errors are good approximations of the error on our fitted values, based on comparing them to the original spectrum.

error of Taylor, Carilli & Perley (1999) is given for the FWHM, and is defined as

$$\frac{\sigma \mathrm{FWHM}}{T_{pk}}. \tag{4.6}$$

We give an example of the peak and FWHM errors applied to both a high signal-to-noise source and a low signal-to-noise source in Figure 4.7.

Column 8

The peak column density is given in Column (8). This is determined on the basis of measuring the peak integrated intensity from the 0th moment map, and using the standard conversion factor of 1.8×10^{18} to convert from K km s^{-1} to cm^{-2} of column density (assuming negligible optical depth which may not be true in all cases). The error on this value is assumed to be the nominal GASS noise of 57 mK multiplied by the FWHM of each source.

Column 9

We give the fitted peak brightness temperature of the best-fit spectrum in Column (9) of the table. The fitted peak is given to account for the possible effect of noise, noting that this is based on the assumption of the source as a single-component Gaussian and as such may underestimate the true peak in cases of complex spectra. The error on the peak value is taken to be the RMS of the GASS data, which is in all cases assumed to be 57 mK.

Column 10

The area of each source is given in Column (10). This area is determined starting from the rough area of the source on the sky, shown as rectangles in Figure 4.6. We estimate the noise level σ_0 in the 0th moment map as the spectral width of the cube containing the cloud multiplied by 57 mK, and count all pixels above $2\sigma_0$. The area is the total number of pixels multiplied by the pixel area of $0.08^\circ \times 0.08^\circ$. It is not practical in our case to perform angular fitting for the majority of sources, as many are either complexes of several clouds or resolved with structure (and hence not well approximated as Gaussians).

Column 11–12

The maximum extent of the source above $2\sigma_0$ is given as Δx and Δy in Columns (11) and (12). These dimensions correspond to the x-extent and y-extent of each source in the original zenith-equal-area (ZEA) coordinate system, and are included to give an idea of the source dimensions. The area given in Column (10) will generally be smaller than the combination of Δx and Δy because it only considers the pixels above $2\sigma_0$ as part of the source.

Column 13

The flags in Column (13) are one or more of **T**, **H**, **C**, **A**, **N**. They have the following meaning: A cloud is determined to be better represented by two components if the standard deviation of the single-component residual is > 10% higher than the standard deviation of the two-component residual, and is marked as two-component (**T**). These two-component sources were also checked to make sure they were accurately classified, and removed from the group if their spectrum did not show convincing two-component structure. A flag of $\mathbf{H}_N$ indicates that the region the source occupies contains N HIPASS sources. Sources which sit near the edge of our 30 km s^{-1} deviation velocity cutoff are required to show a well-defined maximum in their spectra,

but due to increased uncertainty in their properties (such as FWHM and $N_{\rm H}$) we also flag any partially cut-off sources with a **C**. If the source does not meet the velocity cut-off criteria of an HVC, it is thus classified as an anomalous-velocity cloud (AVC) and is labelled with an **A** as well as its name changing from GHVC to GAVC. The **A** flag is not the same as the **C** flag because it is possible for a source to not meet the HVC velocity criteria and still be significantly away from the deviation velocity mask (and hence not cut off), however any source with a **C** flag will always have an **A** flag. A flag of **N** indicates a cloud found in the targeted narrow cloud search rather than in the main source-finding process.

Column 14

For GASS sources containing HIPASS clouds, Column (14) gives the name of the 'best match' in HIPASS. This was done using the results of crossmatching with the HIPASS catalogue of HVCs (Putman et al., 2002) in Section 4.4. The best match HIPASS cloud indicates that the corresponding GASS cloud is the closest in spatial and spectral coordinates to the specific HIPASS cloud. For the largest GASS sources which contain many HIPASS sources, we list the name of the region (e.g. Magellanic Clouds) rather than the best match cloud. If the flag column indicates a HIPASS source but the HIPASS ID is blank, this means that although the GASS cloud contains the HIPASS source, a different GASS cloud is a closer match.

Column 15

Column (15) lists all complexes and populations as defined by Wakker & van Woerden (1991) (Table 3) that the particular GASS cloud may be associated with based on its Galactic longitude, Galactic latitude and v_{LSR} velocity. If a cloud is listed to be potentially part of several complexes, this is due to overlap in the longitude/latitude/velocity definitions of regions.

Overall properties

We have summarised the key statistical values for each cloud property in Table 4.3, with histograms for properties of the GASS HVCs shown in Figure 4.8 and Figure 4.9. In each histogram plot, we have separated the HVCs (shown in black) from the AVCs (shown in red). The very largest GASS sources (e.g. the two large positive-velocity sources which appear to be unmasked Galactic plane emission seen in Figure 4.6) are a unique population due to their large area on the sky and were not included in the statistics or histograms. There are six of these large regions in total, covering the Magellanic Clouds, Magellanic Stream, Magellanic Leading Arm, Complex L and the Galactic Centre region.

There is no obvious trend in right ascension or declination for either of the populations, although a slightly increased number of sources near right ascension of 0° is likely due to the influence of the Magellanic Stream. There is an evident gap between 100° to 150° in the AVC distribution due to the effect of deviation velocity masking near the Galactic plane (which occupies most of this angle range). The declination distribution tails off at declinations close to 0° because of the increased noise in the GASS data at declinations that were observed at low elevation by the Parkes telescope. This effect is far less exaggerated for the AVCs, which may be a product of the lower number of AVCs as well as the influence of the Magellanic system on the HVC distribution at declinations $\sim -40°$. Similarly, there are no clear trends in Galactic latitude or longitude due to the limitations of a southern-sky only survey.

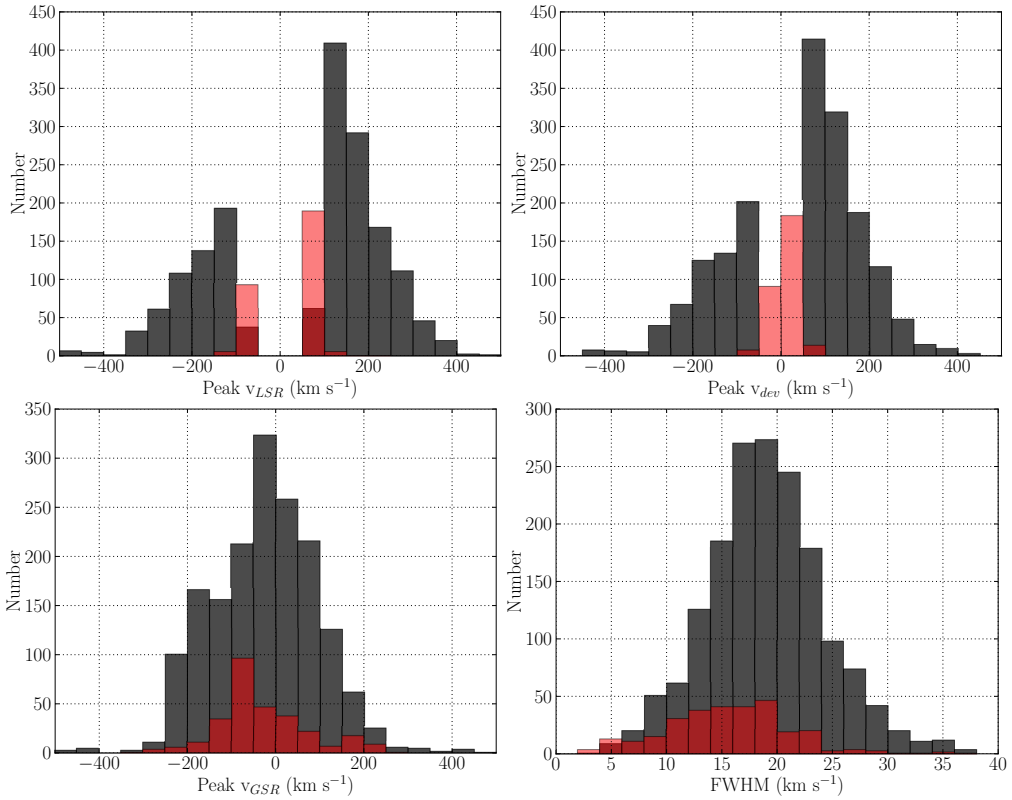

Figure 4.8: Histogram distributions of properties of GASS HVCs and AVCs. In order from top left, across: velocity (Local Standard of Rest), deviation velocity, velocity (Galactic Standard of Rest), and FWHM (single component fit). All velocities are given in relation to the best-fit spectrum (either the peak brightness temperature or the peak column density). In all cases, HVCs are shown in black and AVCs are shown in red.

All velocity properties are shown in Figure 4.8. The distribution in LSR velocity and deviation velocity is dominated by positive clouds due partly to the influence of the Magellanic Clouds and Stream, and partly because the southern view of the Galaxy is also dominated by gas at positive velocities. The gap in the middle of both velocity histograms is due to the effect of searching only at deviation velocities higher than 30 km s^{-1}. The AVC population occupies the low end of both deviation velocity and LSR velocity by definition, although it is worth noting that the AVC population is dominated by sources which have both low deviation velocities *and* low LSR velocities, which is not necessarily to be expected.

We see a preference towards negative velocities with respect to the Galactic Standard of Rest (GSR) in both HVCs and AVCs, although this is evident as an asymmetric distribution for HVCs and as a shifted distribution for AVCs. This bias towards negative velocities is consistent with previous findings in both neutral hydrogen (Stark et al., 1992) and ionised hydrogen (Haffner et al., 2003).

The distribution in FWHM of the HVC population is fairly even around the median value of 19 km s^{-1}, with a slight tail towards higher FWHMs. The AVC population is clearly shifted towards lower FWHMs than the HVC population. Based on inspection of the spectra of AVCs, this shift appears to be genuine but we cannot exclude the possible effect of measuring the FWHM on partially cutoff spectra (which is the case for 213 of the 295 AVCs) leading to increased uncertainty and artificial narrowing. We find our distribution is radically different to the HIPASS HVCs, although this is not surprising given

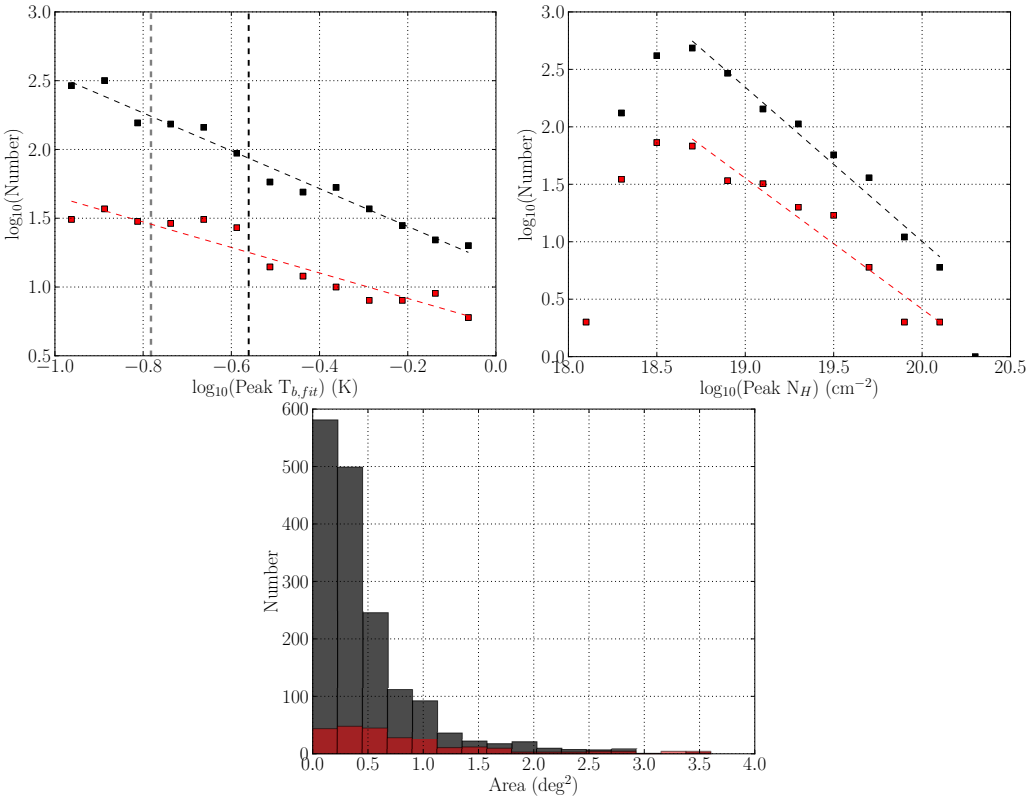

Figure 4.9: Histogram distributions of properties of GASS HVCs and AVCs. In order from top left, across: brightness temperature (fitted), peak column density, and area. The peak brightness temperature is the fitted value as given in the catalogue, with vertical dashed lines indicating 3σ and 5σ. The peak column density is measured at the peak in the integrated intensity map, and so is not necessarily at the same position as the fitted peak brightness temperature. A linear fit in log-space is given for brightness temperature (HVC slope = -1.37 ± 0.07, AVC slope = -0.93 ± 0.09) and column density (HVC slope = -1.34 ± 0.08, AVC slope = -1.14 ± 0.12). In all cases, HVCs are shown in black and AVCs are shown in red.

the much coarser velocity resolution of HIPASS. In the case of HIPASS, the majority of the population was not completely resolved at the large velocity resolution of 26.4 km s^{-1}. A comparison between the two catalogues is shown in Figure 4.10, with the respective velocity resolutions plotted as dashed lines. We show both the measured FWHMs of the HVC population in each survey and the FWHM distribution corrected for velocity resolution, using

$$\mathrm{FWHM}_{observed} = \sqrt{\mathrm{FWHM}^2_{actual} - \Delta v^2}, \tag{4.7}$$

which reveals good agreement between the cloud populations of GASS and HIPASS. We include in this comparison only those HIPASS clouds which are comparable with the GASS population, namely with declinations $< 0°$ and excluding galaxies.

It is worth noting that difference between our distribution centred on a FWHM of 19 km s^{-1} is somewhat different to that found in the northern hemisphere Leiden/Dwingeloo Survey or the later Leiden/Argentine/Bonn survey data which found a distribution centred on ~25–30 km s^{-1} (de Heij, Braun & Burton, 2002; Kalberla & Haud, 2006), and to the distribution found by the 140-foot telescope in Green Bank which centred on 23 km s^{-1} (Cram & Giovanelli, 1976). However we note that both Cram & Giovanelli (1976) and Kalberla & Haud (2006) chose to separate velocity structure into multiple spectral com-

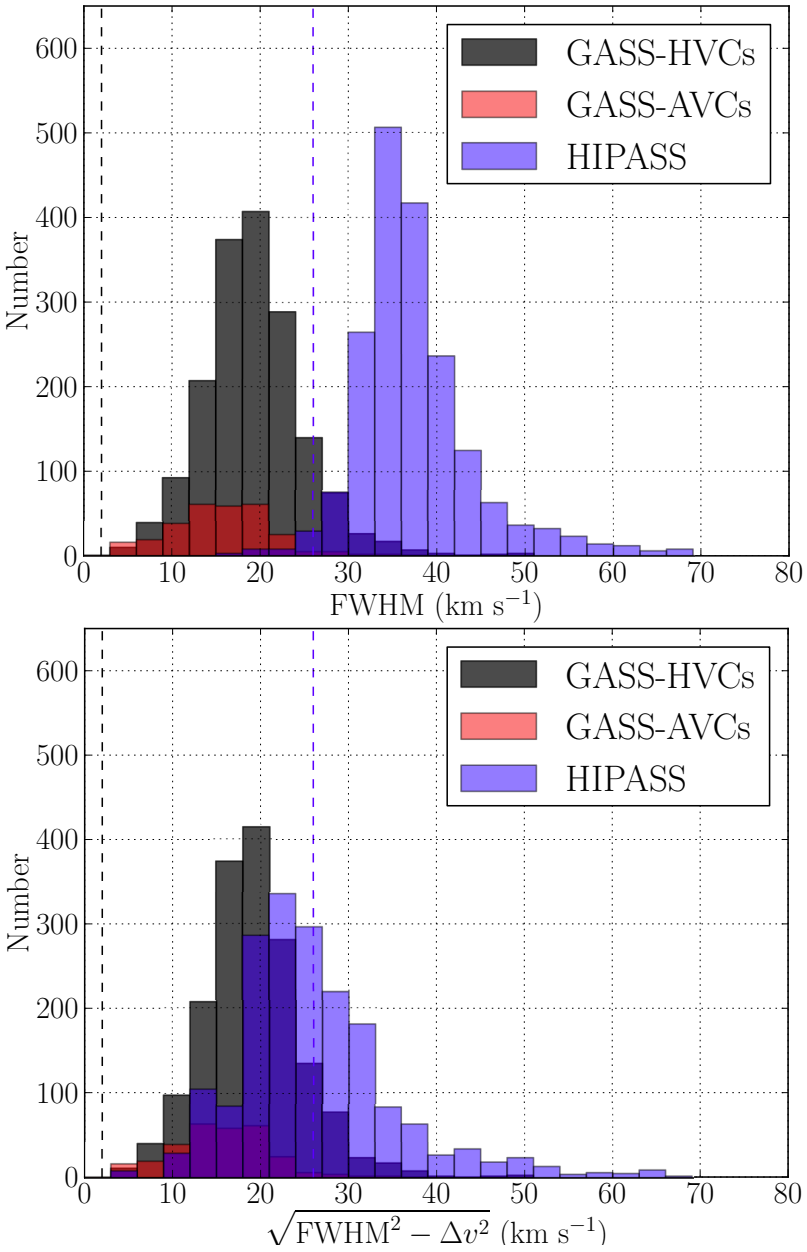

Figure 4.10: The distribution of cloud FWHMs measured through the best-fit spectrum within the GASS HVC catalogue showing HVCs (black) and AVCs (red), compared with the FWHM distribution of the HIPASS HVCs (blue). The respective spectral resolution (incorporating source-finding parameters) is shown in the same colour for each survey. The top figure shows the measured FWHMs from both GASS and HIPASS highlighting the effects of differing velocity resolution, while the bottom figure shows the corrected cloud line-widths taking into account the velocity resolution of each respective survey: $\mathrm{FWHM}_{observed} = \sqrt{\mathrm{FWHM}^2_{actual} - \Delta v^2}$, where $\Delta v = 1$ km s^{-1} for GASS and $\Delta v = 26.4$ km s^{-1} for HIPASS. We see fairly good agreement between the GASS and HIPASS distributions of cloud FWHM in the case of the corrected line-widths.

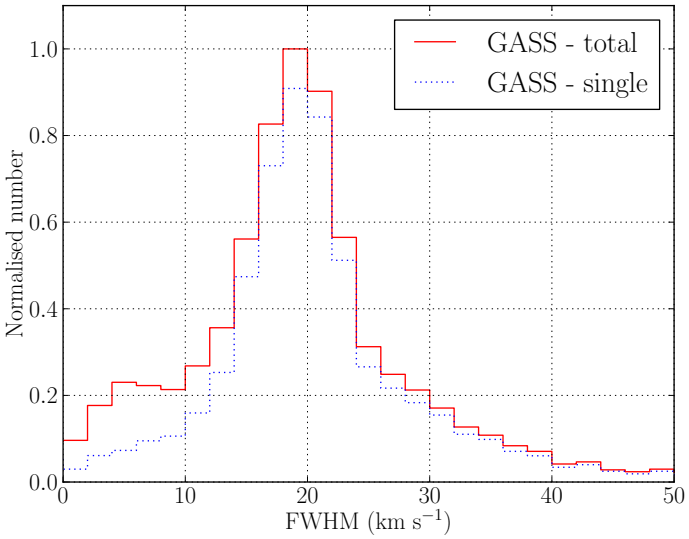

Figure 4.11: The normalised distribution of the measured FWHMs of all spectral components across all GASS HVCs above 5σ and < 5 deg^2 in angular size. The red line is the distribution of all 13593 spectral components, while the blue line shows the 10767 spectral components whose spectra were identified as single component. We have excluded any spectra with measured velocities of < 90 km s^{-1}. The median for this distribution of 21 km s^{-1} (FWHM) is close to that of our catalogued FWHM distribution. We see two distinct populations in the total distribution, one centred at ~5 km s^{-1} and one centred at ~20 km s^{-1}. We also see evidence of structure within the single component distribution, with a narrow concentration at ~20 km s^{-1} as well as a broader distribution that peaks at a slightly higher velocity width.

ponents, including spatial data across their sources. To better investigate our catalogue's trend towards lower FWHMs and closer match the methods of previous studies, we extracted all spectra containing at least a 5σ signal from the spatial regions of all GASS HVCs with a total area < 5 deg^2. This resulted in a total of 13977 spectra, of which 12180 were used as we removed any with fit LSR velocities of < 90 km s^{-1}.

To determine whether a spectrum was better fit with a single component or two components, we performed fitting for both cases and chose a two-component spectrum fit if the standard deviation of the single fit residual was larger by 10% or more than the standard deviation of the two-component fit residual. This gave a total of 13593 individual spectral components within these 12180 spectra, of which 10767 were identified as single component spectra. The results are shown in Figure 4.11. In this case of spectral components distributed spatially across GASS HVCs, we see a median FWHM of 21 km s^{-1} ($\sigma = 9$ km s^{-1}). Compared with the result of Kalberla & Haud (2006), we find that our spectral component distribution is much narrower and concentrated on a significantly lower σ. Although there are similarities in both distributions, our narrow components, although they appear in the total distribution, are not as pronounced and we see evidence for two-component structure in the distribution of spectra identified to be single component. The incongruity is likely due both to the differing angular resolution of GASS and LAB and to the differences between their targeted population of the HVC complexes identified by Wakker & van Woerden (1991) and our all-southern-sky population identified from GASS.

We further investigated the lower median FWHM of the GASS HVCs by measuring

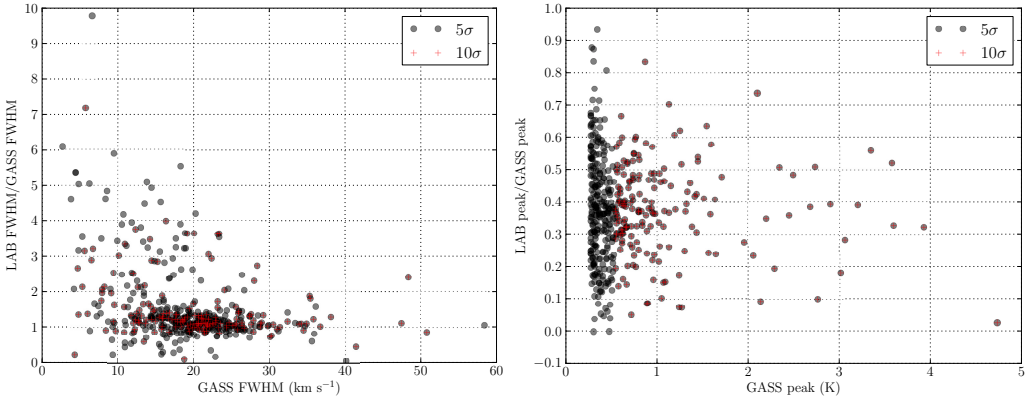

Figure 4.12: Comparative plots showing the difference between the measured FWHMs in GASS and LAB (left) and the difference between the measured peaks in GASS and LAB (right). Equivalence occurs where the y-axis is equal to one. The black circles represent all sources with a peak fitted brightness temperature in GASS of > 5σ, while the red crosses are the sources > 10σ (a subset of the black circles). There is fairly good agreement between GASS and LAB FWHMs, although the distribution is positively shifted indicating a slightly larger FWHM in the LAB data. Because the LAB beam is over 2 times that of GASS, we see that the measured peak in LAB is always less than that of GASS, indicating beam dilution.

their properties as found in the LAB data (Kalberla et al., 2005). We extracted the LAB spectrum closest to the best-fit position of the GASS HVCs with fitted brightness temperatures > 5σ (to aid detection) and performed the same fitting routine on each cloud. We show the results for all 5σ and 10σ clouds in Figure 4.12. In the case of the measured FWHMs in the LAB data, we see fairly good agreement with the GASS FWHM, although the entire distribution is positively biased. We find a median FWHM for our 5σ clouds measured in the LAB data of ~24 km s^{-1} and a mean FWHM of ~28 km s^{-1}. Based on these results, it appears possible that our lower median FWHM of 19 km s^{-1} compared to the previous studies of ~28 km s^{-1} is a combination of the effects of slightly coarser spectral resolution (1.3 km s^{-1}) and lower angular resolution (36′) in the LAB data rather than any significant difference from the HVC populations studied previously. We show the two distributions together in Figure 4.13.

In fitted peak brightness temperature (Figure 4.9), we see a distribution approximately following a power law, with the dashed lines on the histogram corresponding to 3σ and 5σ. Many sources have fitted peak brightness temperatures below this cutoff because their actual peak (which was targeted during the source-finding procedure) is affected by positive noise bias. This effectively increases the sensitivity of the catalogue below our target of 4σ, though the completeness is likely to be limited at lower brightness temperatures. A linear fit for both HVC and AVC distributions gives slopes of −1.37±0.07 and −0.93±0.09 respectively, with good approximation by a power law.

The column density distributions of HVCs and AVCs show an approximate power law distribution that turns over between 10^{18} and 10^{19} cm^{-2}. This suggests that we are particularly incomplete below densities of ~5 × 10^{18} cm^{-2}. If we adopt the median FWHM of 19 km s^{-1}, we see that this corresponds to an average brightness temperature of ~0.15 K, which is just below the 3σ value of 0.165 K. Based on this, we expect our catalogue to be complete to 4σ and to closely approximate the true distribution of sources down to the 3σ level as well. A linear fit for both HVC and AVC distributions gives slopes of −1.34±0.08 and −1.14±0.12 respectively, with good approximation by a power law. In both cases, our fitted slopes for brightness temperature and column density are shallower than those

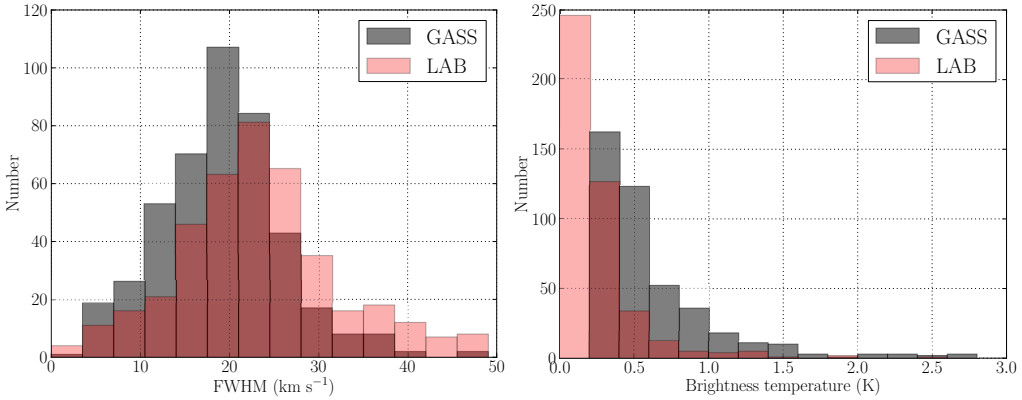

Figure 4.13: Histogram distributions of the FWHMs (left) and fitted brightness temperature peaks (right) of all 5σ GASS clouds as measured in GASS (black) and in LAB (red). We see that the entire FWHM distribution is shifted to larger FWHMs and broadened in the case of measuring the cloud properties in LAB, while the brightness temperature distribution is shifted to lower brightness temperatures. Both of these effects are likely due to the combination of the slightly coarser spectral resolution and lower angular resolution of LAB.

found by Putman et al. (2002), although closer in agreement to those of Wakker & van Woerden (1991). As suggested by Putman et al. (2002), this is likely due to the fact that the GASS clouds are more similar to the complexes of clouds identified by Wakker & van Woerden (1991), resulting in the dominance of the high brightness temperature and column density end of the distribution over the low end which becomes absorbed into the complex structure.

There is a significant spread in area amongst both AVCs and HVCs, with a few extremely large sources amongst a majority of sources below ~1 deg^2 in size. The slight difference between the size of the clouds in the HVC population and the AVC population may indicate that the AVC population is dominated by angularly resolved sources and thus may be closer to us than those in the HVC population, although this depends considerably on the characteristic physical size of clouds.

4.4 Completeness

In order to assess the completeness of our catalogue, we compare with the HIPASS HVC catalogue (Putman et al., 2002). Both catalogues were constructed using data from the Parkes 21 cm multibeam receiver and hence share similar angular resolution (with slight differences due to the gridding process used). The key distinction between the HIPASS data and the GASS data lies in the balance between spectral resolution and sensitivity. The original spectral resolution of the HIPASS data was 18 km s^{-1} (channel resolution of 13.2 km s^{-1}) with a per-channel RMS noise of ~8 mK, while the GASS data has a spectral resolution of 1 km s^{-1} (channel resolution of 0.8 km s^{-1}) with a per-channel RMS noise of ~57 mK. Source finding for the HIPASS HVC catalogue was performed on cubes smoothed with Gaussians (31 km s^{-1}, 19′), while the subsequent measurement of clouds was performed on the Hanning-smoothed data (26.4 km s^{-1}, 15.5′). This width of ~26 km s^{-1} was hence reported as the limit of resolution for the measured FWHMs of the resulting clouds. In the case of GASS, we use the limit at which we can accurately define the width of a cloud, which we assume to be three channels (2.4 km s^{-1}). One further difference between the two data sets lies in the observing mode of HIPASS, which

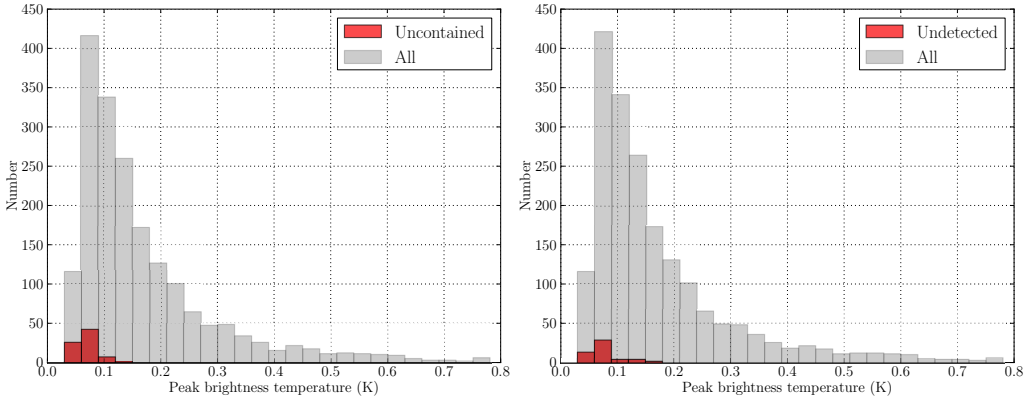

Figure 4.14: The distributions of uncontained and undetected HIPASS sources. Shown are the sources uncontained based on the intensity-weighted or peak position (left) and undetected by the KS two-sample test (right). In both cases, we find that the key limitation of the GASS HVC catalogue compared to the HIPASS catalogue is its lower sensitivity. In the case of containment, 95% of HIPASS HVCs are contained by GASS HVCs, while in the case of detection we find that 97% of HIPASS HVCs are detected in GASS when targeting their spectra.

reduced sensitivity to large-scale structures of the order of 7° and higher by employing the MINMED5 technique to estimate the spectral baseline within each 8 degree scan (Barnes et al., 2001; Putman et al., 2002). Conversely, GASS recovers structure of all scales by using the frequency-switching technique described in Section 4.2. As such, a direct comparison of the two catalogues is not possible.

We compare with the results of HIPASS in two ways: 1) we search for the containment of HIPASS HVCs within GASS HVCs and AVCs, and 2) we perform a targeted search of the GASS II data for the detection of HIPASS HVCs. By containment, we mean that the HIPASS source position falls within the boundaries of a GASS cloud. By detection, we mean how many HIPASS HVCs we can detect if we look specifically in a spectrum expected to contain a signal. There are a total of 1918 HIPASS HVCs that are within the survey limits of GASS (i.e. in regions of α, δ and v_{LSR} shared by both surveys), which excludes sources with $\delta > 0°$ and all sources identified as galaxies. We do not exclude sources on the basis of sensitivity. Given that HIPASS scanned the sky five times versus GASS scanning the sky two times, we expect the HIPASS data to be around three times more sensitive than GASS even after the spectral resolution is accounted for. However, the exact sensitivity cutoff for GASS detection of HIPASS sources is not obvious given the differences between the data collection method, the data processing method, the pre-processing of the data prior to source-finding and the actual source-finding process and criteria. We thus use this analysis of completeness to provide a consideration of this sensitivity relation. The details of these comparisons are given below.

Containment of HIPASS HVCs by GASS HVCs and AVCs

We first checked for the containment of each HIPASS source within the data cube of each GASS cloud. We used two possible positions to define the location of a HIPASS HVC: 1) the intensity-weighted position as given in the HIPASS catalogue and 2) the position of the actual peak brightness temperature in a GASS-extracted cube of the same HIPASS HVC. We included consideration of the second position because the catalogued brightness temperature and FWHM of each HIPASS HVC are measured through the peak of each source (not the intensity-weighted position). We then crossmatched both

the catalogued intensity-weighted position and the position of the maximum brightness temperature against the GASS clouds to check containment. The difference between the containment results for the two positions was two positive velocity sources and three negative velocity sources, so they were in agreement for the majority of sources.

Based on containment of the intensity-weighted and peak positions of the HIPASS sources, our catalogued clouds contain 1193 positive velocity HIPASS HVCs and 646 negative velocity HIPASS HVCs, which leaves 79 sources uncontained within the region of a GASS HVC or AVC. The distribution of uncontained sources is shown on the left (in red) in Figure 4.14, with a clear limitation due to sensitivity. This method results in a containment level of ~95%, which is likely to be skewed positively due to the possibility of chance containment of sources that are not necessarily detectable. This is discussed when we crossmatch the uncontained sources against those sources undetected in Section 4.4. Because the HIPASS HVC catalogue targeted compact, seemingly isolated clouds (due to the reduced sensitivity to large-scale structure), we might expect that multiple HIPASS clouds may be contained within a single GASS source rather than a one-to-one correlation. We checked this by calculating how many GASS clouds contain a HIPASS HVC, which resulted in 1230 GASS clouds containing a total of 1839 HIPASS HVCs.

Detection of HIPASS HVCs in GASS

Another way of approaching the question of the completeness of GASS is to perform a targeted search for all HIPASS HVCs. To do this, we used the same regional definition of a HIPASS HVC as outlined in Section 4.4. From each cube, we extracted two spectra. The first spectrum is taken at the reported HIPASS position, which is the intensity-weighted position of the cloud. However, because the catalogued brightness temperature and FWHM of each HIPASS HVC are measured through the peak of each source, we also extracted a spectrum at the position of the maximum brightness temperature within the cloud.

We used the Kolgomorov-Smirnov (KS) two-sample test (Smirnov, 1944; Bol'Shev, 1963) to determine the detectability of a HIPASS HVC, with incorporated matched filtering as outlined in Jurek (2012). The KS two-sample test allows comparison of representative samples from two distributions and tests the null hypothesis that the samples were drawn from the same distribution. It returns a p-value which gives the probability of expecting a deviation between the two samples greater than that observed under the assumption of the null hypothesis being true, and as such the lower the p-value, the more different the two samples may be.

We first extracted a section of each of the two spectra of a total width that is 6 times the FWHM of the source (to ensure that we contained the source as well as local noise on either side), and then ran a blind matched filtering KS test on the brightness temperatures of this spectrum. We started with a window of 5 channels wide and scanned across the extracted spectrum, comparing the window with the rest of the spectrum via the KS two-sample test. We stored the position of the centre of the window as well as the window width only if the returned p-value was lower than any previous scan through the spectrum at a different window width.

This then guarantees the lowest p-value for each position, with corresponding window width. The window width was widened until a maximum width of half the extracted spectrum. We selected the position with the lowest p-value (hence the greatest difference to the rest of the spectrum) as representative of the most probable location and width of any source within that spectrum. Due to the presence of other emission in the same

spectrum, we adjusted the extracted spectrum width from the default 6 × FWHM for 87 sources.

A source was considered to be detected if the position in either spectrum of the lowest p-value (as found by the matched filtering process) fell within 1.5 times the HIPASS spectral FWHM, or within the inner 75% of the HVC in the spectral dimension. For the 1918 sources searched we detect a total of 1864 clouds, which corresponds to a detection level of just over 97%. The undetected clouds are shown on the right (in red) in Figure 4.14, with again the key limitation being sensitivity. When comparing these results to the results obtained in Section 4.4, we find that we have slightly higher completeness using this method, which makes sense in the context of being able to detect a source given a known position versus ability to source-find blindly on data.

When we crossmatch the undetected clouds against the uncontained clouds, we find only 6 clouds overlap in both samples. This result suggests that the HIPASS sources that are uncontained by GASS HVCs are not uncontained because of undetectability. The fact that they are detected by the KS test and yet do not have their intensity-weighted or peak positions contained by any GASS HVCs indicates that their peaks are still too low compared with our source-finding criteria, but their signatures are still present in the data however faintly. This is not entirely surprising given that HIPASS is more sensitive than GASS. Conversely, some undetected HIPASS clouds are likely to be contained by chance coincidence within GASS HVCs which is why we see some undetected clouds that have been classified as contained.

In the context of the distinction between which HIPASS sources are successfully 'found' within the GASS HVCs versus those which are detectable when we specifically target their region, we note that the KS test method of searching is not an unbiased, blind search for sources. For this case, we targeted known sources with known positions, and as such are source-finding with prior knowledge that there should be a signal present. This prior knowledge is key to why we detect more sources than we contain, because it gives us the ability to differentiate between regions of increased noise, artifacts, interference and actual source signal. Because of this we do not expect to have actually found all of the HIPASS sources (even those that are detectable) with our blind source finder. It is unlikely that a different source finder would do significantly better because source-finding is limited by differentiation between other aspects of the data that look like source signal but are in fact spurious.

Summary of completeness and reliability

We have used two methods to assess the completeness of the GASS HVC catalogue: 1) the containment of HIPASS HVCs and 2) the detection of HIPASS HVCs. We find that the GASS HVCs and AVCs contain 95% of the HIPASS HVCs despite the slightly better sensitivity of the HIPASS data, although this number likely contains a small number of coincidently contained sources beyond our sensitivity limit. Using a blind matched filtering script at the spatial position of each HIPASS HVC, we are able to detect 97% of the HIPASS population.

Based on these results, we conclude that the completeness of the GASS HVC catalogue is at least 95% compared with the HIPASS HVCs (which were found with more sensitive data), and at our 4σ cutoff of 0.22 K it should be close to 100% complete. Due to the manual inspection of candidate sources described in Section 4.2, the catalogue will be almost 100% reliable.

4.5 Summary and future work

We have presented a catalogue of 1693 high-velocity clouds (HVCs) as found in the Galactic All Sky Survey data, which has a sensitivity of ~57 mK, an angular resolution of ~16′ and a spectral resolution of ~1 km s^{-1}. These clouds have been identified using the GASS II data, which includes stray-radiation correction. Our catalogue contains clouds down to peak brightness temperatures of 4σ (~230 mK) at all declinations $\delta < 0°$. There are a total of 1111 positive velocity clouds and 582 negative velocity clouds, distributed inhomogeneously across the southern sky with concentrations correlated with the Magellanic system and with the Galactic disk. Of our sample of HVCs (excluding AVCs), we find that 567 clouds were previously uncatalogued by the HIPASS survey and as such are new in the context of southern sky surveys for HVCs. A total of 758 clouds in our catalogue have no HIPASS counterpart and do not contain a HIPASS cloud in their region. Our final catalogue of GASS HVCs has a reliability close to 100% given that each source has been manually inspected, as well as being complete to the 4σ level within the constraints of our search parameters and masking procedure. In order to find any narrow clouds potentially missed by searching on binned data, we performed a targeted narrow cloud search on the unbinned data. This resulted in adding only 14 narrow clouds to the catalogue, which may suggest that isolated narrow-line clouds (without a co-located broad component) are intrinsically rare or possibly that they are rare at the ~16′ resolution of GASS.

Our catalogue also includes 295 anomalous-velocity clouds (AVCs) which do not meet the velocity criteria associated with the definition of an HVC although they do deviate from Galactic rotation. This sample of AVCs includes 197 positive velocity clouds and 98 negative velocity clouds. As many of these AVCs skirt the tenuous boundary between IVC and HVC, we designate them as AVC pending further investigation. Eventually separating different populations of clouds on the basis of their physical properties, which should correlate with their dynamical properties, may help constrain the current definition of HVCs and help separate them from gas that is more clearly associated with the rotating disk as well as mitigate the effects of line-of-sight projection.

We have investigated the overall properties of the GASS HVC and AVC population and compared these with the results of previous surveys. There is an apparent preference towards negative velocities for our clouds in the Galactic Standard of Rest frame, which is in agreement with previous findings on the high-velocity sky (Stark et al., 1992; Haffner et al., 2003). We find that our median FWHM of 19 km s^{-1} is lower than that of other studies, and a two-component spectral analysis similar to that of Kalberla & Haud (2006) reveals that our distribution of spectral components is similarly centred on a lower FWHM than previous studies. This appears to be predominantly a function of the differing angular and spectral resolution between surveys, but may also be suggestive about the properties of the southern sky distribution of HVCs. Our FWHM distribution compared to that of HIPASS is significantly shifted to lower velocities, indicating that we are probing the true physical distribution of HVC FWHMs without spectral resolution limitations.

We have compared our catalogue with the previous deep HIPASS data in order to judge the completeness of the GASS HVC population. We find that our HVCs contain 95% of the peaks of all HIPASS HVCs. When running a blind matched filtering window on each HIPASS cloud, we find that we are able to detect over 97% of these HVCs within the GASS II data. However we find little overlap in the uncontained versus undetected samples, which is likely due to a combination of chance containment of sources within large HVC complexes and detection limits existing below source-finding limits.

The combination of high angular resolution and high sensitivity with enhanced image

fidelity (via both frequency-switching and stray radiation correction) in an all-sky data set make GASS an excellent means of seeing the large-scale structure of the gaseous halo as well as the composition at smaller scales. The spectral resolution of the GASS data gives us an unprecedented look into the complicated velocity structure of HVCs; we see evidence for multiple spectral components, asymmetries and complex spectral structure. These HVCs are not isolated objects, as they are in the process of interacting with both the gravitational field of the Milky Way and with the high temperature environment of the halo medium. Our upcoming work on the velocity structure of GASS HVCs and AVCs (Moss et al, in preparation) will target clouds which demonstrate head-tail structure, complex spectral structure or extremely narrow line-widths, in order to probe the conditions of clouds which are interacting directly with their surrounding medium and how this relates to disk-halo interaction in the Milky Way. The GASS HVC catalogue combined with the GASS data from which it was derived will be useful to any work which seeks to investigate how gas is infalling into and outflowing out of the Milky Way both morphologically and dynamically, on the largest scales as well as in the fine detail revealed by the high angular and spectral resolution of GASS.

Chapter

5 INTERACTING HIGH-VELOCITY CLOUDS AS PROBES OF THE HALO

Overview

This chapter investigates the properties of interacting high-velocity clouds and their significance as probes of the Galactic halo medium. By comparing the observed physical properties in HI of a sample of extragalactic clouds with a sample of Galactic clouds, it is possible to gain insight into whether the origin or surrounding environment plays a greater role in the properties of a cloud. Spatial spectral mapping, trends with Galactic latitude and statistical comparison of physical properties are used to carry out the investigation.

5.1 Introduction

High-velocity clouds (HVCs) in the Milky Way exist within the tenuous medium surrounding the Galaxy, in regions featuring a variety of temperatures, densities and pressures. As such, these cool and often compact clouds allow the tracing of both the physical properties of clouds and their surrounding environment. For example, head-tail clouds form a specific class of HVCs interacting with their environment, defined by their high column density 'head' with a trailing tail-like structure that is generally much fainter. The most common explanation for their comet-like appearance is ram-pressure stripping as a consequence of the cloud moving through the halo environment (Brüns et al., 2000), with the tail forming an envelope of warmer diffuse gas surrounding a cold core (Kalberla & Haud, 2006). Their lifetimes are thought to be relatively short in the absence of support mechanisms, based on their proximity to known HVC complexes and on the results of simulations (Murali, 2000; Heitsch & Putman, 2009; Putman, Saul & Mets, 2011; Putman, Peek & Joung, 2012). These clouds are believed to have a greater impact on the halo of the Galaxy than the disk, contributing to a large diffuse Galactic halo that extends significantly beyond the Milky Way disk (Putman, Saul & Mets, 2011). The disrupted nature of head-tail clouds reveals how they are interacting with their surrounding medium, while the diversity of environmental conditions in the halo of the Milky Way as well as the cloud origin and properties shape the form of this interaction.

The influence of the multi-phase interstellar medium on the evolution and longevity of cold clouds in the Galactic halo has been the subject of various theoretical investigations (e.g. Wolfire et al., 1995; Sternberg, McKee & Wolfire, 2002), with results suggesting that

core-envelope structure or the presence of dark matter may contribute to the stability of these clouds. The question of environment versus origin in the resulting signatures of interacting clouds has also been the subject of observational work. Hsu et al. (2011) compared the physical properties of clouds in Complex C with the Magellanic Stream and found similarities in line-width, angular size and mass distribution, concluding that this possibly indicated a common physical origin of formation or break-up process despite their different halo environments. Using high-sensitivity observations of the compact cloud HVC 125+41−207, Brüns, Kerp & Pagels (2001) studied the evident head-tail structure, finding that the presence of warmer gas increased towards the tail of the cloud and was consistently at a lower velocity than the cold gas. From their observational results, they suggested that the cloud was ram-pressure stripped and calculated an unusually far distance of ~130 pc (under the tenuous assumptions of equilibrium and no molecular gas content, both of which may be incorrect with implications for future studies of head-tail clouds). Peek et al. (2007) looked at the connection between three associated interacting HVCs and their surrounding environment, using a drag model to estimate the distance to the complex based on their morphological and kinematic structure, a technique which has potential in both distance and origin determination for other halo clouds.

We sought to investigate the effect of varying environments and origins on the conditions of a set of interacting clouds, some of which exhibited notable head-tail structure. We selected three target regions from the HI Galactic All Sky Survey (GASS, McClure-Griffiths et al., 2009) for observation with the ATCA: the Magellanic Leading Arm, Complex L and the Galactic Centre Negative (GCN) complex. In addition, we incorporate into this sample previously observed data of a Leading Arm HVC interacting with the disk of the Milky Way (McClure-Griffiths et al., 2008) and follow-up high-resolution data of an active star forming region with outflow in the form of halo clouds (Ford et al., 2008; Ford, Lockman & McClure-Griffiths, 2010). Each is in a very different region of the Galactic halo, with published evidence in favour of either extragalactic or Galactic origin.

This sample allowed us to pose a number of questions that we aimed to investigate with this work. Can the origin of interacting HVCs be determined through their physical, dynamical or thermal properties? How do clouds break up as they enter or exit the Milky Way, and is the origin or the surrounding medium a greater influence on their evolution and eventual fate? What spatial trends can we see across clouds interacting with a surrounding medium? Our selected regions, and the clouds within them, give an unprecedented insight into the interplay between HVCs and their environments in the complex halo of the Milky Way, through the physically observed properties of line-width, brightness temperature, and velocity.

Within each region, we selected clouds with narrow-line features which likely correspond to temperatures less than 1000 K, as the temperature gradient due to cold gas moving through a hot ~10^6 K halo strongly influences the degree of cloud interaction. The variety of spectral features such as two-component structure and asymmetry that we see in these individual regions necessitated the choice of a sample of clouds from each region, to ensure representative consistency and to check trends on a larger scale.

5.2 Source regions

We describe each of our selected source regions below. A summary of the sources included in the study is given in Table 5.1. In total, we incorporate data from five separate regions, including two regions of extragalactic origin, two regions of Galactic origin and one cloud of unknown origin.

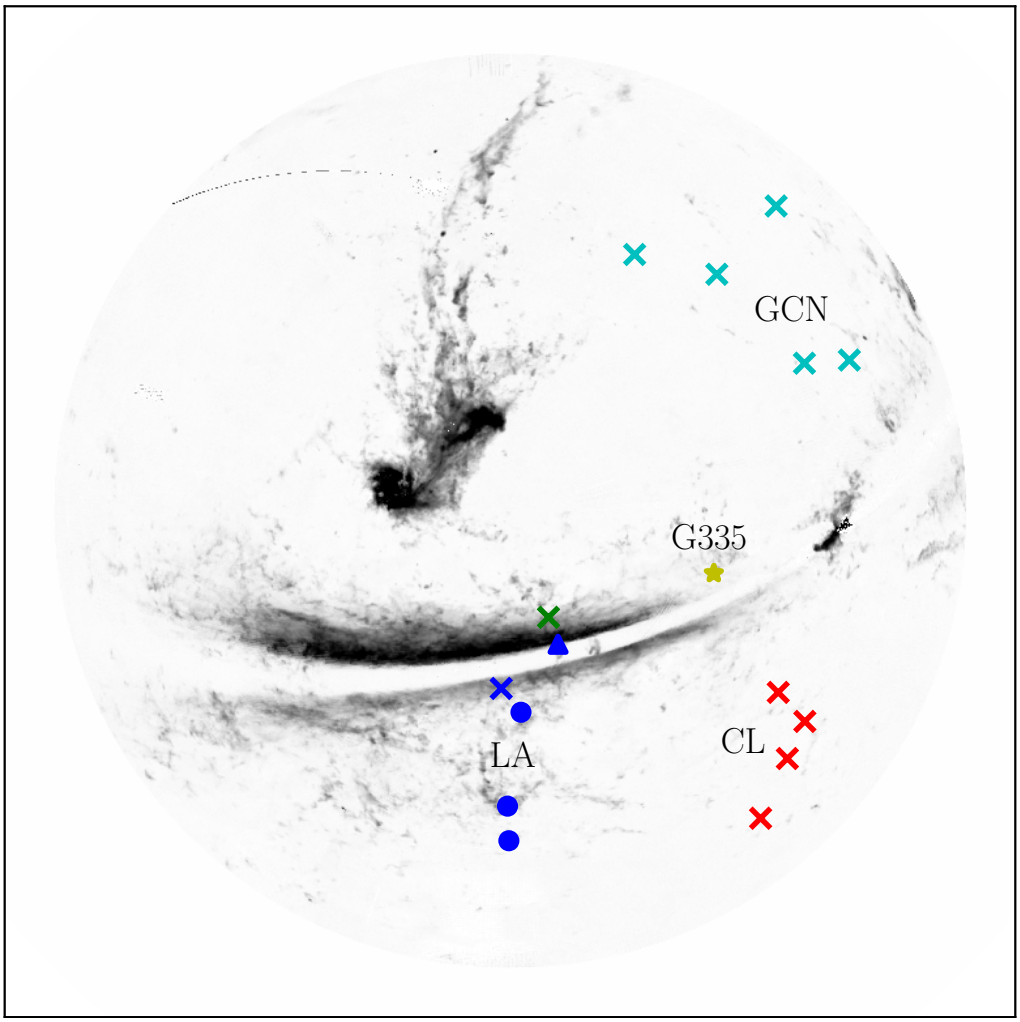

Figure 5.1: Integrated intensity map of the high-velocity emission in the southern-sky from GASS, showing the different regions of study. Our sample includes four distinct regions of known or suspected origins: the Leading Arm shown in blue (LA, extragalactic), Complex L shown in red (CL, Galactic), clouds near the Galactic disk shown in yellow (G335, Galactic) and Galactic Centre Negative shown in cyan (GCN, extragalactic). We also observed a cloud of unknown origin (with distinctly different velocity to nearby LA clouds), GAVC G305.5−06.8−107, which is shown in green. We mark our observed clouds as crosses, while data previously observed with the ATCA is marked with a different marker based on the ATNF project number: C1139 (circle), C1470 (star) and C1747 (triangle). All emission with $|v_{dev}| < 30$ km s^{-1}, declination $> 0°$, $|v_{LSR}| < 50$ km s^{-1} or $|v_{LSR}| > 468$ km s^{-1} is masked. The data are projected on a zenithal-equal-area (ZEA) map where the south celestial pole is in the centre and the celestial equator is at the edge of the image.

The Leading Arm

The Leading Arm (LA) is a well-known source of extragalactic gas, associated with the tidal stripping of the Magellanic system (Mathewson, Cleary & Murray, 1974; Putman et al., 1998). The similar metallicity and velocity of the Leading Arm compared with the Magellanic clouds confirm its origin, with orbital projections predicting that it should pass through the disk (Yoshizawa & Noguchi, 2003; Connors, Kawata & Gibson, 2006; Diaz & Bekki, 2012). As clouds in the Leading Arm are potentially interacting with the disk and have a known origin, they are vital in understanding how gas is accreted into the

Table 5.1: Summary of interacting HVC data used in this study.

Name	Abbreviation	Type	Region	Likely origin	Data
GAVC G005.8−55.9−083	G5	Cloud	Galactic Centre Negative	Extragalactic	Observed (C2849)
GHVC G014.2−43.2−155	G14	Cloud	Galactic Centre Negative	Extragalactic	Observed (C2849)
GHVC G020.0−18.3−242	G20	Cloud	Galactic Centre Negative	Extragalactic	Observed (C2849)
GHVC G038.7−37.3−241	G38	Cloud	Galactic Centre Negative	Extragalactic	Observed (C2849)
GHVC G294.7+03.7+246	G294	Cloud	Leading Arm	Extragalactic	Observed (C2849)
HVC 289+33+251	G289	Cloud	Leading Arm?	Extragalactic	Archival, reduced (C1139)
HVC 291+26+195	G291	Cloud	Leading Arm	Extragalactic	Archival, reduced (C1139)
HVC 297+09+253	G297	Cloud	Leading Arm	Extragalactic	Archival, reduced (C1139)
HVC 306−2+230	G306	Region	Leading Arm	Extragalactic	Archival (C1747)
GHVC G338.7+41.8−069*	G338	Cloud	Complex L	Galactic	Observed (C2849)
GHVC G342.2+19.8−081*	G342	Cloud	Complex L	Galactic	Observed (C2849)
GHVC G343.1+32.0−139	G343	Cloud	Complex L	Galactic	Observed (C2849)
GHVC G347.0+27.0−105*	G347	Cloud	Complex L	Galactic	Observed (C2849)
GAVC G305.5−06.8−107	G305	Cloud	Unknown	Unknown	Observed (C2849)
QIV region	G335	Region	Milky Way disk	Galactic	Archival, reduced (C1470)

* Originally identified in Moss et al. (2013) as part of GAVC G000.2-00.4−109 (Complex L).

Milky Way. For this region, we observed a morphologically and spectrally complex double-headed source which may be undergoing unusual fragmentation. This cloud is identified as GHVC G294.7+03.7+246 in the GASS catalogue of HVCs, and has previously been identified as a head-tail cloud (Putman, Saul & Mets, 2011). GHVC G294.7+03.7+246 also features two-component velocity structure with narrow components in each head of the cloud and a broad diffuse tail.

As well as our targeted observations of GHVC G294.7+03.7+246, we include in this region data on the extended region of a Leading Arm HVC known to be interacting with the Galactic plane (ATCA proposal C1747, *The Interaction of the Magellanic Leading Arm and the Galactic Plane*). This cloud, HVC 306−2+230 (incorporated into the large source GHVC G280.2−31.5+244 in the GASS catalogue of HVCs), is one of few HVCs that cross the Galactic plane and was argued to show evidence of ram pressure as part of the complex LA III (Brüns et al., 2005), based on its steep column density drop off and narrow line-widths near the Galactic plane. It was studied by McClure-Griffiths et al. (2008), who discovered a ridge of Galactic gas at a velocity $v_{LSR} = 122$ km s^{-1} pushed from the disk by the impact of HVC 306−2+230. McClure-Griffiths et al. (2008) also found that HVC 306−2+230 featured prominent head-tail structure, varying velocity width, deceleration at the front of the cloud and agreement with simulations of interacting HVCs, all of which further contributed to the conclusion that this HVC is undergoing a continuing interaction with the disk of the Milky Way. A clear two-component velocity structure was identified in this HVC, particularly around the head, with a narrow component of $\Delta v = 4.9$ km s^{-1} and a broad component of $\Delta v = 16.9$ km s^{-1} suggesting a two-phase structure with gas at temperatures $T \leq 600$ K and ≤ 6000 K respectively.

Our Leading Arm sample also includes three interacting head-tail HVCs previously observed with the ATCA (ATCA proposal C1139, *HI observation of compact high-velocity clouds*). These three clouds are specifically HVC 289+33+251 (GHVC G289.2+32.9+250), HVC 291+26+195 (GHVC G290.9+26.0+195) and HVC 297+09+253 (GHVC G297.1+08.7+252). HVC 289+33+251 was studied by Brüns & Westmeier (2004), who noted that its particularly compact size of just 4.4′ made it one of the most compact HVCs known, and designated it as an 'ultra-compact HVC'. The results of their study, showing evidence of ram-pressure interaction in the cloud, suggested that HVC 289+33+251 was embedded in a low-density medium: either the outer Galactic halo or as an intergalactic

member of the Local Group of nearby galaxies. They argued that the pressure needed to stabilise the cloud was much higher than could be expected based on models of the Milky Way halo and even in typical intergalactic densities, and as such concluded that HVC 289+33+251 was likely to be influenced by the presence of dark matter and located at an upper limit distance of 825 kpc. If their conclusions are correct, then although HVC 289+33+251 is in the vicinity both spatially and spectrally of the Leading Arm, our study may expect to find that its observed physical properties (such as line-width and brightness) are distinct from those of typical Leading Arm clouds and extremely different to Galactic gas.

HVC 291+26+195 and HVC 297+09+253 conversely were found to be likely associated with the Magellanic system, particularly the Leading Arm (Bekhti et al., 2006). They suggested distance estimates to both clouds of 10–60 kpc, placing them within the halo of the Milky Way and at distances comparable to those estimated for the Leading Arm. When studying the line-widths of each cloud, they found that both featured extremely narrow line-widths of $\Delta v \sim 2{-}4$ km s^{-1} while only HVC 297+09+253 featured the broad component at $\Delta v \sim 20$ km s^{-1}. They proposed that HVC 291+26+195 was at a later stage of interaction with the surrounding ambient medium given its greater distance from the Magellanic clouds, such that the diffuse warm gas had already been stripped off to merge with the halo due to friction forces leaving only the neutral cold gas clumps. This later study pointed out that the circumgalactic pressure of the Milky Way was not well-constrained observationally and could be much higher than previously expected, and they also referenced the previous study of HVC 289+33+251 as evidence confirming the multi-component structure of the Leading Arm. This suggests, although not explicitly stated, that the origin of HVC 289+33+251 was revised and that the cloud, along with HVC 291+26+195 and HVC 297+09+253, was considered to be part of the interacting Leading Arm rather than an intergalactic member of the Local Group.

Complex L

Complex L (CL) is believed to be Galactic in origin based on its spectral blending with and gaseous connection to Galactic disk gas, and is also likely to be located above a spiral arm based on the detection of associated Hα emission at a distance between 8–22 kpc and a scale height of ~10 kpc (Weiner, Vogel & Williams, 2001; Putman et al., 2003). Clouds thought to be associated with Complex L have been detected via interstellar absorption in optical spectra towards a distant quasar PKS 1448−232 (Richter, Westmeier & Brüns, 2005), although the lack of constraint on ionisation conditions and dust depletion made it impossible to determine the actual metal abundance in the detected cloud. Based on VLA data of the absorbing cloud, an assumed distance of 4–12 kpc and a $T_{\rm kin} \leq 900$ K based on HI line-widths, Richter, Westmeier & Brüns (2005) found that the implied thermal pressure of $P/k = nT \leq 180$ cm^{-3} K was consistent with Galactic fountain gas of solar abundance with moderate dust destruction at a z-height of 10 kpc based on comparison to the models of Wolfire et al. (1995).

The sample of clouds chosen from Complex L is varied, and includes a cloud with narrow components in the head, a core-only narrow component and a mixture of broad and narrow components throughout. GHVC 342.2+19.8−081 is unusual in that the narrow-line component is spatially asymmetric compared with the broad component, which may indicate interactions with an inhomogeneous medium. We note that of these clouds, only GHVC G343.1+32.0−139 is within the spatial limits of Complex L as defined by Wakker & van Woerden (1991). However, each of the other three clouds was selected from the large

GAVC G000.2-00.4−109, which incorporates all emission from Complex L extended down to Galactic velocities based on the source-finding procedure of Moss et al. (2013). This means that the clouds are likely connected to each other both spatially and spectrally down to the 2σ level. GHVC G338.7+41.8−069 and GHVC G342.2+19.8−081 also have their brightest emission peaking at slightly lower velocities than the lower limit of −85 km s^{-1} of Wakker & van Woerden (1991), however both clouds contain emission peaking at close to −85 km s^{-1} or higher.

Galactic Centre Negative

Galactic Centre Negative (GCN) clouds have been thought to be part of a gaseous stream of infalling gas (Mirabel & Morras, 1984), possibly related to the Magellanic Clouds (Mirabel, 1981; Olano, 2008). Jin (2010) used orbit calculations to conclude that the GCN clouds are likely to be from an accreted dwarf galaxy, though the precise origin of the stream remains unclear. These clouds, if inflowing into the Milky Way, exist in an extremely turbulent medium based on the conclusions of Winkel et al. (2011), who also argued that the GCN complex was in fact made up of several subpopulations of different origin. The distance to Galactic Centre Negative is uncertain, having been so far unconstrained by searches for optical absorption (Smoker et al., 2004). Kerp et al. (1999) attributed an excess in soft X-ray emission towards GCN to be consistent with the findings of Sembach et al. (1995) of association, although noting that the emission did not have a straightforward interpretation. Based on a lack of multi-phase structure evident in the majority of their identified GCN clouds, Winkel et al. (2011) suggested that GCN may be an example of accreting warm gas where the majority of the hydrogen has become ionised in the process of accretion. They found that the column density of clouds decreased at lower absolute radial velocities, which was explicable if GCN was in the process of interacting with the ambient medium of the Milky Way.

Our sample of GCN clouds includes clouds with narrow components along the leading edge or in the core only, one compact spatially unresolved cold cloud and a cloud with several components and significant variation in its spectrum. GAVC G005.8−55.9−083 lies spatially outside the area defined by Wakker & van Woerden (1991) to be part of GCN, and its lower velocity also excludes it from the spectral range attributed to GCN. This technically classifies it as part of the complex N, which was stated to be all negative velocity clouds whose velocities were not high enough to be part of other negative velocity complexes. Its position near the Galactic centre suggests that it could be related to Galactic centre outflow although its high latitude would be unusual for either central outflow or Galactic fountain. If it does indeed originate in the disk, we may expect it to share properties in common with other Galactic clouds.

QIV region

The QIV region includes previously observed data on two HI halo cloudlets suspected to be fountain clouds originating from the Galactic disk identified by Ford et al. (2008) (proposal C1470, *Determining the detailed structure of HI cloudlets*). The inclusion of this data broadens the scope of our regions, and gives us a second Galactic region to draw clouds from. The two cloudlets observed originated from the sample described in the Ford studies (Ford et al., 2008; Ford, Lockman & McClure-Griffiths, 2010), which investigated the properties of cool HI gas at tangent point velocities in two symmetrically opposite regions of the Milky Way. The QIV region from which the clouds were selected targeted clouds above a minor spiral arm, and hence likely has ongoing star-formation in the disk

below the clouds. The two clouds observed were selected based on showing evidence of head-tail structure and interactions with their surrounding medium, as well as sitting on the wings of Galactic emission.

GAVC G305.5−06.8−107

GAVC G305.5−06.8−107 (G305), an anomalous velocity cloud identified by (Moss et al., 2013), was selected for inclusion as part of the LA observations. This was in order to include a cloud with an unknown origin as part of the sample, and determine whether its origin could be discerned in relation to the properties of other clouds. It was selected on the basis of its brightness, head-tail structure, narrow line-widths and proximity to the LA region, minimising slew time. G305 is an interesting case because, based on its spatial location, it could potentially be Leading-Arm material that has been significantly decelerated on its way towards the disk. However, considering its velocity which is both negative and low, it may also be Galactic fountain material that has been ejected from the disk. The GASS data alone make it difficult to tell which of these origins is more likely, and hence G305 was included as part of the sample in order to investigate whether high-resolution observations would better clarify its likely origin.

5.3 Observations: Australia Telescope Compact Array and Parkes

This project involved both using archival data and completing new observations of clouds in different regions on the Australia Telescope Compact Array. For the census, we used the EW352 array operating at a continuum central frequency of 2100 MHz with a specific zoom band at 1420 MHz, to ensure good image fidelity, high spectral resolution and resolved emission on angular scales from 23′ down to 2′ (excluding the longest baselines to CA06). All non-archival clouds listed in Table 5.1 were observed as part of this project (C2849) in June 2013. Depending on the source angular size, 1–5 pointings were chosen on each cloud. We binned the data spectrally to 0.8 km s^{-1} to allow combination with Parkes single dish data, in order to recover emission at low spatial frequencies. This velocity resolution is sufficient to spectrally resolve narrow line components, which are typically ∼5 km s^{-1}.

As mentioned above, a selection of clouds from each region was absolutely critical in order to be able to differentiate between the effects of origin and region while minimising selection bias. For each cloud, the necessary brightness sensitivity was determined based on a 5σ detection of the diffuse emission. The RMS brightness temperatures range from 40 to 80 mK per 0.8 km s^{-1} channel. These sensitivity requirements resulted in a minimum total time of 570+600 minutes for the LA region, 585 minutes for CL and 520 minutes for the GCN region. This time was spread through multiple snapshot observations, giving us sufficient UV coverage to map substructure. In total we requested, and were granted, 4 allocations of 12-h intervals for each region to maximise efficiency, sensitivity and UV coverage. Some time was lost during the observations of CL due to shadowing of the antennas and extremely strong radio frequency interference, and drive-time was an issue near zenith for GCN, but all clouds were detected significantly above the noise level. The observations of CL and GCN were aided by green-time observations a week prior, adding an additional 5 hours of integration time on each region.

All data were reduced using the MIRIAD data reduction package (Sault, Teuben & Wright, 1995). The RMS noise for each cloud ranged from 5 mJy per beam to 25 mJy

per beam, close to the theoretical noise expectations, and all clouds were detected with a signal-to-noise ratio of at least 5. After Fourier-transforming to the image domain, each data cube was deconvolved using *clean* and then restored. We found that *clean* consistently performed better than the maximum entropy method *mosmem*, which may be due to the small angular size of clouds and hence ability to be approximated by a Gaussian. The data from each cloud was then combined with Parkes data using a combination factor of 1.1 in the task *immerge* based on a universally-applied empirical determination of the appropriate scaling factor for the GASS data.

The ATCA data for the previously observed projects C1139 and C1470 was obtained via the Australia Telescope Online Archive, and reduced using the same procedure of data reduction as applied to the newly observed data in C2849. Similarly, we combined the resulting data with GASS in order to recover low spatial frequencies. The data from C1747 was incorporated into the sample in reduced form, having been previously reduced and combined with Parkes data.

5.4 Results

We show each data set in integrated intensity in Figures 5.2 to 5.16, including the single-dish (GASS) data, the interferometric (ATCA) data and the combined data, with the beam of each image plotted in the lower left corner. We also produced spectral plots of each cloud (referred to hereafter by their abbreviations given in Table 5.1) tracing various properties spatially: integrated intensity, T_B, FWHM, v_{LSR}, v_{GSR} and the difference between the two velocities. These are shown in Figures 5.17 to 5.32. Due to the large angular size of G306 and G335, we binned both datasets by 2 and 5 pixels respectively to reduce their spatial pixel dimensions and consequent visualisation runtime. We constrained both G306 and G335 spectrally in order to image the brightest, most distinct emission, but performed fitting routines on the non-constrained data.

Our observations included some clouds at low declinations relative to the E–W array of ATCA at a latitude of $-30.312778°$ and as such have an elongated beam in the N–S direction. The imaging process takes into account this corresponding lack of information in declination by ensuring that this direction is gridded without being over-sampled, producing images that appear distorted but are more reliable for measurement purposes. This is particular affects the following clouds: G20, G38, G338, G343, and G347.

The key results of each section of analysis are summarised in Table 5.2, with the results covered in more detail in this section.

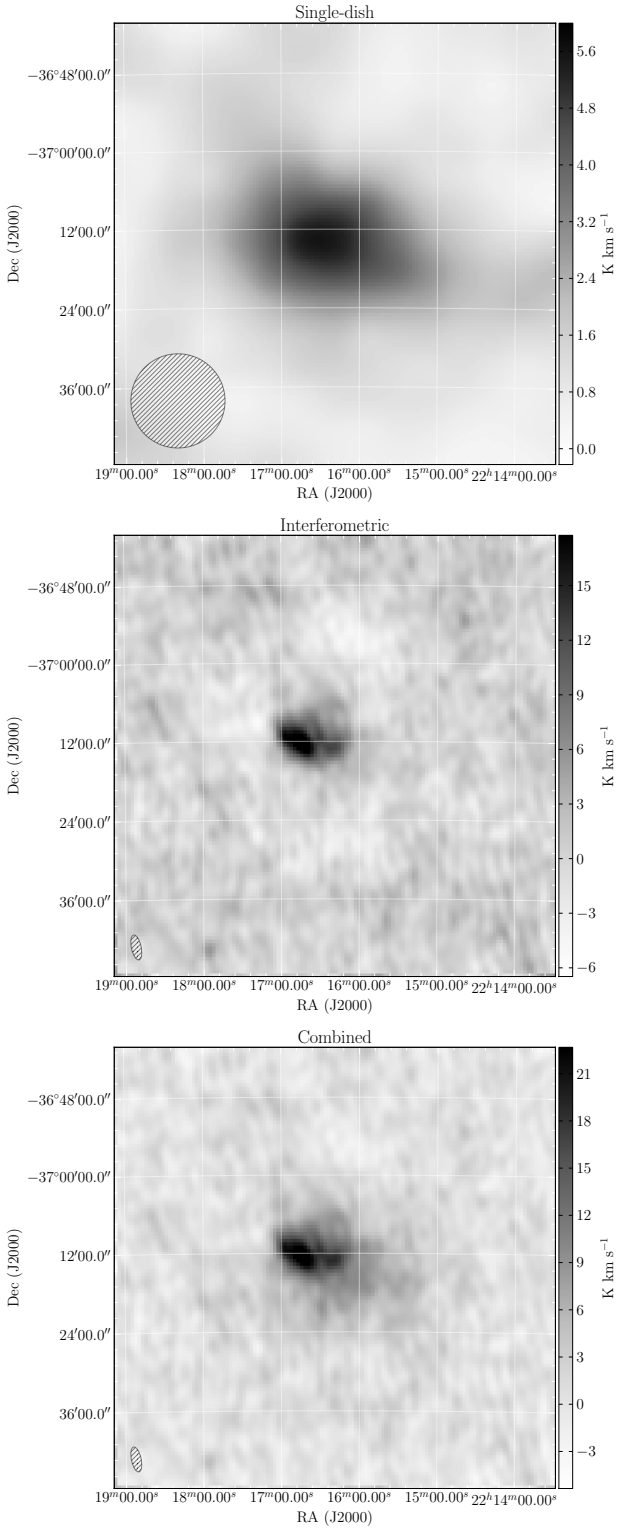

Figure 5.2: HI integrated-intensity maps of G5, in equatorial coordinates. Shown from top: single-dish (Parkes), interferometric (ATCA) and combined images. The beam for each dataset is shown in the bottom left corner, and the colourbar units are K km s^{-1}.

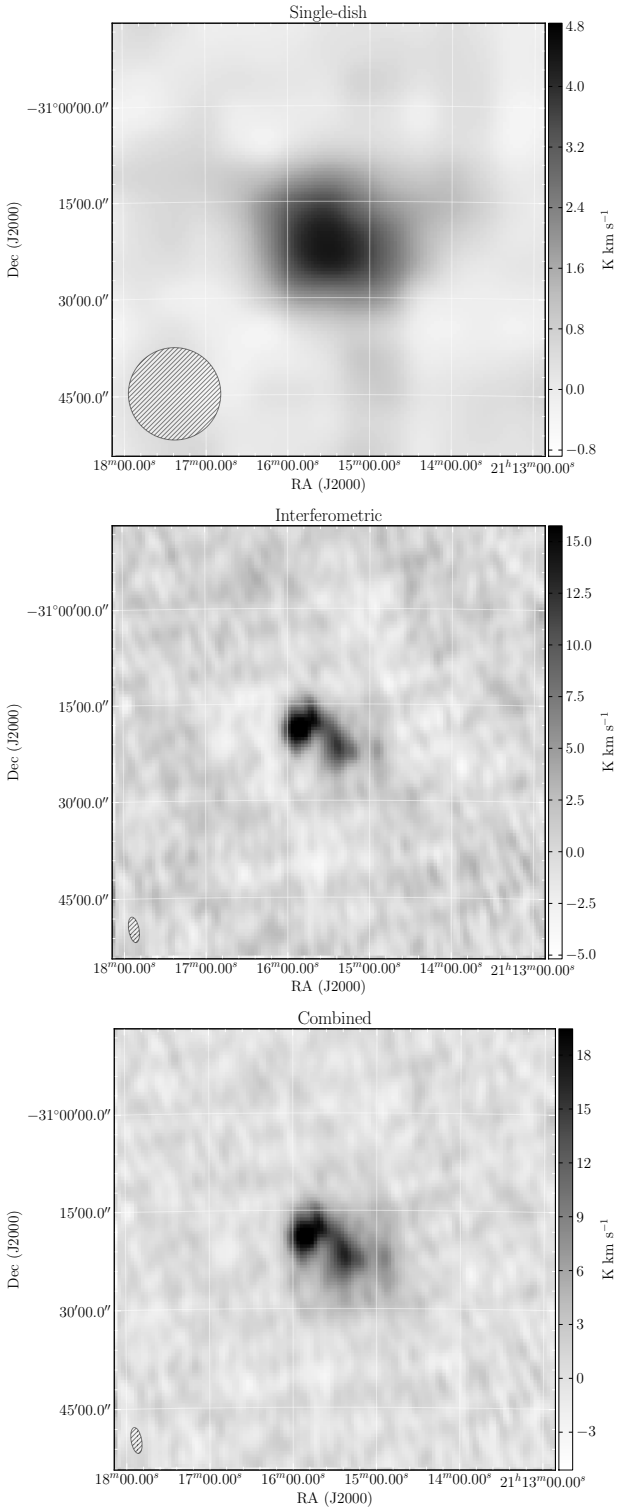

Figure 5.3: HI integrated-intensity maps of G14, in equatorial coordinates. Shown from top: single-dish (Parkes), interferometric (ATCA) and combined images. The beam for each dataset is shown in the bottom left corner, and the colourbar units are K km s^{-1}.

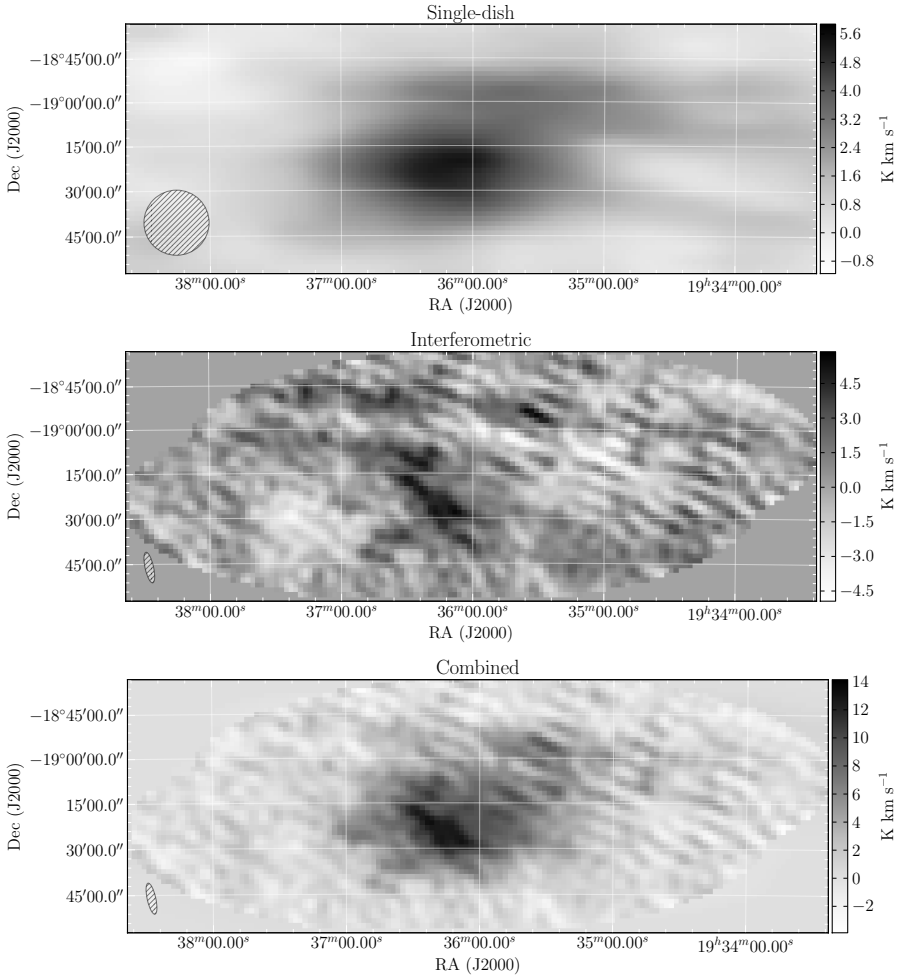

Figure 5.4: HI integrated-intensity maps of G20, in equatorial coordinates. Shown from top: single-dish (Parkes), interferometric (ATCA) and combined images. The beam for each dataset is shown in the bottom left corner, and the colourbar units are K km s^{-1}.

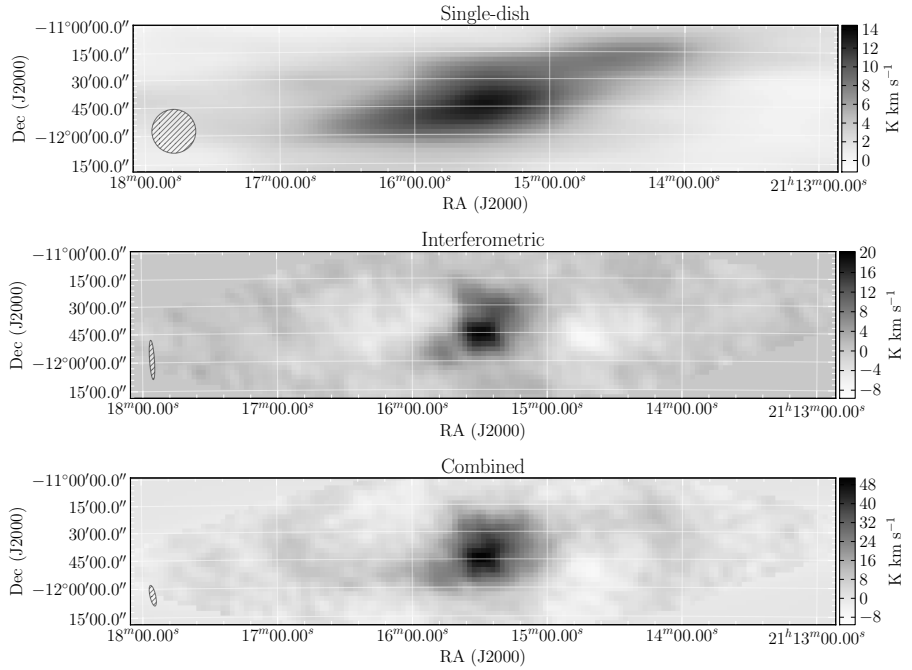

Figure 5.5: HI integrated-intensity maps of G38, in equatorial coordinates. Shown from top: single-dish (Parkes), interferometric (ATCA) and combined images. The beam for each dataset is shown in the bottom left corner, and the colourbar units are K km s^{-1}.

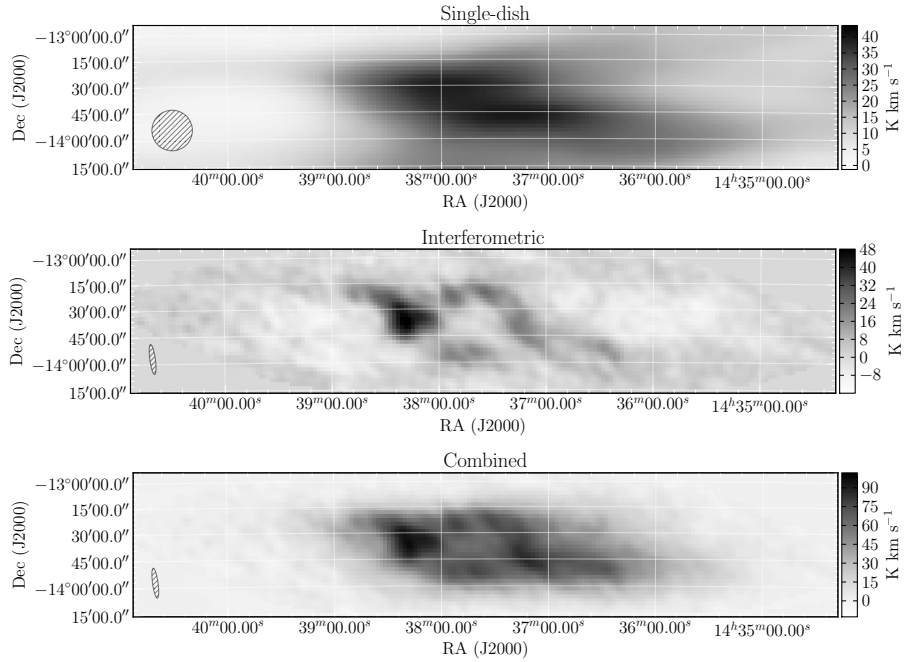

Figure 5.6: HI integrated-intensity maps of G338, in equatorial coordinates. Shown from top: single-dish (Parkes), interferometric (ATCA) and combined images. The beam for each dataset is shown in the bottom left corner, and the colourbar units are K km s^{-1}.

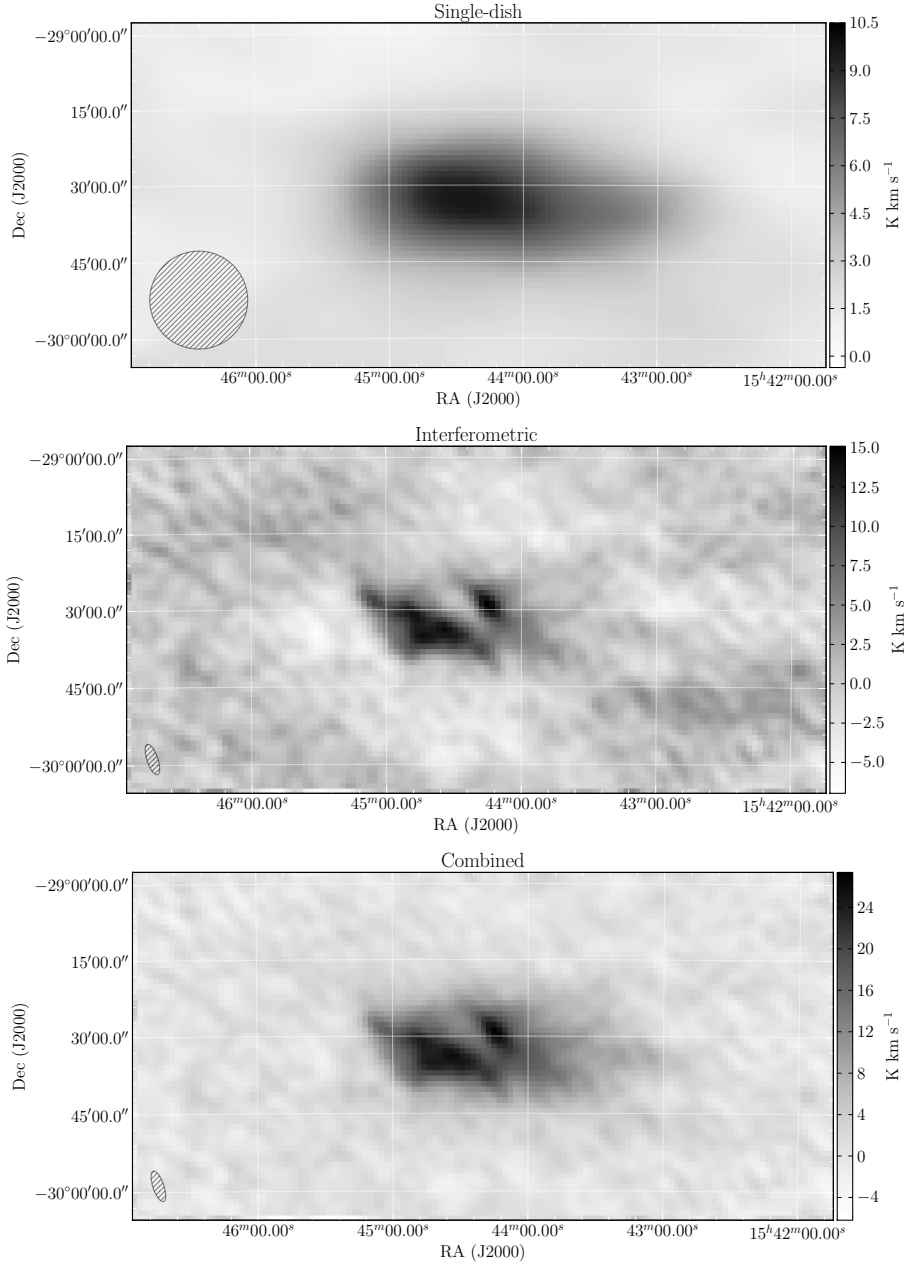

Figure 5.7: HI integrated-intensity maps of G342, in equatorial coordinates. Shown from top: single-dish (Parkes), interferometric (ATCA) and combined images. The beam for each dataset is shown in the bottom left corner, and the colourbar units are K km s^{-1}.

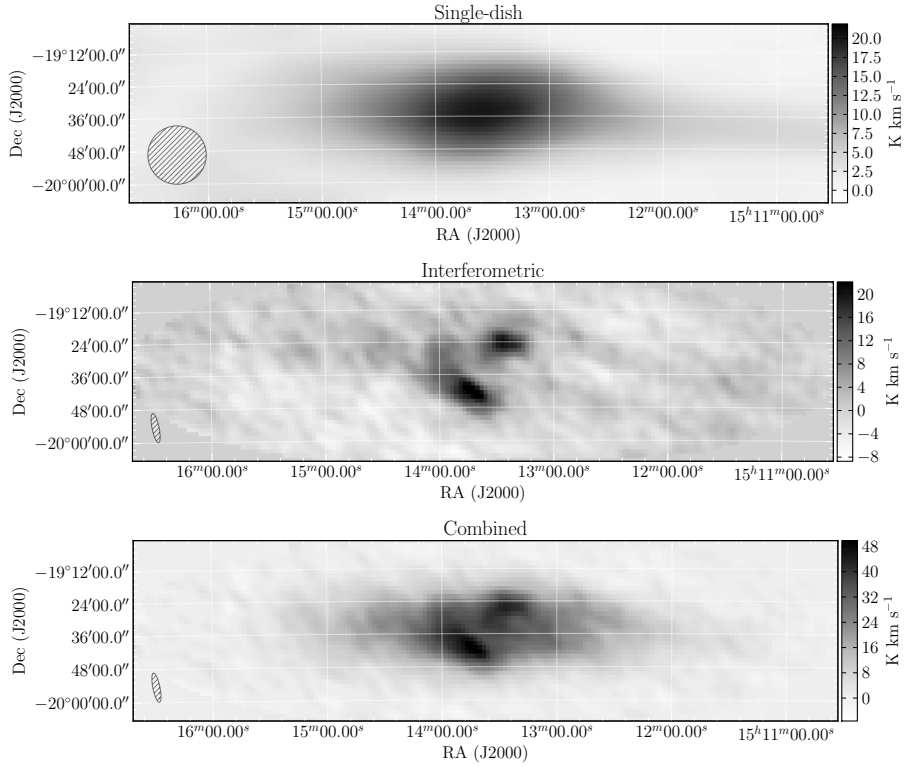

Figure 5.8: HI integrated-intensity maps of G343, in equatorial coordinates. Shown from top: single-dish (Parkes), interferometric (ATCA) and combined images. The beam for each dataset is shown in the bottom left corner, and the colourbar units are K km s^{-1}.

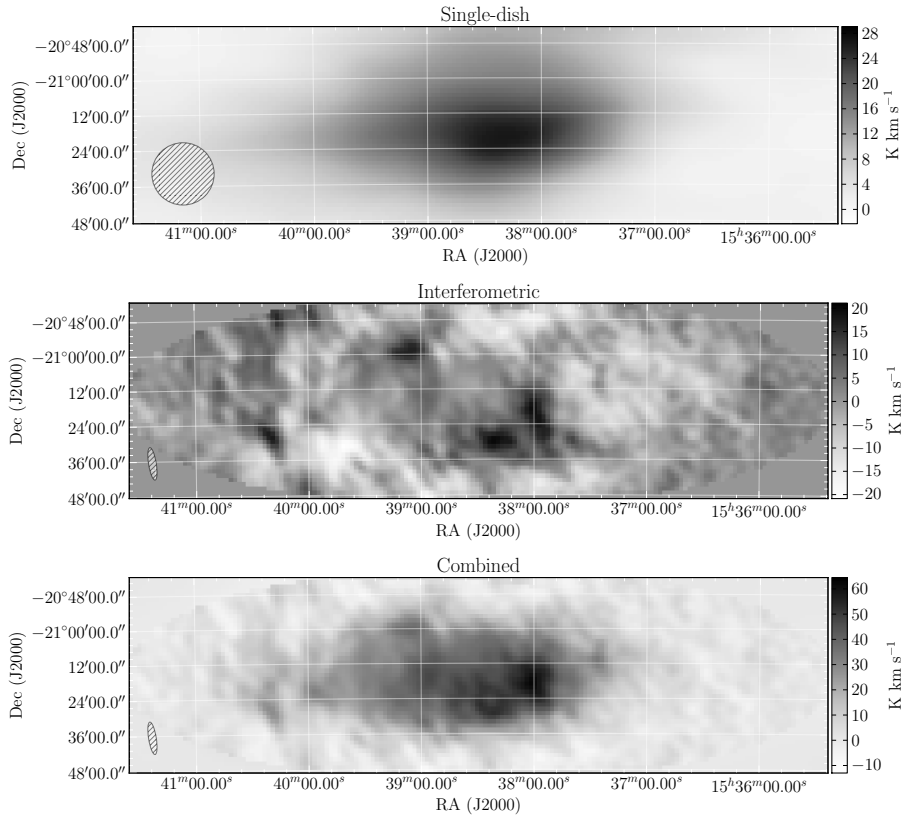

Figure 5.9: HI integrated-intensity maps of G347, in equatorial coordinates. Shown from top: single-dish (Parkes), interferometric (ATCA) and combined images. The beam for each dataset is shown in the bottom left corner, and the colourbar units are K km s^{-1}.

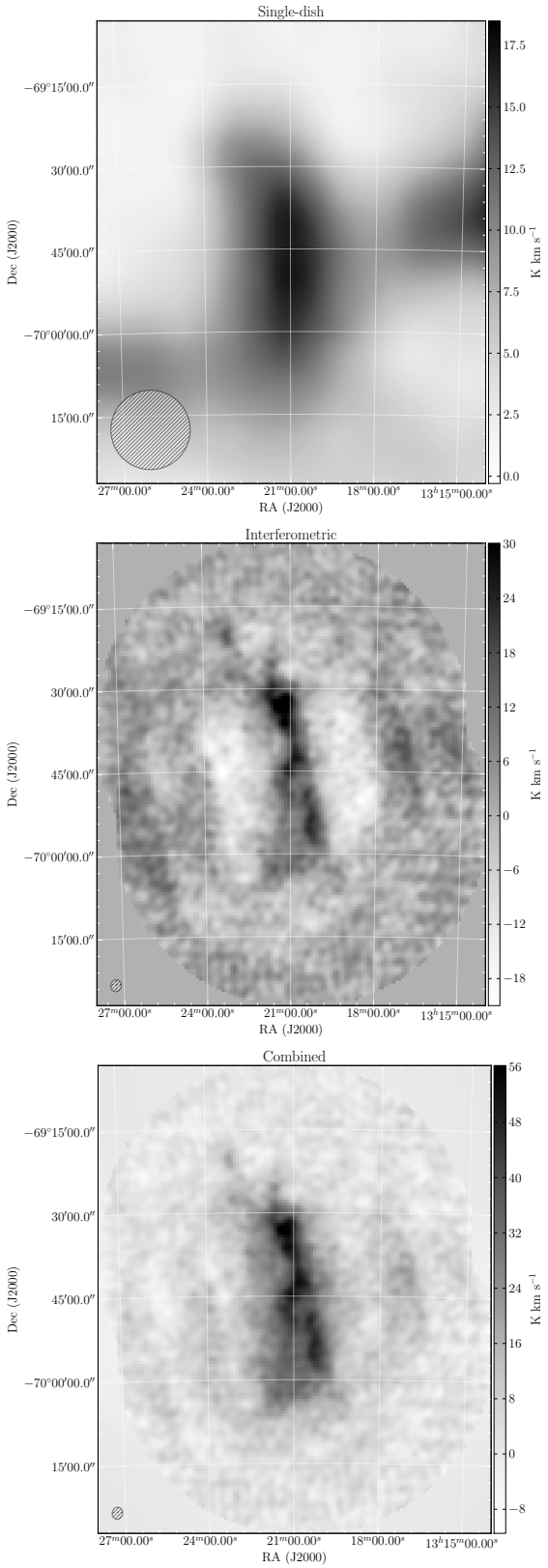

Figure 5.10: HI integrated-intensity maps of G305, in equatorial coordinates. Shown from top: single-dish (Parkes), interferometric (ATCA) and combined images. The beam for each dataset is shown in the bottom left corner, and the colourbar units are K km s^{-1}.

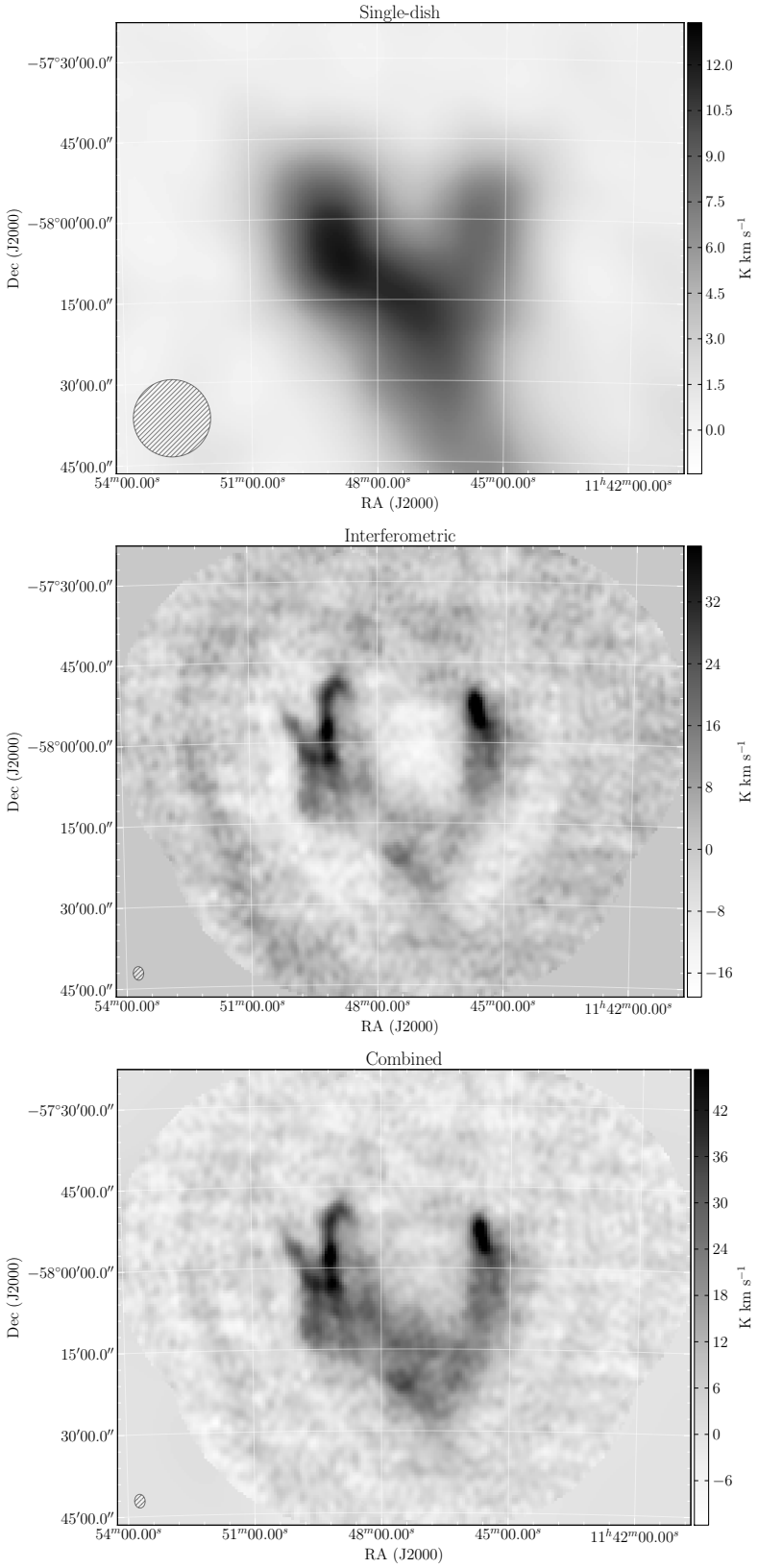

Figure 5.11: HI integrated-intensity maps of G294, in equatorial coordinates. Shown from top: single-dish (Parkes), interferometric (ATCA) and combined images. The beam for each dataset is shown in the bottom left corner, and the colourbar units are K km s^{-1}.

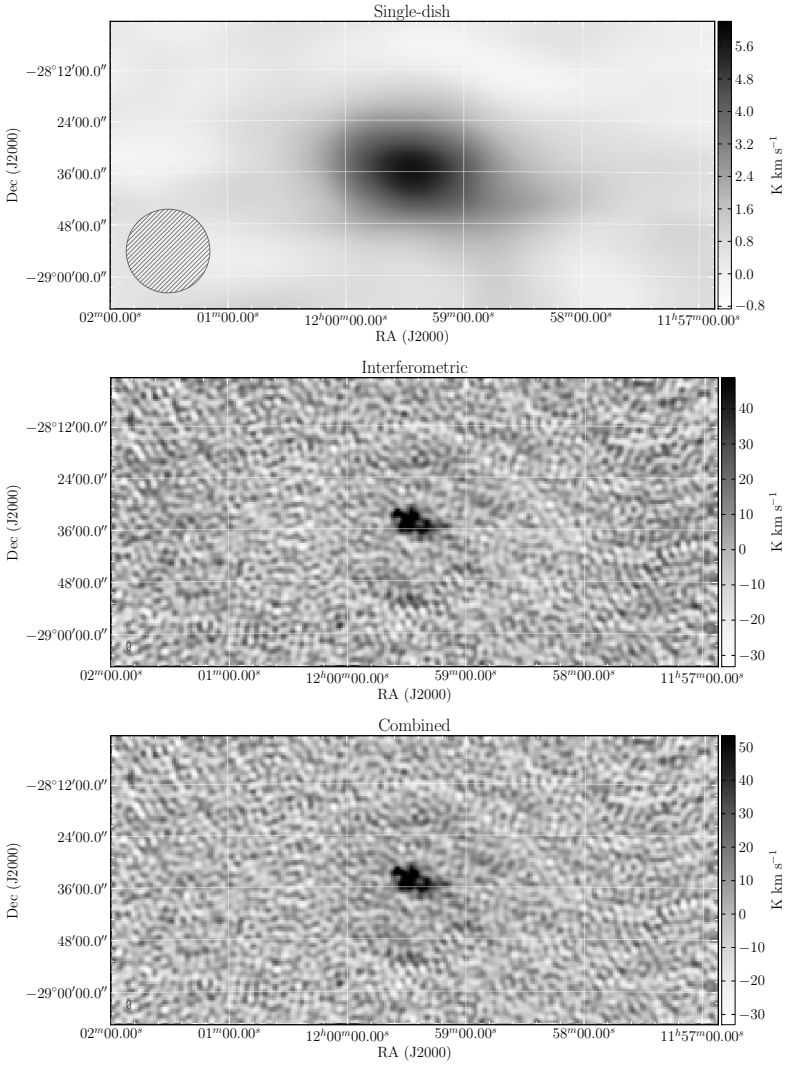

Figure 5.12: HI integrated-intensity maps of G289, in equatorial coordinates. Shown from top: single-dish (Parkes), interferometric (ATCA) and combined images. The beam for each dataset is shown in the bottom left corner, and the colourbar units are K km s^{-1}.

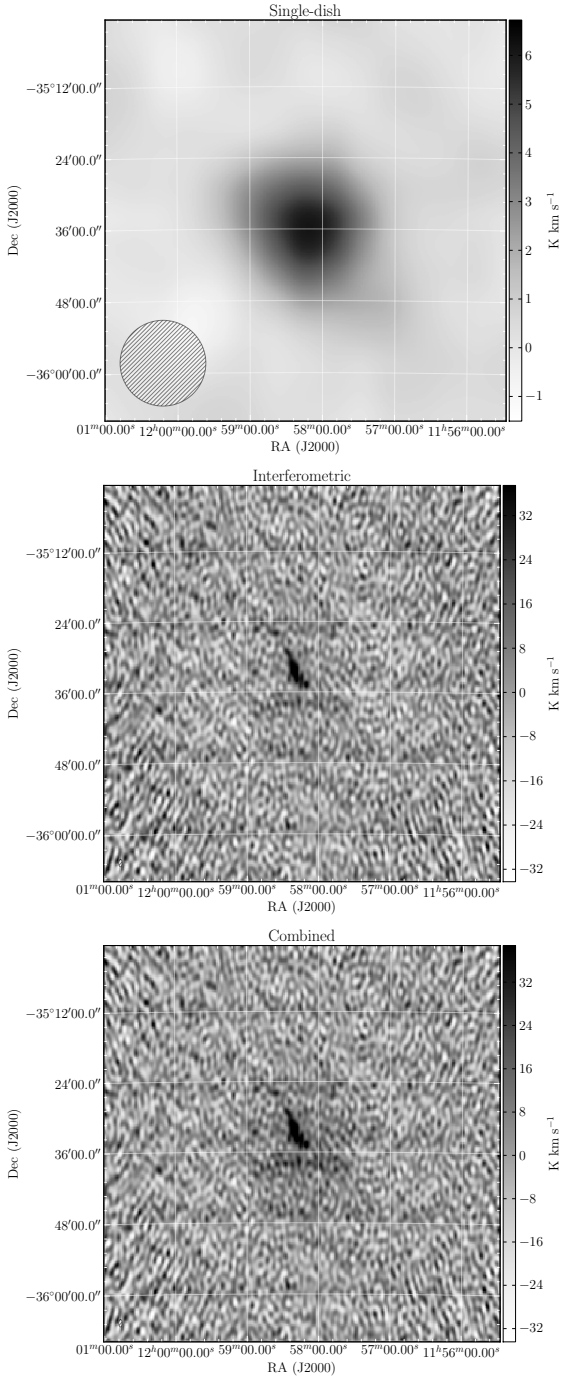

Figure 5.13: HI integrated-intensity maps of G291, in equatorial coordinates. Shown from top: single-dish (Parkes), interferometric (ATCA) and combined images. The beam for each dataset is shown in the bottom left corner, and the colourbar units are K km s^{-1}.

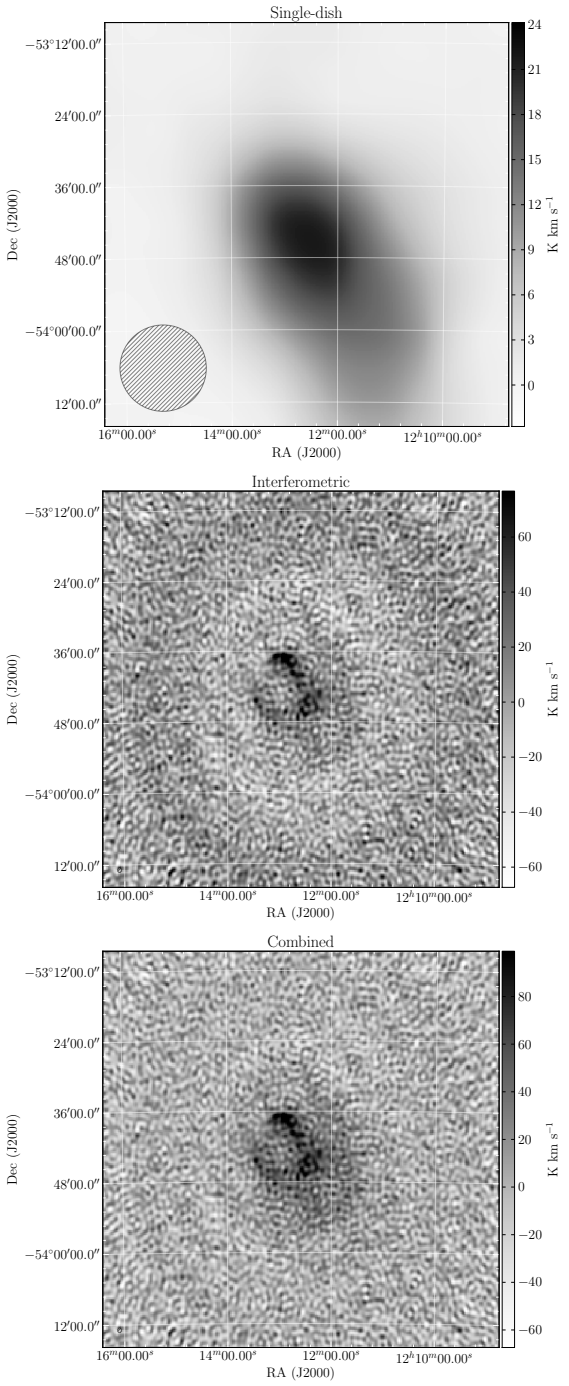

Figure 5.14: HI integrated-intensity maps of G297, in equatorial coordinates. Shown from top: single-dish (Parkes), interferometric (ATCA) and combined images. The beam for each dataset is shown in the bottom left corner, and the colourbar units are K km s^{-1}.

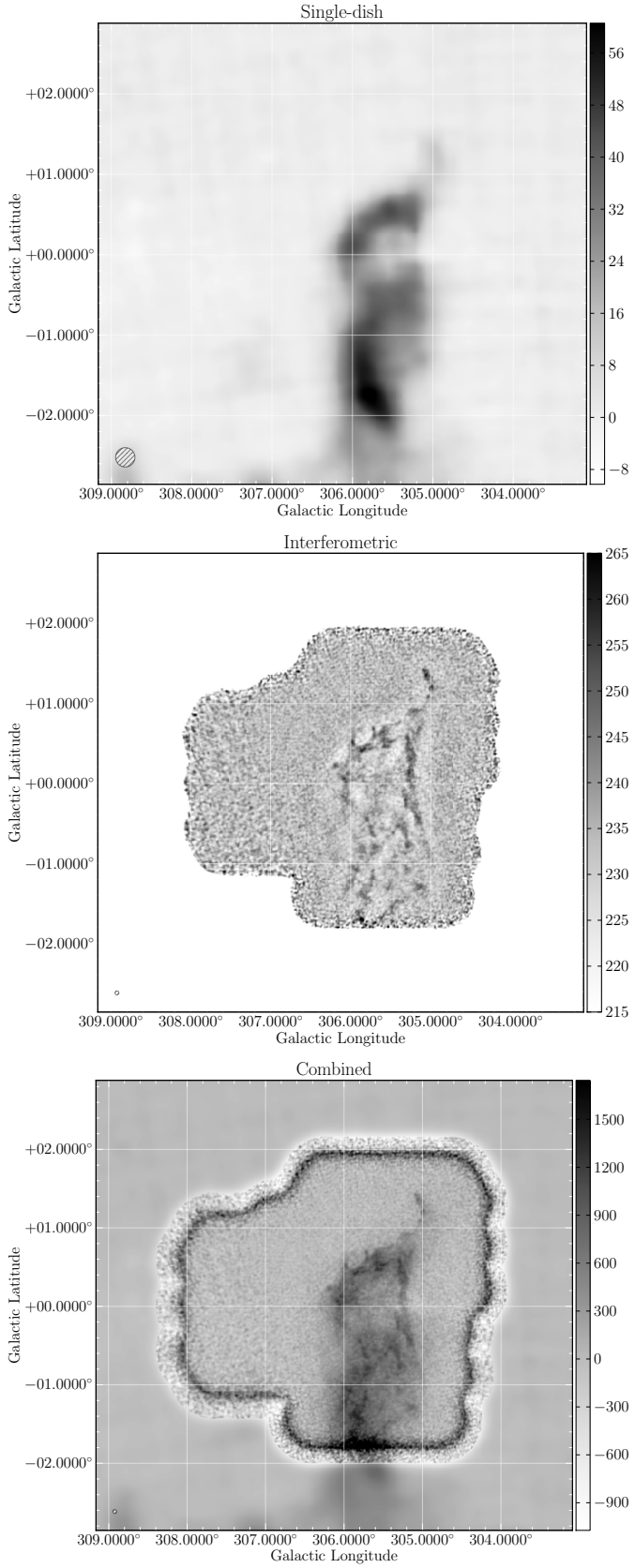

Figure 5.15: HI integrated-intensity maps of G306, in Galactic coordinates. Shown from top: single-dish (Parkes), interferometric (ATCA) and combined images. The beam for each dataset is shown in the bottom left corner, and the colourbar units are K km s^{-1}.

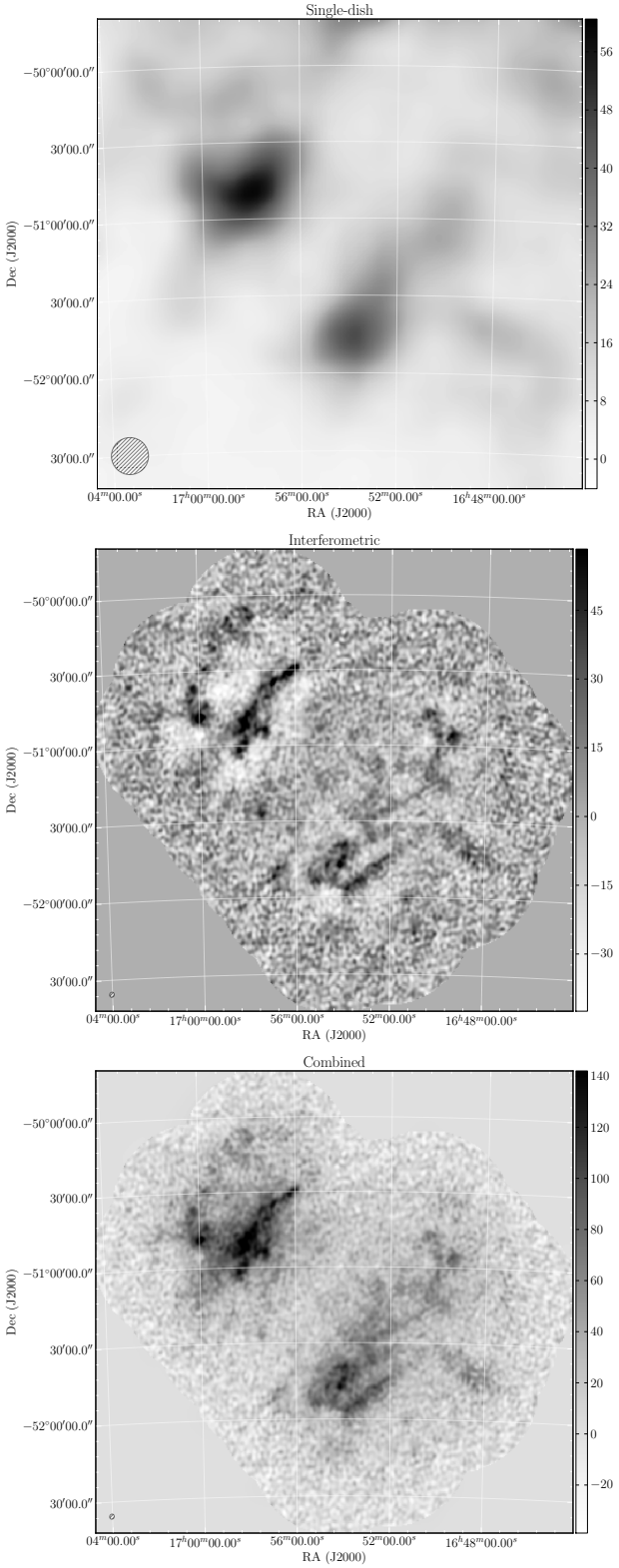

Figure 5.16: HI integrated-intensity maps of G335, in equatorial coordinates. Shown from top: single-dish (Parkes), interferometric (ATCA) and combined images. The beam for each dataset is shown in the bottom left corner, and the colourbar units are K km s^{-1}.

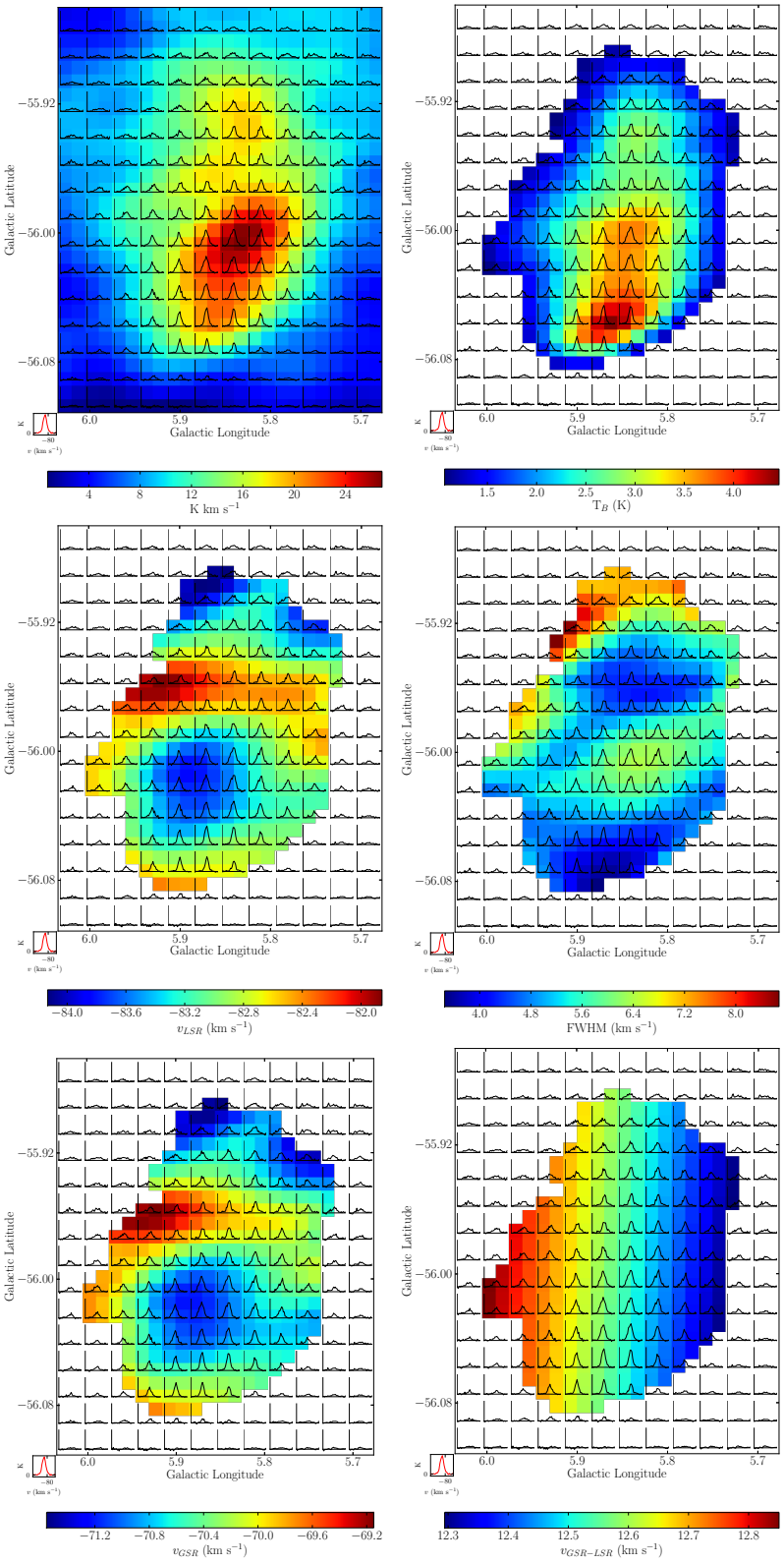

Figure 5.17: Spatial physical property plots of G5 in Galactic coordinates, across from top left: integrated intensity, fitted peak T_B, v_{LSR}, line-width, v_{GSR} and $v_{GSR-LSR}$. Pixels are masked below a peak T_B of 1.4 K in all plots except integrated intensity. Spectra are averaged over 2 pixels.

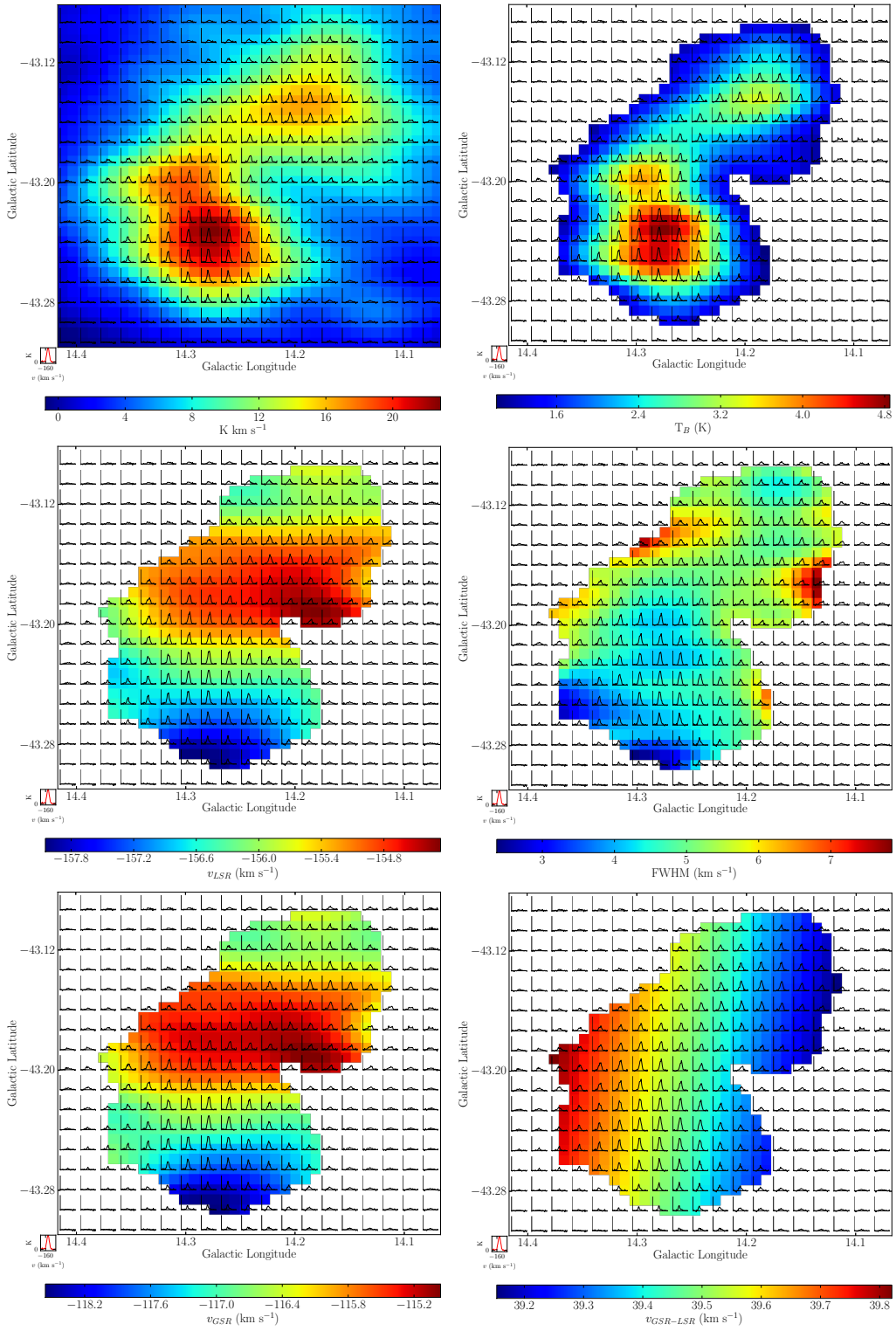

Figure 5.18: Spatial physical property plots of G14 in Galactic coordinates, across from top left: integrated intensity, fitted peak T_B, v_{LSR}, line-width, v_{GSR} and $v_{GSR-LSR}$. Pixels are masked below a peak T_B of 1.4 K in all plots except integrated intensity. Spectra are averaged over 2 pixels.

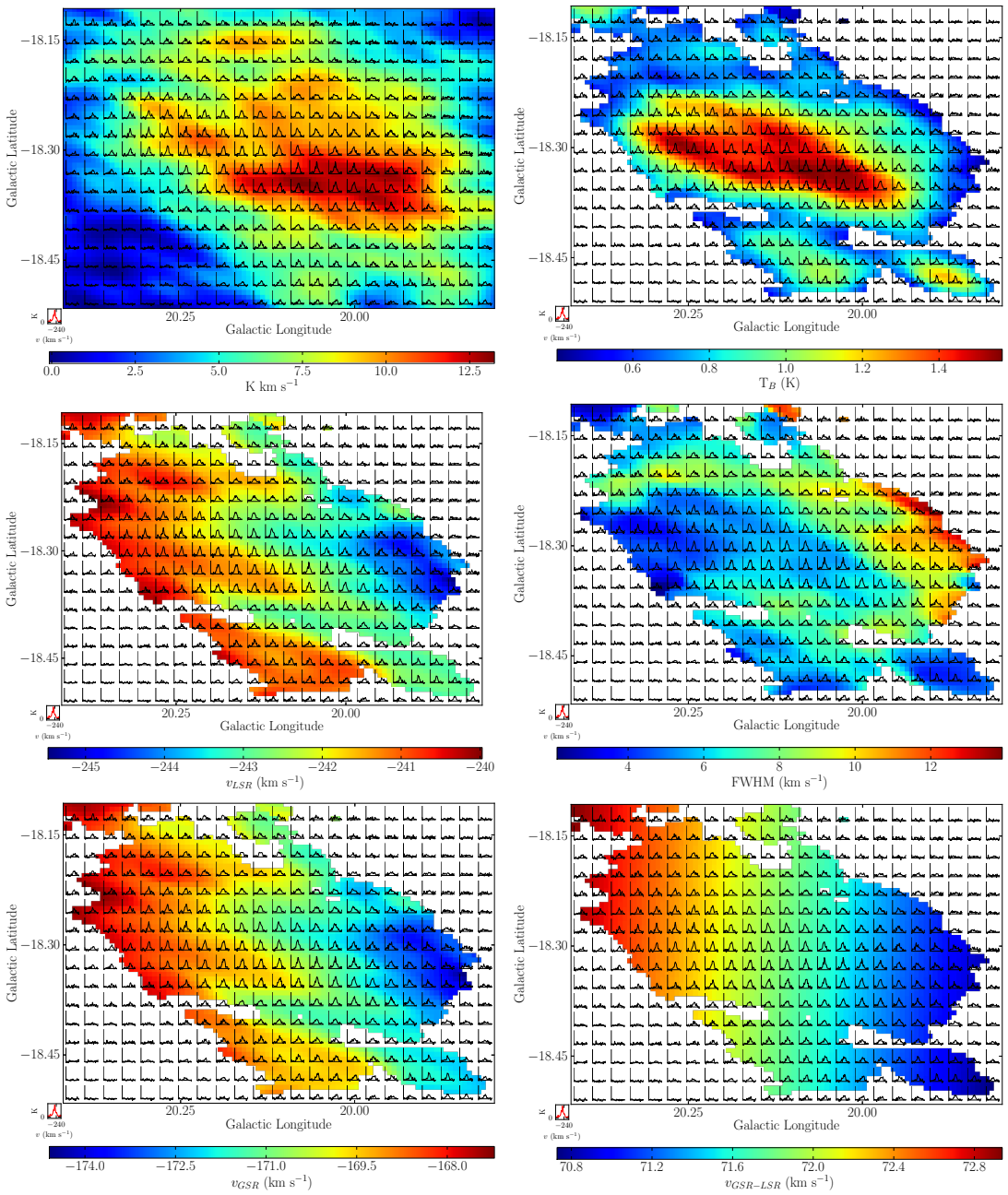

Figure 5.19: Spatial physical property plots of G20 in Galactic coordinates, across from top left: integrated intensity, fitted peak T_B, v_{LSR}, line-width, v_{GSR} and $v_{GSR-LSR}$. Pixels are masked below a peak T_B of 0.8 K in all plots except integrated intensity. Spectra are averaged over 4 pixels.

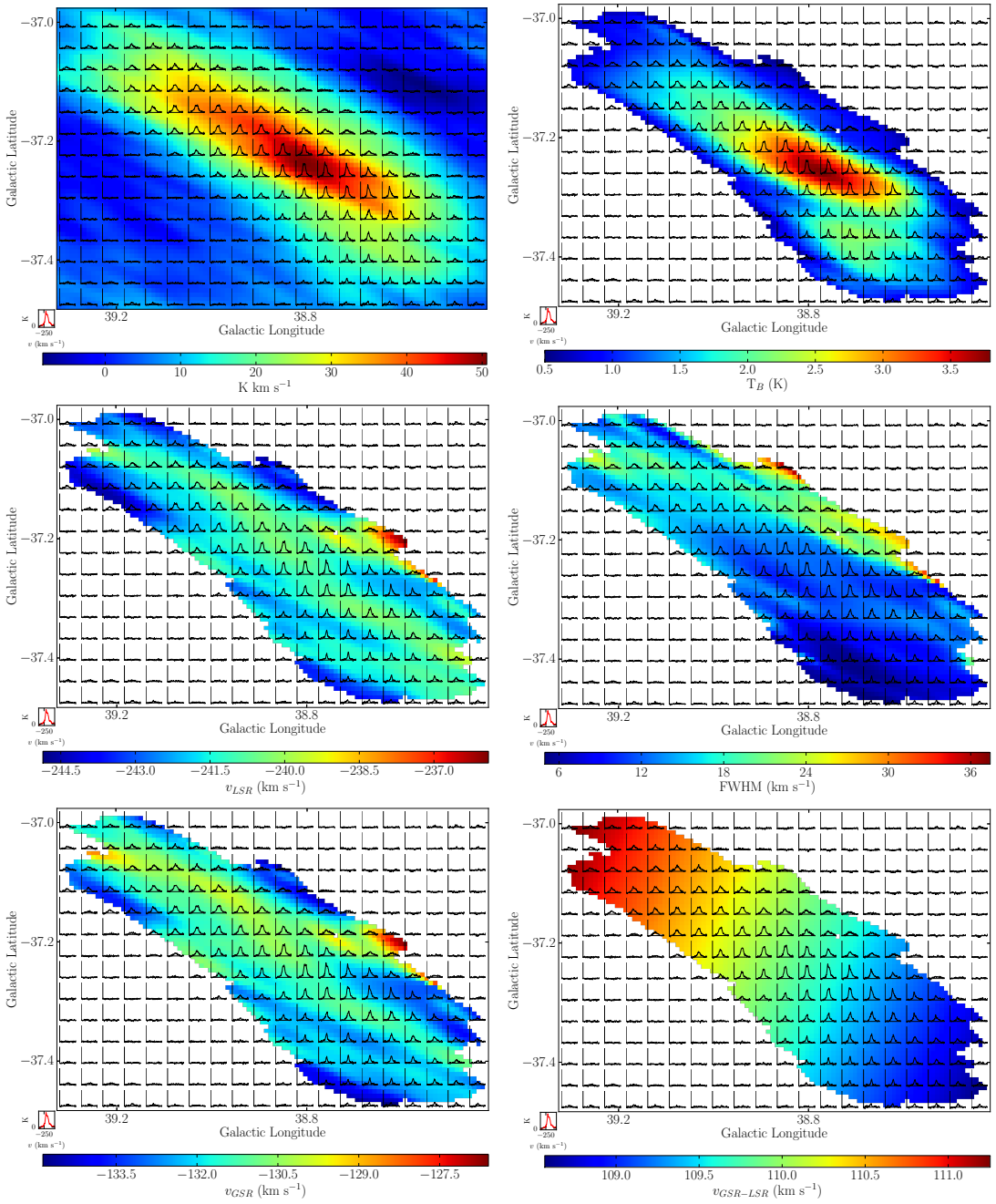

Figure 5.20: Spatial physical property plots of G38 in Galactic coordinates, across from top left: integrated intensity, fitted peak T_B, v_{LSR}, line-width, v_{GSR} and $v_{GSR-LSR}$. Pixels are masked below a peak T_B of 1.0 K in all plots except integrated intensity. Spectra are averaged over 5 pixels.

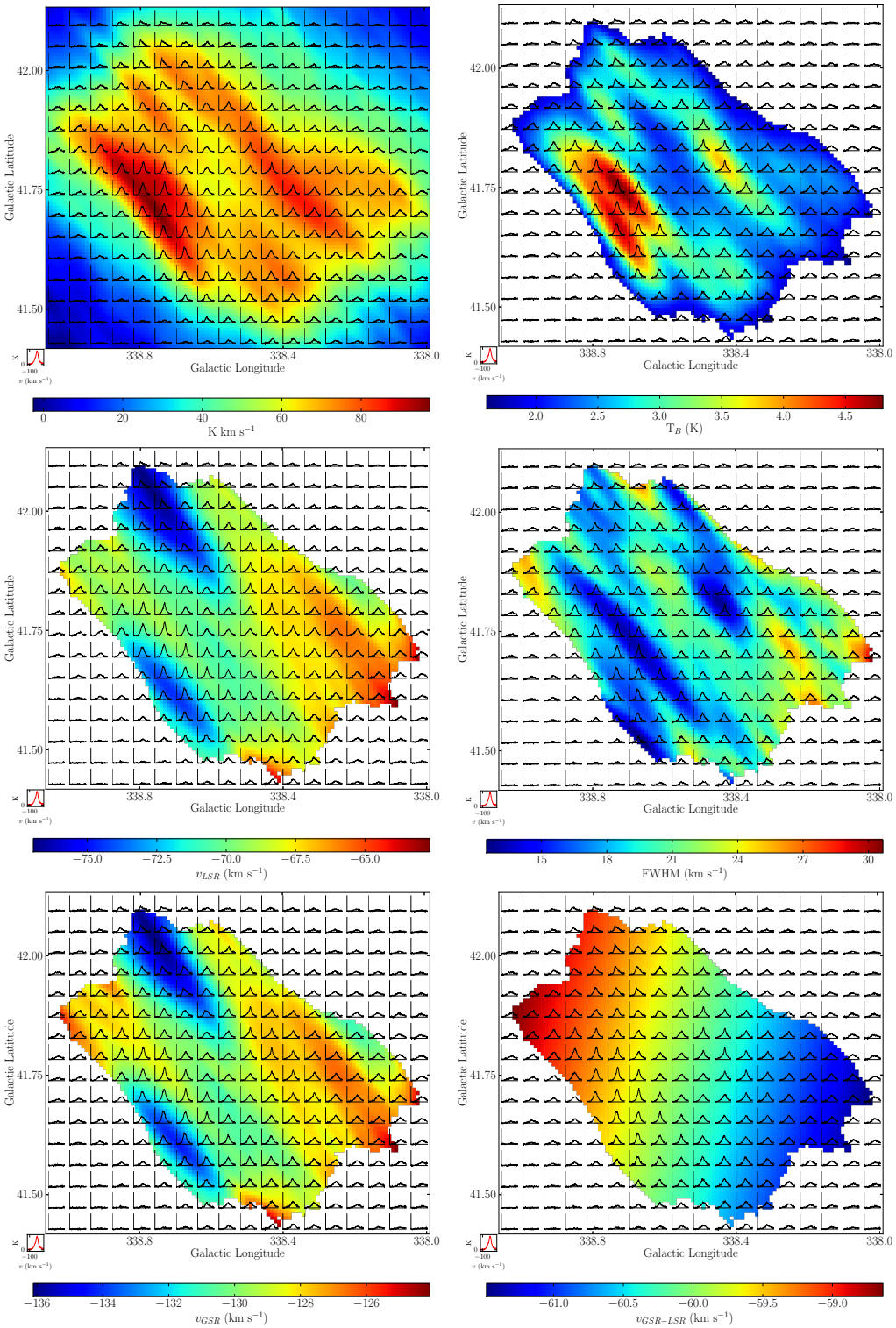

Figure 5.21: Spatial physical property plots of G338 in Galactic coordinates, across from top left: integrated intensity, fitted peak T_B, v_{LSR}, line-width, v_{GSR} and $v_{GSR-LSR}$. Pixels are masked below a peak T_B of 2.2 K in all plots except integrated intensity. Spectra are averaged over 6 pixels.

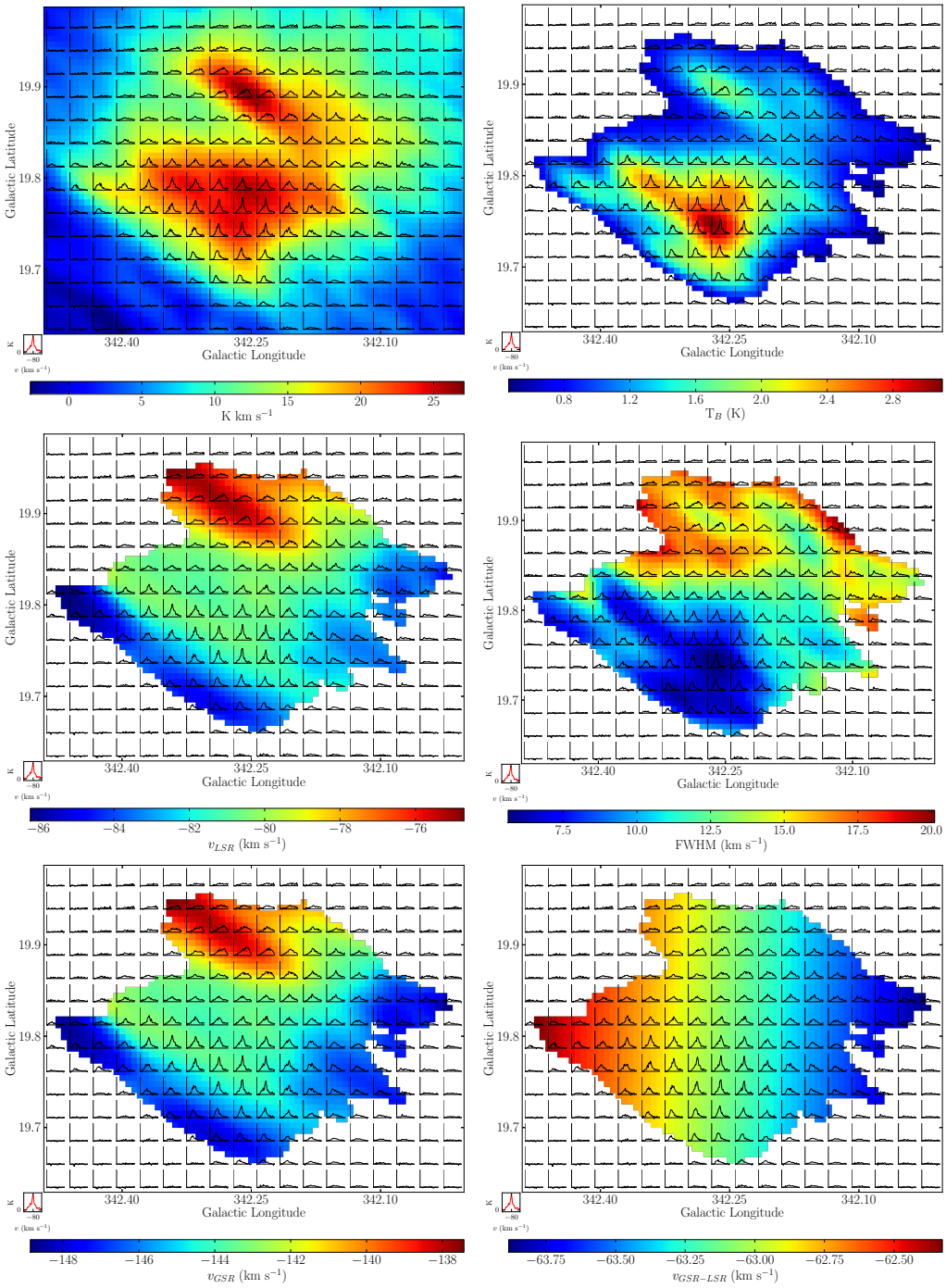

Figure 5.22: Spatial physical property plots of G342 in Galactic coordinates, across from top left: integrated intensity, fitted peak T_B, v_{LSR}, line-width, v_{GSR} and $v_{GSR-LSR}$. Pixels are masked below a peak T_B of 0.9 K in all plots except integrated intensity. Spectra are averaged over 4 pixels.

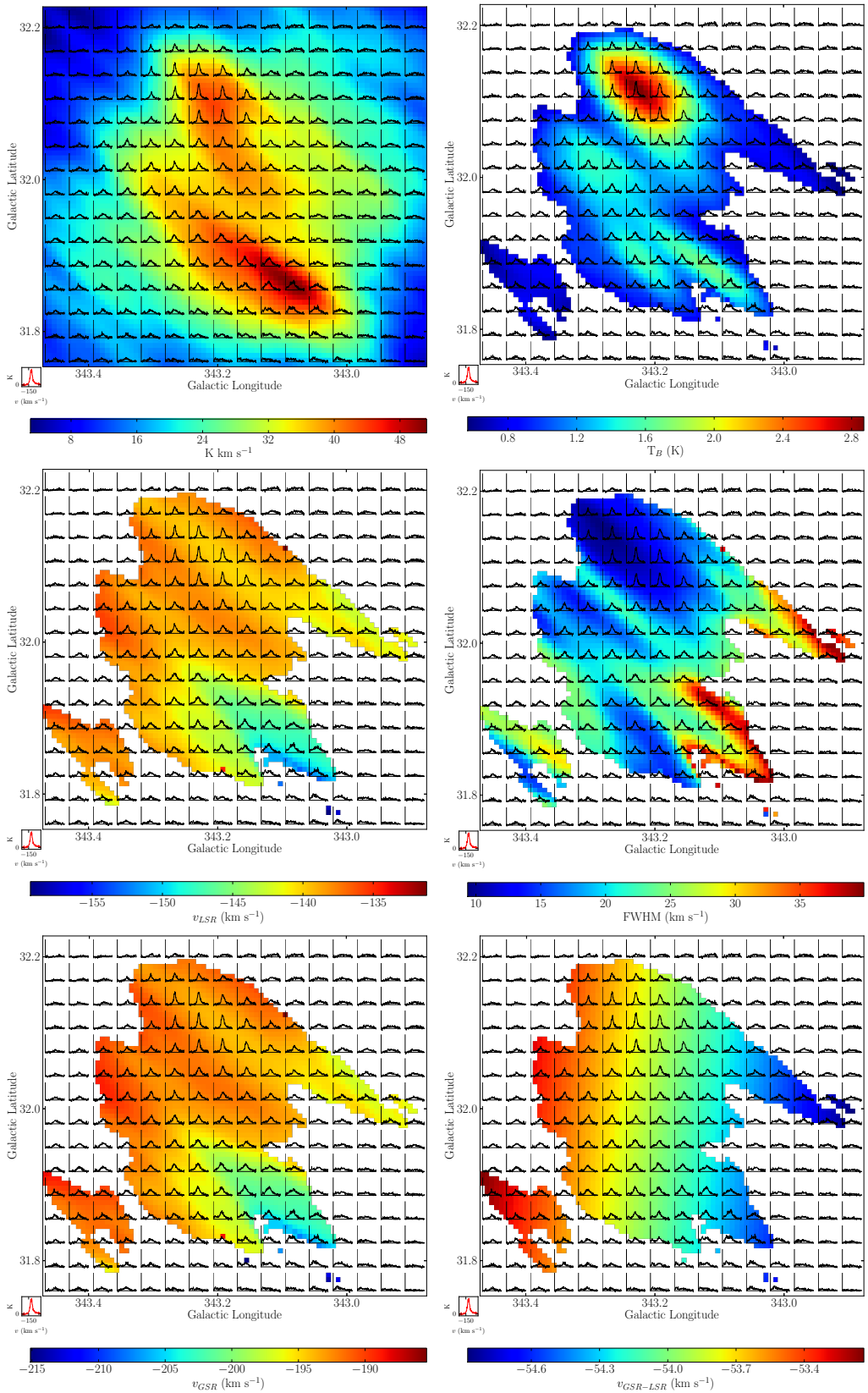

Figure 5.23: Spatial physical property plots of G343 in Galactic coordinates, across from top left: integrated intensity, fitted peak T_B, v_{LSR}, line-width, v_{GSR} and $v_{GSR-LSR}$. Pixels are masked below a peak T_B of 1.1 K in all plots except integrated intensity. Spectra are averaged over 5 pixels.

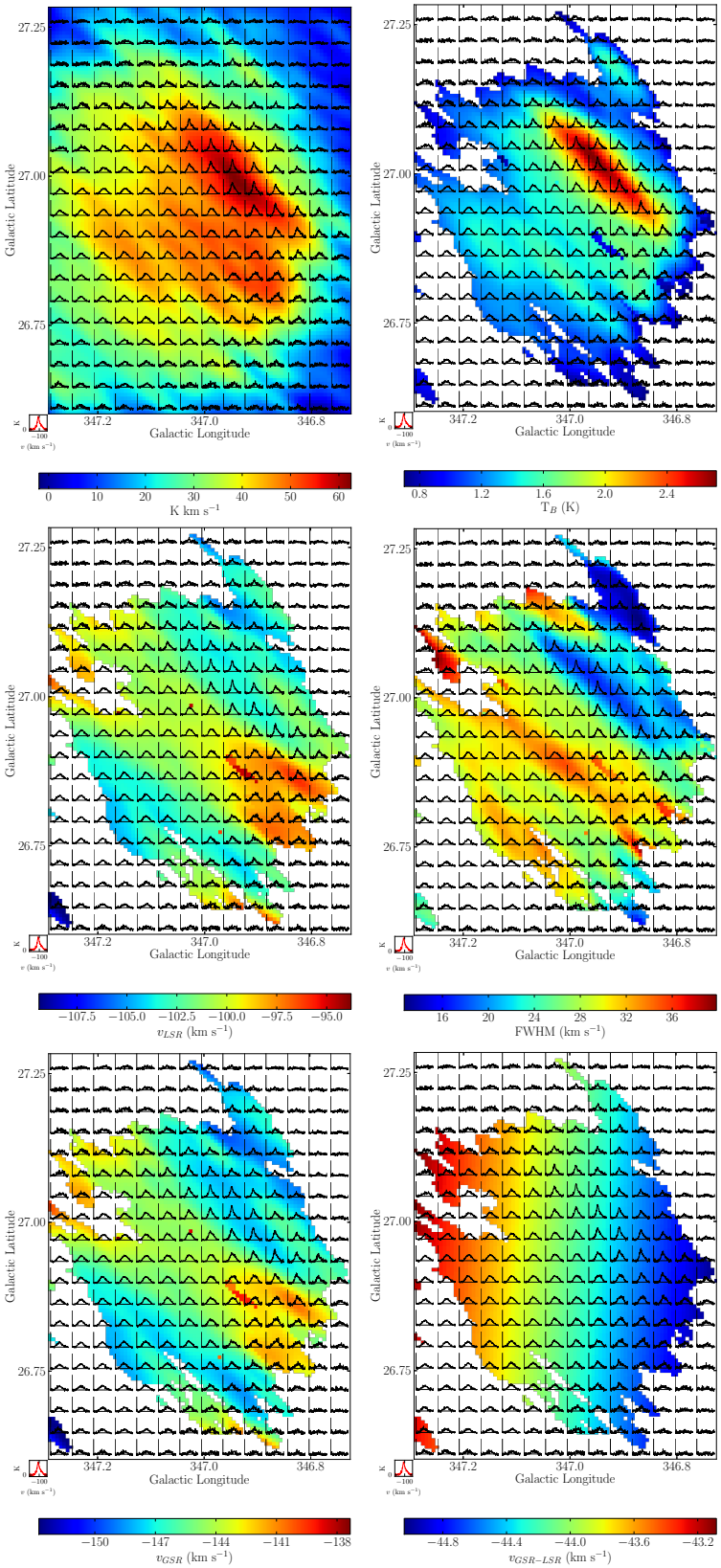

Figure 5.24: Spatial physical property plots of G347 in Galactic coordinates, across from top left: integrated intensity, fitted peak T_B, v_{LSR}, line-width, v_{GSR} and $v_{GSR-LSR}$. Pixels are masked below a peak T_B of 1.4 K in all plots except integrated intensity. Spectra are averaged over 6 pixels.

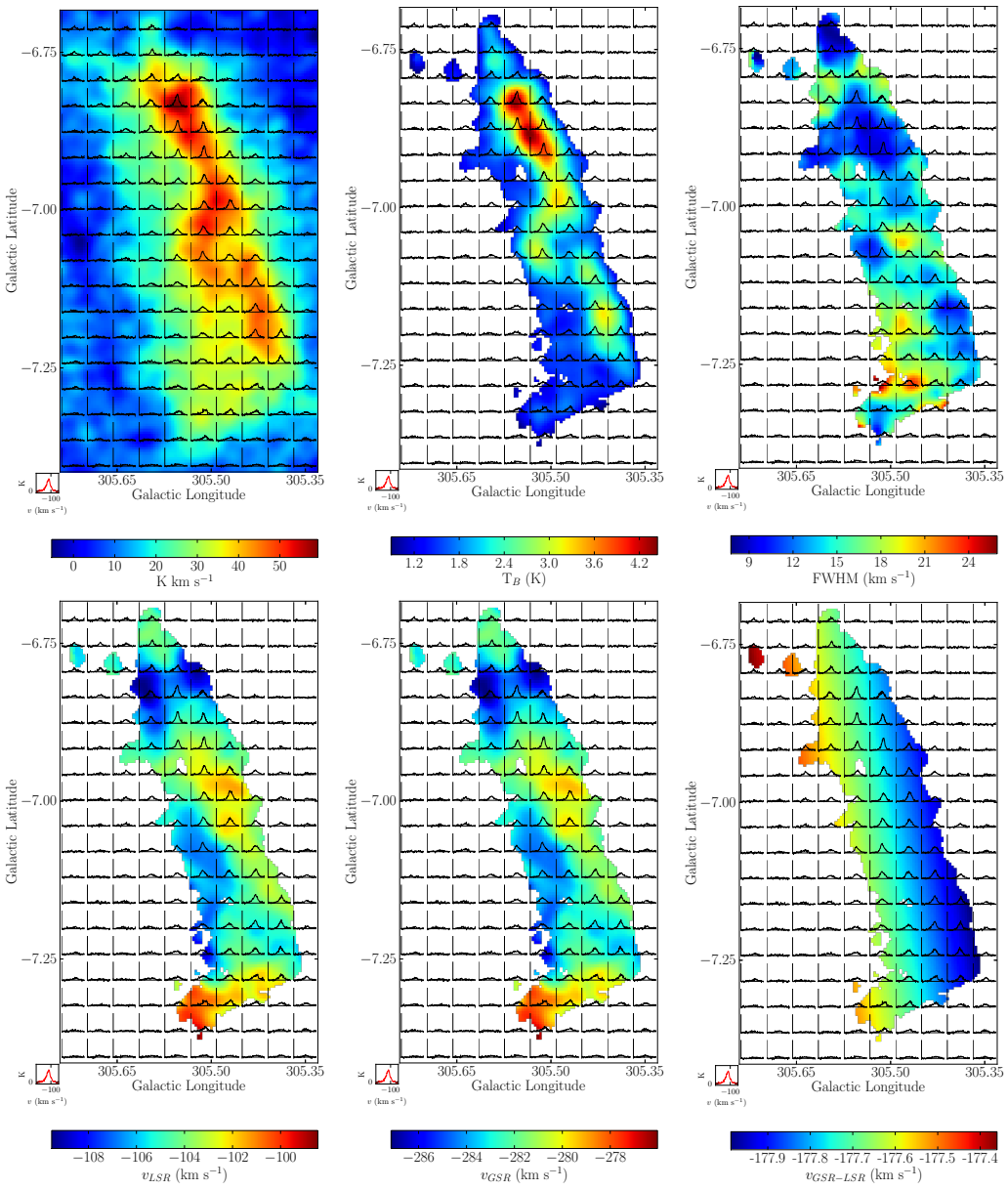

Figure 5.25: Spatial physical property plots of G305 in Galactic coordinates, across from top left: integrated intensity, fitted peak T_B, line-width, v_{LSR}, v_{GSR} and $v_{GSR-LSR}$. Pixels are masked below a peak T_B of 1.75 K in all plots except integrated intensity. Spectra are averaged over 10 pixels.

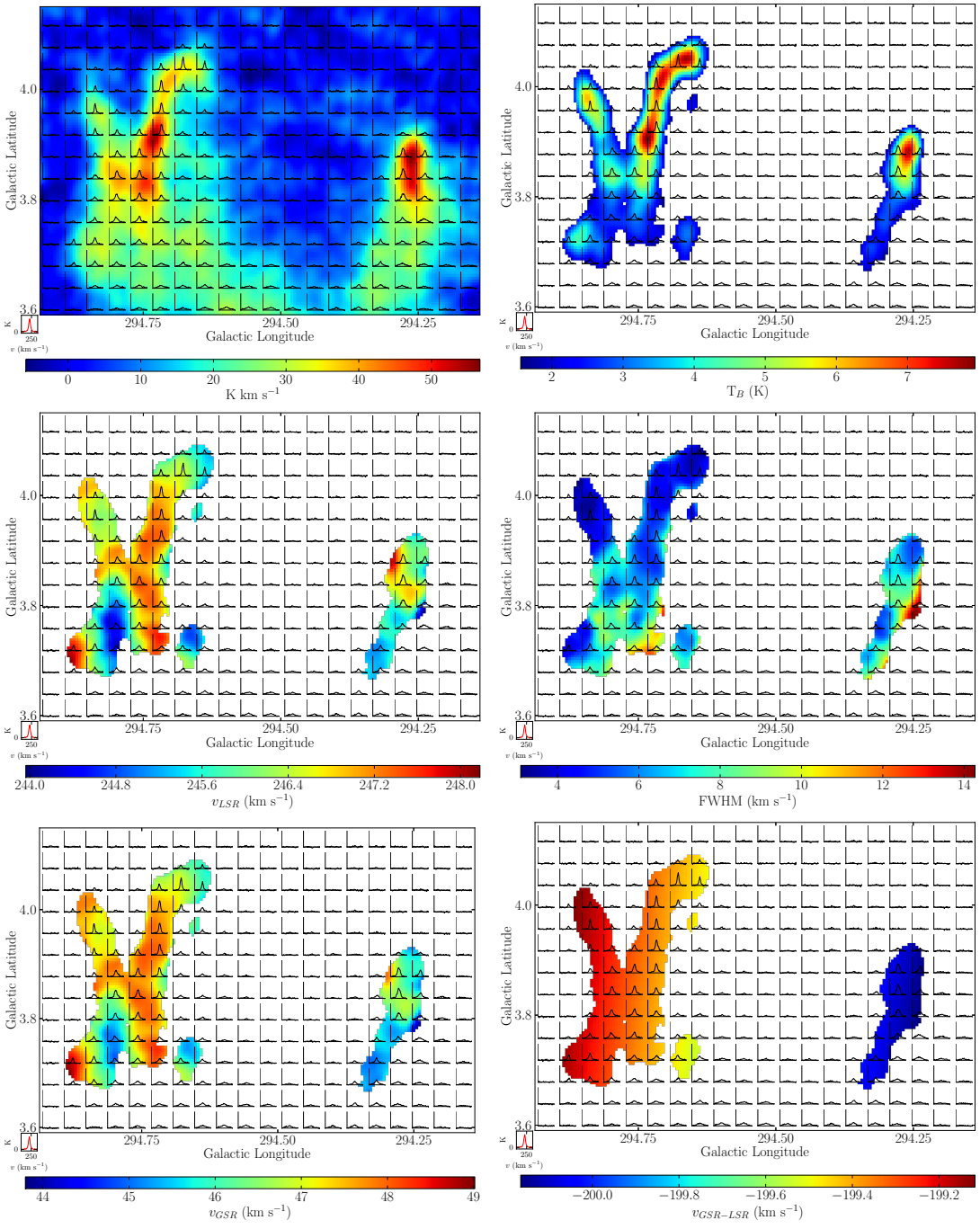

Figure 5.26: Spatial physical property plots of G294 in Galactic coordinates, across from top left: integrated intensity, fitted peak T_B, v_{LSR}, line-width, v_{GSR} and $v_{GSR-LSR}$. Pixels are masked below a peak T_B of 2.5 K in all plots except integrated intensity. Spectra are averaged over 8 pixels.

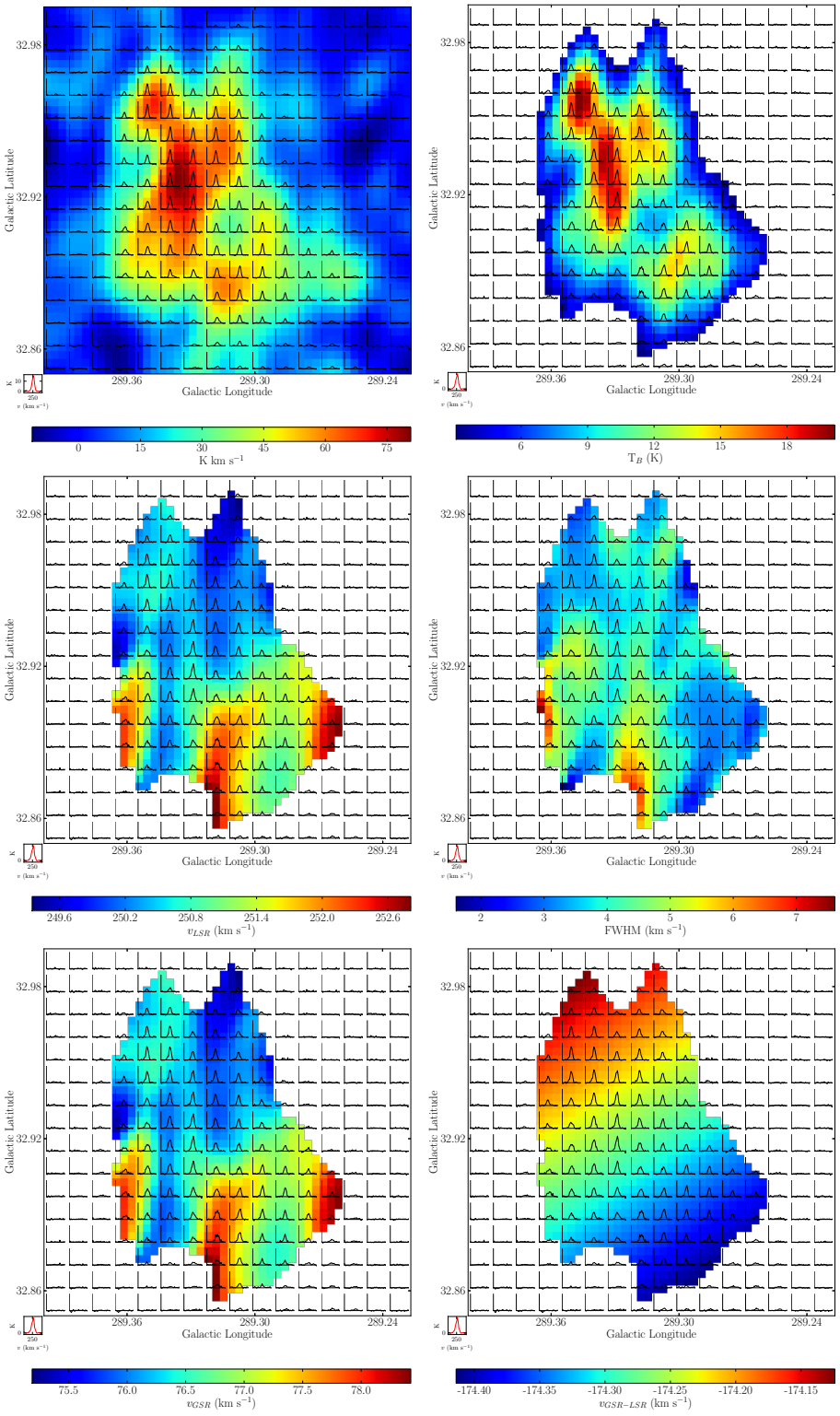

Figure 5.27: Spatial physical property plots of G289 in Galactic coordinates, across from top left: integrated intensity, fitted peak T_B, v_{LSR}, line-width, v_{GSR} and $v_{GSR-LSR}$. Pixels are masked below a peak T_B of 4.5 K in all plots except integrated intensity. Spectra are averaged over 3 pixels.

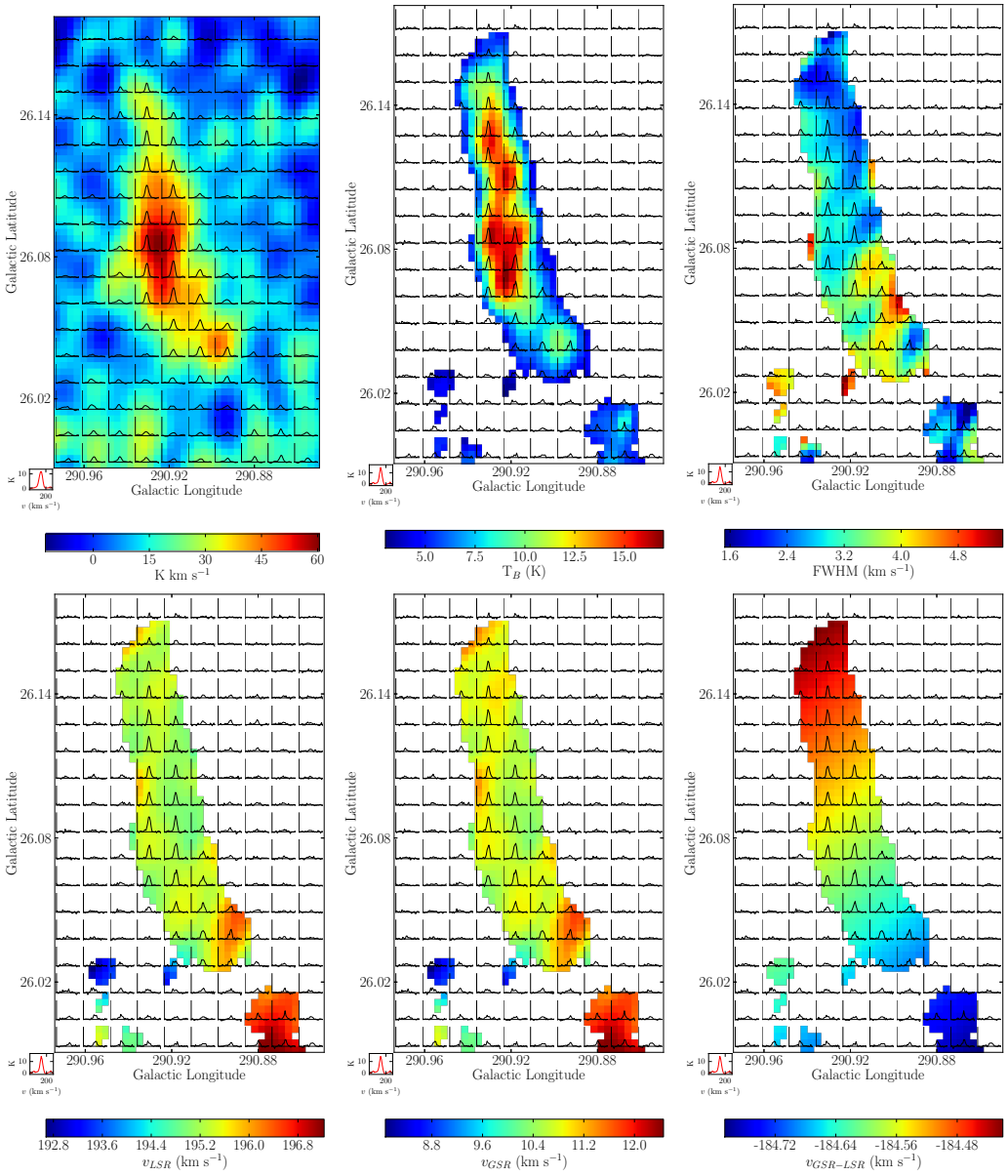

Figure 5.28: Spatial physical property plots of G291 in Galactic coordinates, across from top left: integrated intensity, fitted peak T_B, line-width, v_{LSR}, v_{GSR} and $v_{GSR-LSR}$. Pixels are masked below a peak T_B of 5.25 K in all plots except integrated intensity. Spectra are averaged over 4 pixels.

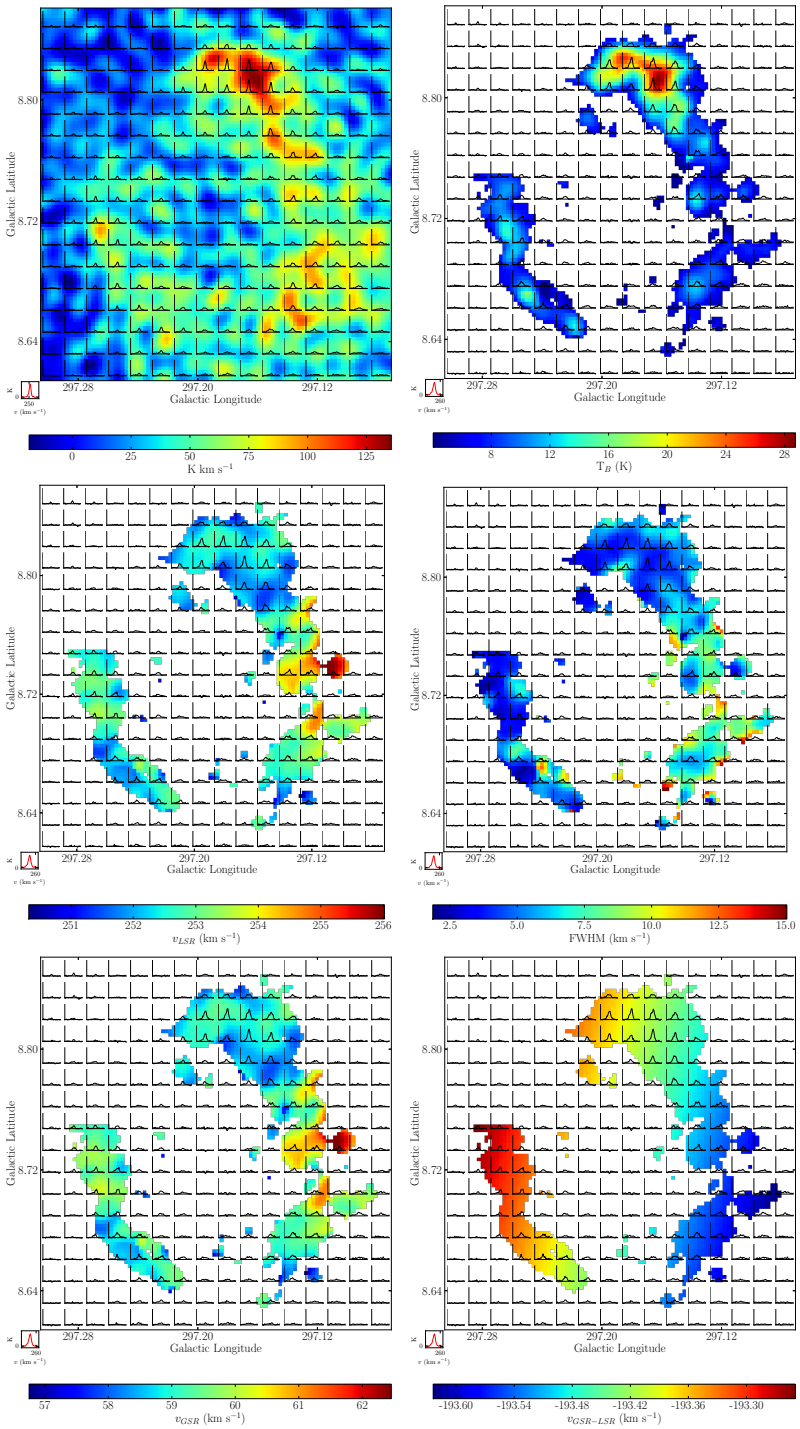

Figure 5.29: Spatial physical property plots of G297 in Galactic coordinates, across from top left: integrated intensity, fitted peak T_B, v_{LSR}, line-width, v_{GSR} and $v_{GSR-LSR}$. Pixels are masked below a peak T_B of 8.0 K in all plots except integrated intensity. Spectra are averaged over 6 pixels.

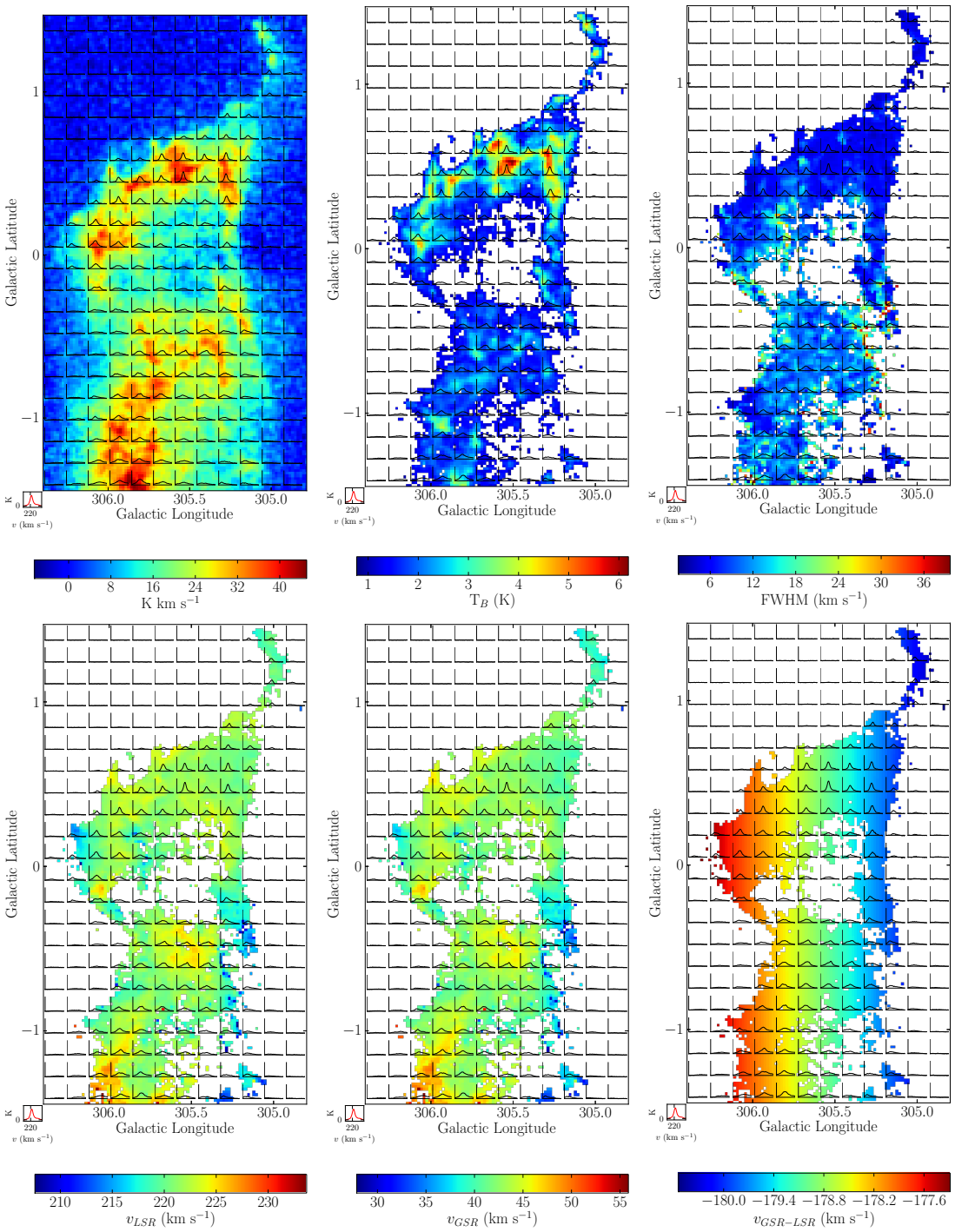

Figure 5.30: Spatial physical property plots of G306 in Galactic coordinates, across from top left: integrated intensity, fitted peak T_B, line-width, v_{LSR}, v_{GSR} and $v_{GSR-LSR}$. Pixels are masked below a peak T_B of 1.5 K in all plots except integrated intensity. Spectra are averaged over 8 pixels.

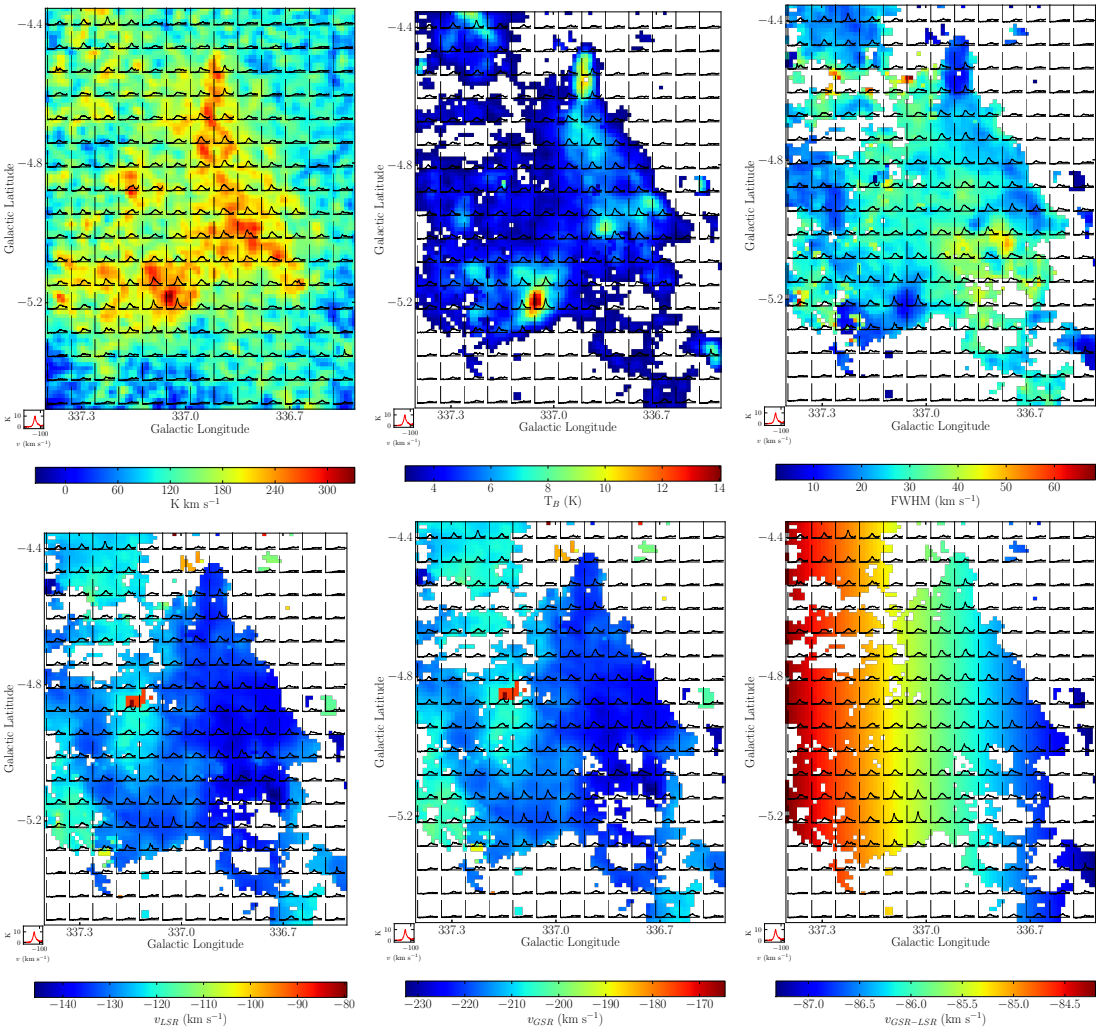

Figure 5.31: Spatial physical property plots of G335a in Galactic coordinates, across from top left: integrated intensity, fitted peak T_B, line-width, v_{LSR}, v_{GSR} and $v_{GSR-LSR}$. Pixels are masked below a peak T_B of 3.0 K in all plots except integrated intensity. Spectra are averaged over 6 pixels.

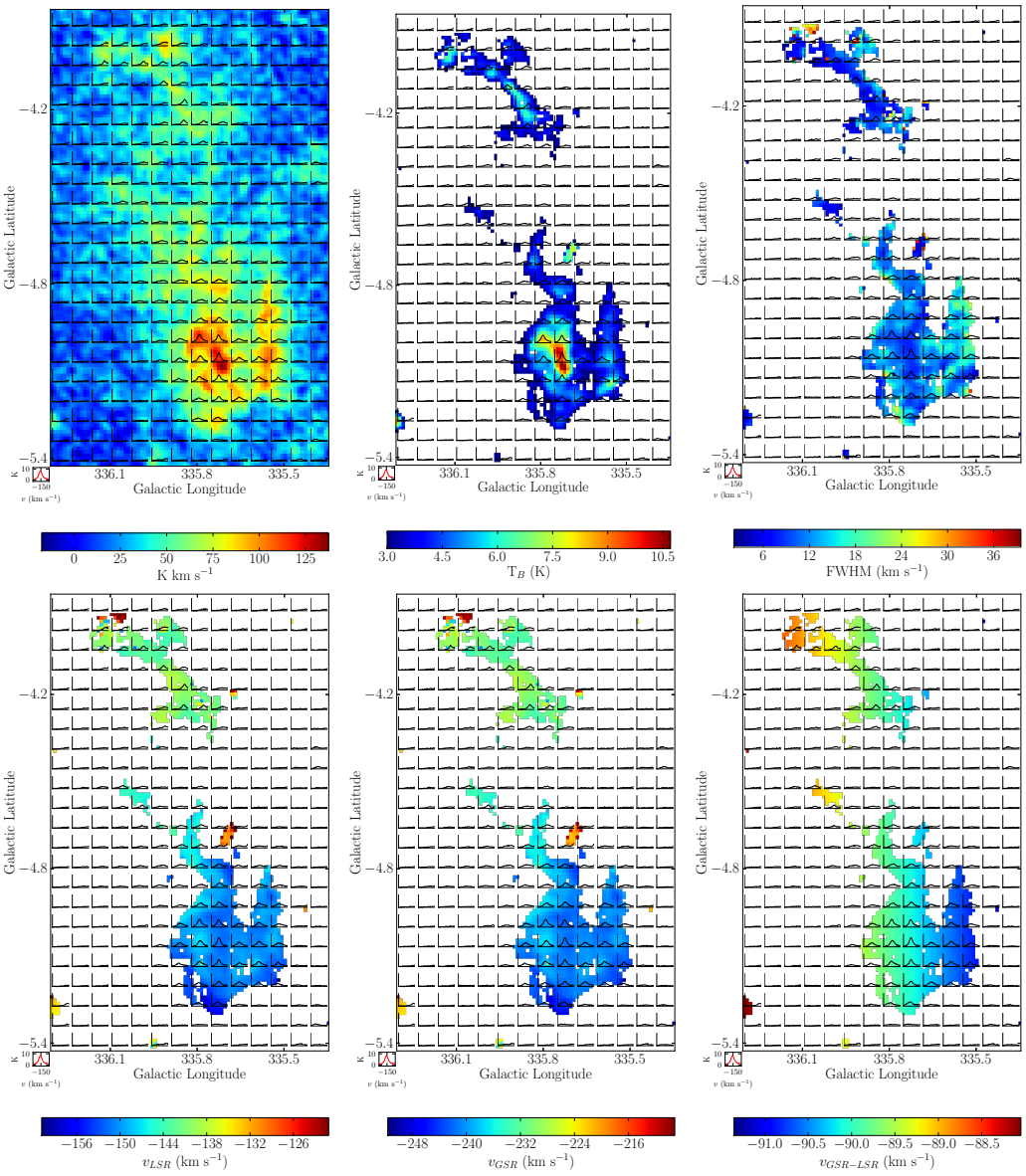

Figure 5.32: Spatial physical property plots of G335b in Galactic coordinates, across from top left: integrated intensity, fitted peak T_B, line-width, v_{LSR}, v_{GSR} and $v_{GSR-LSR}$. Pixels are masked below a peak T_B of 3.0 K in all plots except integrated intensity. Spectra are averaged over 6 pixels.

Spatial physical property plots

Figures 5.17 to 5.32 were produced using VizSpec, which was specifically developed for this project in order to be able to map the changes in physical properties across clouds. As all the clouds in our sample show evidence of interaction, we expect to see spatial variation in measurable physical properties such as the brightness temperature T_B and the FWHM line-width. Plotting spectra across the clouds is a straightforward way to visualise this spatial variation. All plots were made using the combined single-dish/interferometric data for clouds as shown in Figures 5.2 to 5.16.

The top-left plot in each figure shows the spectra across the integrated-intensity map of the cloud, with no masking. Each following plot is masked below an independent cutoff T_B, in order to show only the brightest relevant pixels to the cloud. As the property maps involve fitting the properties of the spectra at each pixel, we incorporate further masking of any fits with a FWHM < 1.5 km s^{-1}, a FWHM > 40 km s^{-1}, a peak T_B < the noise level specified for that cloud, or a fitted T_B < half of the noise level. The specific T_B cutoff for each cloud is given in the caption of the figure. Only the fitted properties of the unmasked pixels were used for later analysis of the cloud properties. In the case of the data for G289, G291 and G297, we smoothed the integrated-intensity map with a Gaussian kernel to reduce noise. We included velocity maps relative to both the Local Standard of Rest (v_{LSR}) and the Galactic Standard of Rest (v_{GSR}) for comparison, and included a map of $v_{GSR} - v_{LSR}$, which is the term (220 cos b sin l) and helps identify potential projection effects on the measured velocity gradients.

Qualitatively, some trends become clear from these plots. Clouds in the sample thought to be extragalactic in origin tend to have small FWHM < 10 km s^{-1} as well as very little spread in the distribution of FWHM. Conversely, clouds thought to be Galactic in origin have much larger spreads in their FWHM distributions, with fitted line-widths from ~5 km s^{-1} up to > 30 km s^{-1}. We can also see a difference in the velocity of the fitted peak amongst the two samples, which is traced by the fitted v_{LSR} and v_{GSR}. The extragalactic clouds tend to have a dispersion in velocity of ~5 km s^{-1} or less, while we see dispersions in velocity for Galactic clouds of ~10 km s^{-1} or more. An exception to this is G38, which was observed as part of the GCN sample but based on its line-width distribution and velocity dispersion appears to have physical properties similar to clouds of Galactic origin. Given that GCN is defined by having negative velocities in the vicinity of the Galactic Centre at relatively high v_{LSR}, it is highly possible that a Galactic cloud could be incorporated into the sample; we consider the case of G38 in further analysis below. Conversely, G5, which fell outside of the GCN spatial/spectral range defined by Wakker & van Woerden (1991), appears to have more in common with G14 and G20 than with Galactic clouds based on its narrow linewidths and small velocity dispersion.

Analysis of the two regions: G335 and G306

We performed a separate analysis on the two large regions, G335 (the two cloudlets above a known star-forming region) and G306 (the Leading Arm cloud currently interacting with the Galactic disk), due to their extended angular size (2° × 1.5° and 2° × 3° respectively). In the case of G306, we included in the analysis spectra with a brightness temperature above 1.5 K. Due to the more confused emission associated with G335 as well as nearby Galactic emission, we only included spectra with a brightness temperature above 4 K. This limit resulted in a total of 41371 spectra across G306, and 19939 spectra across G335. Each spectrum was passed through a fitting pipeline, where both a single component and a two-component fit was attempted.

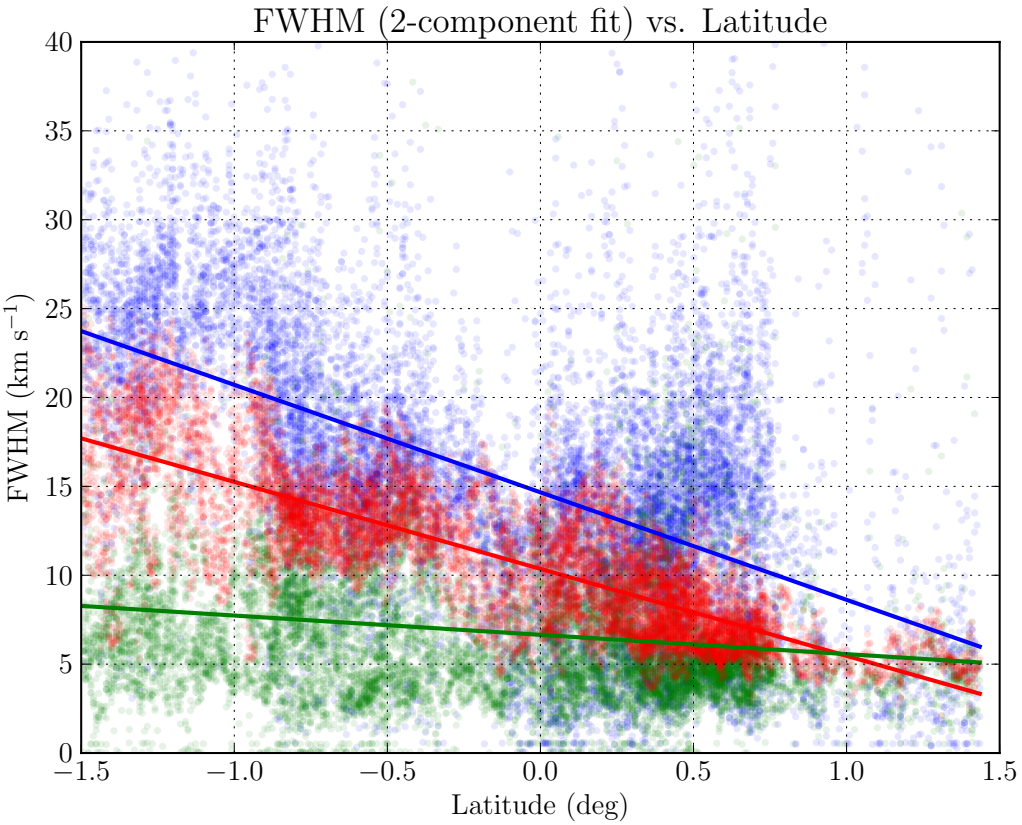

Figure 5.33: Line-width versus Galactic latitude for G306. Shown is the distribution of line-width for a single component fit (red), the narrow component of a two-component fit (green) and the broad component of a two-component fit (blue), with a line fitted through the points in their respective colours. G306 shows an overall increase in line-width with decreasing latitude, which is opposite to the direction of motion. When fit with two-components, the narrow component remains fairly constant at 5–10 km s^{-1} which may indicate that this line-width is intrinsic to the cloud rather than as a result of its interaction with the disk.

In both cases, spectra with a fitted FWHM $<$ 2 km s^{-1} were not included in the sample, as these widths would not be physical given the spectral resolution of the data. For G335, we also implemented a FWHM cutoff at 100 km s^{-1} to reduce susceptibility to Galactic emission or to components sitting on top of broad Galactic wings. A fitted peak brightness temperature cutoff of 1.5 K was kept for G306, while the fitted brightness temperature cutoff was 3 K for G335. The RMS for G306 was ~0.3 K, making this a 5σ cutoff, while the RMS for G335 was ~0.5 K making this a 6σ cutoff. These brightness temperature limits applied to the single component fit, while the two-component fit only had to have components summing to the respective cutoffs. In the case of a two component fit, we removed spectra that were 'confused': if the FWHM of one component was $<$ 2 km s^{-1} while the fitted T_B of the other component was less than the brightness temperature cutoff. As G306 is an interacting HVC at high velocities relative to Milky Way gas, it was useful to implement a velocity criterion such that only spectra with fitted $|v_{LSR}$ − 225 km s$^{-1}| <$ 25 km s^{-1} were included, thus ensuring that the fitted components were within 50 km s^{-1} of the systemic velocity of the cloud. This could not be done for G335, due to the lack of a clearly definable systemic velocity.

We plot the line-widths of each region as a function of latitude in Figures 5.33 and 5.34. We show the results of the single component fit in red, and components of the

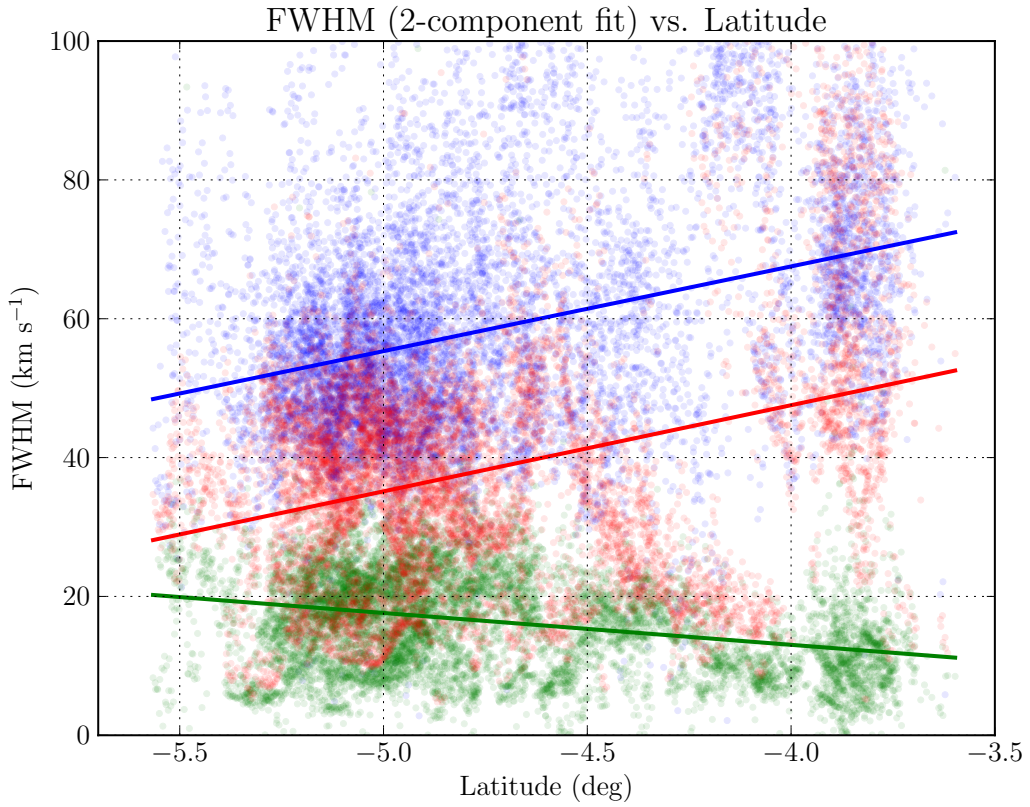

Figure 5.34: Line-width versus Galactic latitude for G335. Shown is the distribution of line-width for a single component fit (red), the narrow component of a two-component fit (green) and the broad component of a two-component fit (blue), with a line fitted through the points in their respective colours. G335 has more complex line-width trends than G306. The line-width overall increases in width with decreasing latitude, and if the clouds are from the Galactic disk, then this is opposite to the direction of motion as with G306. However, the narrow component broadens with decreasing latitude, with both components approaching line-widths of ~30 km s^{-1} with increasing height above the disk.

two-component fit as blue and green. In G306, we see a strong trend with increasing Galactic latitude, particularly in the single component fit. The narrowest line-widths are seen at positive latitudes, while the broadest line-widths occur at the most negative latitudes. When we decompose the spectra into a two-component fit, we see that the broad component (blue) decreases with latitude, while the narrow component (green) is fairly constant with latitude.

This result suggests that the broad component is primarily where we can detect evidence of the interaction of G306 with the Milky Way disk, such that the broadest line-widths occur in the wake of the cloud. In this case, we have prior knowledge that G306 is indeed moving from negative to positive latitudes based on both the location of the Magellanic clouds and on its evident interaction with nearby Milky Way gas at lower velocities. Interestingly, the consistent presence of a narrow component throughout the cloud may indicate that emission at line-widths of 5–10 km s^{-1} is intrinsic to G306 rather than having been formed as a result of its passage through the disk of the Milky Way.

We have included a plot showing all three components (single and the two-component fit) on the same plot, as well as a linear fit to the data to show the general slope. These fits confirm what we can see in the data: both the single component (which is dominated by

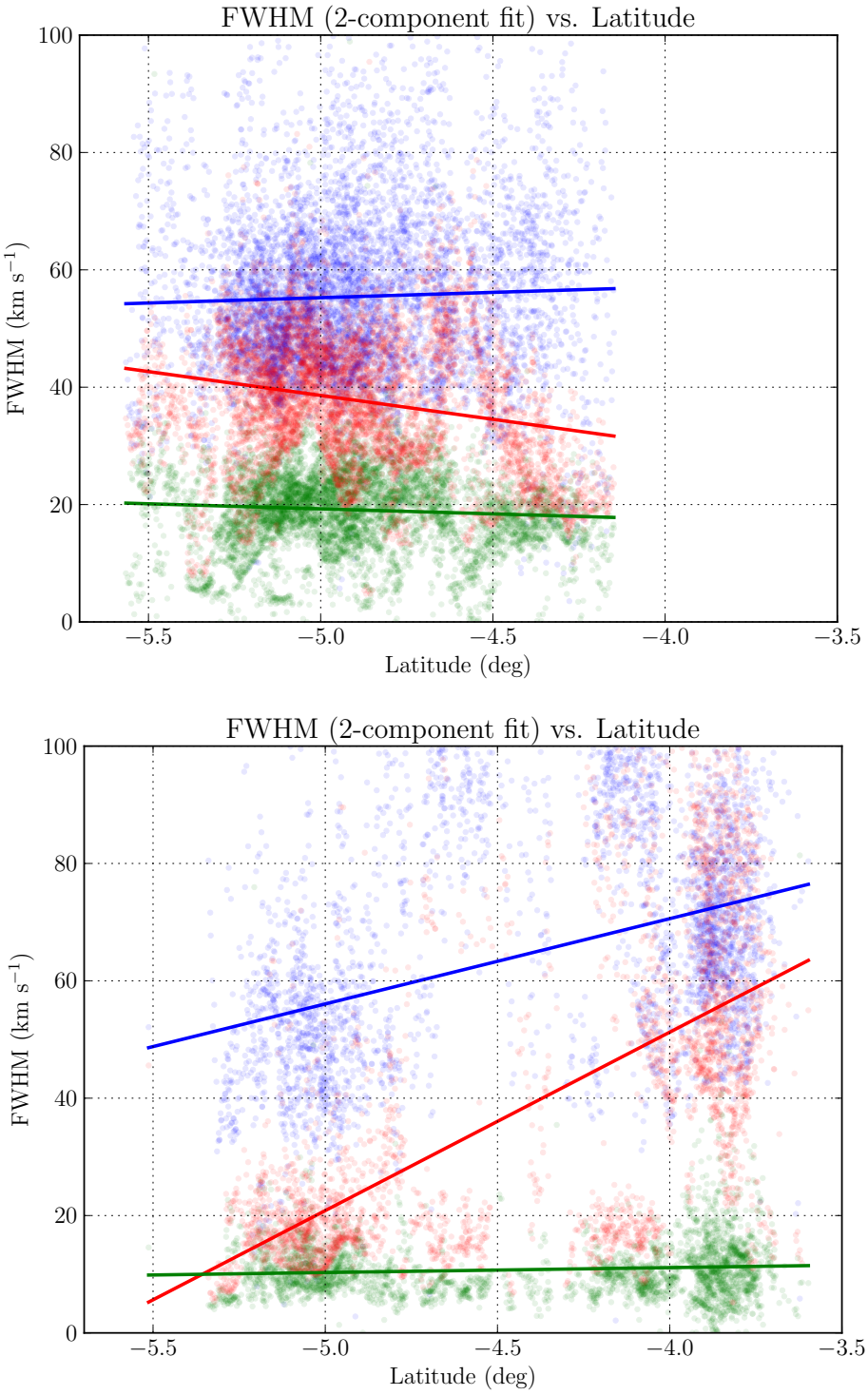

Figure 5.35: Line-width versus Galactic latitude for G335, separated into each cloudlet by a dividing line of $l = 336.4°$. Shown is the distribution of line-width for a single component fit (red), the narrow component of a two-component fit (green) and the broad component of a two-component fit (blue), with a line fitted through the points in their respective colours. The complexity apparent in Figure 5.34 is reduced to an extent by separating into the left and right clouds. G335-L (top) features broader, constant line-widths while G335-R (bottom) has a gradient of increasingly broad line-width with decreasing latitude and a constant narrow component.

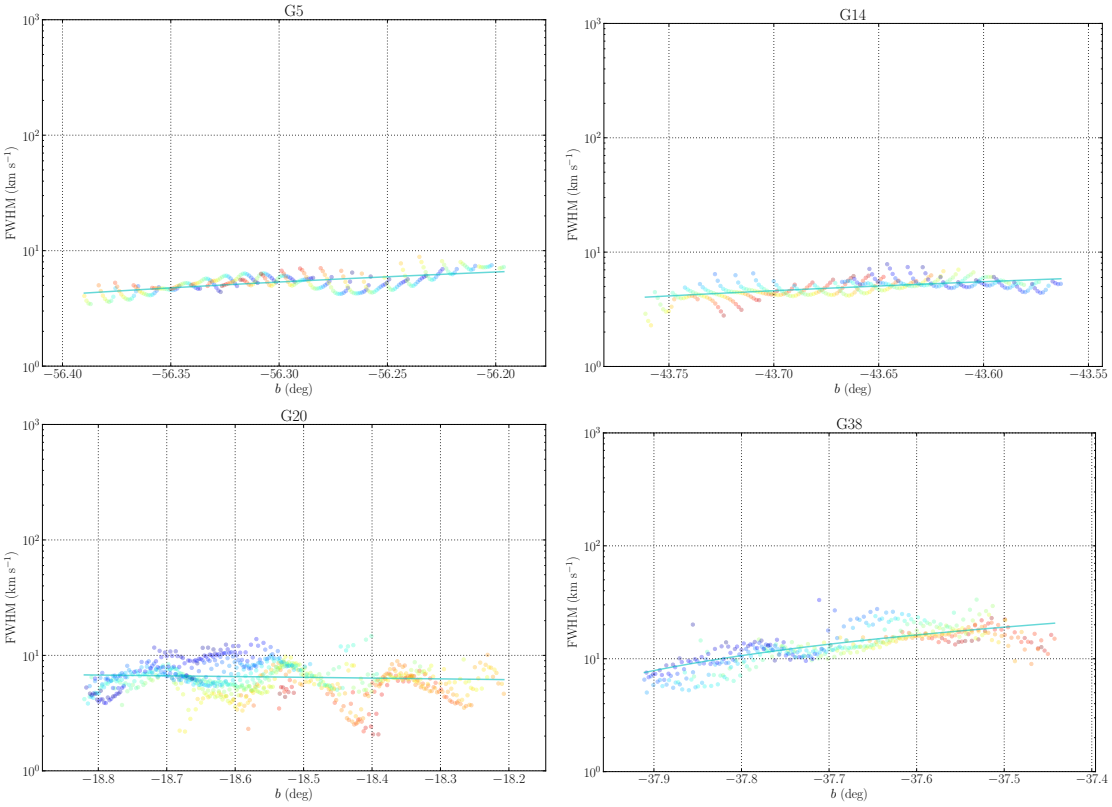

Figure 5.36: Scatter plot of line-width versus Galactic latitude for GCN clouds: G5, G14, G20, G38. Each point represents the measured line-width at a given pixel in the regridded Galactic coordinate cubes of each cloud. A straight line is fitted through each line-width distribution to indicate the overall trend in line-width with latitude. The points are colour-coded by their relative longitude across the cloud, where blue corresponds to the minimum longitude and red corresponds to the maximum longitude.

whichever component is more prominent in a given spectrum) and the broad component decrease in line-width with latitude, while there is an additional narrow component of fairly consistent line-width throughout.

The trends with G335 are not as clear. We see overall much broader line-widths, as well as an extremely messy distribution of line-width with latitude. This is partly due to the more confused and complex spectral structure of gas associated with G335, and partly due to errors in the spectral fitting as a result of this complexity. There is evidence for a broadening of line-widths towards more negative latitudes, away from the Galactic disk, in both the single-component and the broad component. With the narrow component, unlike G306, we see a slight broadening of line-widths towards negative latitudes, from ~10 km s^{-1} to ~20 km s^{-1}.

In order to discern whether part of the confusion for G335 is due to the separate contributions of the two individual cloudlets, we performed the same analysis on spectra separated into each cloud at a dividing line of $l = 336.4°$. The results are shown in Figure 5.35. This separation removes some of the confusion apparent in Figure 5.34, revealing that G335-L (the left cloud, towards increasing Galactic longitudes) is dominated by broader and more constant line-widths than G335-R (the right cloud, towards decreasing Galactic longitudes), which has trends similar to G306 with narrower line-widths overall. G335-R appears explicable in a similar way to G306, with the expected direction of motion to

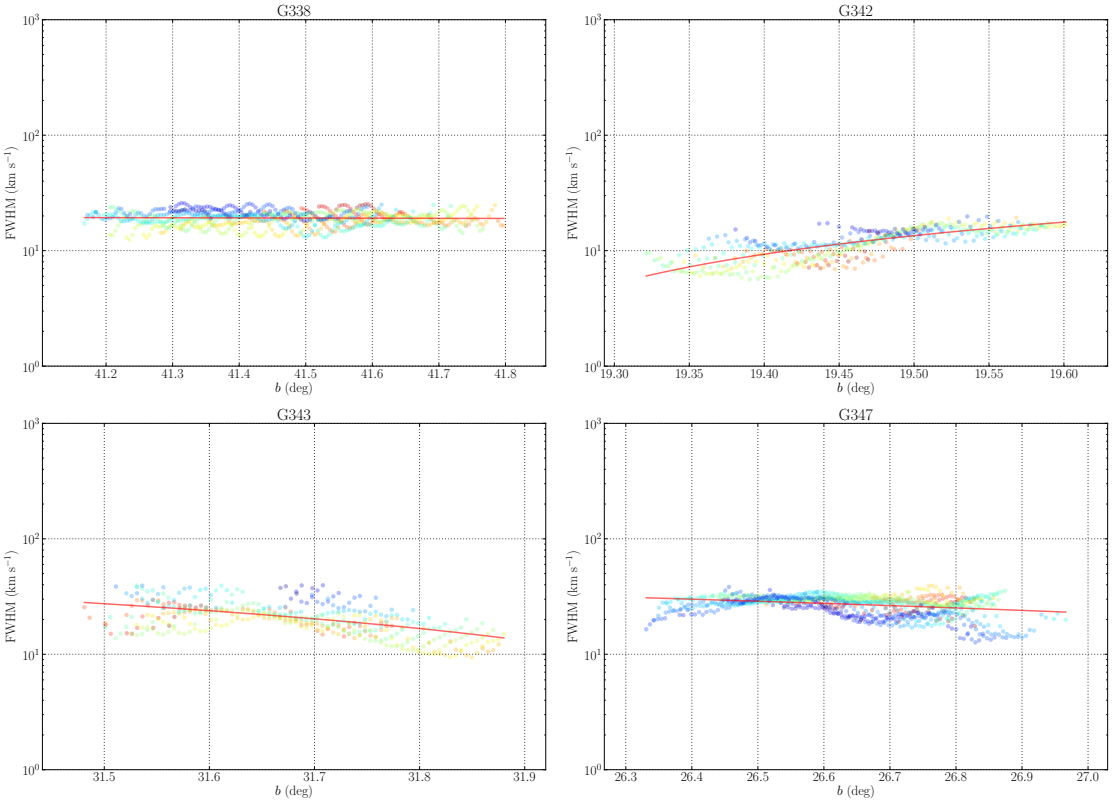

Figure 5.37: Scatter plot of line-width versus Galactic latitude for CL clouds: G338, G342, G343, G347. Each point represents the measured line-width at a given pixel in the regridded Galactic coordinate cubes of each cloud. A straight line is fitted through each line-width distribution to indicate the overall trend in line-width with latitude. The points are colour-coded by their relative longitude across the cloud, where blue corresponds to the minimum longitude and red corresponds to the maximum longitude.

be away from the Galactic plane leaving a trail of broader line-width gas behind. There is also a constant narrow component at a line-width of ~10 km s^{-1}. It is difficult to interpret G335-L due to line-width scatter and the lack of obvious trends with latitude. Both clouds, even as separated objects, have a large degree of scatter in their line-width trends compared with G306.

It is possible that errors on the fitting, due to the complexity of spectra, could be obscuring trends in the FWHM versus latitude plot for G335, even when divided into individual cloudlets. What we can see clearly is that the gas associated with G335, and with the star-forming disk from which it likely came, has extremely messy signatures, larger line-width dispersion and significantly more complex spectra that HVCs at velocities distinct from Milky Way gas. Future re-analysis of the spectra, with fitting to incorporate the effect of Milky Way emission and more accurately separating the effects of halo clouds from disk gas, may better confirm the trends we see for G335.

Trends in line-width versus Galactic latitude

In order to investigate the effect of the halo environment on the physical structure and properties of clouds, we apply a similar method as the previous section on all 15 clouds/regions in our sample. Specifically, we plot the FWHM (based on the single-component fit) as

a function of latitude, in order to visualise trends in line-width with height above the disk. We show the results for each cloud, grouped by complex/association, in Figures 5.36 to 5.39, where Figure 5.39 shows the results for the two large regions along with G305 (which is not associated with any particular region). Here we have included all measured line-widths from the non-masked pixels in Figures 5.17 to 5.29, and the line-widths measured as part of the analysis performed in Section 5.4. Each cloud has been fit with a first-order polynomial to show the general trend of FWHM with latitude. The apparent ripples in line-width are due to line-width variation across the cloud as a function of Galactic latitude, with the effect being more pronounced in clouds that are angularly smaller (resulting in less pixels per latitude slice) and clouds which feature sub-structure. In order to delineate this effect, the points in each scatter plot are coloured by the relative longitude across the given cloud, where blue corresponds to the minimum longitude and red corresponds to the maximum longitude.

In the majority of GCN and LA clouds, we see two striking trends: 1) a decrease in line-width with increasing height above the disk, and 2) a concentrated distribution of line-widths with the majority having FWHM $<$ 10 km s^{-1}. In the case of the Leading Arm, the clouds have leading narrow lines away from the direction of the Magellanic clouds, and hence in the direction of their motion. This trend is also seen in G306, although with much broader components present due to its current interaction with the disk of the Milky Way and also its earlier stage of evolution. The CL clouds, however, do not show any convincing evidence for consistent trend of line-width with Galactic latitude, with G338 showing no correlation, G343 and G347 showing a decrease in line-width with latitude and G342 showing an increase in line-width with latitude. What is consistent, however, is much broader line-widths across the clouds, with average FWHMs closer to 20–30 km s^{-1}. As seen in Section 5.4, the line-width distribution of G335 with latitude is extremely confused with a slight indication of lower FWHM at higher latitudes. G305, the cloud of unknown origin in our sample, shows a slight increase in line-width with increasing latitude and overall broad line-widths that appear consistent with the Galactic sample rather than the extragalactic sample.

We show just the fitted lines through each cloud/region in Figure 5.40. In both figures, we have 'normalised' the fitted line by the latitudinal length to 0° so that the lines can be easily compared in one plot. The bottom figure shows the absolute value of the fitted lines, in order to compare just the trend with increasing latitude irrespective of sign. Again, the clouds from the extragalactic sample (shown as blue and cyan lines) show the two clear trends of decreasing line-width with increasing latitude and narrow, concentrated line-width distributions. The two exceptions to this are G38 (which based on the results of our analysis so far may actually be Galactic in origin rather that being associated with GCN) and G306 (which is currently undergoing significant interactions with the Milky Way disk). In the Galactic sample (shown as red and yellow lines), we see broad line-widths and little evidence for strong trends in line-width versus latitude, which is, as suggested above, possibly telling of their more turbulent and disrupted origins. An exception to this is G342, which is the only cloud in the sample to have a prominent increase in line-width with increasing latitude. That said, we also note that G305 appears to have this trend to a less-exaggerated degree as well as broad line-widths.

KS two-sample test comparisons of physical properties

Finally, we investigate the distribution of measured physical properties amongst our sample by comparing individual clouds as well as comparing clouds against either the ex-

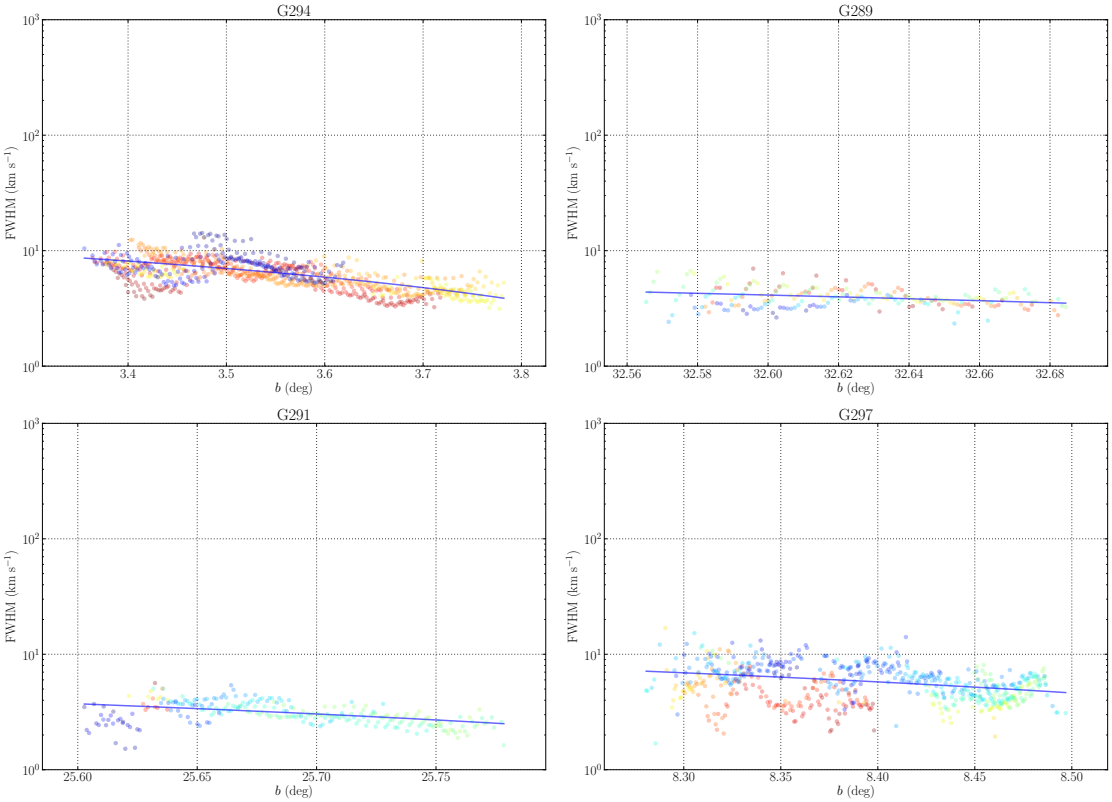

Figure 5.38: Scatter plot of line-width versus Galactic latitude for LA clouds: G294, G289, G291, G297. Each point represents the measured line-width at a given pixel in the regridded Galactic coordinate cubes of each cloud. A straight line is fitted through each line-width distribution to indicate the overall trend in line-width with latitude. The points are colour-coded by their relative longitude across the cloud, where blue corresponds to the minimum longitude and red corresponds to the maximum longitude.

tragalactic or Galactic population. We consider three physical properties measured in our clouds/regions: line-width, velocity and intensity. Specifically, we use the observed properties of FWHM, v_{LSR} and T_B. We use the Kolgomorov-Smirnov (KS) two-sample test for two sets of tests: 1) every cloud is compared with every other cloud, and 2) each cloud is compared against the overall Galactic and extragalactic distributions. The two distributions were formed by combining the individual distributions of all clouds of known extragalactic or Galactic origin, but without the line-width contribution of the cloud being tested to maintain the independence required for the KS statistic. We also excluded G335 and G306 due to their large angular size and hence large number of line-widths which would dominate the distribution, and G305 which is of unknown origin. Although it is possible based on previous analysis that G38 is in fact Galactic, we kept its original classification as part of GCN for the purpose of forming the overall distributions in order to avoid bias from previous analysis. Both FWHM and T_B distributions were used with their original values, but each v_{LSR} velocity distribution was normalised to 0 km s^{-1} to allow comparability of clouds at different velocities and to focus on the velocity dispersion rather than the velocities themselves.

The KS two-sample test works by comparing the cumulative distribution of two samples and measures the maximum difference between these two distributions. It then converts that difference into an estimated probability (p-value), which gives an indication of how

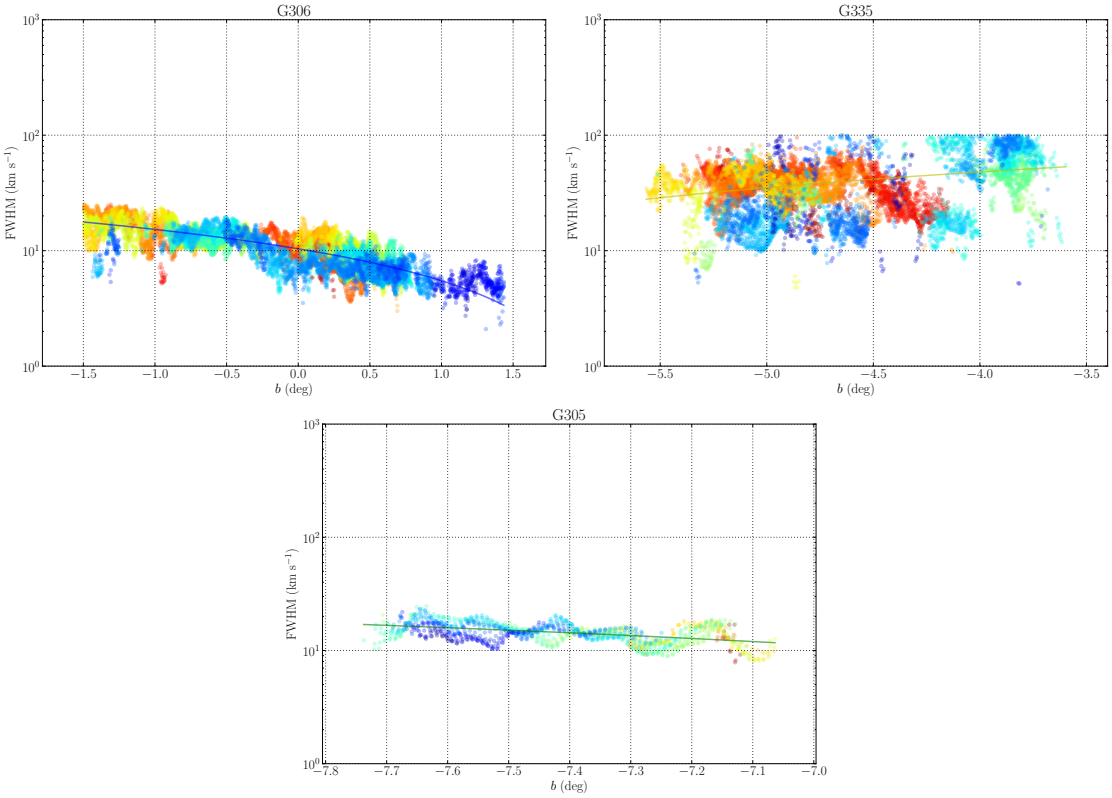

Figure 5.39: Scatter plot of line-width versus Galactic latitude for G306, G335 and G305. Each point represents the measured line-width at a given pixel in the regridded Galactic coordinate cubes of each cloud. A straight line is fitted through each line-width distribution to indicate the overall trend in line-width with latitude. The points are colour-coded by their relative longitude across the cloud, where blue corresponds to the minimum longitude and red corresponds to the maximum longitude.

likely the observed difference would be under the null hypothesis (assumption) that the two samples are drawn from the same underlying distribution. In our case, we are comparing clouds in order to see whether they are similar in the context of being drawn from either a Galactic or extragalactic distribution of line-width, velocity or brightness. Examples of cumulative distribution plots of line-width for different pairs of clouds are shown in Figure 5.41, to emphasise the diversity in cumulative distributions and resultant effect on p-value. The plotted cumulative distribution functions give p-values ranging from 0.27 down to an extremely small 5.1×10^{-110}. The extreme effect of relatively small differences on the order of magnitude of the p-value necessitated the consideration of the $|\log_{10} p|$-value for our sample of clouds. We consider limitations of this approach at the end of this section.

We show the results for both cloud-by-cloud and extragalactic/Galactic comparisons in Figures 5.42 to 5.47. Figures 5.42, 5.44 and 5.46 show the result of the cloud-by-cloud comparison for line-width, velocity and brightness temperature, with duplication around the diagonal to aid interpretation of results for a single cloud. Similarly, Figures 5.43, 5.45 and 5.47 show the distribution of properties assigned to either the extragalactic (blue) or Galactic (green) distribution (top) and the results for each cloud against the extragalactic and Galactic distributions (bottom). We have grouped the clouds into extragalactic and Galactic distributions along the axes of the plots where relevant, to highlight trends based on origin.

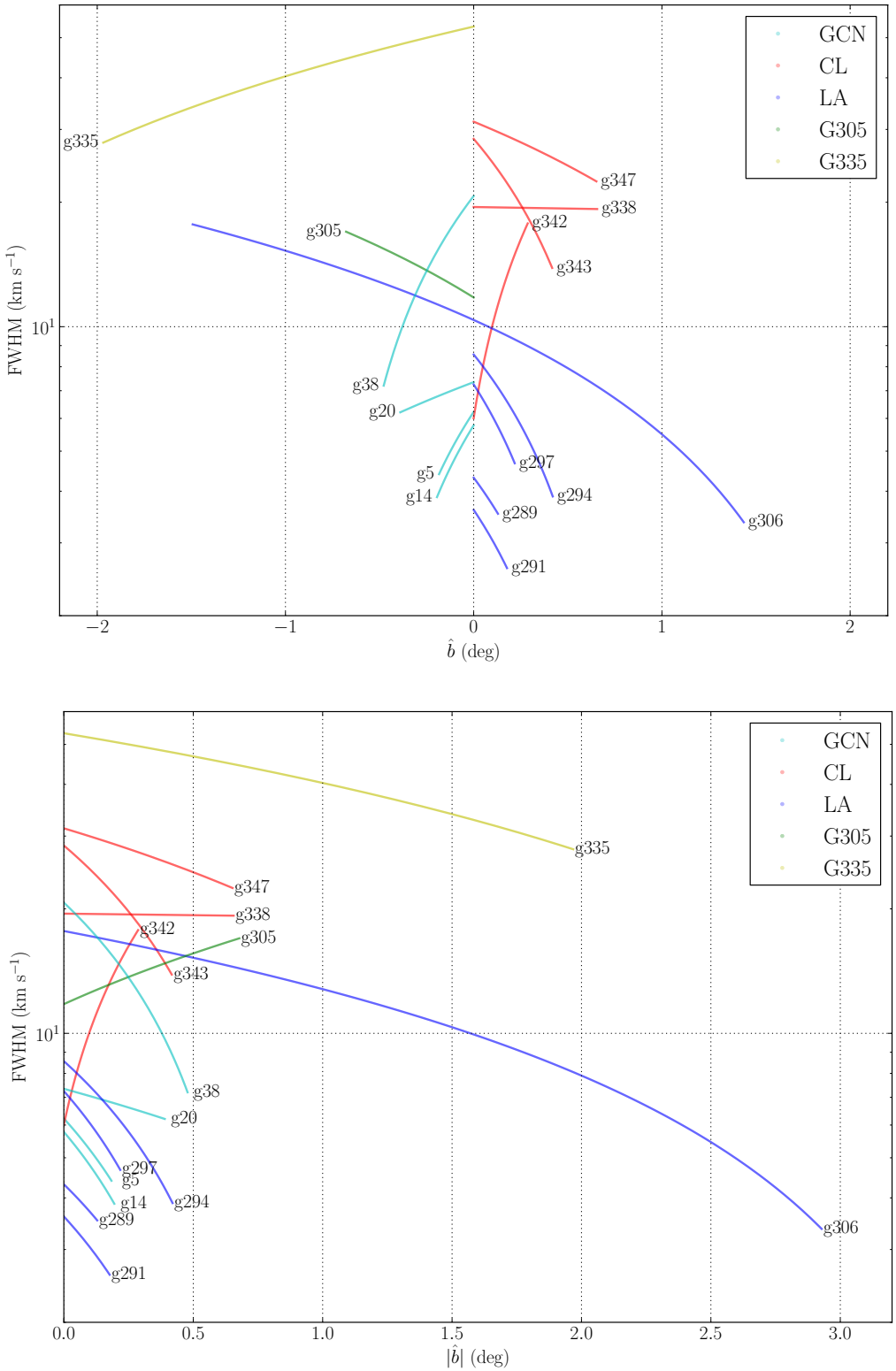

Figure 5.40: Fitted lines through each cloud in the sample, showing the overall trend of the sample with Galactic latitude. In both figures, we have 'normalised' the fitted line by the latitudinal length to 0° so that the lines can be easily compared in one plot. The bottom figure shows the absolute value of the fitted lines, in order to compare just the trend with increasing latitude irrespective of which side of the Galactic disk the clouds are on.

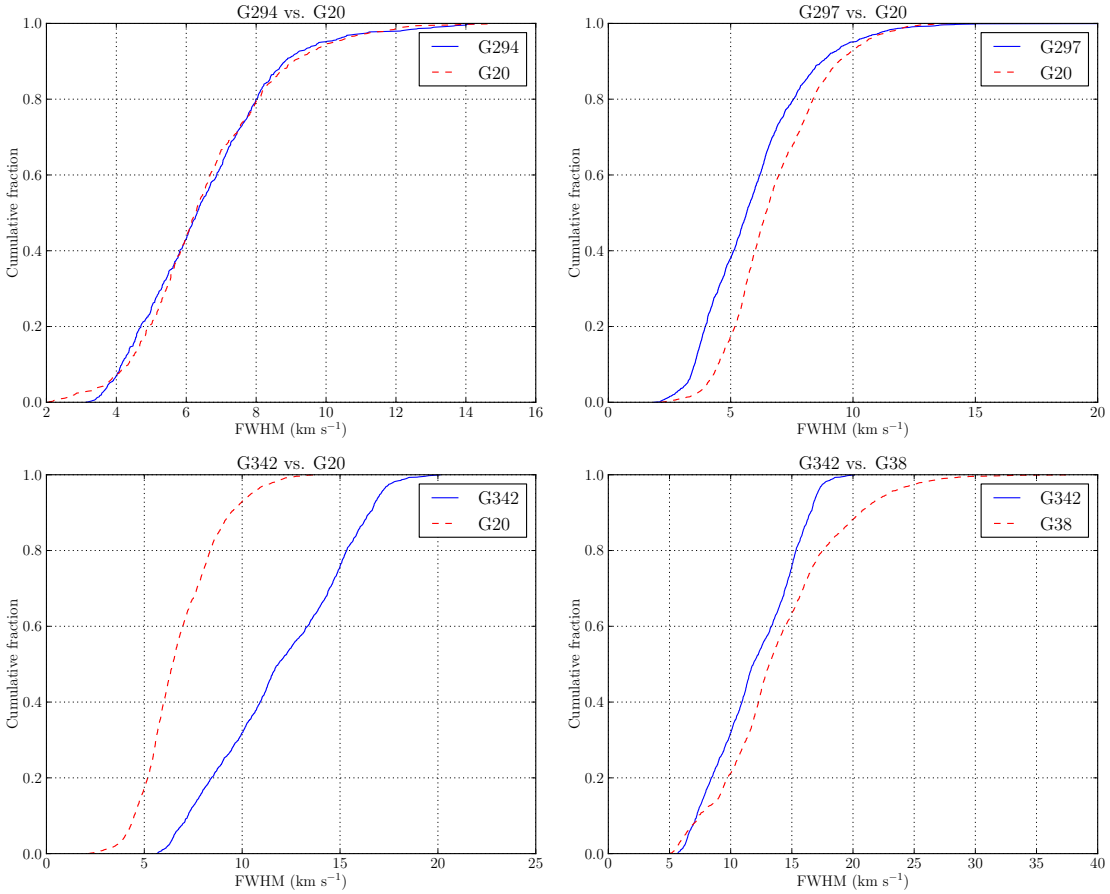

Figure 5.41: Examples of the cumulative distribution plots of line-width for different pairs of clouds, to show the diversity in cumulative distributions and resultant effect on p-value. The KS two-sample test measures the maximum difference between two cumulative distributions and converts it to a probability of this difference occurring under the null hypothesis that the two samples are drawn from the same parent distribution. The above differences between the plotted distributions give p-value probabilities of: 0.27 (G294 vs. G20), 7.7×10^{-12} (G297 vs. G20), 5.1×10^{-110} (G343 vs. G20) and 5.8×10^{-7} (G342 vs. G38). The extreme effect of relatively small differences on the order of magnitude of the p-value necessitated the consideration of the $|\log_{10} p|$-value for our sample of clouds.

Of the three physical properties we tested, line-width is the property which shows the most promise as a diagnostic. Figure 5.42 reveals a concentration of relatively high (green) p-values including the majority of the extragalactic population. There are two exceptions to this: G38, which we have already identified above as a potential contaminant cloud based on the analysis in Sections 5.4 and 5.4, and G306, which is distinct from the extragalactic population due to its current interaction with the disk and its large size. There is almost no similar trend for the Galactic clouds of our sample, although the p-values of G343 shows a clear agreement with the Galactic clouds and with G38, as well as evident similarity between G338/G343 and G342/G305. This is not surprising given our results above, which already showed that Galactic clouds have much more complex spectral structure than extragalactic clouds in our sample. We also note that G289 has shown no obvious physical difference to other LA clouds G291, G297 or G294, suggesting that it is likely to be part of the Leading Arm.

In Figure 5.43, we see a strong difference in the Galactic and extragalactic line-width

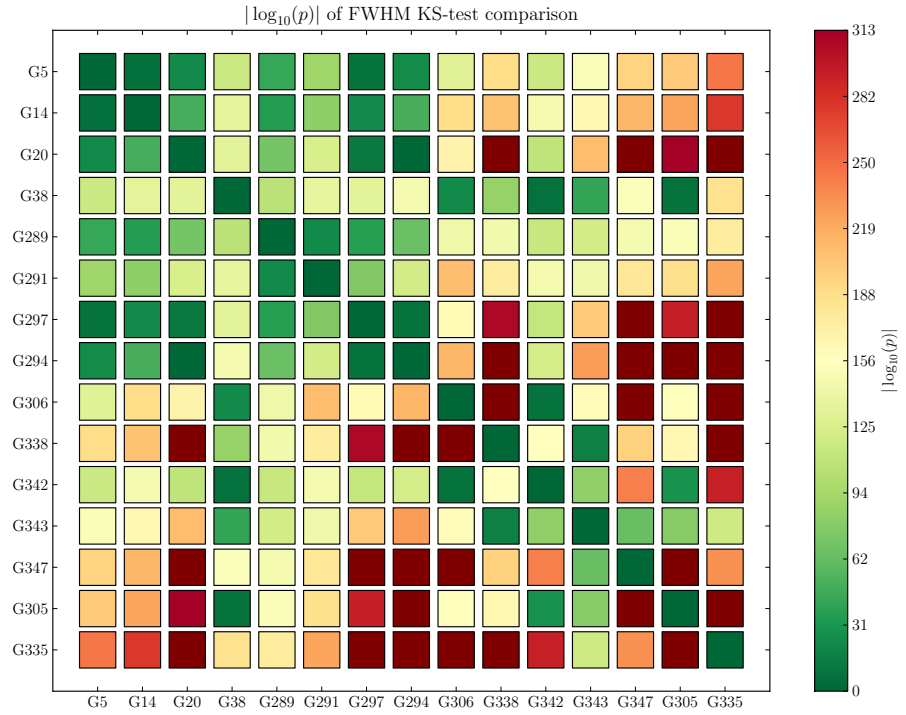

Figure 5.42: Cloud-by-cloud comparison of FWHM line-width. Each square is coloured based on the resultant $|\log_{10} p|$-value, with green indicating the most similar and red indicating the most different. Results are mirrored around the diagonal to aid interpretation of a particular cloud.

distributions formed, and find that the distribution test produces similar results to the cloud-by-cloud case. The extragalactic clouds (G5, G14, G20, G289, G291, G297, G294) are found to be in agreement with the extragalactic distribution, while the Galactic clouds have less clear distinction but typically show more agreement with the Galactic distribution. G38, again, is grouped into the Galactic distribution. G305 does not agree particularly well with either distribution in this case, but is more in favour of a Galactic origin. G306 and G335 agree with neither overall distribution, which is understandable given that both clouds have numerically large distributions and hence are strongly distinguished from the extragalactic and Galactic distribution as far as the KS two-sample test is concerned.

Both the v_{LSR} and T_B distributions are far less useful in terms of separating the two populations. Cloud-by-cloud, we see that neither physical property reveals any systematically accurate trends. The velocity distribution finds agreement in all extragalactic clouds, but also includes G38 (which we suspect to be Galactic), G338, G342 and G305. Conversely these is little to no trend evident for Galactic clouds. In comparing against the extragalactic or Galactic velocity distribution, we see a similar lack of accurate diagnosis, although G5, G14, G289 and G294 are more convincingly found to be associated with the extragalactic distribution and G306 is found to be more extragalactic than Galactic. In order to be able to compare the velocities across the clouds, we needed to 'normalise' the v_{LSR} distribution first. This involved shifting the distribution to be centred on 0 km s^{-1}. This enabled comparison but resulted in a large amount of overlap between the Galactic and extragalactic distributions, although their shape is quite different. This is likely the key reason that the v_{LSR} diagnostic fails in the distribution case, because it is probabilistically reasonable for clouds to be group into either distribution. The T_B cloud-by-cloud comparison finds similarities in clouds all over the place, which is likely a testament to the

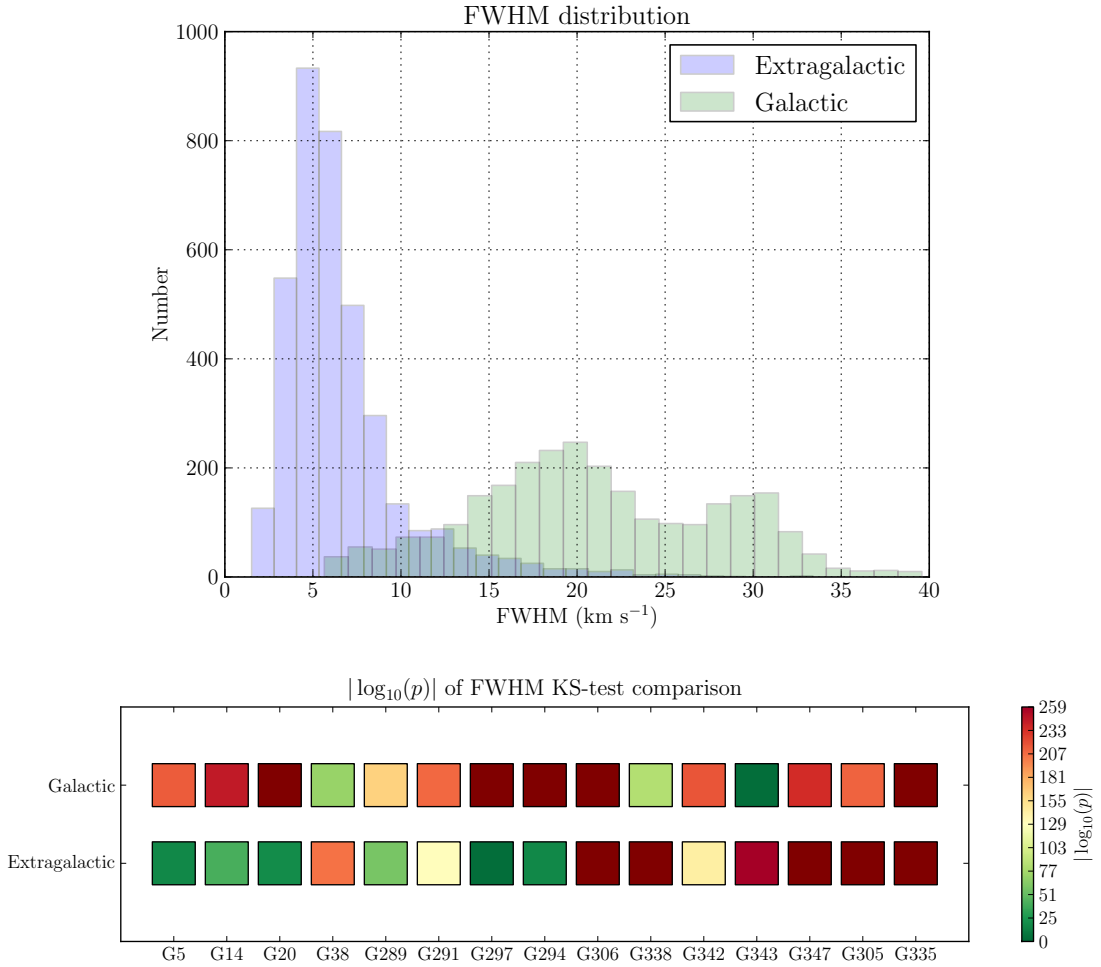

Figure 5.43: Overall FWHM line-width distributions for extragalactic (blue) and Galactic (green) clouds (top), and the results of comparing each cloud against these distributions (bottom). Each square is coloured based on the resultant $|\log_{10} p|$-value, with green indicating the most similar and red indicating the most different.

fact that we only observed clouds that were bright enough to be detected in their allotted amount of time (hence sharing similar intensities). This is similarly explicable when we look at the extragalactic and Galactic distributions, which completely overlap at $T_B <$ 5 K. Both v_{LSR} and T_B, at least as far as we have compared them, do not offer a reliable diagnostic for separating extragalactic and Galactic clouds.

We have made one key assumption in performing this analysis. The p-values associated with each of our comparisons are considerably lower than what would reasonably be considered evidence of cloud properties being drawn from the same distribution (e.g. typical values of $p > 0.05$). Our p-values are orders of magnitude below this number. Our current sample of clouds is not large, and the dispersion amongst their properties is considerable, both of which lead to very small p-values. The assumption we have made is that there is information contained within the order of magnitude of a resultant p-value, since the p-value is a quantitative measure of the difference between two populations; given the trends in p-value visible in Figure 5.41 with relatively small changes in cumulative distribution, this is not an extreme assumption to make. What is in question is whether it is valid to consider the implications of extremely small p-values. Based on

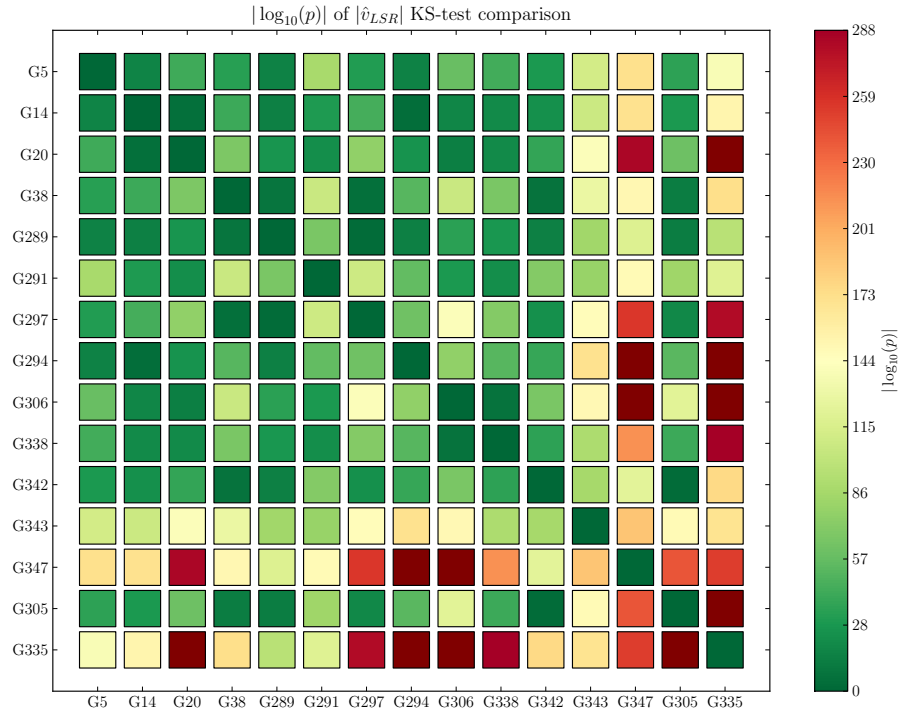

Figure 5.44: Cloud-by-cloud comparison of v_{LSR} velocity. Each square is coloured based on the resultant $|\log_{10} p|$-value, with green indicating the most similar and red indicating the most different. Results are mirrored around the diagonal to aid interpretation of a particular cloud.

our results so far, it appears that the relative order of magnitude of a p-value can potentially be used to determine information about populations within a sample even when the p-values are small.

This method, when applied to the FWHM line-width of clouds, accurately grouped the majority of extragalactic clouds together, was consistent with our previous findings that the Galactic distribution is much less internally coherent and identified G38 as a possible imposter in the extragalactic sample. Further, it revealed that both velocity and brightness are not particularly reliable methods of distinguishing clouds due to overlap in their distributions, which is in agreement with the expectation that both distributions are significantly more affected by the (unknown) distance of the cloud. The 15 clouds/regions used in this sample are only a small portion of the total gas present in the halo, and as such we have only probed a fraction of the true distribution of physical properties. The reliability of this method will be better determined with future measurements of cloud properties in different regions to our current sample, and the distributions will in addition become better defined for more accurate results.

Overall, our results suggest that the line-width distribution of an interacting HVC is the most likely physical property to aid diagnosis of the cloud's possible origin, and particularly may be able to tell if it is likely to come from an extragalactic origin consistent with the extragalactic clouds in our sample. Extending the sample to include clouds of varied location and at different stages of their evolution will help determine the reliability of this result, and combining our results with diagnostics inferred from other wavelengths such as optical and infrared will aid interpretation of clouds of unknown origin. Our findings of complex narrow/broad line structures within Galactic clouds appear at odds with the Galactic cold LVC population identified by Saul et al. (2012), most likely due to the larger

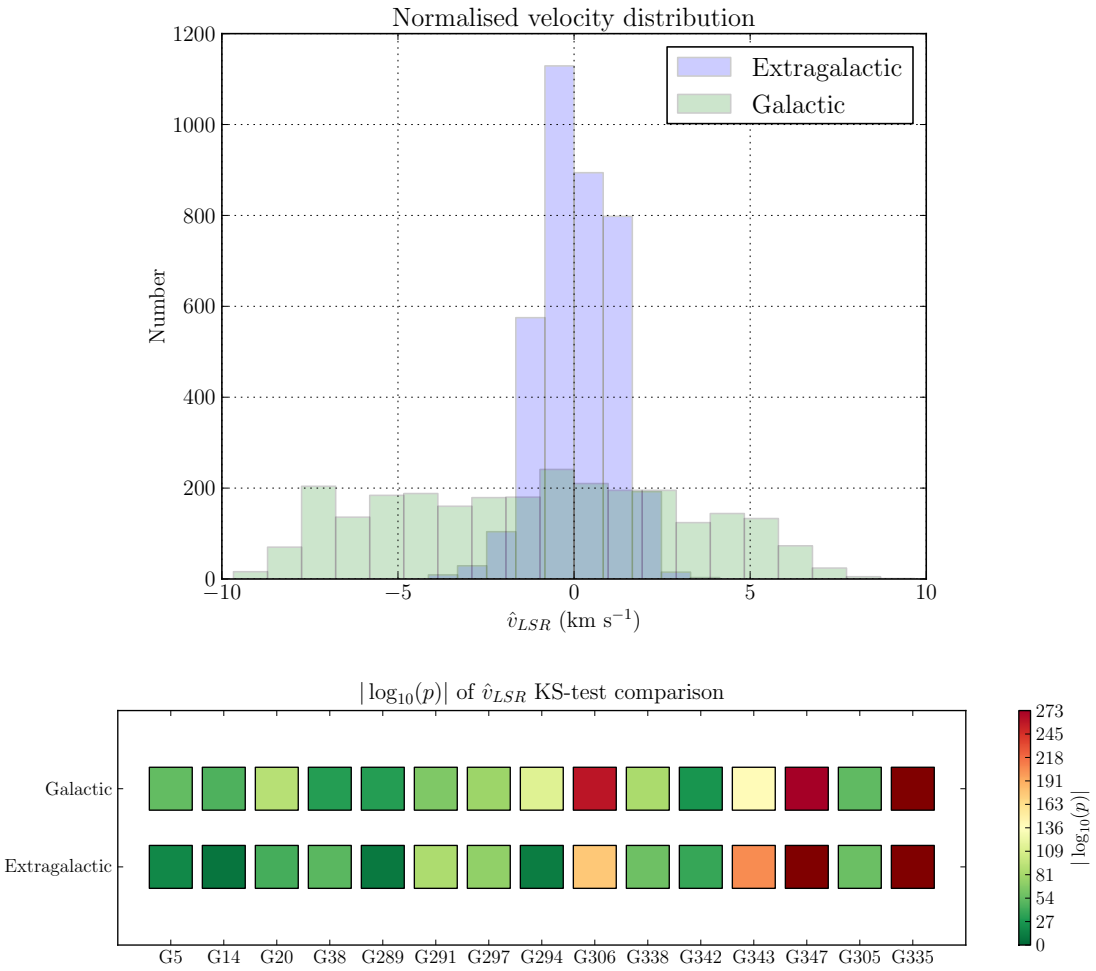

Figure 5.45: Overall v_{LSR} velocity distributions for extragalactic (blue) and Galactic (green) clouds (top), and the results of comparing each cloud against these distributions (bottom). Each square is coloured based on the resultant $|\log_{10} p|$-value, with green indicating the most similar and red indicating the most different.

angular size and higher velocities of our cloud sample, and thus it would be useful in future to compare a subset from this population with our existing data. It would also be illuminating to compare our results found here with those discovered through a more traditional analysis of the cloud properties, such as Gaussian decomposition into warm/cold components. Gaussian decomposition into broad and narrow components in this way would allow investigation into the fraction of sightlines with warm/cold/multiphase gas, relative mass ratios of cold versus warm gas and potential velocity or spatial shift between cold and warm components, which could then be directly compared to the outcomes of our analysis here in order to assess this method's accuracy and agreement with other forms of cloud interpretation.

It is important here to consider that two possible interpretations of the observed dichotomy in line-width disitribution remain: line-width may be an indicator of a Galactic versus extragalactic origin, or it may simply trace ongoing interactions between a cloud and its environment. We expect that our extragalactic clouds from GCN and LA, with the exception of G306 which is currently passing through the disk, have already interacted with the disk of the Milky Way and as such may be largely done with their interactions.

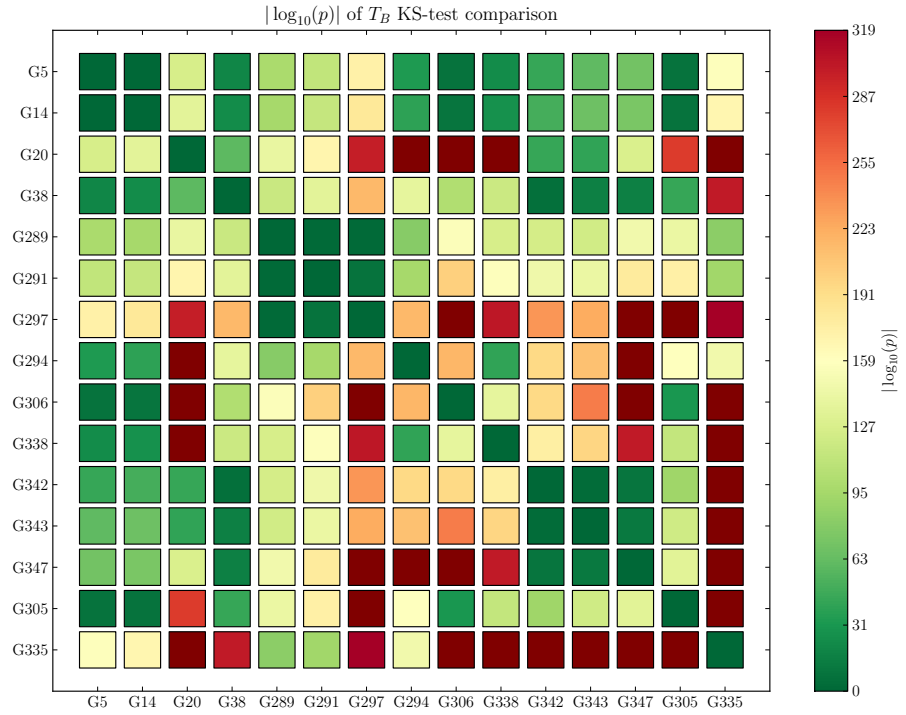

Figure 5.46: Cloud-by-cloud comparison of T_B brightness temperature. Each square is coloured based on the resultant $|\log_{10} p|$-value, with green indicating the most similar and red indicating the most different. Results are mirrored around the diagonal to aid interpretation of a particular cloud.

Conversely, the Galactic clouds (CL and G335) both show evidence of ongoing interaction with subsequent broadening of line-widths. The line-width of a cloud is determined by the combined processes of thermal broadening (due to the temperature of the gas) and kinematic broadening (due to turbulence of the gas), and the relative impact of each process is often difficult to disentangle. If temperature alone was controlling the FWHM distribution of the clouds we have observed here, then we would expect extragalactic gas (with its lower metallicity and less access to cooling metals such as carbon and oxygen as well as expected lower densities leading to less shielding against heating radiation) to have broader line-widths while Galactic gas would be much more efficiently cooled. This is certainly true of the gas in the disk of the Milky Way, where line-widths are typically much lower than the general HVC population line-widths of ~20 km s^{-1}, with strong constraints on the existence and survival of multi-phase halo gas depending on its metallicity and dust content (Wolfire et al., 1995). However, our observations have shown the opposite, with our extragalactic cloud sample featuring less velocity dispersion and narrower line-widths compared with the Galactic sample. This is a potential indication that environment may be the driving factor affecting the physical properties of the clouds, rather than their origin. In order to further investigate what we have observed and determine the dominant factor, it is necessary to attempt disentanglement of the two possible explanations we have identified for a dichotomy in line-width: origin or interactions with environment. For this, future investigations would target clouds in the Magellanic stream (as pre-interaction extragalactic clouds) and high-latitude known Galactic clouds that would be expected to be mostly non-interacting at their later evolutionary stage.

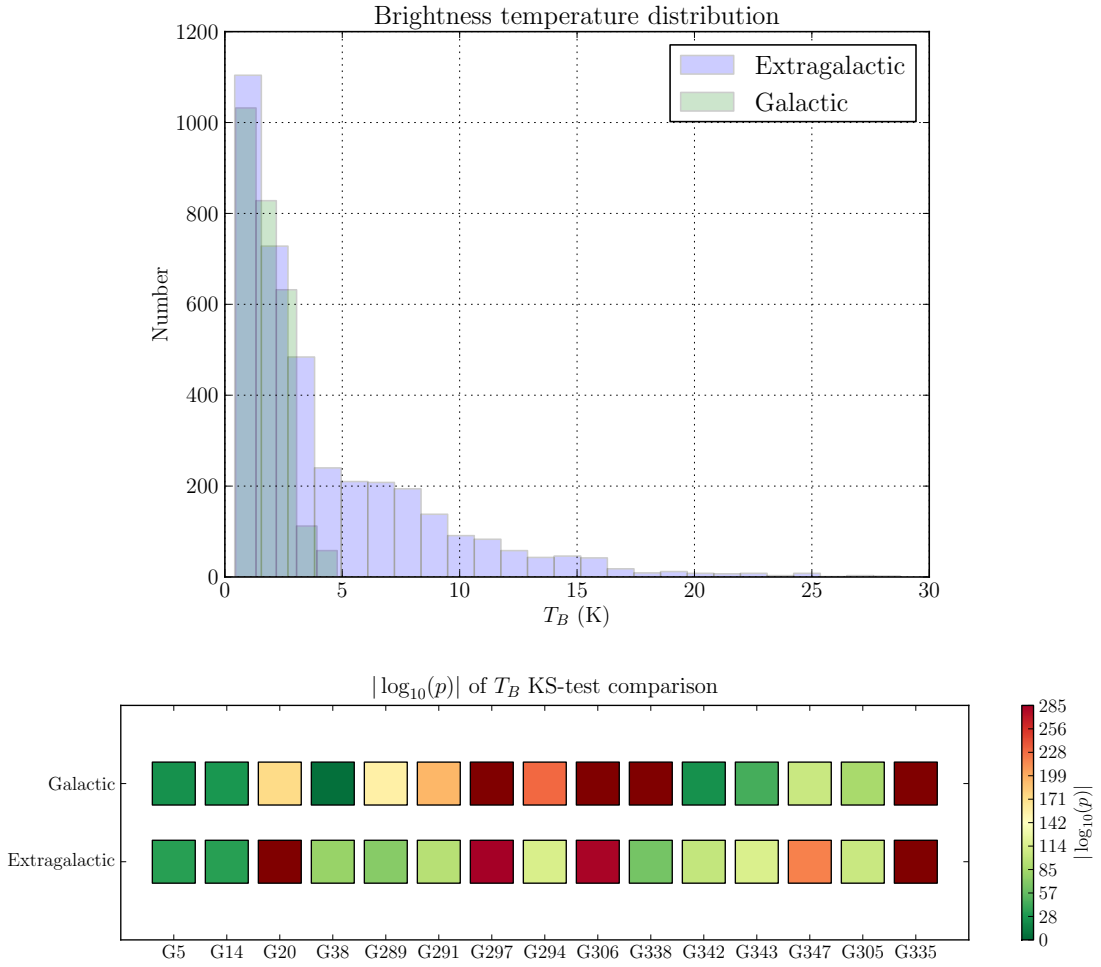

Figure 5.47: Overall T_B brightness temperature distributions for extragalactic (blue) and Galactic (green) clouds (top), and the results of comparing each cloud against these distributions (bottom). Each square is coloured based on the resultant $|\log_{10} p|$-value, with green indicating the most similar and red indicating the most different.

5.5 Conclusion

We have presented a study of 15 interacting neutral hydrogen clouds of suspected extragalactic and Galactic origin. This sample included ten clouds from the Leading Arm, Complex L and Galactic Centre Negative regions observed with ATCA as part of this project (C2849), three re-reduced Leading Arm clouds from the previously proposed C1139, one re-reduced region near the Galactic disk (C1470) and one HVC/region interacting with the Milky Way disk (C1747). Excluding the two regions (G306 and G335), we visualised the physical properties across each cloud to examine and determine differences in spectral properties (T_B, v_{LSR}, v_{GSR}, FWHM and v_{GSR}-v_{LSR}). We found that the extragalactic clouds in our sample tended to have small line-widths, more concentrated line-width distributions and very little dispersion in their fitted velocities, while Galactic clouds typically had broader line-widths, a complex and dispersed line-width distribution and a larger dispersion in their fitted velocities. A coherent, consistent velocity across a cloud would suggest a less disturbed cloud, while emission at a wider spread of velocities would be more indicative of turbulence or instability in the cloud. Since Galactic clouds are primarily

Table 5.2: Quantitative summary of results and likely cloud origin.

Cloud [1]	$\langle \mathrm{FWHM} \rangle \pm \sigma$ [2]	$\langle v_{LSR} \rangle \pm \sigma$ [3]	$\delta \mathrm{FWHM} / \delta \lvert b \rvert$ [4]	$\lvert \log_{10} p \rvert_{g,FWHM}$ [5]	$\lvert \log_{10} p \rvert_{e,FWHM}$ [6]	Likely origin [7]
G5	5.4 ± 1.0	−83.0 ± 0.5	−9.9	214	15	Extragalactic
G14	5.0 ± 0.8	−155.8 ± 0.9	−9.8	244	36	Extragalactic
G20	6.5 ± 2.0	−242.0 ± 1.1	−2.9	∞	13	Extragalactic
G38	13.9 ± 4.9	−241.6 ± 1.1	−28.2	73	165	Galactic
G294	6.5 ± 2.0	246.3 ± 0.8	−11.1	∞	10	Extragalactic
G289	4.0 ± 0.8	250.9 ± 0.7	−6.1	163	54	Extragalactic
G291	3.1 ± 0.7	195.3 ± 0.8	−5.6	210	114	Extragalactic
G297	5.8 ± 2.1	252.7 ± 0.8	−11.8	∞	2	Extragalactic
G306	11.0 ± 4.2	221.5 ± 1.9	−4.9	∞	∞	Extragalactic
G338	19.2 ± 2.6	−89.6 ± 2.5	−0.3	44	∞	Galactic
G342	11.9 ± 3.4	−81.1 ± 2.4	+41.0	152	143	Galactic
G343	21.0 ± 6.7	−140.3 ± 3.0	−35.0	2	259	Galactic
G347	27.1 ± 4.8	−100.9 ± 2.6	−13.6	112	∞	Galactic
G305	14.4 ± 2.8	−104.6 ± 1.8	+7.7	211	∞	Galactic
G335	38.9 ± 18.4	−119.9 ± 19.2	−12.9	∞	∞	Galactic

[1] Abbreviated cloud name [2] Mean FWHM and standard deviation [3] Mean v_{LSR} and standard deviation [4] gradient of FWHM with absolute Galactic latitude [5] p-value for cloud against Galactic FWHM distribution [6] p-value for cloud against extragalactic FWHM distribution [7] Likely origin based on results presented here

thought to get to the halo as the outflowing remnants of supernova explosions, it is not surprising that their spectral structure might reflect their more violent origins compared with relatively steady inflowing gas.

Overall, we find that FWHM is the most telling of the various observable physical properties for interacting HVCs. Although we find that the dispersion in fitted velocity of clouds is larger for clouds assumed to be Galactic, the velocity alone does not offer a conclusive diagnostic for making predictions about a cloud's origin. This is likely due to the influence of distance and the effects of projection on the measured velocity and velocity dispersion of a cloud. Similarly, we find that brightness temperature does not allow distinguishing between different populations of gas as it is strongly affected by the distance of the cloud, which is in the majority of cases unknown.

The line-width of the cloud, conversely, offers insight into the physical state of the neutral hydrogen and may be used to infer the likely origin of a cloud. Particularly, we find that clouds in our sample of extragalactic origin have consistently lower FWHMs as well as far less dispersion in the line-width distribution. There is less consistency amongst the Galactic sample of line-widths, which may be suggestive of the effects of a more turbulent and disrupted origin, although we do see that there is a general mix of both narrow and broad line-widths. While studies have suggested that infalling primordial gas can cool and condense as it approaches the disk, our results suggest that some cold gas may be intrinsic to extragalactic clouds. The process of interaction, primarily via ram-pressure stripping, then potentially leads to gas being stripped off and broadening. Given that in G306 we see a narrow component throughout the cloud independent of latitude combined with the narrow components dominating in the leading part of clouds in our sample, we find that the narrow component is more useful as a trace of the direction of movement of a cloud, independent of a column density map. Based on our sample and in the latitude trends we see, it does not seem likely that the cold gas is formed solely from the passage through the disk.

We have summarised the quantitative results of this work in Table 5.2 for each cloud. We qualitatively argued that extragalactic clouds featured narrow line-widths, minimal dispersion in the line-width distribution and minimal dispersion in velocity based on Fig-

ures 5.17 to 5.32; these arguments are reproduced quantitatively in column 2 and column 3. The change in line-width with absolute increasing Galactic latitude is given in column 4, highlighting that the extragalactic clouds in our sample have narrower line-widths at higher latitudes above the disk which also corresponds with their likely direction of motion. Galactic clouds do not feature the same trend. The $|\log_{10} p|$-value for each cloud against the overall Galactic and extragalactic distributions of line-width is given in column 5 and 6, where ∞ indicates a cloud where the p-value is numerically zero. Finally, based on the results of our analysis here, we suggest a likely origin for each cloud in column 7. These origins have not changed from their initial definition, except in the case of G38 and G305, both of which have been classified as Galactic.

We thus present five diagnostic outcomes based on the results of our study for interacting HVCs:

1. Narrow line-widths < 10 km s^{-1} with little dispersion in the line-width distribution suggest an extragalactic origin and/or a non-interacting cloud.

2. A mix of broad and narrow line-widths from 5–30 km s^{-1} combined with dispersion in the line-width distribution suggests a Galactic origin and/or an interacting cloud.

3. The 'head' (or direction of movement) of an interacting HVC will be marked by the presence of the narrowest line-widths, with broad components tracing warmer diffuse gas left behind in the 'tail' of the cloud.

4. A KS two-sample test comparing line-width distributions either cloud-by-cloud or to a Galactic/extragalactic distribution can potentially distinguish relatively between clouds of different origins, particularly finding consistency amongst clouds of extragalactic origin.

5. The velocity or brightness of a cloud does not appear useful as a diagnostic unless the distance to the cloud is known, as both are considerably affected by distance.

We note a limitation of our extragalactic sample in that both clouds from the Leading Arm and from Galactic Centre Negative are in advanced stages of interaction with the Milky Way. We would expect that most of our extragalactic clouds, with the exception of G306 which is currently impacting the disk, have already passed through the Galactic disk given that the LA clouds are on the other side of the disk and GCN is completely fragmented, leaving them in a state that would be typical of extragalactic clouds post-interaction with the majority of their interaction with Milky Way gas having taken place at an earlier stage. We suggest that a future study targeting similarly compact HVCs showing evidence of interaction on the side of the Galactic disk closer to the Magellanic Clouds or the Magellanic Bridge will reveal extragalactic clouds at the earlier stage of evolution, confirming whether extragalactic gas is consistently identifiable both before and after interaction with the disk or whether it is interaction with the environment rather than origin that determines the observed physical properties of clouds in the halo of the Milky Way.

Chapter

6 TRACING DENSE AND DIFFUSE COMPONENTS OF HIGH-VELOCITY NEUTRAL HYDROGEN IN THE MILKY WAY

Overview

This chapter investigates the large-scale structure of the Galactic halo by combining the GASS HVCs with the results of a very sensitive sightline search for neutral hydrogen at high velocity. By combining the two surveys, the connection between HVCs and a ubiquitous diffuse gas is uncovered, with important implications for the relationship between dense and diffuse halo gas and the overall mass of neutral hydrogen in the halo of the Milky Way.

6.1 Introduction

The complicated galactic ecosystem of outflow, infall and circulation is known to play a key role in galaxy evolution. Outflowing gas in the form of supershells, chimneys and high-mass star formation provides an avenue for material to escape the disk into the haloes of galaxies (McClure-Griffiths et al., 2006b; Ford, Lockman & McClure-Griffiths, 2010) leading to thicker gaseous disks (Oosterloo, Fraternali & Sancisi, 2007; Kamphuis et al., 2013), metal transport to the halo (Werk et al., 2011), and condensed material for new stars (Dawson et al., 2011). Conversely, infalling gas through mergers, interactions with other galaxies or interactions with the intergalactic medium drives change and causes disruption in galaxies and their environments (Chung et al., 2006; Westmeier, Koribalski & Braun, 2013; Johnson, 2013), potentially providing new fuel for star formation (Lockman et al., 2008; Hill, Haffner & Reynolds, 2009; Tumlinson et al., 2011; Lehner & Howk, 2011; Wolfe et al., 2013b). The energetic feedback processes going on at the centre of galaxies have a complex role to play in the continuation and cessation of star formation in galaxy hosts (Sanders et al., 2009; Vogt, Dopita & Kewley, 2013; Newton & Kay, 2013), the structure of galactic haloes (Tang et al., 2008) and the circulation and entrainment of cold neutral material such as atomic hydrogen and molecular hydrogen (McClure-Griffiths et al., 2013). Many of these mechanisms driving galaxy evolution should lead to observable effects on the haloes of galaxies, which is the main concern of our study here. Specifically, we aim to observationally uncover the hidden structure of faint neutral hydrogen in the halo of the Milky Way and how it relates to the prominent and well-known high-velocity cloud population, thus gaining a clearer picture of the Galactic ecosystem of the Milky Way through its halo environment.

Hints of a connection between the brighter HVCs and a faint diffuse background have been revealed in previous high-sensitivity work. Nigra et al. (2012) studied a small isolated cloud in the Magellanic Strea and discovered an extremely faint broad component of width ~60 km s^{-1} co-located with the brighter 20 km s^{-1} main component. They interpreted this multi-phase cloud as a warm neutral medium/warm ionised medium core surrounded by a turbulent mixing layer, giving insight into the potential connection between the neutral and ionised components of hydrogen in the halo. Studies of interacting hydrogen clouds (known as head-tail or core-envelope clouds) have revealed clear signatures of interaction between the clouds and their surrounding halo enviroment (e.g. Brüns et al., 2000; Brüns, Kerp & Pagels, 2001; Bekhti et al., 2006; Putman, Saul & Mets, 2011), though with focus on individual clouds or subsets of clouds in a specific region rather than on the overall neutral hydrogen sky.

We present here a study of neutral atomic hydrogen gas at high velocity in the Milky Way, combining the very sensitive 21 centimetre Green Bank survey for high-velocity HI (Lockman et al., 2002) with the search for high-velocity HI in the Galactic All Sky Survey (Moss et al., 2013). These two surveys target distinct aspects of the HI content of the Milky Way halo: Lockman et al. (2002) sampled the halo with high sensitivity ($\sigma \sim 3.4$ mK) at random positions (some towards extragalactic objects bright in optical and UV) with the 140 ft (43 m) NRAO telescope at Green Bank, while Moss et al. (2013) use automated source-finding to identify all southern-sky high-velocity clouds (HVCs) above a brightness of 4σ (~230 mK) in the Parkes 64 m radio telescope Galactic All Sky Survey (GASS, McClure-Griffiths et al., 2009; Kalberla et al., 2010), which has a sensitivity of 57 mK. Together these different surveys reveal new insights into the structure of the neutral hydrogen in the halo of the Milky Way.

We outline the properties of each survey in Section 6.2 and describe the sample used from the GASS catalogue of high-velocity clouds. We present our results and analysis in Section 6.3, as well as a consideration of selection effects and survey limitations. Finally, we summarise our results and present avenues for future investigation in Section 6.4.

6.2 Survey details and data

Lockman et al. (2002, hereafter L02) used the 140 ft (43 m) NRAO telescope at Green Bank to conduct a very sensitive search for faint high-velocity HI lines in 860 directions. The angular resolution of the data was ~21′, with a velocity resolution of 5 km s^{-1} over the v_{LSR} range −1000 km s^{-1} to +800 km s^{-1}. The median RMS sensitivity of the pointed observations was 3.4 mK, which gives a median 4σ detection limit of $N_{HI} \sim 8 \times 10^{17}$ cm^{-2} (for an assumed typical line-width of 30 km s^{-1}). This sensitivity is much higher than any previous large-scale survey of Galactic HI and offers a unique insight into the faint high-velocity Galactic halo that was previously only sampled effectively by UV absorption lines. Part of the motivation of the study was to investigate the incongruity between the amount of high-velocity neutral hydrogen revealed by current HI surveys and the amount that should be present based on the results from UV absorption studies (Savage & Sembach, 1996). As such, one third of the observations were made specifically towards extragalactic objects visible at optical and infrared wavelengths in order to facilitate future follow-up. L02 detected high-velocity HI in 37% of their observed sightlines, with the detected lines generally found to be associated with known high-velocity complexes (such as the Magellanic system and Complex C) and typically extended over several degrees rather than being compact in structure. They concluded based on these results that most HVCs do not have sharp edges, and that their detected high-velocity HI was likely to be

associated with the faint edges of HVC complexes not detectable by previous HI surveys. They also raised an extremely critical point regarding HVC populations: if HVCs are, in general, bright condensations within a diffuse ubiquitous halo medium, then a particular cloud may be counted many times if observations are not sensitive enough to reveal the faint gaseous connections between clumps. As such, it is more useful to consider the sky-covering fraction of detected clouds rather than the absolute number of clouds, since the boundaries of a particular cloud are set by instrumentation and integration time.

The Galactic All Sky Survey (McClure-Griffiths et al., 2009) was made using the 21 cm multibeam receiver on the Parkes 64-m radio telescope to survey the entire southern sky in neutral hydrogen, complete over the Galactic velocity range of $v_{LSR} = \pm 468$ km s^{-1}. It features an effective angular resolution of $\sim 16'$, a spectral resolution of 1 km s^{-1} and an average RMS sensitivity of 57 mK. Because GASS was completed using frequency-switching, it contains all spatial scales of HI emission. The combination of high angular resolution, high sensitivity and high spectral resolution found in GASS makes it an excellent southern-sky survey of Galactic neutral hydrogen, particularly of relatively cold gas with narrow line-widths throughout the Milky Way as well as relatively faint gaseous structures in the Galactic halo.

The GASS catalogue of HVCs (Moss et al., 2013) was constructed using automated source-finding on the Galactic All Sky Survey second release (Kalberla et al., 2010). To identify clouds, Moss et al. (2013) adopted the source-finding algorithm developed and used by Murphy et al. (2007), extended to a three-dimensional cube. In this catalogue, Moss et al. (2013) identified 1111 positive velocity HVCs and 582 negative velocity HVCs in the southern sky with a peak brightness temperature $T_B > 4\sigma$ (~230 mK). The catalogue also included 295 anomalous velocity clouds (AVCs) which did not meet the traditional velocity criteria to be classified as an HVC. The sensitivity of GASS is notably less than that of the HI targeted with the very sensitive Green Bank survey of Lockman et al. (2002), and as such the GASS catalogue of HVCs selects for relatively bright high-velocity HI clouds. However, the sensitivity to large-scale structure of GASS compared to previous southern-sky surveys of HI is particularly important in the context of HVCs as bright clumps connected by fainter diffuse gas, meaning that it was possible to identify complexes of clouds connected by faint gas as well as more isolated clumps of gas down to a threshold limit of 2σ (~110 mK).

Sampling spectra across HVCs in GASS

With GASS, it is possible to investigate how spectral structure (and hence physical properties) change across individual clouds. An example of spectral variation across HVCs is shown in Figure 6.1, for GHVC G297.1+08.7+252, for integrated intensity, brightness temperature (T_B), full-width at half-maximum (FWHM) and velocity relative to the Galactic Standard of Rest (v_{GSR}). This particular cloud has been argued to be ram-pressure stripped as it moves through the hot halo of the Milky Way producing a head-tail structure(Bekhti et al., 2006), with a concentration of bright, narrow, cold components in the head and broad, faint, warm components in the tail. Head-tail HVCs like GHVC G297.1+08.7+252 are not unique, but are found all over the Galactic halo with distinct column density and velocity gradients (Putman, Saul & Mets, 2011). These clouds show clear evidence of interacting with the surrounding halo medium, and allow us to probe both their physical conditions and environment through their disrupted spectral properties. The existence of these clouds and their structure make it vital to consider spectra across each cloud, as the physical conditions of the cloud are likely to change in a

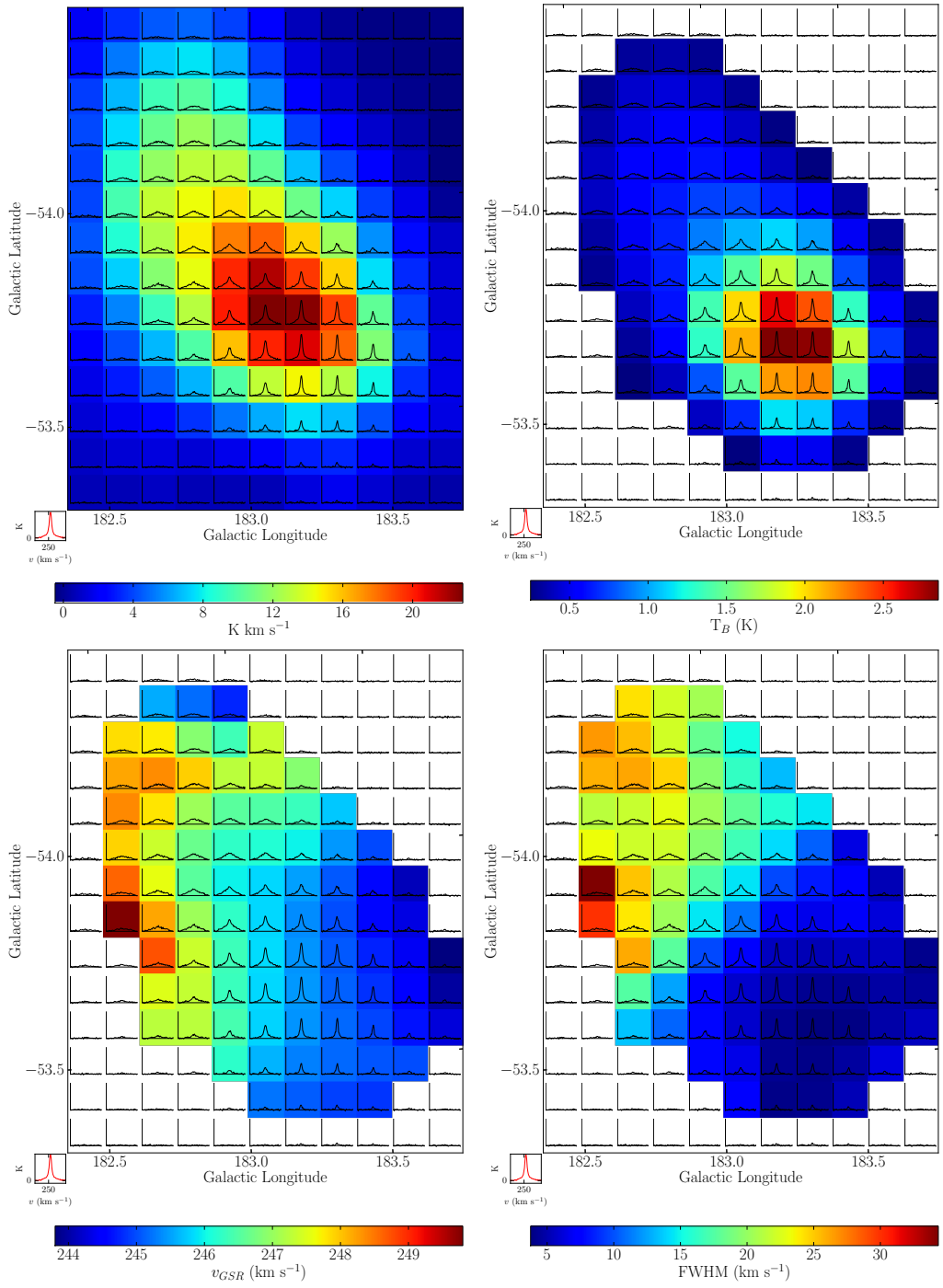

Figure 6.1: Example of the variation in spectra across HVCs in the GASS catalogue. Shown is GHVC G297.1+08.7+252, a well-known example of a head-tail cloud, with spectra over-plotted on different background images: (clockwise from top left) integrated intensity, brightness temperature, full-width at half-maximum and velocity relative to the Galactic Standard of Rest. Based on its physical structure, this cloud is argued to be ram-pressure stripped as it moves through the hot halo of the Milky Way (Bekhti et al., 2006), with bright, narrow components in the head and faint diffuse components in the tail. The existence of objects such as GHVC G297.1+08.7+252 shows that HVCs are not isolated clouds of neutral hydrogen in the halo, but are interacting with their environment in an observable and measurable way.

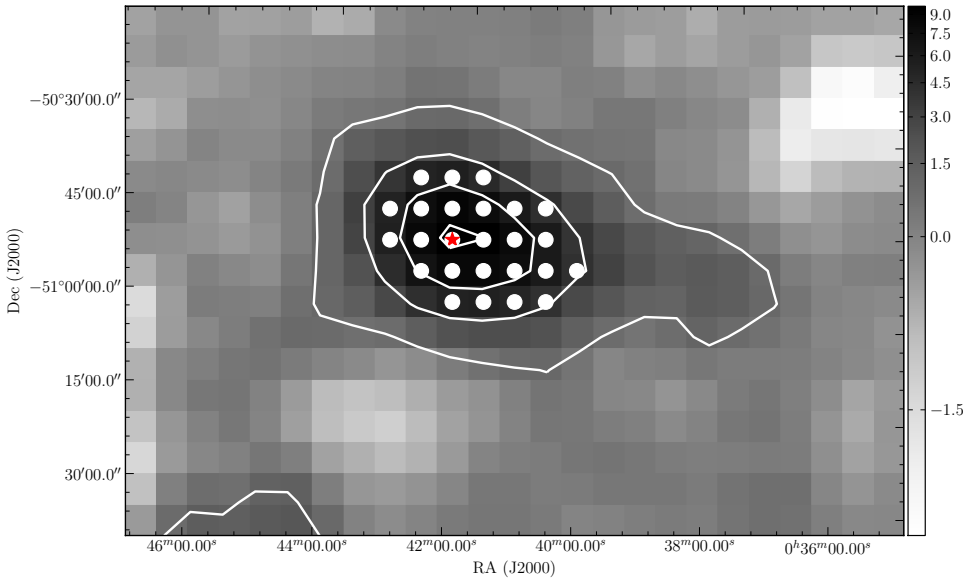

Figure 6.2: Example of the distribution of spectral components across a single GASS HVC, GHVC G306.9−66.0+166. Each white point indicates a position at which the spectrum through the source contains a peak brightness temperature $T_B > 5\ \sigma$. The red star indicates the catalogued position (cloud core) as in Moss et al. (2013). The background is the integrated intensity image of all velocity slices of the cloud which contain emission brighter than 2σ (0.11 K), with white contours (4 equally-spaced levels from 25% to the maximum of the image) overlaid of the same cube to aid in highlighting the source.

detectable way at the GASS angular and spectral resolution.

Here we use the same sample as described in Moss et al. (2013): we obtain all spectral components with a peak brightness temperature above 5σ (285 mK in GASS) in all clouds with a total size < 5 deg^2. Considering only the high-velocity gas to be that with $|v_{LSR}| \geq 90$ km s^{-1}, we obtained a total of 12210 spectra across a total of 549 GHVCs. For the purposes of this analysis, we consider only a single-component fit to each spectrum as a means of differentiation between broad and narrow lines, with the goal that a spectrum dominated by either a narrow component or a broad component will be characterised as such by the single-component fit. An example of the spectra included in the case of a single cloud, GHVC G306.9−66.0+166, is shown in Figure 6.2, where the white points indicate positions at which spectra were included in the sample.

We applied the following flags to this sample of spectra:

1. We obtain the column density for each cloud using

$$N_{HI} = 1.8 \times 10^{18} \sqrt{\frac{\pi}{4 \ln 2}}\ T_{B,fit}\ \Delta v\ \text{cm}^{-2}, \tag{6.1}$$

   where $T_{B,fit}$ is the brightness temperature in K and Δv is the line-width in km s^{-1}, and then ignore any spectral components with a column density $N_{HI} < 10^{18}$ cm^{-2} as this is below the reasonable sensitivity limit to be expected from the GASS data.

2. Any clouds contributing > 300 components across the cloud are treated as contaminated, and removed from the sample. This applied to GHVC G222.2−87.9−263, GHVC G280.6−05.6+186 and GHVC G075.8−73.6−121. Clouds like these contributing a few hundred components are located close to the Magellanic emission or to Galactic emission, and are not useful in this sample.

3. Any clouds with > 30% of spectral components that have a column density $N_{HI} < 10^{18}$ cm^{-2} are flagged as bad clouds and removed from the sample. This applied to a total of 12 clouds.

Upon applying these filters to our data, we obtain a total of 10455 useable spectra across 534 clouds. This filtered sample of GASS HVC spectra is what we proceed to use for the rest of our analysis.

6.3 Dense and diffuse neutral hydrogen in the halo

Figure 6.3 shows the results of combining the L02 sample with our sample of spectra across GASS HVCs as described in Section 6.2, for both brightness temperature T_B and FWHM versus column density N_{HI}. The properties at the catalogued position (hereafter referred to as cloud core) of each GASS HVC are plotted as a red circle, while the population of all spectral components is plotted as black circles. For comparison, we plot the L02 distribution of spectral components as cyan triangles. In this case, there are 10455 GASS spectral components plotted, 534 GASS cloud cores plotted and 305 L02 spectral components plotted.

What is evident in both plots is a clear distinction between two populations of neutral hydrogen: a bright, narrow population typical of the majority of GASS HVC components, and a faint, broad population that aligns well with that of the population found by L02. We henceforth refer to the two evident populations as the dense population and the diffuse population, respectively.

Selection effects and sample limitations

To examine possible systematic effects between the two surveys, which have significantly different sky coverage and observational parameters, we reproduce the earlier $T_B(N_{HI})$ and FWHM(N_{HI}) correlations in Figure 6.4, using data only from the part of the sky covered by both ($-43° < \delta < 0°$). In this case, there are 6851 GASS spectral components plotted, 394 GASS cloud cores and 83 L02 spectral components plotted. These spectra in the overlap region represent 66%, 74% and 27% of the full sample respectively. This figure shows the same overall trend as Figure 6.3: most GASS HVC lines cluster near the GASS cloud cores, with a branch of the spectral components that aligns with the brightest parts of the L02 distribution. This confirms our previous result for the full sample, and suggests that the distinction applies to both the northern and southern hemisphere sky.

We also considered the effect of velocity coverage on the sample obtained. As mentioned previously, GASS is completed within velocities $v_{LSR} = \pm 468$ km s^{-1} while L02 covered the v_{LSR} range -1000 km s^{-1} to $+800$ km s^{-1}. The results are shown in Figure 6.5, with the GASS spectral components in black and the L02 components in cyan. What is clear immediately is that, in both surveys, the majority of observed HVCs are within the GASS coverage of $v_{LSR} = \pm 468$ km s^{-1}. This indicates that despite the more extended velocity coverage of L02, there is no kinematic difference in the detected HVC populations. There is the noticeable dominance of positive velocities in GASS and negative velocities in L02; this is due to the rotation of LSR around the Galactic anticentre and is an artifact of the LSR frame of reference (Wakker, 1991).

To assess the overall comparability of the L02 data with GASS, we extracted GASS spectra at the position of all L02 spectra with declinations $\delta < 0°$. We then excluded spectra that either had velocities beyond the GASS range of $|v_{LSR}| < 468$ km s^{-1} or with fitted peak brightness temperatures $T_{B,fit}$ in L02 < 171 mK (3σ in GASS). This came

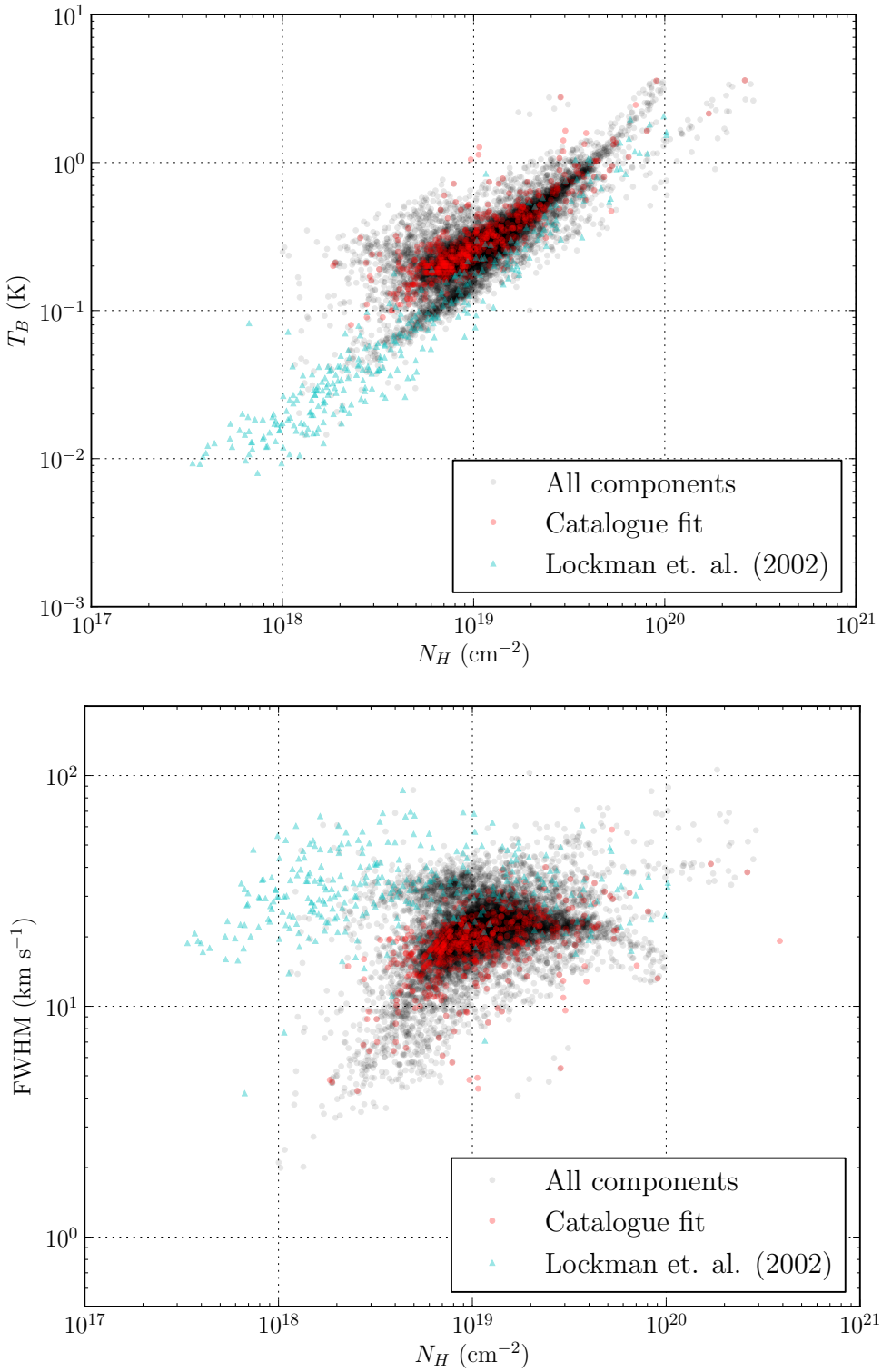

Figure 6.3: Scatter plots of both the GASS HVC population and the L02 population, in T_B vs. N_{HI} space (top) and FWHM vs. N_{HI} space (bottom). The properties at the cloud cores of the GASS HVCs used in our sample are shown as red circles, while the spectral components across the clouds are shown as black circles. Overlaid are the properties of the L02 population as cyan triangles. In both cases, we see that the GASS HVC spectral components are clearly divisible into two populations: a minority of components which align with the L02 distribution, and the majority of components which are brighter and narrower in line-width.

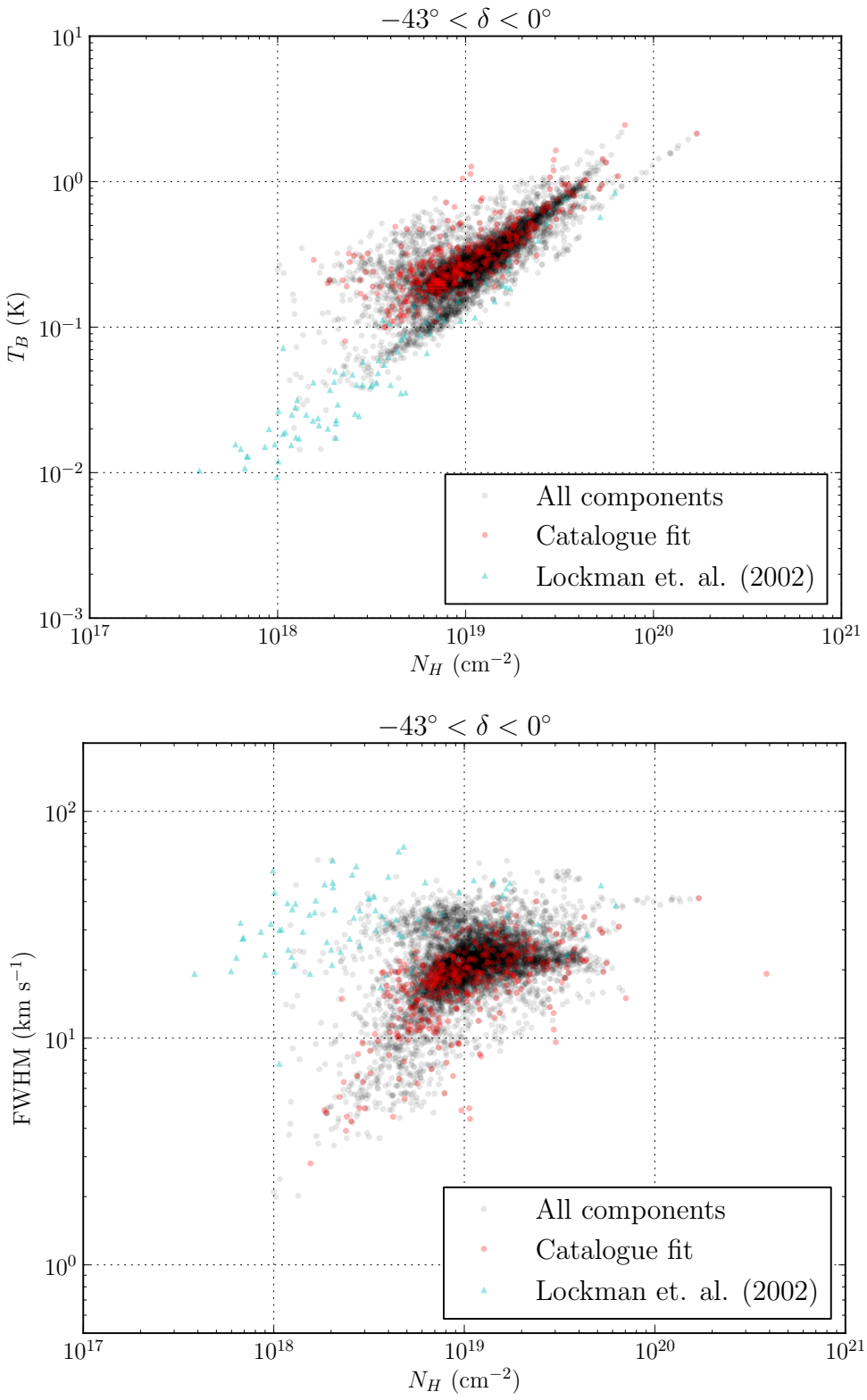

Figure 6.4: Scatter plots of both the GASS HVC population and the Lockman et al. (2002) population, in T_B vs. N_{HI} space (top) and FWHM vs. N_{HI} space (bottom), in only the overlap region between the two surveys of $-43° < \delta < 0°$. The same trends as seen in the entire sample are seen in this directly comparable subset, confirming our result and negating the potential influence of selection effects.

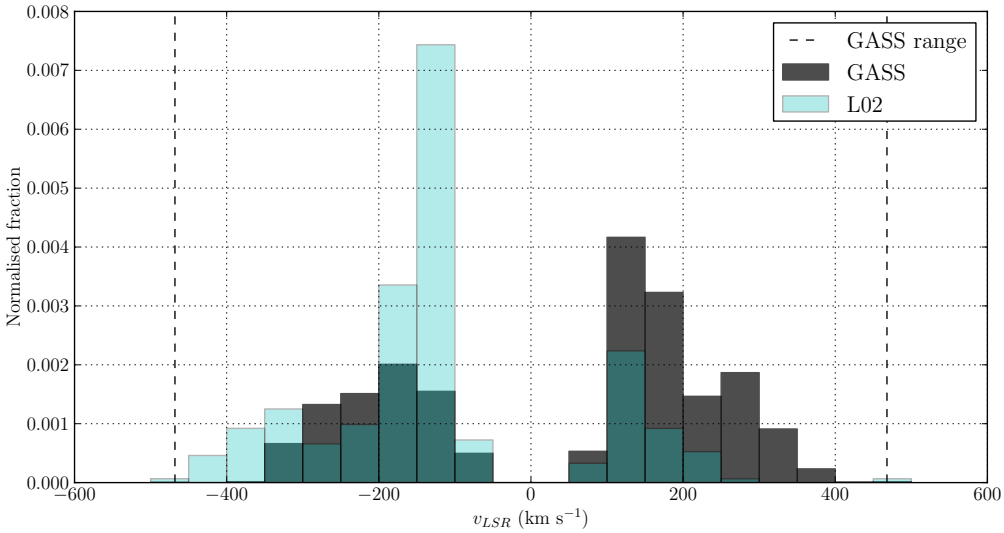

Figure 6.5: Comparison of the velocity coverage of GASS and L02. Shown is the distribution of all 10455 GASS spectral components in black and all 305 L02 components in cyan. The published velocity coverage of GASS ($v_{LSR} = \pm 468$ km s^{-1}) is shown as two dashed lines. This highlights that the extended velocity coverage of L02 does not result in any significant difference in the observed HVC population, as the majority of HVCs detected in both surveys fall within the GASS velocity limits. The dominance of negative velocities in L02 and positive velocities in GASS is due to rotation of the Milky Way (Wakker, 1991). The histogram is normalised to enable compatibility due to the large number of GASS components.

to a total of 15 comparable spectra out of a total of 83 spectra at southern declinations. We then fit a Gaussian to each GASS spectrum (both unsmoothed and smoothed to $21'$ resolution) to obtain the fit parameters for comparison with L02. The results are shown in Figure 6.6, for T_B, v_{LSR}, FWHM and N_{HI}. Overall, there is good agreement between the two surveys with the majority of lines in GASS deviating by less than 20% from the L02 measurement. The most agreement is seen in velocity, confirming that each cloud has been detected in both surveys at the same velocity. There is some scatter in brightness temperature and line-width, also evident in the resulting column density; this is largely because these parameters are averaged over the beam and thus reflect the fact that the Parkes beam is smaller than that of the 140-ft telescope. The mean ratios for each property are 1.07 (T_B), 0.92 (FWHM), 0.99 (N_{HI}) and 0.99 (v_{LSR}), indicating that there is a systematically brighter T_B and narrower FWHM measured in GASS compared with L02.

However, given that the deviation is small and typically within the errors of GASS measurements, we conclude that the agreement between the two surveys is strong enough to justify direct comparison. This comparison is framed by two key questions: 1) where is each type of component (dense or diffuse) spatially located when we look across each GASS HVC, and 2) is the distribution across GASS HVCs of each type of component random or ordered in some way. To answer these questions, we use the L02 distribution as our starting point to quantitatively separate the two populations of neutral hydrogen.

Separating the two populations

In order to identify the spectral components of GASS HVCs that are quantitatively associated with the diffuse population of L02, we applied polynomial fitting to determine the

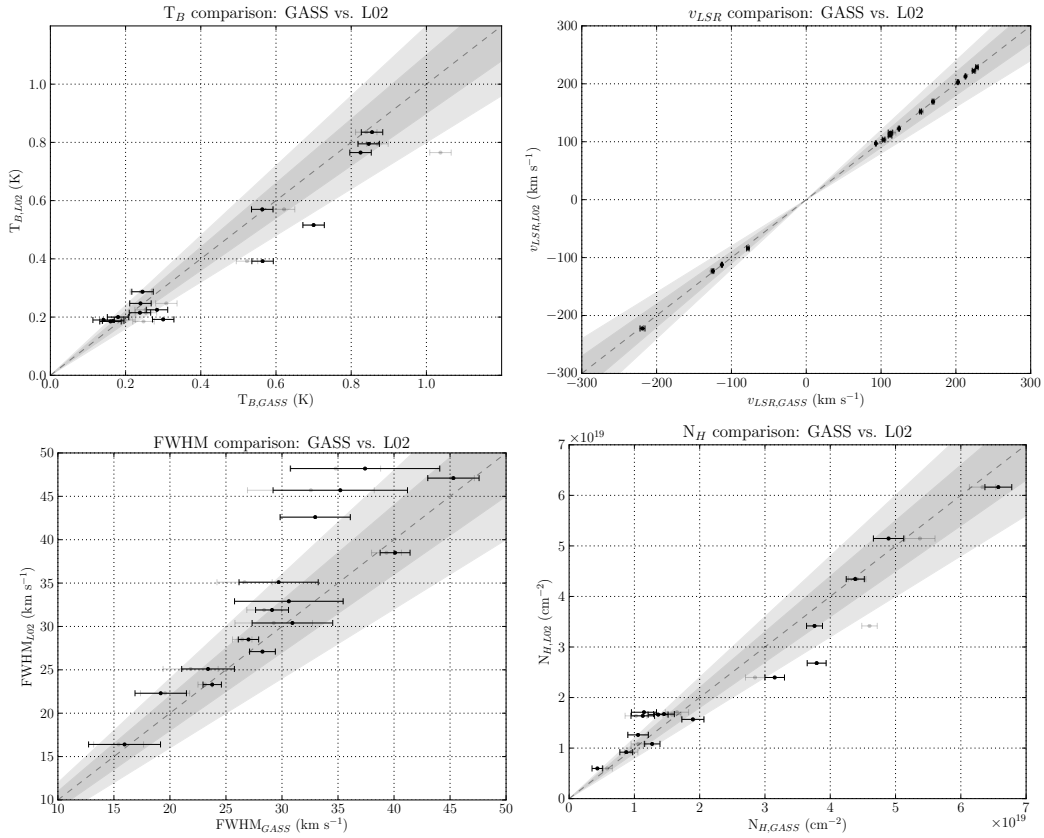

Figure 6.6: Comparison of measured properties for L02 sightlines visible in GASS. A total of 15 L02 sightlines with $T_{B,L02} > 171$ mK are detectable in GASS, plotted on each graph above. The compared properties are brightness temperature T_B (top left), velocity v_{LSR} (top right), linewidth FWHM (bottom left) and column density N_{HI} (bottom right). The grey shaded areas are ±10% and 20% of the dashed line, which represents the 1:1 ratio. The black points represent measurements performed on GASS data smoothed to 21′ resolution to match L02, while the grey points show the measurements on the unsmoothed GASS data. Overall, the velocity shows the most agreement, while there is deviation in the other properties. The agreement between the two surveys, despite these differences, is strong enough to justify direct comparison.

general trend of the low-brightness gas. The two populations are visually distinct particularly in T_B vs. N$_H$ space, and so we used this parameter space for fitting. We limit the L02 spectral components to only those located in the overlap region to ensure consistency with the GASS HVC spectral components and reduce scatter in the sample. We divided the column density space into six equally-spaced blocks in log-space ($10^{[17,17.5,18,18.5,19,19.5]}$ cm^{-2}) and found the mean value of both the brightness temperature T_B and the column density N_{HI} for the brightest five components. By taking an average of a small range, we were able to average out the effect of extreme values and more accurately trace the top of the L02 distribution.

We fit a third-order polynomial to the data (due to both first- and second-order fits poorly tracing the divide visible in the GASS data), and obtained an equation describing the trend of the brightness proportion of the distribution:

$$T_B \sim 9.634 \times 10^{60} {N_{HI}}^3 - 7.224 \times 10^{40} {N_{HI}}^2 + 2.785 \times 10^{20} N_{HI} - 0.003439, \qquad (6.2)$$

where T_B is in K and N_{HI} is in cm^{-2}. The points used as well as the resultant fit are shown on the T_B vs. N_{HI} plot in Figure 6.7 in cyan. We used this fit in order to

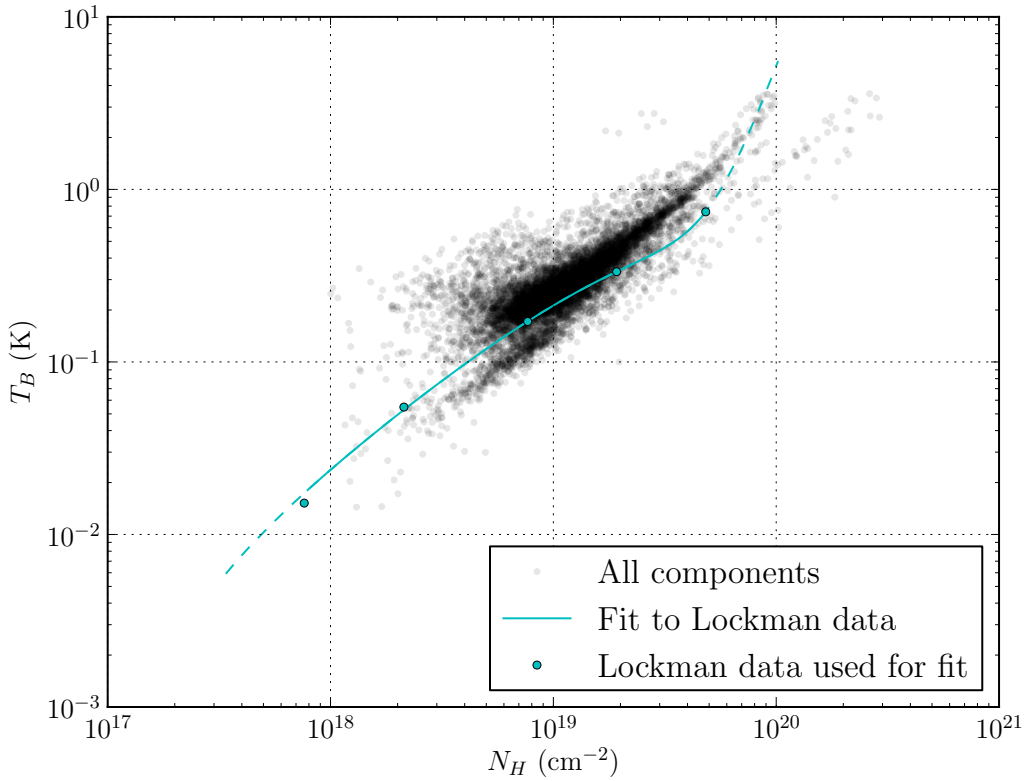

Figure 6.7: Scatter plot of spectral components of the GASS HVC population (black circles) in T_B vs. N_{HI} space, with the polynomial fit used to distinguish the two evident populations of gas overlaid. A third-order polynomial was fit to the average of the brightest five spectral components in the L02 distribution (limited to spectral components in the overlap sample described in Section 6.3) over six equally-spaced blocks in column-density log-space ($10^{[17,17.5,18,18.5,19,19.5]}$). The resultant fit is shown as a solid line (cyan) with cyan circles representing the average point of both brightness temperature and column density in each block. The dotted cyan line shows where the fit is unreliable due to a lack of available data. We use this fit to divide the GASS HVC spectral components into a dense population and a diffuse population.

differentiate the GASS HVC spectral components that were related to the low-brightness distribution of gas based on their brightness temperature at a given column density, and recorded all components that were likely to be tracing parts of the L02 distribution. This enabled us to visualise, across each cloud, the two populations of gas. We show two examples of the population separation in Figure 6.8, for GHVC G273.0−70.2+375 and GHVC G310.5−68.8+162. The blue circles represent the spectral components that correspond to the bulk of the distribution, whereas the cyan triangles highlight components that overlap with L02.

Of our total sample of 10455 useable spectra, 7796 spectra are classified as part of the dense population and 2659 spectra are classified as part of the diffuse population, giving relative percentages of 74.6% and 25.4% respectively. If we consider what fraction of the 534 GASS HVCs used in our analysis have at least one diffuse spectral component, we find this comes to a total of 241 clouds (~45%), with ~55% of the GASS HVC sample of clouds containing only dense spectral components with no evidence of diffuse gas. Comparatively, just 18 clouds (~3%) feature solely diffuse components, with diffuse components comprising an average of 13% of the total spectral components found in the GASS HVCs.

We can also consider the spatial location of each population, by calculating the angular distance between the cloud core of each GASS HVC and its associated spectral components. We show the results for this in Figure 6.9, with a normalised histogram (such that the area underneath is equal to 1) for both the diffuse and dense populations. Although there are fewer diffuse components evident in GASS, we see that the diffuse components are generally further away from the cloud cores while the dense components are closer. This result is consistent with the idea that diffuse gas traces the edge of HVCs, while dense gas is correlated with HVC cores.

Quantitatively, we find that the median distance for dense gas is ~0.2° and the median distance for diffuse gas is ~0.4°, while the mean distance for dense gas is ~0.3° and the mean distance for diffuse gas is ~0.65°. This suggests that generally, diffuse gas is located twice as far away from the core of an HVC as the dense gas.

What does the average diffuse vs. dense spectrum look like?

Based on our analysis so far, we have separated all available GASS HVC spectral components into one of two populations: diffuse faint components that are similar to those found by L02, and dense components that are brighter, narrower and generally coincident with the cores of HVCs. We can visualise what the average spectrum of each population type looks like, in order to gain an insight into the physical properties of each population on a large scale. To do this, we obtained the actual spectrum corresponding to each GASS spectral component, shifted the peak fitted velocity to be centralised at 0 km s^{-1}, and over-plotted each spectrum onto a plot of either diffuse or dense components respectively. We only considered spectra which met the same criteria as our scatter plots: not associated with flagged clouds, $|v_{LSR}| \geq 90$ km s^{-1} and $N_{HI} > 10^{18}$ cm^{-2}. In addition, they also had to have available spectral data spanning ±55 km s^{-1} (diffuse) or ±30 km s^{-1} (dense) of the central peak. Due to contamination of bright signal evident through inspection (associated with spiral arms rather than isolated clouds), any diffuse spectra with peak $T_B > 1$ K were removed. With these filters applied, this came to a total of 1139 diffuse components and 6522 dense components.

We show the average (solid line) and median (dashed line) spectrum for both the diffuse (in cyan) and dense (in blue) population in Figure 6.10, over-plotted on all spectra used to calculate both the average and the median spectrum. A simplified version without all spectra plotted is given in Figure 6.11, where the shaded area represents the standard deviation on each spectrum to give an indication of the overall error. The median spectrum is visually more representative of the bulk of the spectra, since it is less subject to skew by extremely bright spectra. Not surprisingly, we find that the diffuse components are on average fainter and broader and the dense components are brighter and narrower. What is useful here is that there is a clear concentration of components associated with each population type, even if there is a reasonable amount of scatter around this trend.

Based on the fit to the mean diffuse spectrum, we find that FWHM$_{diff} = 34$ km s^{-1} and $T_{B,diff} = 0.27$ K. For the fit to the average dense spectrum, FWHM$_{dens} = 20$ km s^{-1} and $T_{B,dens} = 0.35$ K. In the case of the median spectrum, we find that FWHM$_{diff} = 30$ km s^{-1} and $T_{B,diff} = 0.20$ K, while FWHM$_{dens} = 21$ km s^{-1} and $T_{B,dens} = 0.29$ K. In both cases, the fit to the average diffuse gas is distinct from the fit to the dense gas with the dense spectrum being both narrower and brighter. The median fit makes the most difference in fitted properties for the diffuse gas due to the higher standard deviation in the population. Our results in both cases show that the general dense spectrum is very close

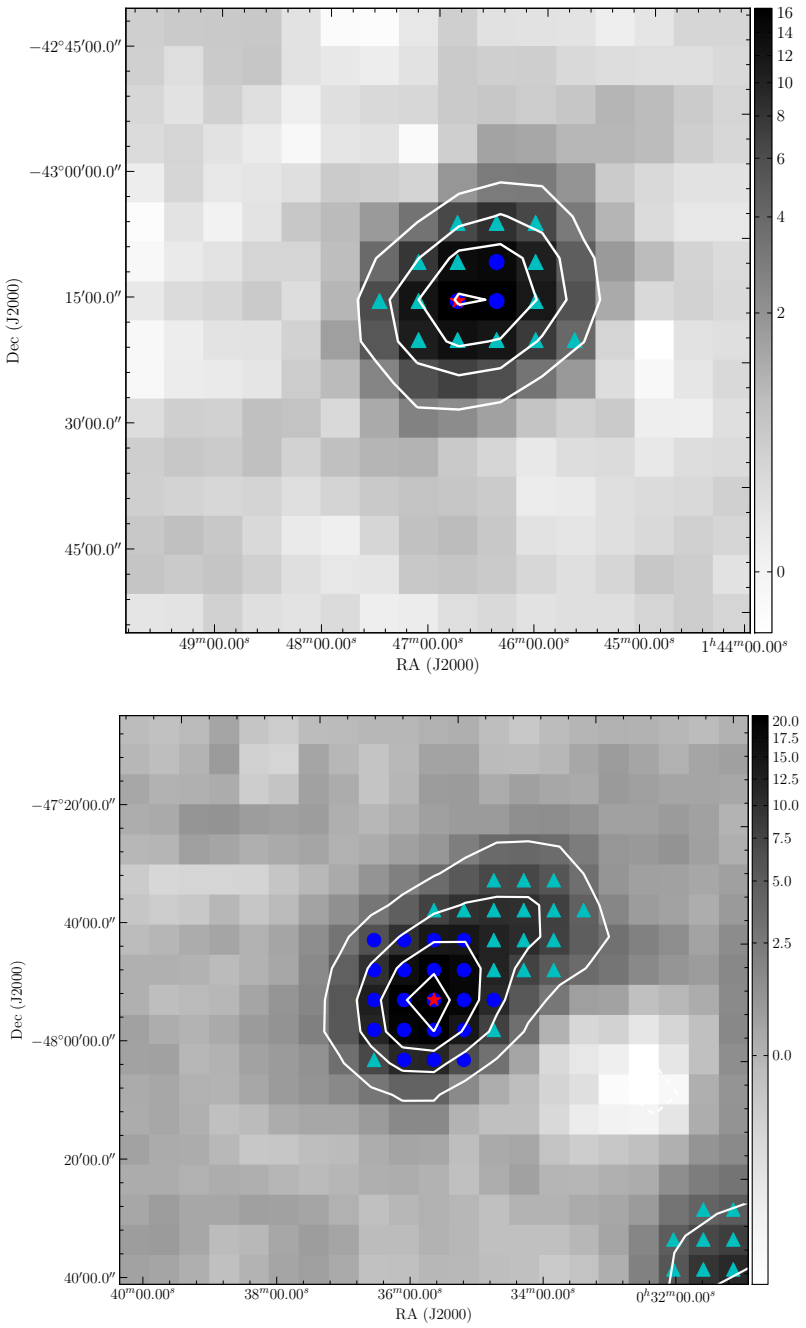

Figure 6.8: To characterise the distribution of neutral hydrogen across the GASS HVCs, we incorporated all spectra with a peak $T_B > 5\sigma$ across clouds with a maximum area of 5°. Shown here are two examples of the clouds in this sample, GHVC G273.0−70.2+375 and GHVC G310.5−68.8+162. We have divided the gas found in GASS HVCs into two populations based on overlap with the distribution of L02, and find that gas tending to overlap with L02 is found on the outskirt and in the tails of GASS clouds, tracing where the denser HVCs merge with a diffuse surrounding medium. The red star indicates the cloud core. The circles and triangles indicate the positions at which spectra were obtained of the cloud. Gas that is typical of the GASS HVC distribution in FWHM vs. N_{HI} space is shown as a blue circle, while gas that more closely follows L02 is shown as a cyan triangle. White contours at 4 equally-spaced levels from the 25% to the maximum of the image are shown to highlight the cloud.

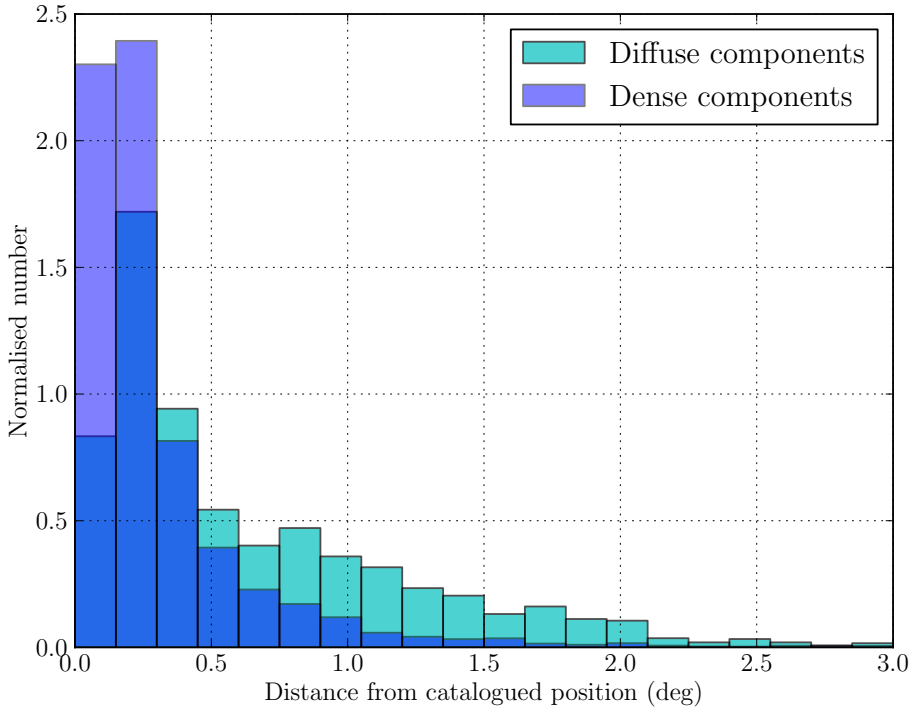

Figure 6.9: Normalised histogram of the angular distance between diffuse/dense spectral components and the cloud core of the GASS HVC with which the components are associated. There is a clear difference in the diffuse and dense populations of gas, where diffuse components are likely to be found twice as distance from the core of the HVC as the dense components. This corroborates with the diffuse gas tending to trace the edges and tails of HVCs, while dense gas traces the cores of HVCs.

to the standard spectrum of known HVCs in other surveys of ~20–25 km s^{-1} (Wakker & van Woerden, 1997; Bekhti et al., 2006; Moss et al., 2013), while the diffuse components are probing neutral hydrogen in a significantly different state that is not typically sampled by surveys of halo gas. The diffuse spectrum is broader and fainter, and in the case of GASS appears to trace the transition between the cores of HVCs and where they merge with the surrounding medium based on where diffuse components are typically found. For comparison, we also over-plot a spectrum representative of the L02 distribution, which has a median FWHM of 30.3 km s^{-1} and a median T_B of 57 mK. We see that L02 is clearly similar to the diffuse spectrum (but at a fainter level due to the lower sensitivity of GASS to the diffuse population), with the neutral hydrogen likely to be in the same physical state as our GASS diffuse components.

It is worth noting here that the angular resolution of a survey makes a significant difference to the measured FWHM, with surveys at $> 30'$ resolution finding in general broader spectra due to the merging at this angular scale of the diffuse and dense spectra. This has been pointed out by Wakker & van Woerden (1997), and was also found by Moss et al. (2013) in addressing incongruities in the spectral distribution between high-velocity gas found in GASS with a median FWHM of ~19 km s^{-1} and the Leiden/Argentine/Bonn (LAB) survey with a median FWHM of ~28 km s^{-1} (Kalberla & Haud, 2006). Given our result here where many HVCs can be separated into core components surrounded by diffuse components and the average HVC size of ~1 deg^2, the difference in measured line-width made by angular resolution is thus understandable.

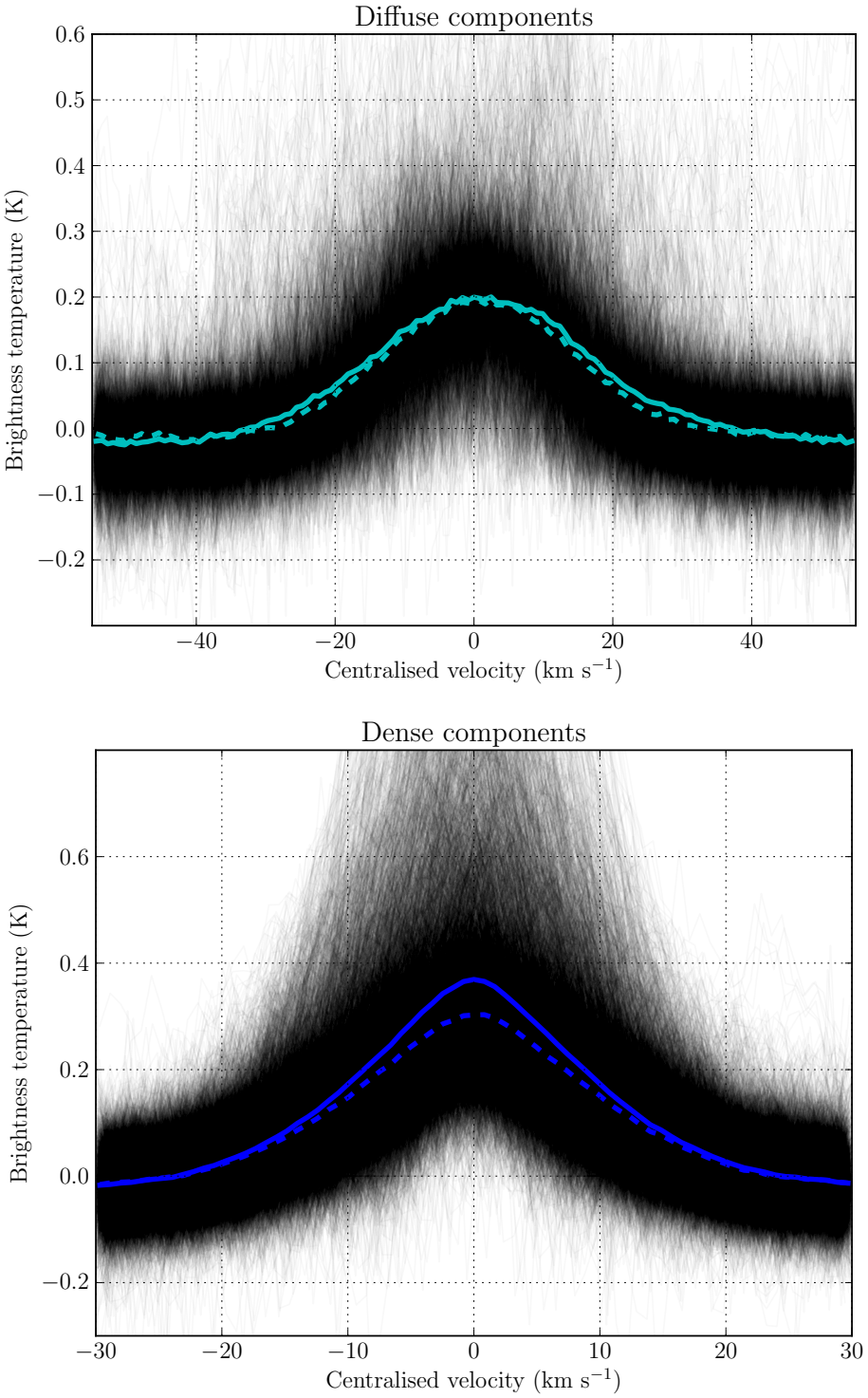

Figure 6.10: All spectral components incorporated into our analysis across the GASS HVCs are plotted in black, separated into either the dense (top) or the diffuse (bottom) population. We over-plot the average spectrum (solid line) and median spectrum (dashed line) in each case, with the diffuse spectra in cyan and the dense spectra in blue. We see that the average in both cases is skewed upwards by bright spectra, and that the median spectrum is more visually representative of the data. The diffuse components show a large degree of scatter in their structure, whereas the dense components are generally clearer and more isolated. The dense population is notably narrower in line-width than the diffuse population.

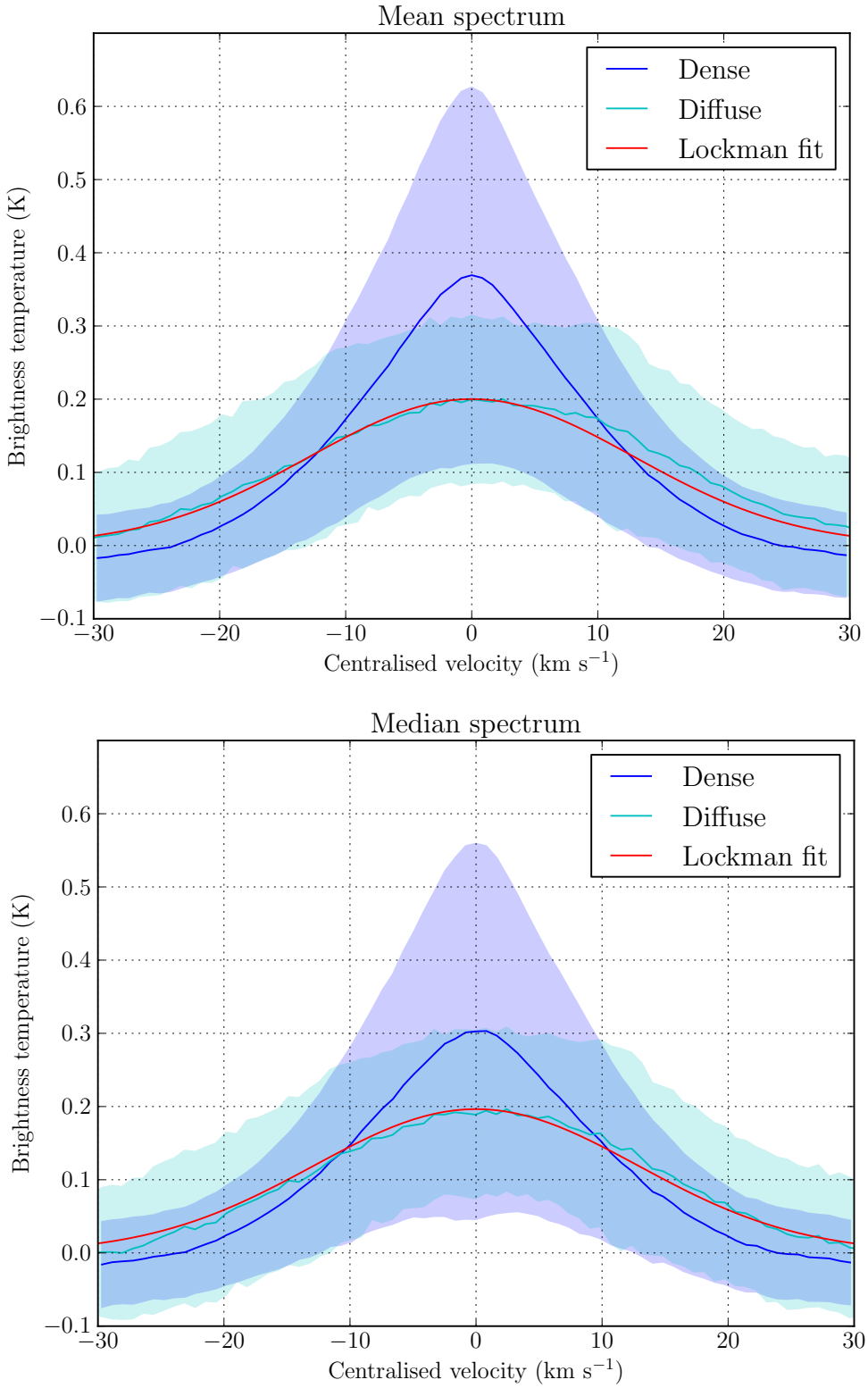

Figure 6.11: Simplified version of Figure 6.10 without the raw spectra shown. Shown are the mean spectra (top) and median spectra (bottom), for both dense components (blue) and diffuse components (cyan). The average diffuse spectrum in both cases is fainter and broader than the average dense spectrum. The filled areas represent the standard deviation of each population, giving an indication of the errors on the average spectrum in each case. For reference, we also over-plot a spectrum representative of the properties of L02 (red solid line), scaled to the peak value of the mean/median diffuse distribution.

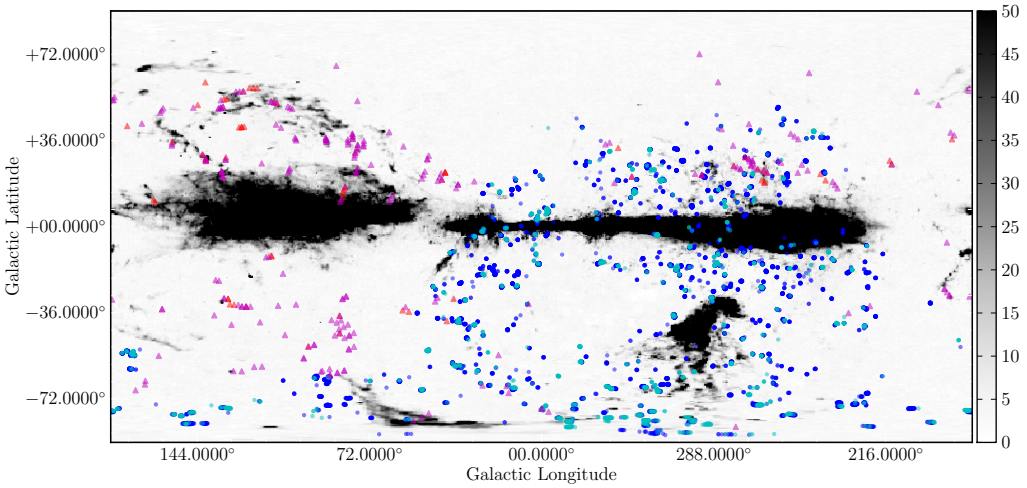

Figure 6.12: The distribution of both diffuse and dense spectral components on the sky. All components incorporated from both surveys are plotted, separated into the categories of GASS dense (blue circles), GASS diffuse (cyan circles), L02 dense (red triangles) and L02 diffuse (magenta triangles). Both types of gas are found all over the sky, with no obvious region of preference. The background map is the integrated-intensity Leiden/Argentina/Bonn survey of HI (Kalberla et al., 2005), excluding emission at velocities $|v_{LSR}| < 90$ km s^{-1}.

Sky-covering fraction of the diffuse and dense halo gas

Based on the information about the Galactic halo revealed by both the GASS HVC population and the L02 distribution, we obtain a new understanding of the neutral hydrogen halo of the Milky Way. In the GASS HVCs, we found that our polynomial fit to the L02 data results in 74.6% GASS HVC spectra classified as dense components, while 25.4% are classified as diffuse components that overlap with the faint population revealed in L02. Our average and median spectra calculations were performed on the filtered sample described previously, with the relative proportions shifting to 85.1% and 14.9% respectively. Given this spread in relative proportion, we can represent the fractions in GASS as ~80% dense components and ~20% diffuse components. In general, we see that the dense components dominate the GASS sample, which is a strong function of the limited sensitivity of GASS to faint diffuse components compared with L02. We plot both samples on the Galactic sky in Figure 6.12, with the GASS population shown in blue (dense components) and cyan (diffuse components) circles and L02 shown in red (dense components) and magenta (diffuse components) triangles. We see that the combined populations cover a significant proportion of the Galactic halo, and together can offer an insight into structural halo information not previously seen in other surveys of HI.

By combining these two results, we can state some clear expectations about the structure of our halo. The majority of the sensitive L02 sample falls into the diffuse category. Tracing the gaseous outskirts of clouds at high velocity, detections were made in 37% of their 860 sightlines through the Galactic halo. However, since the survey randomly sampled the halo, we expect some fraction of sightlines through dense neutral hydrogen. To put a number on this, we count all L02 spectra that lie above or below the polynomial fit to the data described in Section 6.3 with a column density $N_{HI} > 5 \times 10^{18}$ cm^{-2}, in order to ensure that these spectra overlap with the dominant GASS distribution. This reduces the total L02 sample to 128 components (42% of the total sample). Of these 128 components, we find that 33 are likely associated with the dense population and 95

Table 6.1: Mass fraction estimates for neutral hydrogen in the halo.

Column density	Dense HI	Diffuse HI	Mass fraction ($N_{H,dens}$)	Mass fraction ($N_{H,diff}$)
$N_{H,GASS}$	0.80	0.20	0.73–0.82	0.18–0.27
$N_{H,L02}$	0.80	0.20	0.84–0.91	0.09–0.16
$N_{H,GASS}$	0.25	0.75	0.18–0.28	0.72–0.82
$N_{H,L02}$	0.25	0.75	0.30–0.46	0.54–0.70

are likely associated with the diffuse population. The number of dense components is a relatively high fraction because the polynomial fit in Section 6.3 limited the L02 spectral components to only those located in the overlap region described in Section 6.3. If we convert these to percentages, than we see that the fraction are reversed compared with the GASS sample, with ~25% dense components and ~75% diffuse components.

This indicates, based on a random sample through gas in the halo, that we would expect to find dense gas to diffuse gas in the ratio of 1:3, suggesting that every dense portion of HVC is surrounded by a diffuse medium that covers 3 times as much area on the sky. In GASS, we find the opposite ratio, where dense to diffuse is in the ratio of 4:1. This suggests that in the worst case, due to sensitivity limits, we could be sampling as little as 1/12th of the total neutral hydrogen in our HVC population. Considering the result of Lehner et al. (2012), who found that 74% of their HVC directions featured column densities $N_{HI} < 3 \times 10^{18}$ cm^{-2}, we would expect that GASS would be sensitive to < 25% of the total HI in the halo. Regardless of the exact fraction, it is clear here that studies of HVCs based on large-scale relatively shallow surveys will not accurately sample the diffuse gas, which explains why UV absorption studies through the Galactic halo indicate the presence of more HI than suggested by typical surveys of high-velocity gas in the halo.

If we estimate the average column density (Equation 6.1) of diffuse vs. dense gas from the averaged GASS spectral components (given their large number to be representative of the two populations), we find that these come to be $N_{H,dens}$ = [1.17, 1.34] × 10^{19} cm^{-2} and $N_{H,diff}$ = [1.15, 1.76] × 10^{19} cm^{-2} for the median and mean spectrum properties respectively. While again there is scatter in this result, it implies that the total mass associated with the diffuse HI is likely to be 3–4 times that of the total dense HI, under the assumption that the more sensitive L02 is better representative of the dense and diffuse relative fractions in the halo. That said, we note that the properties of the diffuse population as sampled by GASS are skewed upwards by the GASS sensitivity and as such may be biased to higher column densities than realistic.

By comparison, the average column densities based on L02 are $N_{H,dens}$ = [2.71, 2.88] × 10^{19} cm^{-2} and $N_{H,diff}$ = [1.14, 2.06] × 10^{19} cm^{-2} for the median and mean properties respectively. Repeating the same analysis as above, we find that the diffuse gas may be a tiny fraction of the total HI if the GASS spectral components represent the true ratio of dense and diffuse gas, with a more extreme divide due to an overall higher column density of dense gas as measured in L02. However, if we assume again that L02 is better representative of the dense and diffuse proportions in the halo, then we find the diffuse gas estimated to be approximately equal up to just over two times that of the dense gas. We have summarised all mass fraction estimates in Table 6.1, assuming that: 1) either GASS or L02 better represent the ratio of dense to diffuse gas, and 2) either the average N_{HI} of GASS or L02 is better representative of the overall population. The ranges are given by using the mean or median spectrum.

Overall, it seems reasonable to assume that L02 probes closer to the actual relative proportions of dense versus diffuse gas in the halo of the Milky Way, and as such we

conclude that the diffuse gas is likely to contribute as much mass as the dense gas, and potentially up to 4 times as much. Our results also highlight the potential danger in using sensitivity-limited surveys to measure mass: the same results based on the GASS division of spectral components suggest that dense gas dominates the halo, which is unlikely to be true given the results and much higher sensitivity of L02. A caveat of this analysis is that our GASS HVC spectral components are taken from clouds with a total area < 5 deg^2, and this limit excludes 58 of the 1988 possible HVCs and AVCs in the GASS catalogue. These 58 clouds are not an insignificant fraction of gas in the halo, including the Magellanic system, the Galactic centre region and Complex L amongst their number. Excluding those with $|v_{LSR}| < 90$ km s^{-1} as we have done in our analysis here, this number drops to 34 clouds. However, these clouds stretching over several degrees are not typical of the general Galactic halo, which in the GASS catalogue is comprised largely of small clouds < 5 deg^2. As such, we see our analysis as being applicable to the general halo away from large-scale extreme cases such as the Magellanic system and the Galactic centre, although it is likely that these cases provide insight into the origin of the clouds we analyse and are comprised of similar kinds of clouds on smaller scales.

6.4 Conclusion and future work

We have combined two significantly different samples of neutral hydrogen in the halo of the Milky Way, in order to better understand the structure of halo gas: the very sensitive 21 centimetre Green Bank survey for high-velocity HI (Lockman et al., 2002), and a sample of bright HVCs identified in the Galactic All Sky Survey (Moss et al., 2013). These two samples of gas with their very different properties provide a complementary picture of the halo, with the L02 distribution sampling the halo with high sensitivity (~3.4 mK) at random positions and the GASS HVCs representing bright condensations of gas in the halo above a brightness of 4σ (~230 mK). As such, we gain a new insight into the distribution of both dense (bright, narrow line-widths and relatively cold) and diffuse (faint, broad line-widths and relatively warm) high-velocity neutral hydrogen gas in the halo of the Milky Way. We have discovered in the GASS sample evidence for two distinct populations of gas: the dense distribution which is in accordance with the majority of GASS spectra, and the diffuse distribution which aligns with L02. Based on the L02 data, we find that ~75% of GASS spectra are classified as dense and ~25% are classified as diffuse.

By separating the spectra into these two distributions, we can then visualise the spatial location of each type of gas across the GASS HVCs. We find that the low-brightness, broad-FWHM population of L02 corresponds largely with the edges and tails of the GASS HVC population, identifying where HVCs merge with the prevalent diffuse gas of the Galactic halo. Conversely, the dominant dense components are found in the cores of HVCs. When considering the angular distance between GASS HVC spectral components and the cloud core of the host HVC, the median distance for dense gas is ~0.2° and the median distance for diffuse gas is ~0.4°, while the mean distance for dense gas is ~0.3° and the mean distance for diffuse gas is ~0.65°. This reveals that diffuse gas is located twice as far away from the core of an HVC as the dense gas, which is consistent with diffuse gas as tracing the edges and tails of HVCs. The diffuse gas population is faint in neutral hydrogen, but may be tracing the transition from the cold neutral hydrogen cores to warmer ionised hydrogen envelopes surrounding HVCs as indicated by Lehner et al. (2012).

This division into two populations of gas allows us to visualise what the typical dense or diffuse spectrum looks like, by calculating the mean and median spectra of each type

of gas. We find that the dense distribution of gas is typical of the common properties of HVCs, with a FWHM ~ 20 km s^{-1} and a brightness temperature of T_B ~ 0.3 K, while the diffuse distribution has a FWHM ~ 30 km s^{-1} with a brightness temperature of T_B ~ 0.2 K, which are well-aligned with the median FWHM of 30.3 km s^{-1} and median brightness temperature of 0.057 K found by L02, although the GASS data is sensitivity-limited compared to the L02 sample. Our findings explain the strong effect that angular resolution has on the measured line-widths of HVCs, given their typical angular size of ~1 deg^2 and their blurry edges which merge with a diffuse population of faint, broad line-widths.

These two samples of high-velocity halo gas offer a new insight into the distribution of gas in our Galactic halo, and how survey sensitivity has the potential to affect the population of gas detected. We find that the GASS HVCs feature dense and diffuse components in the ratio of 4:1, while L02 reveals dense and diffuse components in the fraction of 1:3 over the same column density range. This suggests that the less sensitive GASS data is only just beginning to probe the diffuse gas, and may only be sensitive to only 1/12th of the total diffuse gas that could be present surrounding the GASS HVCs. With regards to sky-covering fraction, under the assumption that GASS better traces the physical properties of dense/diffuse neutral hydrogen due to its all-southern-sky coverage and that L02 better traces the ratio of diffuse to dense components, we find that diffuse HI is likely to be 3–4 times more common than dense HI in the halo based on these observations of neutral hydrogen alone.

This is congruent with findings based on UV/optical/X-ray absorption of Milky Way gas arguing the presence of more HI in the halo than revealed by typical surveys of neutral hydrogen, as well as for the dominance of diffuse gas rather than dense gas. These results also agree well with previous findings arguing that classical HVCs cannot account for the Galactic star formation rate alone, with the largest HVC complexes contributing only ~0.08 M$_\odot$ yr^{-1} (Putman, Peek & Joung, 2012), compared with the estimated star formation rate of the Milky Way of ~1 M$_\odot$ yr^{-1} (Robitaille & Whitney, 2010). The origin of the diffuse gas we detect is potentially part of supernova-driven accretion of coronal gas controlled by the Galactic fountain cycle (Fraternali et al., 2013a), where cooling and entrainment of low-metallicity coronal material by passing Galactic metal-rich clouds may be able to completely account for the star-formation rate of the Milky Way. Here, classical HVCs may be a non-Galactic phenomenon unrelated to the fountain cycle but experiencing similar halo interaction and UV absorption (Marasco, Marinacci & Fraternali, 2013), or they may be embedded condensations within warm inflowing gas predicted in simulations (Joung et al., 2012). Similar to the question of the origins of the HVC population, the reality will likely be a combination of both of these influences which thus contribute to the observed Galactic star formation rate. Based on our results for the Milky Way, we have confirmed the existence of two populations of neutral gas in the Galactic halo. The dense distribution is typical of the majority of bright high-velocity gas, while the diffuse distribution is more widespread and far more difficult to detect, although generally associated with the edges of the dense gas. In this picture, we can understand HVCs as the bright dense cores within a ubiquitous diffuse medium surrounding most complexes of neutral hydrogen as they interact with their surrounding environment.

But to what extent is the Milky Way and its halo typical of galaxies in general? With very wide-field radio instruments like ASKAP (Johnston et al., 2007) and ultimately the Square Kilometre Array (Dewdney et al., 2009) coming online, together with the enhanced optical survey capabilities of integral-field spectrographs like WiFEs (Dopita et al., 2007) and SAMI (Croom et al., 2012), we will be in the position to measure the spatial properties

of galactic haloes with unprecedented resolution in order to compare our understanding of the Milky Way's halo with that of other nearby galaxies in the local Universe. It will be critical to understand the ionisation fraction of the diffuse envelopes we see around HVCs, its effect on the overall cloud lifetimes and how this influences the Galactic halo cloud population. This will enable us to see where our Galaxy fits into a larger picture of disk-halo interaction, how strong an effect is played by our interaction with the Magellanic system, and how the distribution and physical state of gas changes depending on the particular galaxy's formation history, dynamics, interactions and evolutionary track.

Chapter

7

THE FUTURE PROSPECTS OF GALACTIC ECOSYSTEM STUDIES

Overview

A summary of the outcomes and conclusions of each chapter of this thesis. Particular emphasis is placed on future directions of research in the field and the exciting and important possibilities in continuing study of galactic ecosystems.

7.1 Introduction

At the beginning of this thesis, I focused on four key aspects of the study of disk-halo interaction. These form critical components in understanding galactic ecosystems, explaining the ongoing star formation rate of the Milky Way, and determining the eventual fate of our galaxy. The four aspects revolve around our ability to:

1. determine how neutral hydrogen gas escapes into the halo from the disk,
2. catalogue and characterise neutral hydrogen present in the halo,
3. differentiate between halo gas that is Galactic or extragalactic in origin,
4. measure the physical properties of gas in the halo to understand both individual clouds and large-scale structure.

In the conclusions presented here, I summarise the outcomes of findings relative to each of these four aspects and identify areas of future investigation to further advance current understanding of Milky Way disk-halo interaction.

7.2 Determining the escape of neutral hydrogen into the halo from the disk

The study of GSH 006−15+7 provides an illuminating insight into the evolutionary characteristics of a supershell nearing blowout. Its lack of kinematic signatures combined with estimated dimensions (reaching a scale height of ~1 kpc) suggests that it is near the end of its life as a coherent gaseous structure, soon to fragment and allow material to escape into the halo. The fortunate positioning of GSH 006−15+7 against the bright Galactic background allowed us to observe and measure HI self-absorption along the edge

of the shell wall, giving a rare insight into the thermal properties of the gas comprising the supershell. We were able to constrain the spin temperature of the shell wall to be 40 K, with the kinetic temperature being roughly equal to this in cold neutral medium gas for temperatures $T_k < 1000$ K. The presence of HI self-absorption in the shell wall allowed us to measure the true opacity of the gas (rather than assuming it to be zero as is typical in studies of the ISM), modifying our measurements of optical depth to be $\tau \sim 3$ which in turn increased our mass and density estimates by up to a factor of five. The coherent morphology of the supershell also passes through the Galactic disk, allowing us to search for likely source regions associated with the formation of GSH 006−15+7 at a kinematically-estimated distance of 1–2 kpc. We found evidence for an origin in the open clusters NGC 6514, NGC 6530 and NGC 6531 combined with the OB association Sgr OB 1, with their estimated stellar wind and supernovae contributions close to that required to form the supershell.

The age of GSH 006−15+7 precludes the detection of the bright multi-wavelength signatures often found in the younger superbubbles, such as in the Orion-Eridanus superbubble. However, a high-latitude Hα feature (named the Cuttlefish because of its morphological similarities to the cephalopod) was discovered near the wall of the supershell, at the largest distance above the disk where the supershell would be likely to fragment first. We were able to confirm spectral agreement between HI and Hα using the Wisconsin H-Alpha Mapper at a velocity of ~7 km s^{-1}. We have since combined this result with follow-up in the optical emission lines of Hα, Hβ, [S II], [N II], [O III] and He I, with strong detections in all lines despite their high energy requirements for ionisation. We also obtained high-resolution HI observations with the Australia Telescope Compact Array to resolve the HI at a more comparable resolution to that of Southern H-Alpha Sky Survey Atlas, identifying that the Hα emission traces the edge of the HI emission suggesting a complex interaction where the ionised gas is offset from the neutral gas. In our preliminary analysis, we have been able to rule out all possible origins except for supershell association, extremely nearby planetary nebulae and nearby supernova remnants.

GSH 006−15+7 is a unique supershell in a population comprised largely of younger supershells with clear expansion signatures and older supershells with very little coherent structure. Given its size and age, it should be starting to undergo the process of fragmentation. If the Cuttlefish, as well as the filamentary HI associated with it, is the first signature of this fragmentation beginning to take place, this will place GSH 006−15+7 in the position of being the only supershell discovered so far that is undergoing this transition from supershell to chimney with detectable multi-wavelength signatures. This transition process is critical in understanding the escape of neutral hydrogen from the disk into the halo of the Milky Way.

Spatial mapping of optical emission lines will allow us to measure emission line ratios across the region, and combining these measurements with modelling of the radiative transfer ionisation necessary to produce the Cuttlefish will help to rule out particular origins such as supernova remnants depending on the ionisation structure. Obtaining observations of [S II] λ6731 and [N II] λ6548 to complement our existing measurements of [S II] λ6716 and [N II] λ6584 will allow us to place the Cuttlefish exactly on diagnostic diagrams, and its proximity to different populations within those diagrams will also aid identification of its origin. While an origin in association with the fragmentation of GSH 006−15+7 would be a useful probe of supershell blowout and the process of outflow from the disk into the halo, the high-energy signatures of the Cuttlefish at a large latitude above the disk render it an intriguing astrophysical object regardless of its origin.

7.3 Cataloguing and characterising neutral hydrogen in the halo

The Galactic All Sky Survey (GASS), updated to include stray-radiation correction, offers an in-depth view into the southern Galactic sky as mapped by neutral hydrogen gas. The combination of reasonable sensitivity, angular resolution, sensitivity to large-scale structure and high velocity resolution made GASS an ideal survey to provide a catalogue of neutral hydrogen in the halo of the Milky Way, resolving for the first time the spectral sub-structures of southern sky HVCs on a large scale.

We catalogued a total of 1988 clouds as part of the GASS catalogue of HVCs, including 1693 clouds traditionally classified as HVCs based on their velocities and 295 clouds which fall below typical velocity cutoffs which we defined as AVCs. The resulting catalogue is the most up-to-date survey of southern sky neutral hydrogen with high enough spectral resolution to fully resolve the spectral structure of the majority of clouds and will be of use to studies of halo gas on both small and large angular scales, although high-resolution follow-up will still be necessary to trace physical substructures within clouds such as compact cores. The identified AVCs trace the tenuous boundary between intermediate and high-velocity clouds, and will be useful in providing steps towards a classification of HVCs based more on physical properties than on arbitrary velocity cutoffs.

The next key developments in cataloguing and measuring the properties of neutral hydrogen in the halo of the Milky Way, particularly in the southern sky, lie in two directions: increasing angular resolution and increasing sensitivity. The Australian Square Kilometre Array Pathfinder (ASKAP), a precursor instrument to the Square Kilometre Array, will be a ground-breaking instrument in completing high-resolution large-scale surveys on short time-scales. Although ASKAP will be prioritised for optimal completion of extragalactic continuum and spectral-line surveys, its baseline structure is well-suited to Galactic surveys and its operational frequency range of 700 MHz to 1.8 GHz easily includes all Milky Way neutral hydrogen emission. Galactic HI using ASKAP will be mapped on 30–60″ scales using the shortest baselines, and absorption towards continuum sources will be possible at 10″ resolution (Dickey et al., 2013). The Galactic component of ASKAP, GASKAP, consists of four different surveys as shown in Figure 7.1: the low-latitude disk, the intermediate-latitude disk, the Magellanic clouds and the Magellanic Leading Arm/Bridge/Stream. Of most interest to HVC studies will be the relatively large area covered by the last of these surveys, which will naturally include halo gas that is not associated with the Magellanic system as part of its spatial coverage.

The low-latitude and intermediate-latitude surveys will also be of great use in the context of AVCs, for mapping the bridge between the disk and the halo, for identifying halo clouds that are less distinguished from Galactic emission than high-latitude HVCs and IVCs and for potentially identifying new populations such as those seen in Peek et al. (2009) and Saul et al. (2012). To analyse these cloud populations in a large-scale automated way will not be possible using current popular source-finding algorithms such as flood-fill or Gaussian fitting due to confusion of emission. New techniques for identifying embedded emission will be necessary such as the wavelet reconstruction implemented by Flöer & Winkel (2012) and Whiting (2012), although this method performs best for more isolated emission and will require adaptation for most use in identifying low-velocity halo clouds. In all cases, the 5.5°× 5.5° field of view of ASKAP will enable high sensitivities to be reached in relatively short amounts of time, although GASKAP is still expected to be take 8000 hours to complete at three different sensitivity levels.

In terms of increasing sensitivity, the Five-hundred-meter Aperture Spherical Radio

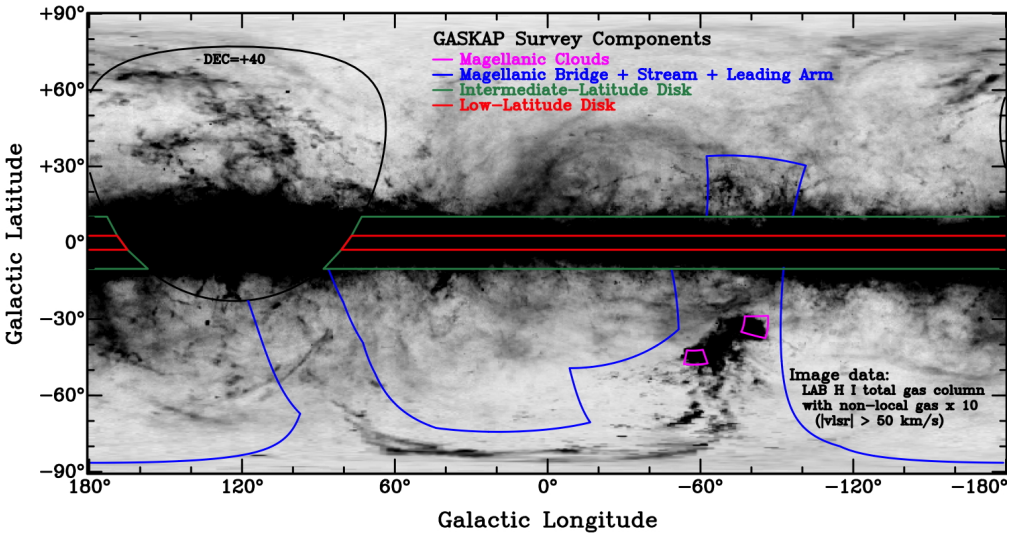

Figure 7.1: All-sky map of the Milky Way in neutral hydrogen, showing the planned GASKAP survey components: Magellanic Clouds (pink), Magellanic Bridge/Stream/Leading Arm (blue), Intermediate-Latitude Disk (green) and Low-Latitude Disk (red). Image is from Dickey et al. (2013).

Telescope (FAST) under construction in China will be the world's first 500-m and most sensitive radio telescope with an effective illuminated aperture of 300-m (Nan et al., 2011; Li, Nan & Pan, 2012). It is expected to be able to observe as far south as the Galactic centre, with a predicted zenith angle coverage of 40° to 60° (depending on whether different feed technologies such as phased-array-feeds can be employed). FAST is predicted to be three times more sensitive than the 300-m Arecibo telescope and if so will be able to probe neutral hydrogen emission at flux density levels never before detected. While it will not necessarily aid large-scale surveys for HVCs, particularly in the southern sky, FAST will be able to image individual HVCs at a resolution comparable to current interferometers ($2.9'$) but with extraordinary sensitivity, offering potential for probing entirely different physical aspects of the HVC population.

7.4 Differentiating between halo gas of Galactic and extragalactic origin

The main aim of studying subsets of clouds sampled from different known regions in the Galactic halo was to ascertain whether there were any thermal or kinematic signatures that distinguished clouds of Galactic origin from clouds of extragalactic origin. We selected clouds associated with different regions based on their position and velocity, and included previously observed clouds associated with the Leading Arm and with the halo above a star-forming region. Our sample of 15 clouds, while not exhaustive, incorporates the Magellanic Leading Arm, Complex L, Galactic Centre Negative and halo clouds associated with a star-forming region. We analysed the clouds of our sample using spatial visualisation of spectra and physical properties across clouds, line-width trends with height above the disk and the KS-test of both clouds against clouds and clouds against distributions representing either the Galactic or extragalactic population. We found evidence for consistency amongst the clouds of extragalactic origin in this sample (associated with the

Magellanic system and Galactic Centre Negative), particularly traceable in the distribution of line-width across clouds. Galactic clouds, conversely, feature far more dispersion in all of their physical properties. These preliminary results on a relatively small sample of clouds across different regions in the Milky Way are promising in helping to determine cloud origin and dynamics along with other diagnostic measures in both HI and other wavelengths.

There are a few obvious steps to further the results of this study. Increasing the size of the sample with a selection of clouds from other regions, both Galactic and extragalactic in origin, will be particularly useful in order to determine whether the KS-test on line-width distribution remains a useful diagnostic for identifying clouds of likely extragalactic origin. Another important selection effect applied to our current sample was an emphasis on narrow line-widths and on clouds with multi-component spectral structure as a tracer of interaction. In order to check whether our results apply to a wider sample of clouds and how line-width affects the comparability of HVCs, the same comparison of Galactic with extragalactic clouds (of similar line-width) should be completed, ideally with clouds selected from the same regions as our current sample as well as from elsewhere.

Finally, we note that our key result from the KS-test comparison indicates that clouds of extragalactic origin typically feature narrow, coherent line-widths. Both clouds from the Magellanic Leading Arm and Galactic Centre Negative are expected to have passed through the Galactic disk already, and hence would be in an advanced state of interaction with the disk-halo medium. It is vital to compare these clouds with clouds of extragalactic origin that are in an earlier, pre-disk stage of evolution to see whether it is primarily the effect of passing through the disk that has produced their observed spectral features. An obvious candidate region for selecting clouds for this sample would be near the Magellanic clouds, in the region closest to the disk but not currently passing through, as these clouds may likely follow the path of the Magellanic Leading Arm in future.

7.5 Measuring the physical properties of gas in the halo

Our work in combining the results of the GASS catalogue of HVCs with the high-sensitivity sightline survey of Lockman et al. (2002) enabled us to study the structure of the Milky Way halo as traced by both bright dense clouds and by ubiquitous faint diffuse gas. The two different populations of gas, classified as dense (the bright narrow-line clumps found in the form of HVCs) and diffuse (the faint broad-line gas widespread in the halo), are the key components of neutral hydrogen in the Galactic halo. We used the L02 distribution to separate GASS spectra across HVCs into either of the two distributions, in order to gauge what fraction of each population is sampled by the less sensitive but southern-sky complete GASS data. We found that the diffuse gas is typically found at the edges and in the tails of classical HVCs, identifying where bright clumps merge with the diffuse surrounding gas.

We were also able to construct the average dense and diffuse spectrum as detected in GASS, comparing this result with the L02 sample. Overall the dense gas is found to have a line-width of ~20 km s^{-1} while the diffuse gas has a line-width of ~30 km s^{-1}, with the diffuse gas also being significantly fainter although its true brightness temperature distribution is not properly sampled by GASS and is better reflected in the L02 data. Dividing both the GASS and the L02 spectra into the dense or diffuse population, we find that GASS features 25% diffuse and 75% dense gas while L02 finds 80% diffuse and 20% dense gas. This suggests that typical surveys of HI are, not surprisingly, targeting the brightest neutral hydrogen in the Galactic halo and may only be sampling as little

as 1/12th of the total neutral hydrogen content present. Our results also suggest that the diffuse gas could contribute up to 4 times more neutral hydrogen to the halo than the dense component, with the total neutral hydrogen content in better agreement with surveys of the halo in UV absorption lines.

There are various avenues to proceed with from this critical result. We addressed selection effects that could potentially arise from the various differences between the two surveys, the most important two being angular resolution ($15'$ versus $21'$) and sky coverage ($\delta < 0°$ versus $\delta > -40°$). A key way to remove both of these selection effects would be to complete a survey equivalent to that of the L02 survey with the Parkes radio telescope, in order to obtain a randomly-sampled sightline survey that matches the GASS data both in angular resolution and in sky coverage. The 64-m diameter of Parkes is 50% larger than the 140-ft diameter of the Green Bank telescope used for L02, and as such would require considerably less integration time to achieve a southern survey of equal sensitivity. Further, L02 spectra at declinations $\delta < 0°$ would be observable by Parkes to check consistency and agreement between the two surveys. Conducting this survey of the southern sky to match L02 would be of high priority in continuing this work.

Similarly, comparing the L02 survey in the same way with a GASS-equivalent set of spectra across HVCs covering the northern hemisphere would also be of importance, particularly in separating the effects of the Magellanic system from that of the overall halo. Combining the results of this work with information on sightlines as revealed by UV absorption as well as comparing it with the expected structures based on the findings of Fraternali et al. (2013a) may also help reveal the dominant origin of HVCs and how the dense-diffuse structure of the Milky Way halo initially came into existence. In addition, our results have important implications for other nearby galaxies that can be resolved with current radio instruments. Future radio telescopes such as the SKA will have the angular resolution necessary to resolve HVCs in other galaxies, and will potentially render this kind of analysis possible in the haloes of nearby galaxies other than the Milky Way. Even on larger spatial scales than our analysis of the Milky Way, it would be illuminating to complete this analysis of dense and diffuse gas in other galaxies to investigate the effects of galaxy mass, luminosity, star-formation activity, age and metallicity on the properties of the neutral hydrogen halo as divided into the two populations of gas we find in the Milky Way.

7.6 The Galactic ecosystem: a new picture

This thesis has sought to investigate the Galactic ecosystem, which encapsulates the influential and connected processes of infall, outflow and circulation in the Milky Way. The structure and content of the Galactic halo is known to be balanced by two forces: the explosive ability to expel gas into the halo and the cannibalistic ability to accrete new gas. Through the studies presented here of supershells, high-velocity clouds and large-scale halo structure, it is possible to illuminate critical new aspects of the overall ecosystem that determine the future of our home Galaxy. These key results are summarised schematically together in Figure 7.2, in the environment of the Milky Way.

How has current understanding of the Galactic ecosystem been modified by the outcomes presented in this thesis? It remains clear that both expelled gas from the disk and accreted gas from external sources play an important role in the wider functioning of the Milky Way. Supershells, linked to extreme star-formation activity in the disk, are still one of the most likely avenues by which disk gas can escape into the halo, and may be responsible for multi-wavelength signatures at high Galactic latitude. The observed kinematic

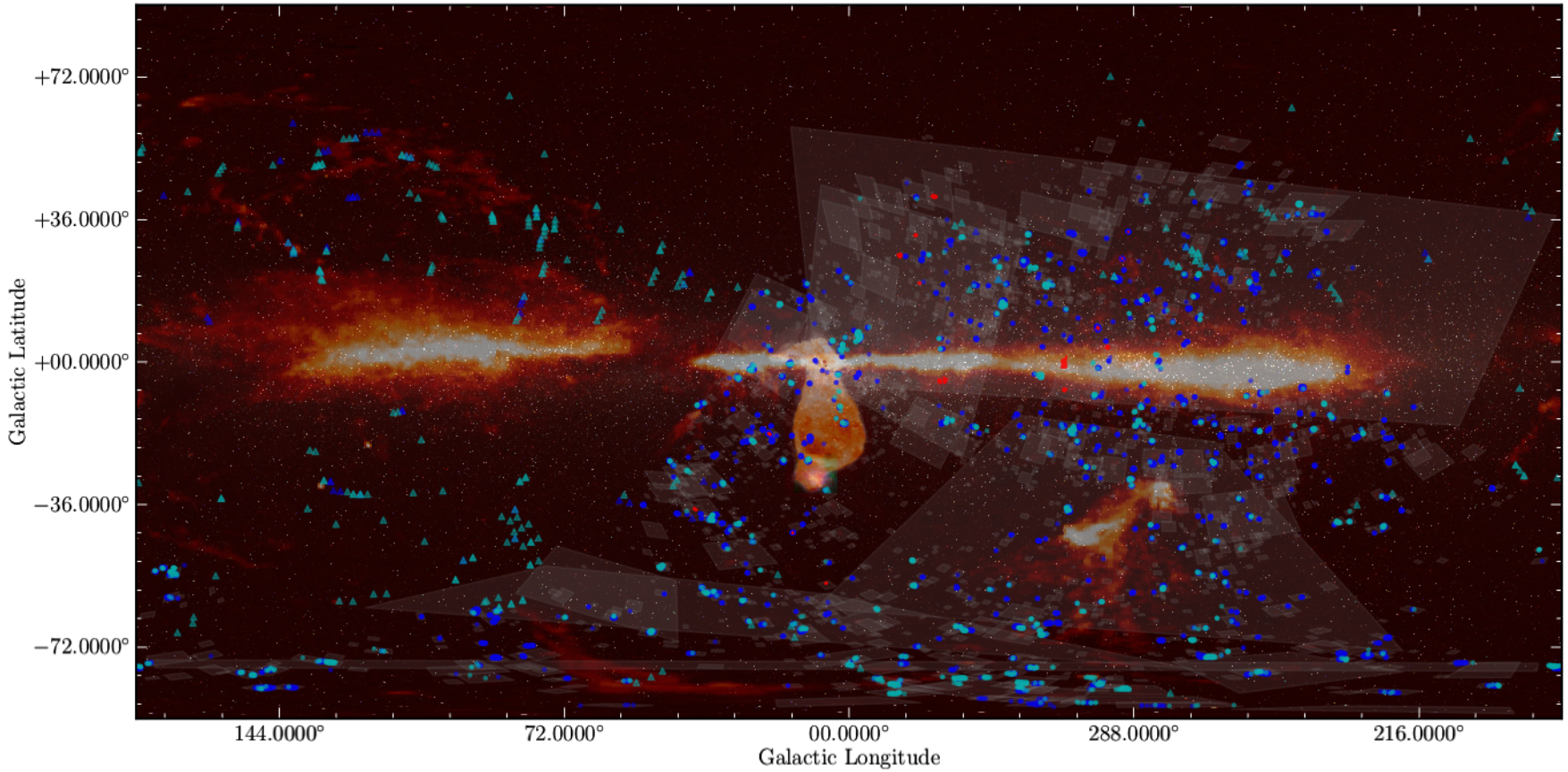

Figure 7.2: A new picture of the Galactic ecosystem, based on the outcomes of this thesis. Included in the image is data from every chapter excluding the introduction: 2) GSH 006−15+7 shown as an overlay in neutral hydrogen, 3) the Cuttlefish RGB image from WHAM, in Hα (red), S [II] (green) and O [III] (blue), 4) the GASS HVC and AVC population shown as transparent white boxes reprojected from zenith-equal-area coordinates, 5) all 15 clouds from the interacting HVC sample shown as red contours, and 6) the GASS HVC (circles) and L02 spectral components (triangles), divided in the dense (blue) and diffuse (cyan) population. All data is first overlaid on the LAB HI survey masked below $|v_{LSR}| < 90$ km s^{-1} to show the location of high-velocity HI. Finally, the Milky Way panorama of Mellinger (2009) is used as the base layer to show the distribution of stars relative to the hydrogen in the Galaxy.

differences between interacting high-velocity clouds of Galactic versus extragalactic origin hints at potential differentiation between the two on large scales, and implies that the effects of turbulence may be highly influential and detectable in Galactic clouds. Typical surveys of high-velocity neutral hydrogen appear to only catch the very tip of the iceberg in the context of halo gas, highlighting bright condensations in a largely hidden sea of ubiquitous diffuse gas.

Overall, the studies in this thesis have revealed an active and dynamic Galaxy that maintains strong connections between its disk and the surrounding halo environment, in which neutral hydrogen remains a pivotal and powerful key to unlocking its evolutionary past and star-forming future. Future work further characterising the Milky Way in greater detail and determining the similarities with, and differences to, other galaxies both locally and at high redshift will undoubtedly shed new light on galaxy formation and evolution, revealing the Milky Way's (and thus our) place in an incredibly vast Universe.

Bibliography

Abbott D. C., 1982, ApJ, 263, 723

Acker A., Neiner C., 2003, A&A, 403, 659

Anathpindika S., 2011, NewA, 16, 323

Baba J., Asaki Y., Makino J., Miyoshi M., Saitoh T. R., Wada K., 2009, ApJ, 706, 471

Bagetakos I., Brinks E., Walter F., Blok W. D., Usero A., Leroy A., Rich J., Kennicutt R. C. J., 2011, AJ, 141, 23

Barnes D. G. et al., 2001, MNRAS, 322, 486

Bekhti N. B., Brüns C., Kerp J., Westmeier T., 2006, A&A, 457, 917

Bekhti N. B., Richter P., Winkel B., Kenn F., Westmeier T., 2009, A&A, 503, 483

Berkhuijsen E. M., 1971, A&A, 14, 359

Berkhuijsen E. M., Haslam C. G. T., Salter C. J., 1971, Astron. Astrophys., 14, 252

Blair W. P., Long K. S., 1997, ApJS, 108, 261

Bland-Hawthorn J., Cohen M., 2003, ApJ, 582, 246

Blitz L., Spergel D. N., Teuben P. J., Hartmann D., Burton W. B., 1999, ApJ, 514, 818

Boer K. D., Altan A., Bomans D., Lilienthal D., Moehler S., van Woerden H., Wakker B., Bregman J., 1994, A&A, 286, 925

Bol'Shev L., 1963, Theory of Probability & Its Applications, 8, 121

Boomsma R., Oosterloo T., Fraternali F., Hulst J. V. D., Sancisi R., 2008a, A&A, 490, 555

Boomsma R., Oosterloo T. A., Fraternali F., van der Hulst J. M., Sancisi R., 2008b, A&A, 490, 555

Bot C., Helou G., Boulanger F., Lagache G., Miville-Deschenes M.-A., Draine B., Martin P., 2009, ApJ, 695, 469

Bovy J., Hogg D. W., Rix H.-W., 2009, ApJ, 704, 1704

Bowen D. V., Blades J. C., 1993, ApJ, 403, L55

Braun R., Burton W. B., 1999, A&A, 341, 437

Bregman J. N., Miller E. D., Seitzer P., Cowley C. R., Miller M. J., 2013, ApJ, 766, 57

Brinks E., Bajaja E., 1986, A&A, 169, 14

Brown A. G. A., Hartmann D., Burton W. B., 1995, A&A, 300, 903

Bruhweiler F. C., Gull T. R., Kafatos M., Sofia S., 1980, ApJ, 238, L27

Brüns C., Kerp J., Kalberla P. M. W., Mebold U., 2000, A&A, 357, 120

Brüns C., Kerp J., Pagels A., 2001, A&A, 370, L26

Brüns C. et al., 2005, A&A, 432, 45

Brüns C., Westmeier T., 2004, A&A, 426, L9

Calabretta M. R., Staveley-Smith L., Barnes D. G., 2014, PASA, 31, 7

Cannon J. M. et al., 2011, ApJ, 735, 36

Casetti-Dinescu D. I., Bidin C. M., Girard T. M., Méndez R. A., Vieira K., Korchagin V. I., van Altena W. F., 2014, ApJL, 784, L37

Chen L., de Grijs R., Zhao J. L., 2007, AJ, 134, 1368

Cheng K.-S., Chernyshov D. O., Dogiel V. A., Ko C.-M., Ip W.-H., 2011, ApJL, 731, L17

Chevalier R. A., Gardner J., 1974, ApJ, 192, 457

Chiosi C., Bertelli G., Bressan A., 1992, ARA&A, 30, 235

Christiansen W. N., Hindman J. V., 1952, Obs, 72, 149

Chung A., Koribalski B., Bureau M., van Gorkom J. H., 2006, MNRAS, 370, 1565

Churchwell E. et al., 2009, PASP, 121, 213

Collaboration P. et al., 2011, A&A, 536, 24

Collins J. A., Shull J. M., Giroux M. L., 2007, ApJ, 657, 271

Combes F., Charmandaris V., 2000, A&A, 357, 75

Connors T. W., Kawata D., Gibson B. K., 2006, MNRAS, 371, 108

Cox D. P., Smith B. W., 1974, ApJL, 189, L105

Cram T. R., Giovanelli R., 1976, A&A, 48, 39

Crocker R. M., Aharonian F., 2011, PhRvL, 106, 101102

Crocker R. M., Jones D. I., Aharonian F., Law C. J., Melia F., Ott J., 2011, MNRAS, 411, L11

Croom S. M. et al., 2012, MNRAS, 421, 872

Crowther P. A., 2004, EAS Publications Series, 13, 1

Danly L., Albert C. E., Kuntz K. D., 1993, ApJL, 416, L29

Davies J., Sabatini S., Davies L., Linder S., Roberts S., Smith R., Evans R., 2002, MNRAS, 336, 155

Dawson J., McClure-Griffiths N., Kawamura A., Mizuno N., Onishi T., Mizuno A., Fukui Y., 2011, ApJ, 728, 127

Dawson J., McClure-Griffiths N., Wong T., Dickey J., Hughes A., Fukui Y., Kawamura A., 2013, ApJ, 763, 56

Dawson J. R., Mizuno N., Onishi T., McClure-Griffiths N. M., Fukui Y., 2008, MNRAS, 387, 31

de Boer K. S., Savage B. D., 1983, ApJ, 265, 210

de Gouveia Dal Pino E. M., Melioli C., D'Ercole A., Brighenti F., Raga A. C., 2009, Magnetic Fields in the Universe II: From Laboratory and Stars to the Primordial Universe, 36, 17

de Heij V., Braun R., Burton W. B., 2002, A&A, 391, 159

Dessauges-Zavadsky M., Combes F., Pfenniger D., 2007, A&A, 473, 863

Deul E. R., den Hartog R. H., 1990, A&A, 229, 362

Dewdney P. E., Hall P. J., Schilizzi R. T., Lazio T. J. L. W., 2009, Proceedings of the IEEE, 97, 1482

Dias W. S., Alessi B. S., Moitinho A., Lépine J. R. D., 2002, A&A, 389, 871

Diaz J., Bekki K., 2012, ApJ, 750, 36

Dickey J. et al., 2013, PASA, 30, 3

Dickey J. M., Lockman F. J., 1990, ARA&A, 28, 215

Dieter N. H., 1964, AJ, 69, 288

Dobler G., Finkbeiner D. P., Cholis I., Slatyer T., Weiner N., 2010, ApJ, 717, 825

Dopita M., Hart J., McGregor P., Oates P., Bloxham G., Jones D., 2007, Ap&SS, 310, 255

Dove J. B., Shull J. M., Ferrara A., 2000, ApJ, 531, 846

Dudziak G., Péquignot D., Zijlstra A. A., Walsh J. R., 2000, A&A, 363, 717

Eddington A. S., 1924, MNRAS, 84, 308

Egger R. J., Aschenbach B., 1995, A&A, 294, L25

Ehlerova S., Palous J., 1996, A&A, 313, 478

Ehlerová S., Palouš J., 2005, A&A, 437, 101

Ewen H. I., Purcell E. M., 1951, Nature, 168, 356

Feldt C., 1993, A&A, 276, 531

Fesen R. A., Blair W. P., Kirshner R. P., 1985, ApJ, 292, 29

Fich M., Blitz L., Stark A. A., 1989, ApJ, 342, 272

Field G. B., Saslaw W. C., 1965, ApJ, 142, 568

Figer D. F., 2005, Nature, 434, 192

Finkbeiner D. P., 2003, ApJS, 146, 407

Flöer L., Winkel B., 2012, PASA, 29, 244

Forbes D., 1996, AJ, 112, 1073

Ford H. A., Lockman F. J., McClure-Griffiths N. M., 2010, ApJ, 722, 367

Ford H. A., McClure-Griffiths N. M., Lockman F. J., Bailin J., Calabretta M. R., Kalberla P. M. W., Murphy T., Pisano D. J., 2008, ApJ, 688, 290

Fox A. J., Richter P., Wakker B. P., Lehner N., Howk J. C., Bekhti N. B., Bland-Hawthorn J., Lucas S., 2013, ApJ, 772, 110

Fox A. J., Savage B. D., Wakker B. P., Richter P., Sembach K. R., Tripp T. M., 2004, ApJ, 602, 738

Fox A. J. et al., 2014, ApJ, 787, 147

Franco J., Ferrini F., Barsella B., Ferrara A., 1991, ApJ, 366, 443

Fraternali F., Marasco A., Marinacci F., Binney J., 2013a, ApJ, 764, L21

Fraternali F., Marasco A., Marinacci F., Binney J., 2013b, ApJL, 764, L21

Frew D. J., Parker Q. A., 2010, PASA, 27, 129

Fujii K. et al., 2014, ApJ, 796, 123

Fukui Y., Kawamura A., 2010, ARA&A, 48, 547

Gaustad J. E., McCullough P. R., Rosing W., van Buren D., 2001, PASP, 113, 1326

Ghez A. et al., 2008, ApJ, 689, 1044

Gibson S. J., Taylor A. R., Higgs L. A., Dewdney P. E., 2000, ApJ, 540, 851

Gillessen S., Eisenhauer F., Trippe S., Alexander T., Genzel R., Martins F., Ott T., 2009, ApJ, 692, 1075

Giovanelli R., Haynes M. P., Kent B. R., Adams E. A. K., 2010, ApJL, 708, L22

Giovanelli R., Verschuur G., Cram T., 1973a, A&AS, 12, 209

Giovanelli R., Verschuur G. L., Cram T. R., 1973b, A&AS, 12, 209

Gómez G. C., 2006, AJ, 132, 2376

Green D. A., 2009, BASI, 37, 45

Gringel W., Barnstedt J., Boer K. D., Grewing M., Kappelmann N., Richter P., 2000, A&A, 358, L37

Gupta A., Mathur S., Krongold Y., Nicastro F., Galeazzi M., 2012, ApJ, 756, L8

Guseinov O., Yusifov I., 1985, Afz, 25, 525

Haffner L. et al., 2009, RvMP, 81, 969

Haffner L. et al., 2010, Astronomical Society of the Pacific Conference Series, 438, 388

Haffner L. M., 2005, Extra-Planar Gas, 331, 25

Haffner L. M., Reynolds R. J., Tufte S. L., Madsen G. J., Jaehnig K. P., Percival J. W., 2003, ApJS, 149, 405

Hartmann D., Burton W. B., 1997, Atlas of Galactic Neutral Hydrogen

Hatzidimitriou D., Stanimirovic S., Maragoudaki F., Staveley-Smith L., Dapergolas A., Bratsolis E., 2005, MNRAS, 360, 1171

Hausen N. R., Reynolds R. J., Haffner L. M., Tufte S. L., 2002, ApJ, 565, 1060

Heald G., Allan J., Zschaechner L., Kamphuis P., Rand R., Józsa G., Gentile G., 2011, Tracing the Ancestry of Galaxies (on the land of our ancestors), 277, 59

Heeschen D. S., 1955, ApJ, 121, 569

Heiles C., 1976, ApJ, 208, L137

Heiles C., 1979, ApJ, 229, 533

Heiles C., 1984, ApJS, 55, 585

Heiles C., 1987, ApJ, 315, 555

Heiles C., Haffner L. M., Reynolds R. J., 1999, New Perspectives on the Interstellar Medium, 168, 211

Heiles C., Troland T. H., 2003, ApJ, 586, 1067

Heitsch F., Putman M. E., 2009, ApJ, 698, 1485

Herbstmeier U., Mebold U., Snowden S. L., Hartmann D., Burton W. B., Moritz P., Kalberla P. M. W., Egger R., 1995, A&A, 298, 606

Hewett P., Irwin M., Skillman E., Foltz C., Willis J., Warren S., Walton N., 2003, ApJ, 599, L37

Higgs L. A., Kerton C. R., Knee L. B. G., 2001, AJ, 122, 3155

Hill A., Joung M., Low M.-M. M., Benjamin R., Haffner L., Klingenberg C., Waagan K., 2012, ApJ, 750, 104

Hill A. S., Haffner L. M., Reynolds R. J., 2009, ApJ, 703, 1832

Hill A. S., Mao S. A., Benjamin R. A., Lockman F. J., McClure-Griffiths N. M., 2013, ApJ, 777, 55

Hirth W., Mebold U., Mueller P., 1985, A&A, 153, 249

Hopp U., Schulte-Ladbeck R. E., Kerp J., 2003, MNRAS, 339, 33

Hsu W.-H., Putman M. E., Heitsch F., Stanimirović S., Peek J. E. G., Clark S. E., 2011, AJ, 141, 57

Hu E. M., 1981, ApJ, 248, 119

Hulsbosch A., Raimond E., 1966, BAN, 18, 413

Hulsbosch A. N. M., 1978, A&A, 66, L5

Hulsbosch A. N. M., Wakker B. P., 1988, A&AS, 75, 191

Hulst H. V. D., Muller C., Oort J., 1954, BAN, 12, 117

Humphreys R. M., 1978, Astrophys. J., 38, 309

Ivezic Z., Christodoulou D. M., 1997, ApJ, 486, 818

Jansky K., 1932, Radio Engineers

Jansky K., 1933a, PA, 41, 548

Jansky K., 1933b, Nature, 132, 66

Jin S., 2010, MNRAS, 408, L85

Jo Y.-S., Min K., Seon K., 2014, American Astronomical Society, 223

Johnson M., 2013, AJ, 145, 146

Johnston S. et al., 2007, PASA, 24, 174

Jones T., Ryu D., Tregillis I., 1996, ApJ, 473, 365

Joung M., Bryan G., Putman M., 2012, ApJ, 745, 148

Joung M., Putman M., Bryan G., Fernández X., Peek J., 2012, ApJ, 759, 137

Jurek R., 2012, PASA, 29, 251

Kalberla P. M. W., Burton W. B., Hartmann D., Arnal E. M., Bajaja E., Morras R., Pöppel W. G. L., 2005, A&A, 440, 775

Kalberla P. M. W., Haud U., 2006, A&A, 455, 481

Kalberla P. M. W. et al., 2010, A&A, 521, 17

Kamphuis J., Sancisi R., van der Hulst T., 1991, A&A, 244, L29

Kamphuis P., Peletier R. F., van der Kruit P. C., Heald G. H., 2011, MNRAS, 414, 3444

Kamphuis P. et al., 2013, MNRAS, 434, 2069

Kereš D., Katz N., Fardal M., Davé R., Weinberg D. H., 2009, MNRAS, 395, 160

Kereš D., Katz N., Weinberg D. H., Davé R., 2005, MNRAS, 363, 2

Kerp J., Burton W. B., Egger R., Freyberg M. J., Hartmann D., Kalberla P. M. W., Mebold U., Pietz J., 1999, A&A, 342, 213

Kerton C. R., 2005, ApJ, 623, 235

Kewley L. J., Dopita M. A., Sutherland R. S., Heisler C. A., Trevena J., 2001, ApJ, 556, 121

Kim S., Dopita M. A., Staveley-Smith L., Bessell M. S., 1999, AJ, 118, 2797

Kingsburgh R. L., Barlow M. J., 1994, MNRAS, 271, 257

Konz C., Brüns C., Birk G., 2002, A&A, 391, 713

Kroupa P., 2001, MNRAS, 322, 231

Kuilenburg J. V., 1972, A&AS, 5, 1

Kuntz K. D., Danly L., 1996, ApJ, 457, 703

Kwak K., Shelton R. L., Raley E. A., 2009, ApJ, 699, 1775

Lehner N., Howk J. C., 2010, ApJL, 709, L138

Lehner N., Howk J. C., 2011, Sci, 334, 955

Lehner N., Howk J. C., Thom C., Fox A. J., Tumlinson J., Tripp T. M., Meiring J. D., 2012, MNRAS, 424, 2896

Lehner N., Staveley-Smith L., Howk J. C., 2009, ApJ, 702, 940

Li D., Nan R., Pan Z., 2012, IAU Symposium, 291, 325

Liszt H., 2001, A&A, 371, 698

Lockman F., 2002, ApJ, 580, L47

Lockman F., Benjamin R., Heroux A., Langston G., 2008, ApJ, 679, L21

Lockman F. J., Murphy E. M., Petty-Powell S., Urick V. J., 2002, ApJS, 140, 331

Low M.-M. M., McCray R., 1988, ApJ, 324, 776

Madsen G., Reynolds R., Haffner L., 2006, ApJ, 652, 401

Madsen G. J., Reynolds R. J., 2005, ApJ, 630, 925

Maíz-Apellániz J., Walborn N. R., Galué H. Á., Wei L. H., 2004, ApJS, 151, 103

Marasco A., Fraternali F., Binney J., 2013, MNRAS, 419, 1107

Marasco A., Marinacci F., Fraternali F., 2013, MNRAS, 433, 1634

Marinacci F., Binney J., Fraternali F., Nipoti C., Ciotti L., Londrillo P., 2010, MNRAS, 404, 1464

Martins F., Schaerer D., Hillier D. J., 2005, A&A, 436, 1049

Mashchenko S., Thilker D., Braun R., 1999, A&A, 343, 352

Mason B. D., Gies D. R., Hartkopf W. I., Bagnuolo W. G., ten Brummelaar T., McAlister H. A., 1998, AJ, 115, 821

Massey P., Lang C. C., Degioia-Eastwood K., Garmany C. D., 1995, ApJ, 438, 188

Mathewson D., Meng S., Brundage W., Kraus J., 1966, AJ, 71, 863

Mathewson D. S., Cleary M. N., Murray J. D., 1974, ApJ, 190, 291

McClure-Griffiths N. et al., 2008, ApJ, 673, L143

McClure-Griffiths N. M., Dickey J. M., Gaensler B. M., Green A. J., 2001, ApJ, 562, 424

McClure-Griffiths N. M., Dickey J. M., Gaensler B. M., Green A. J., 2002, ApJ, 578, 176

McClure-Griffiths N. M., Dickey J. M., Gaensler B. M., Green A. J., Haverkorn M., 2006a, ApJ, 652, 1339

McClure-Griffiths N. M., Dickey J. M., Gaensler B. M., Green A. J., Haverkorn M., Strasser S., 2005, ApJS, 158, 178

McClure-Griffiths N. M., Dickey J. M., Gaensler B. M., Green A. J., Haynes R. F., Wieringa M. H., 2000, AJ, 119, 2828

McClure-Griffiths N. M., Ford A., Pisano D. J., Gibson B. K., Staveley-Smith L., Calabretta M. R., Dedes L., Kalberla P. M. W., 2006b, ApJ, 638, 196

McClure-Griffiths N. M., Green J. A., Hill A. S., Lockman F. J., Dickey J. M., Gaensler B. M., Green A. J., 2013, ApJL, 770, L4

McClure-Griffiths N. M., Madsen G. J., Gaensler B. M., Mcconnell D., Schnitzeler D. H. F. M., 2010, ApJ, 725, 275

McClure-Griffiths N. M. et al., 2009, ApJS, 181, 398

McCray R., Kafatos M., 1987, ApJ, 317, 190

McKee C. F., Ostriker J. P., 1977, ApJ, 218, 148

McSwain M. V., Gies D. R., 2005, ApJS, 161, 118

Mellinger A., 2009, PASP, 121, 1180

Mermilliod J., Paunzen E., 2003, A&A, 410, 511

Mermilliod J.-C., Maeder A., 1986, A&A, 158, 45

Meyerdierks H., 1991, A&A, 251, 269

Miller E. D., Bregman J. N., Wakker B. P., 2009, ApJ, 692, 470

Mirabel I., 1981, ApJ, 250, 528

Mirabel I. F., Morras R., 1984, ApJ, 279, 86

Miville-Deschênes M.-A., Boulanger F., Reach W. T., Noriega-Crespo A., 2005, ApJ, 631, L57

Miville-Deschênes M.-A., Lagache G., 2005, ApJS, 157, 302

Moss V. A., McClure-Griffiths N. M., Braun R., Hill A. S., Madsen G. J., 2012, MNRAS, 421, 3159

Moss V. A., McClure-Griffiths N. M., Murphy T., Pisano D. J., Kummerfeld J. K., Curran J. R., 2013, ApJS, 209, 12

Muller C. A., Oort J. H., 1951, Nature, 168, 357

Muller C. A., Oort J. H., Raimond E., 1963, Comptes Rendus l'Academie des Sciences, 257, 1661

Murali C., 2000, ApJ, 529, L81

Murphy T., Mauch T., Green A., Hunstead R. W., Piestrzynska B., Kels A. P., Sztajer P., 2007, MNRAS, 382, 382

Nan R. et al., 2011, IJMPD, 20, 989

Newton R. D. A., Kay S. T., 2013, MNRAS, 434, 3606

Nicastro F. et al., 2005, Nature, 433, 495

Nigra L., Stanimirović S., Gallagher J. S., Wood K., Nidever D., Majewski S., 2012, ApJ, 760, 48

Normandeau M., Taylor A. R., Dewdney P. E., 1996, Nature, 380, 687

Oey M. S., Watson A. M., Kern K., Walth G. L., 2005, AJ, 129, 393

Ogura K., Ishida K., 1975, PASJ, 27, 119

Olano C. A., 2008, A&A, 485, 457

Oort J. H., 1966, BAN, 18, 421

Oosterloo T., Fraternali F., Sancisi R., 2007, AJ, 134, 1019

Ortega V. G., Jilinski E., de la Reza R., Bazzanella B., 2009, AJ, 137, 3922

Park B.-G., Sung H., Kang Y. H., 2001, JKAS, 34, 149

Park G. et al., 2013, ApJ, 777, 14

Pawsey J., 1951, Nature, 168, 358

Pawsey J., Hill E., 1961, RPPh, 24, 69

Peek J., Putman M., Mckee C., Heiles C., Stanimirović S., 2007, ApJ, 656, 907

Peek J., Putman M., Sommer-Larsen J., 2008, ApJ, 674, 227

Peek J. E. G. et al., 2012, ApJS, 194, 20

Peek J. E. G., Heiles C., Putman M. E., Douglas K., 2009, ApJ, 692, 827

Perryman M. A. C. et al., 1997, A&A, 323, L49

Pidopryhora Y., Lockman F. J., Shields J. C., 2007, ApJ, 656, 928

Pier J., Harris H., Dahn C., Monet D., 1993, New Horizons from Multi-Wavelength Sky Surveys, 155, 175

Pisano D. J., Barnes D. G., Gibson B. K., Staveley-Smith L., Freeman K. C., Kilborn V. A., 2004, ApJ, 610, L17

Plöckinger S., Hensler G., 2012, A&A, 547, 43

Prisinzano L., Damiani F., Micela G., Sciortino S., 2005, A&A, 430, 941

Putman M., Grcevich J., Peek J., 2008, Formation and Evolution of Galaxy Disks, 396, 233

Putman M., Peek J., Joung M., 2012, ARA&A, 50, 491

Putman M. E., Bland-Hawthorn J., Veilleux S., Gibson B. K., Freeman K. C., Maloney P. R., 2003, ApJ, 597, 948

Putman M. E. et al., 2002, AJ, 123, 873

Putman M. E. et al., 1998, Nature, 394, 752

Putman M. E., Saul D. R., Mets E., 2011, MNRAS, 1786

Rand R. J., Stone J. M., 1996, AJ, 111, 190

Raymond J. C., Hester J. J., Cox D., Blair W. P., Fesen R. A., Gull T. R., 1988, ApJ, 324, 869

Reber G., 1940, ApJ, 91, 621

Reber G., 1944, ApJ, 100, 279

Reynolds R., 1990, ApJ, 348, 153

Reynolds R. J., Tufte S. L., Haffner L. M., Jaehnig K., Percival J. W., 1998, PASA, 15, 14

Richter P., de Boer K. S., Widmann H., Kappelmann N., Gringel W., Grewing M., Barnstedt J., 1999, Nature, 402, 386

Richter P., Sembach K., Wakker B., Savage B., 2001a, ApJ, 562, L181

Richter P., Sembach K. R., Wakker B. P., Savage B. D., Tripp T. M., Murphy E. M., Kalberla P. M. W., Jenkins E. B., 2001b, ApJ, 559, 318

Richter P., Westmeier T., Brüns C., 2005, A&A, 442, L49

Robitaille T., Whitney B., 2010, ApJ, 710, L11

Roy N., Chengalur J. N., Srianand R., 2006, MNRAS, 365, L1

Salpeter E. E., 1955, ApJ, 121, 161

Sancisi R., Fraternali F., Oosterloo T., van der Hulst T., 2008, A&ARv, 15, 189

Sanders D., Kartaltepe J., Kewley L., U V., Yuan T., Evans A., Armus L., Mazzarella J., 2009, Neutron Stars in Supernova Remnants, 408, 3

Sankrit R., Dixon W. V. D., 2007, PASP, 119, 284

Saul D. R. et al., 2012, ApJ, 758, 44

Sault R., Teuben P., Wright M., 1995, Astronomical Data Analysis Software and Systems IV, 77, 433

Savage B. D. et al., 1993, ApJ, 413, 116

Savage B. D., Sembach K. R., 1996, ARA&A, 34, 279

Schlegel D., Finkbeiner D., Davis M., 1998, ApJ, 500, 525

Sembach K., Howk J., Savage B., Shull J., 2001, AJ, 121, 992

Sembach K., Savage B., Lu L., Murphy E., 1995, ApJ, 451, 616

Sembach K. R., Gibson B. K., Fenner Y., Putman M. E., 2002, ApJ, 572, 178

Seon K.-I., Witt A., Kim I.-J., Shinn J.-H., Edelstein J., Min K.-W., Han W., 2011, ApJ, 743, 188

Shapiro P. R., Field G. B., 1976, ApJ, 205, 762

Shelton R., Kwak K., Henley D., 2012, ApJ, 751, 120

Shull J., Jones J., Danforth C., Collins J., 2009, ApJ, 699, 754

Shull J. M., 1995, Astronomical Society of the Pacific, 73, 365

Shull J. M., Slavin J. D., 1994, ApJ, 427, 784

Siegel M. H., Majewski S. R., Gallart C., Sohn S. T., Kunkel W. E., Braun R., 2005, ApJ, 623, 181

Simon J. D., Blitz L., 2002, ApJ, 574, 726

Smirnov N., 1944, Uspekhi Matematicheskikh Nauk, 10, 179

Smith G., 1963, BAN, 17, 203

Smith N., 2006, MNRAS, 367, 763

Smoker J. V., Fox A. J., Keenan F. P., 2011, MNRAS, 415, 1105

Smoker J. V. et al., 2004, MNRAS, 352, 1279

Snowden S. L. et al., 1995, ApJ, 454, 643

Spitzer L., 1956, ApJ, 124, 20

Stalbovsky O. I., Shevchenko V. S., 1981, AZh, 58, 45

Stanimirović S. et al., 2006, ApJ, 653, 1210

Stark A. A., Gammie C. F., Wilson R. W., Bally J., Linke R. A., Heiles C., Hurwitz M., 1992, ApJS, 79, 77

Steiman-Cameron T. Y., Wolfire M., Hollenbach D., 2010, ApJ, 722, 1460

Sternberg A., McKee C. F., Wolfire M. G., 2002, ApJS, 143, 419

Su M., Slatyer T. R., Finkbeiner D. P., 2010, ApJ, 724, 1044

Suad L. A., Caiafa C. F., Arnal E. M., Cichowolski S., 2014, Astro, 564, 116

Sung H., Chun M.-Y., Bessell M. S., 2000, AJ, 120, 333

Tang S., Wang Q., Lu Y., Mo H., 2008, MNRAS, 392, 77

Taylor A. R., Stil J. M., Sunstrum C., 2009, ApJ, 702, 1230

Taylor G. B., Carilli C. L., Perley R. A., 1999, Synthesis Imaging in Radio Astronomy II, 180

Tenorio-Tagle G., Bodenheimer P., 1988, ARA&A, 26, 145

Testori J. C., Reich P., Reich W., 2008, A&A, 484, 733

Tetzlaff N., Neuhäuser R., Hohle M. M., 2011, MNRAS, 410, 190

Thilker D. A., Braun R., Walterbos R. A. M., Corbelli E., Lockman F. J., Murphy E., Maddalena R., 2004, ApJ, 601, L39

Tripp T. M., Song L., 2012, ApJ, 746, 173

Tripp T. M. et al., 2003, AJ, 125, 3122

Tufte S. L., Reynolds R. J., Haffner L. M., 1998, Astrophysics From Antarctica Edited by Giles Novak and Randy Landsberg; ASP Conference Series; Vol. 141; 1998, 141, 169

Tufte S. L., Wilson J. D., Madsen G. J., Haffner L. M., Reynolds R. J., 2002, ApJ, 572, L153

Tumlinson J. et al., 2011, ApJ, 733, 111

Tweedy R. W., Martos M. A., Noriega-Crespo A., 1995, ApJ, 447, 257

van Woerden H., Rougoor G., Oort J., 1957, CRAS, 244, 1691

van Woerden H., Wakker B. P., 2004, High Velocity Clouds. Edited by Hugo van Woerden, 312, 195

Vogt F., Dopita M., Kewley L., 2013, ApJ, 768, 151

Wakker B., 2001, ApJS, 136, 463

Wakker B., Howk C., Schwarz U., van Woerden H., Beers T., Wilhelm R., Kalberla P., Danly L., 1996, ApJ, 473, 834

Wakker B. P., 1991, A&A, 250, 499

Wakker B. P., 2004, Ap&SS, 289, 381

Wakker B. P., 2006, ApJS, 163, 282

Wakker B. P., Boulanger F., 1986, A&A, 170, 84

Wakker B. P., Murphy E. M., van Woerden H., Dame T. M., 1997, ApJ, 488, 216

Wakker B. P., Oosterloo T. A., Putman M. E., 2002, AJ, 123, 1953

Wakker B. P., van Woerden H., 1991, A&A, 250, 509

Wakker B. P., van Woerden H., 1997, ARA&A, 35, 217

Wakker B. P. et al., 2007, ApJ, 670, L113

Wannier P., Wrixon G. T., Wilson R. W., 1972, A&A, 18, 224

Warren S. et al., 2011, ApJ, 738, 10

Weaver H., Williams D. R. W., 1973, A&AS, 8, 1

Weaver R., Mccray R., Castor J., Shapiro P., Moore R., 1977, ApJ, 218, 377

Weidner C., Vink J. S., 2010, A&A, 524, 98

Weiner B., Vogel S., Williams T., 2001, Gas and Galaxy Evolution, 240, 515

Weisz D. R., Skillman E. D., Cannon J. M., Walter F., Brinks E., Ott J., Dolphin A. E., 2009, ApJL, 691, L59

Werk J. K., Putman M. E., Meurer G. R., Santiago-Figueroa N., 2011, ApJ, 735, 71

Werner K., Dreizler S., Wolff B., 1995, A&A, 298, 567

West J. L., English J., Normandeau M., Landecker T. L., 2007, ApJ, 656, 914

Westmeier T., Braun R., Brüns C., Kerp J., Thilker D. A., 2007, New Astronomy Reviews, 51, 108

Westmeier T., Braun R., Thilker D., 2005, A&A, 436, 101

Westmeier T., Brüns C., Kerp J., 2008, MNRAS, 390, 1691

Westmeier T., Koribalski B., Braun R., 2013, MNRAS, 434, 3511

Whiting M., 2012, MNRAS, 421, 3242

Williams R. J., Mathur S., Poindexter S., Elvis M., Nicastro F., 2012, AJ, 143, 82

Willman B., Dalcanton J., Ivezić Ž., Schneider D., York D., 2002, AJ, 124, 2600

Wilson W. E. et al., 2011, MNRAS, 416, 832

Winkel B., Bekhti N. B., Darmstädter V., Flöer L., Kerp J., Richter P., 2011, Astro, 533, 105

Witt A. N., Gold B., Barnes F. S., DeRoo C. T., Vijh U. P., Madsen G. J., 2010, ApJ, 724, 1551

Wolfe S., Pisano D., Lockman F., Mcgaugh S., Shaya E., 2013a, Nature, 497, 224

Wolfe S. A., Pisano D. J., Lockman F. J., McGaugh S. S., Shaya E. J., 2013b, Nature, 497, 224

Wolfire M. G., McKee C. F., Hollenbach D., Tielens A. G. G. M., 1995, ApJ, 453, 673

Wood K., Hill A., Joung M., Low M.-M. M., Benjamin R., Haffner L., Reynolds R., Madsen G., 2010, ApJ, 721, 1397

Wood K., Mathis J. S., 2004, MNRAS, 353, 1126

Yang H., Ruszkowski M., Zweibel E., 2014, MNRAS, 436, 2734

Yao Y., Shull J. M., Danforth C. W., 2011, ApJL, 728, L16

Yoshizawa A. M., Noguchi M., 2003, MNRAS, 339, 1135